ISSN 0368-0797
eISSN 2410-2091

МИСИС
УНИВЕРСИТЕТ НАУКИ И ТЕХНОЛОГИЙ

СибГИУ
Сибирский государственный индустриальный университет

ИЗВЕСТИЯ ВЫСШИХ УЧЕБНЫХ ЗАВЕДЕНИЙ ЧЕРНАЯ МЕТАЛЛУРГИЯ

IZVESTIYA. FERROUS METALLURGY

fermet.misis.ru

2023 Том Vol. 66 № No. 5

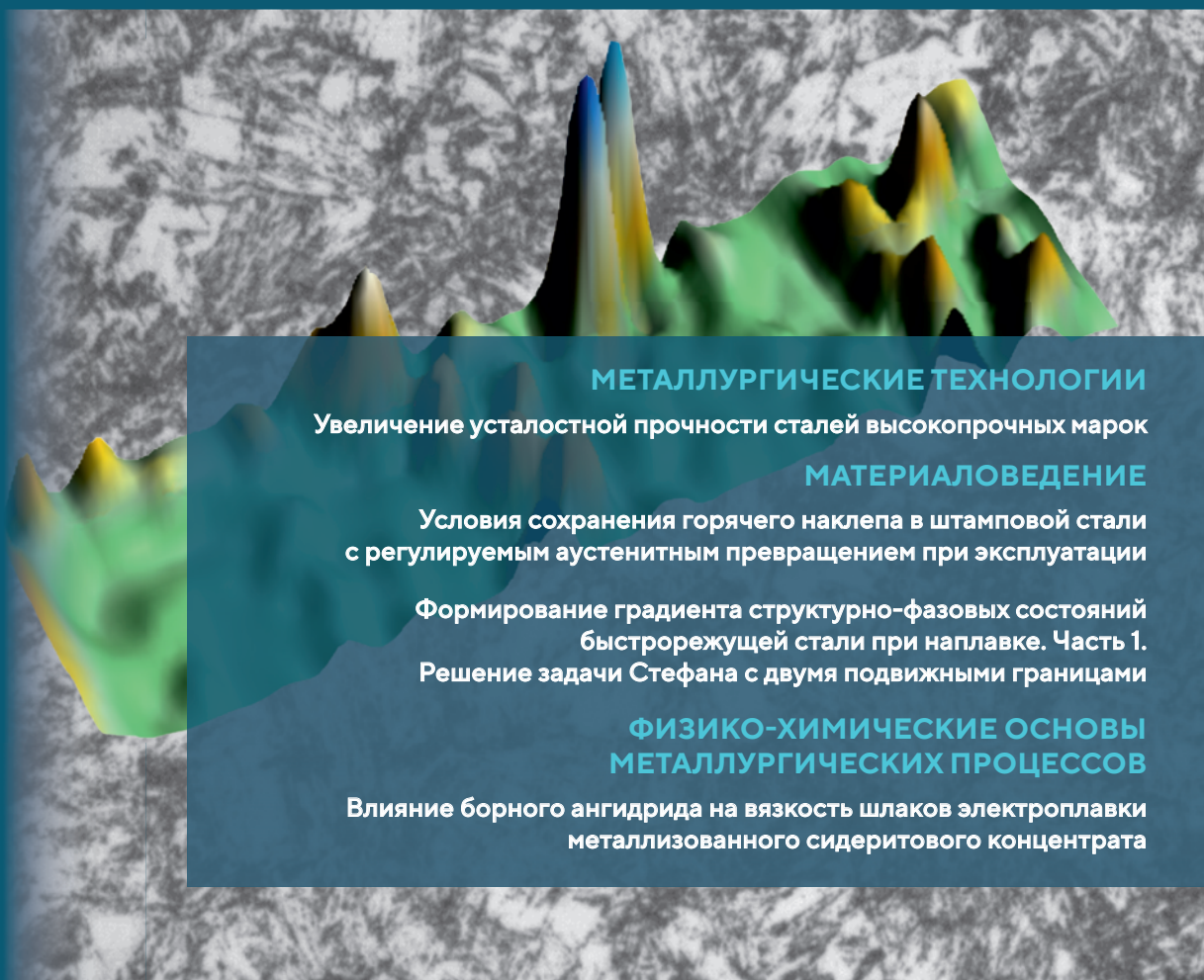

МИСИС УНИВЕРСИТЕТ

СибГИУ
Сибирский государственный индустриальный университет

ISSN 0368-0797
eISSN 2410-2091

ИЗВЕСТИЯ ВЫСШИХ УЧЕБНЫХ ЗАВЕДЕНИЙ ЧЕРНАЯ МЕТАЛЛУРГИЯ

Научно-технический журнал

Издается с января 1958 г. Выпускается 6 раз в год

2023 Том Vol. 66 № No. 5

IZVESTIYA FERROUS METALLURGY

Scientific and Technical Journal

Published since January 1958. Issued 6 times a year

IZVESTIYA FERROUS METALLURGY

www.fermet.misis.ru

ISSN 0368-0797 *(Print)* ISSN 2410-2091 *(Online)*

Alternative title:

Izvestiya vuzov. Chernaya metallurgiya

Founders:

MISIS
UNIVERSITY OF SCIENCE AND TECHNOLOGY

SibSIU
Siberian State Industrial University

Publisher:

National University of Science and Technology "MISIS"

Editorial Office Address:

in Moscow
4 Leninskii Ave., Moscow 119049, Russian Federation
National University of Science and Technology "MISIS"
Tel.: +7 (495) 638-44-11
E-mail: fermet.misis@mail.ru, ferrous@misis.ru

in Novokuznetsk
42 Kirova Str., Novokuznetsk, Kemerovo Region – Kuzbass
654007, Russian Federation
Siberian State Industrial University
Tel.: +7 (3843) 74-86-28 *E-mail*: redjizvz@sibsiu.ru

In accordance with paragraph 5 of the Rules for the formation of the Higher Attestation Comission list journal "Izvestiya. Ferrous metallurgy" is included in the list of leading peer-reviewed scientific journals, publication in which is taken into account in the defense of candidate and doctoral dissertations, as indexed in internatonal data bases.

Indexed: Scopus, Russian Science Citation Index (RSCI), Research Bible, Chemical Abstracts, OCLC and Google Scholar

Registered in Federal Service for Supervision in the Sphere of Mass Communications **PI number FS77-35456**.

ИЗВЕСТИЯ
ВЫСШИХ УЧЕБНЫХ ЗАВЕДЕНИЙ
ЧЕРНАЯ МЕТАЛЛУРГИЯ

www.fermet.misis.ru

ISSN 0368-0797 *(Print)* ISSN 2410-2091 *(Online)*

Варианты названия:

Известия вузов. Черная металлургия

Izvestiya. Ferrous Metallurgy

Учредители:

МИСИС
УНИВЕРСИТЕТ НАУКИ И ТЕХНОЛОГИЙ

СибГИУ
Сибирский государственный индустриальный университет

Издатель:

Национальный исследовательский технологический университет «МИСИС»

Адреса подразделений редакций:

в Москве
Россия, 119049, Москва, Ленинский просп., д. 4, стр. 1
Национальный исследовательский технологический университет «МИСИС»
Тел.: +7 (495) 638-44-11 *E-mail*: ferrous@misis.ru

в Новокузнецке
Россия, 654007, Новокузнецк,
Кемеровская обл. – Кузбасс, ул. Кирова, зд. 42
Сибирский государственный индустриальный университет
Тел.: +7 (3843) 74-86-28 *E-mail:* redjizvz@sibsiu.ru

В соответствии п. 5 Правил формирования перечня ВАК журнал «Известия вузов. Черная металлургия» входит в перечень ведущих рецензируемых научных журналов и изданий, публикация в которых учитывается при защитах кандидатских и докторских диссертаций как индексируемый в МБД.

Индексирование: Scopus, Russian Science Citation Index (RSCI), Research Bible, Chemical Abstracts, OCLC и Google Scholar

Зарегистрирован Федеральной службой по надзору в сфере связи и массовых коммуникаций **ПИ № ФС77-35456**.

Izvestiya. Ferrous Metallurgy.
2023;66(5)

Известия вузов. Черная металлургия.
2023;66(5)

CONTENTS / СОДЕРЖАНИЕ

METALLURGICAL TECHNOLOGIES

ECOLOGY AND RATIONAL USE OF NATURAL RESOURCES

MATERIALS SCIENCE

МЕТАЛЛУРГИЧЕСКИЕ ТЕХНОЛОГИИ

ЭКОЛОГИЯ И РАЦИОНАЛЬНОЕ ПРИРОДОПОЛЬЗОВАНИЕ

МАТЕРИАЛОВЕДЕНИЕ

CONTENTS *(Continuation)* / СОДЕРЖАНИЕ *(продолжение)*

PHYSICO-CHEMICAL BASICS OF METALLURGICAL PROCESSES

INFORMATION TECHNOLOGIES AND AUTOMATIC CONTROL IN FERROUS METALLURGY

BASED ON THE MATERIALS OF THE INTERNATIONAL CONFERENCE "SCIENTIFIC AND PRACTICAL SCHOOL FOR YOUNG METALLURGISTS"

ФИЗИКО-ХИМИЧЕСКИЕ ОСНОВЫ МЕТАЛЛУРГИЧЕСКИХ ПРОЦЕССОВ

ИНФОРМАЦИОННЫЕ ТЕХНОЛОГИИ И АВТОМАТИЗАЦИЯ В ЧЕРНОЙ МЕТАЛЛУРГИИ

ПО МАТЕРИАЛАМ МЕЖДУНАРОДНОЙ КОНФЕРЕНЦИИ «НАУЧНО-ПРАКТИЧЕСКАЯ ШКОЛА ДЛЯ МОЛОДЫХ МЕТАЛЛУРГОВ»

METALLURGICAL TECHNOLOGIES / МЕТАЛЛУРГИЧЕСКИЕ ТЕХНОЛОГИИ

UDC 621.791.75
DOI 10.17073/0368-0797-2023-5-516-521

Original article
Оригинальная статья

Changes in structure, hardness and crack resistance of plasma-strengthened steel 65G

I. M. Kossanova[1], A. T. Kanayev[1], T. A. Tolkynbayev[2], M. A. Jaxymbetova[2], T. E. Sarsembaeva[1]

[1] **S. Seifullin Kazakh AgroTechnical University** (62 Zhenis Ave., Astana 010000, Republic of Kazakhstan)
[2] **L.N. Gumilev Eurasian National University** (2 Satpaeva Str., Astana 010008, Republic of Kazakhstan)

ind_jm@mail.ru

Abstract. The present paper describes the research of structure, hardness and crack resistance indicators before and after plasma treatment of 65G steel of a ploughshare part. As a result of plasma treatment, we obtained the modified layer with increased hardness in the range of 980 – 3558 HV with increase in 3.6 times. Metallographic studies showed that pearlitic-ferritic structure of the original metal transforms into needle martensite with high hardness and strength due to plasma hardening. It is recommended to determine the impact toughness by the Drozdowski method, in which a fatigue crack is pre-created on a special vibrator. Also, before the fatigue crack was grown, lateral *V*-shaped notches of different depths were made on the sample lateral surface. The relative crack length, λ, varied from 0.27 to 0.65. According to the results of compression tests, it was found that there was a small movement of cracks in the hardened samples in the range from 1.3 to 5.6 mm. The initial unstrengthened samples are in a more brittle state than the quenched ones, and accordingly, significant fracture is observed in the conditions of artificial cracking. The evaluation of 65G steel samples for crack resistance by impact bending tests with subsequent oscillographing showed that plasma hardening inhibits crack growth by increasing impact toughness. Thus, the use of plasma hardening is effective in surface hardening of 65G steel, in particular ploughshares which are constantly exposed to mechanical stresses, friction and wear.

Keywords: steel, hardness, plasma treatment, surface layer, microhardness, crack resistance assessment, impact bending test

For citation: Kossanova I.M., Kanayev A.T., Tolkynbayev T.A., Jaxymbetova M.A., Sarsembaeva T.E. Changes in structure, hardness and crack resistance of plasma-strengthened steel 65G. *Izvestiya. Ferrous Metallurgy*. 2023;66(5):516–521.
https://doi.org/10.17073/0368-0797-2023-5-516-521

Исследование изменения структуры, показателей твердости и трещиностойкости плазменно-упрочненной стали 65Г

И. М. Косанова[1], А. Т. Канаев[1], Т. А. Толкынбаев[2], М. А. Джаксымбетова[2], Т. Е. Сарсембаева[1]

[1] **Казахский агротехнический университет имени Сакена Сейфуллина** (Казахстан, 010000, Астана, пр. Женис, 62)
[2] **Евразийский национальный университет им. Л.Н. Гумилева** (Казахстан, 010008, Астана, ул. Сатпаева, 2)

ind_jm@mail.ru

Аннотация. Проведены исследования структуры, показателей твердости и трещиностойкости до и после плазменной обработки стали марки 65Г лемешной части плуга. В результате плазменной обработки получен модифицированный слой с повышенной в 3,6 раза твердостью в интервале 980 – 3558 HV. Металлографические исследования показали, что перлитно-ферритная структура исходного металла вследствие плазменной закалки превращается в игольчатый мартенсит с высокими твердостью и прочностью. Усталостную трещину на образцах создавали на вибраторе Дроздовского. Перед выращиванием усталостной трещины на боковую поверхность образца наносились боковые *V*-образные надрезы различной глубины. Относительная длина трещины λ изменялась в пределах от 0,27 до 0,65. По результатам испытаний на сжатие установлено небольшое перемещение трещин в закаленных образцах в диапазоне 1,3 – 5,6 мм. Исходные неупрочненные образцы находятся в более хрупком состоянии, чем закаленные, соответственно наблюдается значительное разрушение их в условиях нанесения искусственной трещины. Проведенная оценка образцов стали 65Г на трещиностойкость путем испытания на ударный изгиб с последующим осциллографированием показала, что плазменная закалка способствует торможению увеличения трещины за счет роста ударной вязкости. Таким образом, применение плазменной закалки эффективно при поверхностном

упрочнении стали марки 65Г, в частности лемехов плуга, которые постоянно подвергаются механическим воздействиям, трению и износу.

Ключевые слова: сталь, твердость, плазменная обработка, поверхностный слой, микротвердость, оценка трещиностойкости, испытание на ударный изгиб

Для цитирования: Косанова И.М., Канаев А.Т., Толкынбаев Т.А., Джаксымбетова М.А., Сарсембаева Т.Е. Исследование изменения структуры, показателей твердости и трещиностойкости плазменно-упрочненной стали 65Г. *Известия вузов. Черная металлургия*. 2023;66(5):516–521. https://doi.org/10.17073/0368-0797-2023-5-516-521

Introduction

In Kazakhstan today, efforts are underway to enhance the quality of machinery and components through studies focused on the strength properties achieved by employing plasma hardening techniques on heavily stressed parts. The use of the promising method of plasma treatment appears rational for enhancing strength parameters, such as hardness, wear resistance, and crack resistance [1; 2]. This method impacts solely on the surface layer of the components, avoiding deformation of the metal and facilitating the creation of a modified layer exhibiting high strength characteristics on the product's surface. Alterations in the structure and properties of the surface layer take place under conditions of ultra-rapid heating and cooling rates (ranging from 10^3 to 10^5 K/s) and brief exposure to the processed material [3 – 5].

Materials and methods

The research focused on studying steel 65G, specifically the ploughshare component of a plough, designed to slice through soil layers and consistently subjected to friction and wear [6; 7].

Templates were cut using a Labotom-3 cutting machine from Struers (Switzerland). Throughout the cutting process, both the sample and cutting disc were cooled using water and a specialized lubricant to prevent oxidation [8; 9]. Following the cutting of appropriately sized samples, the steel's chemical composition was analyzed to determine the presence of additives, utilizing a Niton XL2 *X*-ray fluorescence analyzer (Table 1).

Plasma hardening was performed using a UDGZ-200 plasma hardening facility. This facility operates by employing indirect plasma arc technology, enabling the heating of a 1 – 2 mm surface area without causing internal deformations to the components [10 – 12].

The steel surface was examined using a Carl Zeiss metallographic microscope with a 200× magnification level.

The surface hardness of the samples was measured using a Wilson VH 1150 Vickers hardness macro tester, employing an indenter load of 30 kg.

Impact bending tests were conducted following the guidelines outlined in State Standard GOST 9454–78, incorporating measurements of impact strength. This method involves the deliberate initiation of sample fracture at a point of concentration in the middle by a single strike from a pendulum pile driver. Impact tests were performed using a KM-30 pendulum impact driver, employing impact samples sized at 6.5×11.5×55 mm. To induce fatigue cracks on the samples, a Drozdowsky vibrator was utilized, resulting in a relative crack length λ ranging from 0.27 to 0.65 [13 – 15]. Evaluation of impact strength under assured plane deformation conditions was conducted on samples featuring two additional lateral *V*-shaped notches, each with a depth of 1.0 mm. This assessment of impact toughness on notched samples allows for the determination of the specific work involved in crack propagation during fracture under plane-strain state (PSS) conditions [16 – 18].

Results and discussion

Metallographic examinations have revealed that the mechanical attributes such as strength, hardness, and crack resistance of plasma-hardened components are influenced by the configuration, dimensions, and alignment of subgrains (Fig. 1).

The structural-phase analysis indicated that the initial metal comprises pearlite grains and ferrite. However, through the process of plasma hardening, these structures undergo a transformation into acicular martensite, exhibiting heightened hardness and improved crack resistance [19; 20].

Table 1

Results of spectral analysis of 65G steel samples

Таблица 1. **Результаты спектрального анализа образцов стали 65Г**

Sample No.	Content of dopants, wt. %	±2σ
1	0.840 Mn	0.122 Mn
2	0.676 Mn	0.113 Mn
3	0.757 Mn; 0.142 Cu	0.127 Mn; 0.069 Cu
4	0.640 Mn; 0.104 Cr	0.112 Mn; 0.043 Cr
5	0.551 Mn	0.102 Mn
6	0.585 Mn	0.102 Mn
7	1.03 Mn	0.130 Mn
8	0.739 Mn; 0.148 Ti	0.116 Mn; 0.064 Ti
9	0.684 Mn	0.103 Mn

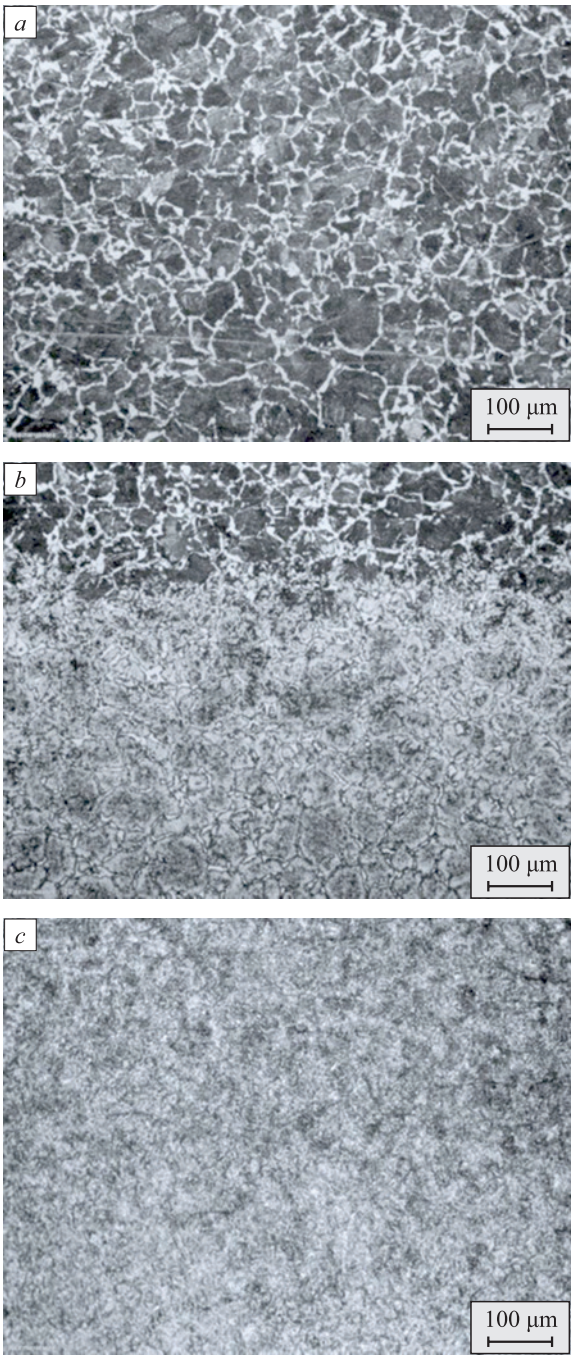

Fig. 1. Metallographic structure of 65G steel after surface plasma hardening:
a – base metal; *b* – transition layer; *c* – hardened layer

Рис. 1. Металлографическая структура стали 65Г после поверхностной плазменной закалки:
a – основной металл; *b* – переходной слой; *c* – закаленный слой

Material hardness measurement

Table 2 outlines the outcomes of hardness measurements conducted both before and after the plasma treatment of 65G steel.

The data presented demonstrate a notable elevation in the hardness of 65G steel resulting from plasma quenching. The average hardness value before and after hardening was derived from three measurements for each sample, showcasing an approximate 3.6-fold increase in hardness.

Table 2

Results of hardness measurements on the surface of 65G steel samples

Таблица 2. **Результаты измерений твердости на поверхности образцов стали 65Г**

Sample No.	Plasma treatment at the measurement site	HV_{30}			Average HV_{30}
		1	2	3	
1	W/o treatment	484.7	422.7	653.6	520.3
	With treatment	1519.7	1780.2	2398.5	1899.5
2	W/o treatment	764.6	762.9	698.3	741.9
	With treatment	3423.5	2476.8	1931.1	2610.5
3	W/o treatment	609.0	640.0	621.0	623.3
	With treatment	2348.0	1483.9	1766.8	1866.2
4	W/o treatment	553.4	354.4	855.3	587.7
	With treatment	3554.3	4589.2	3467.7	3870.4
5	W/o treatment	368.5	345.1	368.2	360.6
	With treatment	554.1	686.0	900.5	713.5
6	W/o treatment	418.6	355.3	344.4	372.8
	With treatment	980.8	2418.5	2832.3	2077.2
7	W/o treatment	404.5	370.4	361.7	378.9
	With treatment	1407.2	960.5	860.7	1076.1
8	W/o treatment	998.3	453.1	1287.9	913.1
	With treatment	1133.4	1317.6	2302.8	1584.6

Following the plasma hardening process, the crack resistance of the steel was evaluated via impact bending tests accompanied by oscillography. The impact strength of the hardened samples was recorded as 127, 116, 110, 104, 98, 106, 94 and 102 J/cm^2.

Fig. 2 illustrates the findings of impact strength studies correlating with crack length. Notably, a gradual escalation in impact toughness is observed as the initiator crack length increases.

Using the outcomes from fracture analyses, the primary dynamic test characteristic, impact strength *KCT*, was calculated.

Fig. 3 displays the assessment results of impact toughness for 65G steel samples before and after plasma hardening. A dynamic growth of *KCT* following plasma quenching is evident, signifying its role in impeding further crack propagation by elevating the *KCT*. Consequently, the original samples exhibit a comparatively more brittle state than the quenched ones, highlighting a

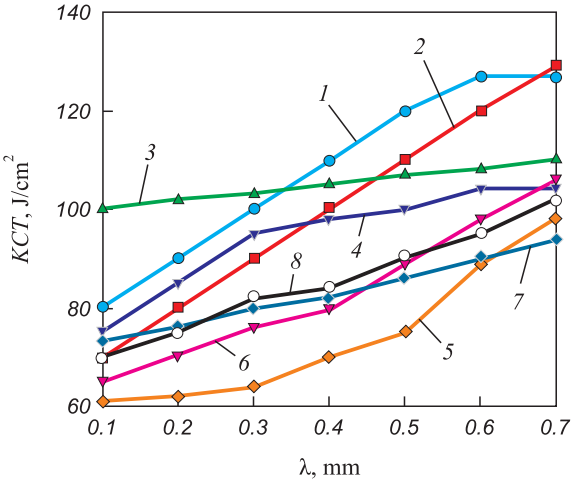

Fig. 2. Dependence of impact strength on crack length (samples *1* – *8*)

Рис. 2. Зависимость ударной вязкости от длины трещины (образцы *1* – *8*)

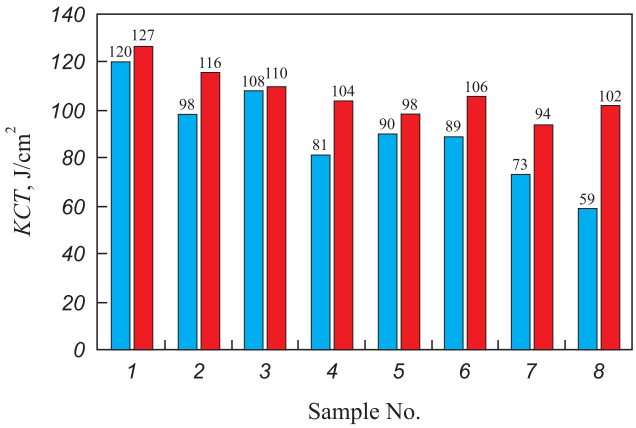

Fig. 3. Diagram of dynamic crack resistance of initial (■) and hardened (■) samples

Рис. 3. Диаграмма динамической трещиностойкости исходных (■) и закаленных (■) образцов

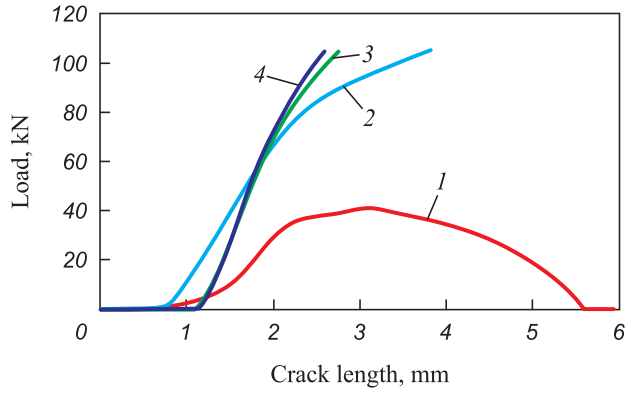

Fig. 4. Cracks' length at linear load (hardened samples *1* – *4*)

Рис. 4. Длина трещин при линейной нагрузке (закаленные образцы *1* – *4*)

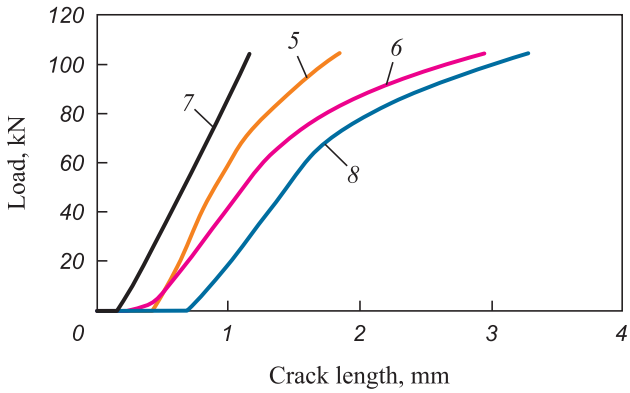

Fig. 5. Cracks' length at linear load (hardened samples *5* – *8*)

Рис. 5. Длина трещин при линейной нагрузке (закаленные образцы *5* – *8*)

substantial vulnerability to failure under plane deformation conditions [21; 22].

During the compression testing of samples under a linear load of up to 120 kN, crack displacement within the range of 1.3 – 5.6 mm was observed (Figs. 4, 5).

The observed crack movement led to a slight reduction in the live cross-sectional area of the sample. Consequently, an increase in the work of fracture (A_p) is evident (Fig. 4, 5).

Conclusions

Metallographic examinations conducted on 65G steel revealed that upon plasma hardening of its surface within a hardened zone of 2 mm thickness, a gradient-layer structure with varying hardness spanning from 980 to 3558 HV is formed. This process induces a notable increase in microhardness, reaching up to 3.6 times, a significantly higher enhancement compared to other hardening methods. For example, electric plasma hardening resulted in an increase in hardness by 2.16 times.

Investigations into impact toughness and the behavior of impact-induced cracks indicated that plasma arc hardening effectively impedes the dynamic expansion of cracks within the surface layer.

Thus, the study outcomes affirm the viability and effectiveness of employing plasma arc hardening as a means to fortify the surface layer of heavily stressed components, specifically exemplified in the case of 65G steel.

References / Список литературы

1. Kossanova I.M., Kanayev A.T., Jaxymbetova M.A., Akhmedyanov A.U., Kirgizbayeva K.Zh. Effect of electrolytic-plasma surface treatment on structure, mechanical, and tribological properties of grade 1 wheel steel. *Metallurgist*. 2022;66(7):69–73. https://doi.org/10.1007/s11015-022-01393-0
2. Korotkov V.A. Influence of plasma quenching on the wear resistance of 45 and 40X steel. *Russian Engineering*

Research. 2016;36(11):916–919.
https://doi.org/10.3103/S1068798X16110125

3. Kanayev A.T., Jaxymbetova M.A., Kossanova I.M. Quantitative assessment of the yield stress of ferrite-pearlitic steels by structure parameters. *News of the National Academy of Sciences of the Republic of Kazakhstan*. 2021;3(447):65–71. https://doi.org/10.32014/2021.2518-170X.64
4. Xiang Y., Yu D., Cao X., Liu Y., Yao J. Effects of thermal plasma surface hardening on wear and damage properties of rail steel. *Journal of Engineering Tribology*. 2017;232(7): 787–796. https://doi.org/10.1177/1350650117729073
5. Jaxymbetova M., Kanayev A., Kossanova I., Mazur I., Akhmedyanov A., Kirgizbayeva K. Improvement of the mechanical properties of reinforcing bar steel by combined deformation-heat treatment. *International Review of Mechanical Engineering*. 2022;16(9):460–466. https://doi.org/10.15866/ireme.v16i9.21521
6. Toktarbayeva G.M., Alpysbayev S.K., Rakhadilov B.K., Satbayeva Z.K., Zhaparova M.S. Effect of electrolyte-plasma surface hardening on the structure and properties of 40KhN steel. *Vestnik VKGTU*. 2020;87(1):200–205. (In Russ.).

   Токтарбаева Г.М., Алпысбаев С.К., Рахадилов Б.К., Сатбаева З.А., Жапарова М.С. Влияние электролитно-плазменного упрочнения поверхности на структуру и свойства стали 40ХН. *Вестник ВКГТУ*. 2020;87(1):200–205.
7. Petrov S.V., Saakov A.G. Technology and equipment for plasma surface hardening of heavy-duty parts. *Materials and Manufacturing Processes*. 2017;17(3)363–378. https://doi.org/10.1081/AMP-120005382
8. Korotkov V.A., Ananyev S.A., Shekurov A.V. Investigation of the effect of the cooling rate on the structure and mechanical properties of metal in plasma quenching. *Welding International*. 2014;28(2):140–142. https://doi.org/10.1080/09507116.2013.796665
9. Q'Donnelly B.E., Reuben R.L., Baker T.N. Quantitative assessment of strengthening parameters in ferrite-pearlite steels from microstructural measurements. *Metals Technology*. 2013;11(1):45–51. https://doi.org/10.1179/030716984803274837
10. Ramazanova Zh.M., Kirgizbayeva K.Zh., Akhmedyanov A.U., Jaxymbetova M.A. Influence of the process of microplasma treatment in electrolyte solutions on the oxide coating properties. *International Journal of Mechanical Engineering and Technology*. 2018;9(12):709–721.
11. Yong X., Yu D., Li Q., Huabei P., Xiuquan C., Jin Ya. Effects of thermal plasma jet heat flux characteristics on surface hardening. *Journal of Materials Processing Technology*. 2015;226(12):238–246. https://doi.org/10.1016/j.jmatprotec.2015.07.022
12. Bespalova A., Lebedev V., Florenkova O., Knysh A. Increasing efficiency of plasma hardening by local cooling of surface by air with negative temperature. *Eastern-European Journal of Enterprise Technologies*. 2019;4(12):52–57. https://doi.org/10.15587/1729-4061.2019.176825
13. Yan M.F., Chen B.F., Li B. Microstructure and mechanical properties from an attractive combination of plasma nitriding and secondary hardening of M50 steel. *Applied Surface Science*. 2018;455:1–7. https://doi.org/10.1016/j.apsusc.2018.04.213
14. Esfandiari M., Dong H. Plasma surface engineering of precipitation hardening stainless steels. *Surface Engineering*. 2006;22(2):86–92. https://doi.org/10.1179/174329406X98368
15. Martynov V., Brzhozovsky B., Zinina E., Yankin I., Susskiy A. Fluctuations in the process plant as a quality assessment criterion of low-temperature plasma hardening process. *Procedia Engineering*. 2017;176:451–460. https://doi.org/10.1016/j.proeng.2017.02.344
16. Semboshi S., Iwase A., Takasugi T. Surface hardening of age-hardenable Cu–Ti alloy by plasma carburization. *Surface and Coatings Technology*. 2015;283:262–267. https://doi.org/10.1016/j.surfcoat.2015.11.003
17. Lebrun J.P. Plasma-assisted processes for surface hardening of stainless steel. *Thermochemical Surface Engineering of Steels*. 2015;6(16):615–632. https://doi.org/10.1533/9780857096524.4.615
18. Okolovich G.A., Sharikova T.G., Petrova E.V. Increasing durability of the tool under mutual influence of wear and fatigue of steel. *Polzunovskii vestnik*. 2015;(2):33–36. (In Russ.).

   Околович Г.А., Шарикова Т.Г., Петрова Е.В. Повышение долговечности инструмента в условиях взаимного влияния износа и усталости стали. *Ползуновский вестник*. 2015;(2):33–36.
19. Rasshupkin V.P., Akimov V.V. Fatigue strength and wear resistance of high manganese steel. *Omskii nauchnyi Vestnik*. 2006;35(2):78–80. (In Russ.).

   Расщупкин В.П., Акимов В.В. Усталостная прочность и износостойкость высокомарганцовистой стали. *Омский научный Вестник*. 2006;35(2):78–80.
20. Mohd I., Zahari T. Surface hardening of tool steel by plasma arc with multiple passes. *International Journal of Technology*. 2014;5(1):79–87. https://doi.org/10.14716/ijtech.v5i1.156
21. Zhao K., Yan G., Li J., Guo W., Gu J., Li Ch. The resistance to wear and thermal cracking of laser surface engineered P20 steel. *Metallic Materials*. 2023;13(1):97–105. https://doi.org/10.3390/coatings13010097
22. Medina L., Marcus V.T., Paschalidou M., Lindwall G., Riekehr L. Enhancing corrosion resistance, hardness, and crack resistance in magnetron sputtered high entropy CoCrFeMnNi coatings by adding carbon. *Materials and Design*. 2021; 205:109–121. https://doi.org/10.1016/j.matdes.2021.109711

Information about the Authors / Сведения об авторах

Indira M. Kossanova, *Master Student, Doctoral,* S. Seifullin Kazakh AgroTechnical University
ORCID: 0000-0002-9092-8982
E-mail: ind_jm@mail.ru

Индира Муратовна Косанова, *магистр, докторант,* Казахский агротехнический университет имени Сакена Сейфуллина
ORCID: 0000-0002-9092-8982
E-mail: ind_jm@mail.ru

***Amangel'dy T. Kanayev*,** *Dr. Sci. (Eng.), Prof. of the Chair of Standardization, Metrology and Certification*, S. Seifullin Kazakh AgroTechnical University
ORCID: 0000-0002-2530-038X
E-mail: aman-kanaev2012@yandex.ru

***Temirkhan A. Tolkynbayev*,** *Dr. Sci. (Eng.), Prof.,* L.N. Gumilyov Eurasian National University
ORCID: 0000-0002-8549-3064
E-mail: temtol1961@mail.ru

***Makpal A. Jaxymbetova*,** *Senior Lecturer*, L.N. Gumilyov Eurasian National University
ORCID: 0000-0002-3345-4071
E-mail: dzhaksymbetov@list.ru

***Tolkyn E. Sarsembaeva*,** *PhD, Senior Lecturer*, S. Seifullin Kazakh Agrotechnical University
ORCID: 0000-0002-7674-313X
E-mail: tolkyn-adil@mail.ru

***Амангельды Токешович Канаев*,** *д.т.н., профессор кафедры стандартизации, метрологии и сертификации*, Казахский агротехнический университет имени Сакена Сейфуллина
ORCID: 0000-0002-2530-038X
E-mail: aman-kanaev2012@yandex.ru

***Темирхан Анапияевич Толкынбаев*,** *д.т.н., профессор*, Евразийский национальный университет им. Л.Н. Гумилева
ORCID: 0000-0002-8549-3064
E-mail: temtol1961@mail.ru

***Макпал Адликановна Джаксымбетова*,** *старший преподаватель*, Евразийский национальный университет им. Л.Н. Гумилева
ORCID: 0000-0002-3345-4071
E-mail: dzhaksymbetov@list.ru

***Толкын Ержановна Сарсембаева*,** *к.т.н., старший преподаватель*, Казахский агротехнический университет имени Сакена Сейфуллина
ORCID: 0000-0002-7674-313X
E-mail: tolkyn-adil@mail.ru

Contribution of the Authors / Вклад авторов

I. M. Kossanova – assessment of crack resistance of plasma-hardened steel, statistical processing of the obtained data.
A. T. Kanayev – statement the problem, analysis of the research results, formulation of the conclusions.
T. A. Tolkynbayev – complex metallographic and electron microscopic testing.
M. A. Jaxymbetova – measurement of steel hardness, tabular and graphical representation of the results.
T. E. Sarsembaeva – description of the results, formulation of the conclusions, critical literary analysis.

И. М. Косанова – оценка трещиностойкости плазменно-упрочненной стали, статистическая обработка полученных данных.
А. Т. Канаев – постановка задачи, анализ результатов исследований, формулировка выводов.
Т. А. Толкынбаев – комплексное металлографическое и электронно-микроскопическое исследование.
М. А. Джаксымбетова – измерение твердости стали, табличное и графическое представление результатов.
Т. Е. Сарсембаева – описание результатов, формулировка выводов, критический анализ литературы.

Received 16.04.2023
Revised 28.07.2023
Accepted 04.09.2023

Поступила в редакцию 16.04.2023
После доработки 28.07.2023
Принята к публикации 04.09.2023

METALLURGICAL TECHNOLOGIES / МЕТАЛЛУРГИЧЕСКИЕ ТЕХНОЛОГИИ

UDC 691.714
DOI 10.17073/0368-0797-2023-5-522-528

Original article
Оригинальная статья

Increasing the fatigue strength of high-strength steel grades

V. V. Pavlov[1], M. V. Temlyantsev[2] ✉, V. V. Bukhmirov[3]

[1] **Siberian Mining and Metallurgical Company** (37a Kutuzova Str., Novokuznetsk, Kemerovo Region – Kuzbass 654007, Russian Federation)
[2] **Siberian State Industrial University** (42 Kirova Str., Novokuznetsk, Kemerovo Region – Kuzbass 654007, Russian Federation)
[3] **Ivanovo State Power University named after V.I. Lenin** (34 Rabfakovskaya Str., Ivanovo 153003, Russian Federation)

✉ uchebn_otdel@sibsiu.ru

Abstract. The paper considers the issue of increasing the fatigue strength of high-strength steel grades. Based on the results of experimental measurements of the fatigue strength limit (σ_{-1}) of spring steel grades, we analyzed the effect of tensile strength, ratio of the yield strength during shear and the fatigue strength limit. The absence of statistical relationship between fatigue strength limit and tensile strength ($\sigma_{-1} \neq f(\sigma_u)$) was established. The ratio τ_t/σ_{-1} is the stress concentration coefficient (SCC), which is closely related to the tensile strength of steel. From the theoretical analysis, it follows that in the presence of the same morphological type and size of non-metallic inclusions (NMI) in steel, relationship of SCC with the strength properties of steel is functional. Spread of its actual values is associated with the presence of various morphological types and sizes of NMI in the metal. Each morphological type of NMI is characterized by corresponding physical and mechanical properties (modulus of elasticity, tensile strength and various SCC). SCC increases both with an increase in the strength of steel and with an increase in diameter (thickness) of NMI. It was established that the intensity (rate) of the increase in SCC depends on the size and elastic modulus E_{MNI} of NMI (ratio of mass fractions of SiO_2 and Al_2O_3 oxides in NMI). The average intensity of the change in SCC obtained by processing experimental data corresponds to similar indicators for NMI: 13 % SiO_2; 87 % Al_2O_3 (4.0 μm thick); 20 % SiO_2, 80 % Al_2O_3 (5.0 μm thick); 25 % SiO_2; 75 % Al_2O_3 (7.0 μm thick). According to the obtained connections, dimensions of NMI and their morphology are approximately indicated, which make it possible to increase the fatigue properties of spring steels grades in the tensile strength range from 1200 to 2000 MPa. To increase the fatigue life of steel (especially in high-strength condition), it is recommended to use the technology of aluminum-free metal deoxidation during smelting. At the same time, a favorable morphology of NMI with SCC less than 1.0 is provided. Formation of a fine-grained structure of steel after heat treatment is obtained in the absence of aluminum during deoxidation with small additives of vanadium, niobium or titanium.

Keywords: strength properties of steel, yield strength, stress concentration coefficient, non-metallic inclusions, fatigue strength

For citation: Pavlov V.V., Temlyantsev M.V., Bukhmirov V.V. Increasing the fatigue strength of high-strength steel grades. *Izvestiya. Ferrous Metallurgy*. 2023;66(5):522–528. https://doi.org/10.17073/0368-0797-2023-5-522-528

Увеличение усталостной прочности сталей высокопрочных марок

В. В. Павлов[1], М. В. Темлянцев[2] ✉, В. В. Бухмиров[3]

[1] **Сибирская горно-металлургическая компания** (Россия, 654041, Кемеровская обл. – Кузбасс, Новокузнецк, ул. Кутузова, 37а)
[2] **Сибирский государственный индустриальный университет** (Россия, 654007, Кемеровская обл. – Кузбасс, Новокузнецк, ул. Кирова, 42)
[3] **Ивановский государственный энергетический университет им. В.И. Ленина** (Россия, 153003, Иваново, ул. Рабфаковская, 34)

✉ uchebn_otdel@sibsiu.ru

Аннотация. Рассматривается вопрос увеличения усталостной прочности сталей высокопрочных марок. По результатам экспериментальных измерений предела усталостной прочности (σ_{-1}) стали пружинных марок проведен анализ влияния временного сопротивления, отношения предела текучести при сдвиге и предела усталостной прочности. Установлено отсутствие статистической связи предела усталостной прочности и временного сопротивления ($\sigma_{-1} \neq f(\sigma_в)$). Отношение τ_t/σ_{-1} есть коэффициент концентрации напряжений (ККН), который находится в тесной связи с временным сопротивлением стали. Из проведенного теоретического анализа следует, что при наличии в стали неметаллических включений (НВ) одного морфологического типа и одинаковых размеров связь ККН с прочностными свойствами стали

функциональна. Разброс фактических его значений связан с наличием в металле НВ различных морфологических типов и размеров. Каждый морфологический тип НВ характеризуется соответственными физико-механическими свойствами (модулем упругости, пределом прочности и различным ККН). Коэффициент концентрации напряжений возрастает как с ростом прочности стали, так и с увеличением диаметра (толщины) НВ. Установлено, что интенсивность (скорость) повышения ККН зависит от размера НВ и от модуля упругости $E_{НВ}$ (соотношение массовых долей оксидов SiO_2 и Al_2O_3 в НВ). Средняя интенсивность изменения ККН, полученная путем обработки экспериментальных данных, соответствует аналогичным показателям для НВ: 13 % SiO_2; 87 % Al_2O_3 (толщиной 4,0 мкм); 20 % SiO_2, 80 % Al_2O_3 (толщиной 5,0 мкм); 25 % SiO_2; 75 % Al_2O_3 (толщиной 7,0 мкм). По полученным связям примерно указаны размеры НВ и их морфология, позволяющие повышать усталостные свойства сталей пружинных марок в диапазоне временного сопротивления от 1200 до 2000 МПа. Для повышения ресурса усталостной прочности стали (особенно в высокопрочном состоянии) рекомендовано использовать технологию безалюминиевого раскисления металла при выплавке. При этом обеспечивается благоприятная морфология НВ с ККН не более 1,0. Формирование мелкозернистой структуры стали после термической обработки получают при отсутствии алюминия при раскислении, небольшими добавками ванадия, ниобия или титана.

Ключевые слова: прочностные свойства стали, предел текучести, коэффициент концентрации напряжений, неметаллические включения, предел усталостной прочности

Для цитирования: Павлов В.В., Темлянцев М.В., Бухмиров В.В. Увеличение усталостной прочности сталей высокопрочных марок. *Известия вузов. Черная металлургия*. 2023;66(5):522–528. https://doi.org/10.17073/0368-0797-2023-5-522-528

Introduction

The fatigue strength stands as a critical parameter for metals and alloys, profoundly influencing their potential applications as structural materials across diverse industrial sectors [1; 2]. Among the spectrum of structural metal alloys, steels persist as the most prevalent choice for fabricating a wide range of metal products and structures, especially those subjected to heavy-duty operations. In instances such as rail and spring steels enduring dynamic and fluctuating loads [3; 4], the fatigue strength assumes paramount importance, directly dictating the operational lifespan of metal products [5; 6]. It's noteworthy that fatigue strength isn't solely contingent upon the chemical and phase compositions of steel or its structural configuration [7; 8], but also on factors such as dimensions, non-metallic inclusion morphology, and operational conditions of the metal products [9; 10]. Notably, strain hardening emerges as a viable method to influence fatigue strength positively [11 – 13]. Consequently, enhancing steel's fatigue strength remains a pressing research imperative in contemporary materials science endeavors [14].

Materials and methods

The known relationship $\sigma_{-1} = 0.5\sigma_u$ (where σ_{-1} is fatigue strength and σ_u is tensile strength) is valid for steel with the tensile strength not exceeding 900 MPa [15; 16]. However, as the strength surpasses this threshold, the actual values of fatigue strength significantly deviate from the calculated ones [17; 18] (Fig. 1). This study focuses on exploring the correlation between fatigue strength and tensile strength in spring steel using regression analysis methods. The specific values of tensile strength (σ_u) and fatigue strength limit (σ_{-1}) used in this study are extracted from [19 – 23] (refer to the Table).

The statistical regression model $\sigma_{-1} = 0.028\sigma_u + 566.4$ is inadequate. Fisher's criterion, at 0.206, falls below the significance value (0.657), indicating a low statistical significance. Additionally, the correlation coefficient stands at a meager 0.120.

The results of regression analysis reveal a lack of a meaningful relationship between the function and the parameter. Notably, there's a noteworthy trend: as the tensile strength of steel escalates, the disparity between actual and calculated results widens.

Consequently, it can be inferred that the factor affecting the reduction of fatigue strength, contingent upon the tensile strength of the metallic matrix (MM), is subject to alteration. Steel products are typically designed considering the fatigue strength of steel. Under these circumstances, it becomes challenging to fully utilize the available strength potential (indicated by high σ_t and σ_u levels), thereby limiting the potential to reduce the material intensity of metal structures.

The papers [18; 24] demonstrate that in the non-metallic inclusion – metallic matrix (NMI – MM) system subjected to external impacts, shear stress occurs at their interface within the MM, while NMIs, acting as stress concentrators, have the potential to amplify the effects of these impacts.

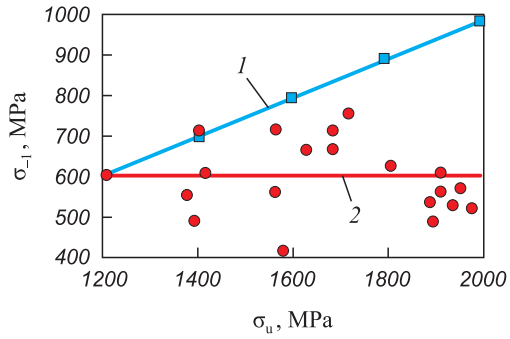

Fig. 1. Dependence of fatigue strength limit on tensile strength of spring steel: *1* – $\sigma_{-1} = 0.5\sigma_u$ (■, theory); *2* – $\sigma_{-1} = 0.028\sigma_u + 566.4$ (●, fact)

Рис. 1. Зависимость предела усталостной прочности от временного сопротивления пружинной стали: *1* – $\sigma_{-1} = 0{,}5\sigma_u$ (■, теория); *2* – $\sigma_{-1} = 0{,}028\sigma_u + 566{,}4$ (●, факт)

Mechanical properties of spring steel grades

Механические свойства сталей пружинных марок

Steel grade	Heat treatment	Source	σ_t, MPa	σ_u, MPa	σ_{-1}, MPa	E^*, hPa
60G	quenching 800 °C, tempering 380 °C	[20]	1180	1370	529	204
65G	n/a	[20] [22] [22]	1220 1280 1440	1470 1420 1690	578 647 725	215
55S2	quenching 880 °C, tempering 400 – 460 °C	[19]	1050 1300 1690	1200 1400 1710	598 720 769	196
60S2	quenching 860 °C, oil, tempering 400 – 550 °C n/a	[19]	n/a 1370	1380 1580	490 421	212
60S2A	isothermal quenching, 330 °C, 1 h, tempering 300 °C quenching, oil, tempering 420 °C quenching, oil, tempering 400 °C	[21]	n/a	1680 1810 1900	686 637 500	212
50KhFA	quenching 850 °C, oil, tempering 175 °C quenching 860 °C, oil, tempering 500 °C	[20] [21]	1590 1430	1630 1570	666 725	218
60S2KhA	quenching, oil, tempering 400 °C Isothermal quenching, soaking 290 °C isothermal quenching, soaking 290 °C, tempering 325 °C	[21]	1830 1720 1430	1980 1950 1920	540 568 578	196
60S2KhFA	quenching, oil, tempering 415 °C isothermal quenching, soaking 290 °C isothermal quenching, soaking 290 °C, tempering 325 °C	[21]	1810 1780 n/a	1900 1960 1920	549 588 613	191

Notes. * – data from the paper [23].

Once the stress level attains or surpasses the yield strength under shear (τ), the local regions of the NMI – MM interface activate the Frank-Read sources [16 – 18]. This activation induces local plastic deformation within the metal. With the escalation of dislocation density in these zones, initial cracks begin to propagate, eventually reaching a critical size, thereby instigating material fracture.

The magnitude of resultant shear stresses is assessed using the following equation [18; 24]:

$$\tau = \sigma_u \frac{E_{NMI}}{E_{MM}} \frac{d}{l_s}, \quad (1)$$

where τ is shear stress; σ_n is external tensile stress; E_{NMI} and E_{MM} are modulus of elasticity of the NMI and the MM, respectively; d is diameter (thickness) of the NMI; l_s is the sum of maximum lengths of the zone of shear stresses in the MM at the boundary with NMI.

Consequently, the factor $\frac{E_{NMI}}{E_{MM}} \frac{d}{l_s}$ represents the stress concentration coefficient (SCC). The equations governing the fatigue strength limit are expressed as follows: $\sigma_{-1} = \frac{\tau_t}{SCC}$ or $SCC = \frac{\tau_t}{\sigma_{-1}}$.

In instances where compressive stresses affect the NMI – MM system, shear stresses arise at their interface. However, their magnitude is significantly lower compared to tension scenarios [18]. Henceforth, only tensile forces are further considered.

A close statistical association is evident between the yield strength and tensile strength in spring grade steels (Fig. 2). The relationship is mathematically expressed as $\sigma_T = 1.08\sigma_u - 312$, presenting the regression model's statistical parameters as follows: a standard error of 104.5 MPa; a correlation coefficient of 0.94; Fisher's criterion standing at 100.86, with a significance level of $9 \cdot 10^{-8}$. The dependences of the strength limit, yield strength under shear, and tensile strength of the steel are derived from the equation $\tau = 0.7 - 0.75\sigma_T$.

When τ is divided by σ_T using the corresponding values of σ_u, a statistical model of the Stress Concentration Coefficient (SCC) dependency on steel strength is obtained (Fig. 3).

The model appears as follows

$$SCC = 0.00167\sigma_u - 1.04 \quad (2)$$

with statistical parameters indicating a Pearson coefficient is 0.70; a standard error of 0.31; and Fisher's criterion measuring 15.98, showing a significance level of 0.00093.

Consequently, the SCC exhibits a fairly strong statistical association with the tensile strength of steel. It suggests that as the strength properties increase, so does SCC.

For specific thicknesses of NMIs (d) and their particular morphology, the equation is formulated as follows [18]

$$SCC = \frac{E_{NMI}}{E_{MM}} \frac{d}{l_s} = 2\frac{E_{NMI}}{E_{MM}} \frac{\tau_u^{MM}}{\sigma_u^{NMI}}, \quad (3)$$

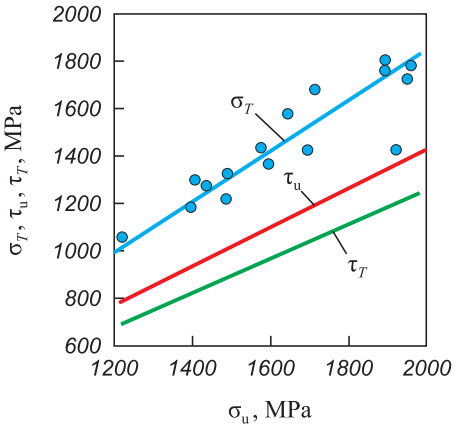

Fig. 2. Dependences $\sigma_T = f(\sigma_u)$; $\tau_u = f\sigma_u$; $\tau_T = f\sigma_u$ for spring steel grades

Рис. 2. Зависимости $\sigma_T = f(\sigma_u)$; $\tau_u = f\sigma_u$; $\tau_T = f\sigma_u$ для сталей пружинных марок

where τ_u^{MM} represents the MM strength limit during shear and σ_u^{NMI} denotes the tensile strength of the NMI.

Results and discussion

The theoretical analysis suggests that when identical NMIs of the same morphological type and the same size coexist within the steel, the relationship between SCC and the steel's strength properties becomes functional. However, the observed variability in the actual SCC values (Fig. 3) is linked to the presence of diverse morphological types and sizes of NMIs within the metal. The morphology of internally formed NMIs during the steel's deoxidation process is contingent upon the ratio of oxygen to aluminum dissolved within it [25 – 27]. These endogenous NMIs exhibit varying physical properties, which are notably influenced by the proportion of SiO_2 and Al_2O_3 basic oxides present in them. This variation spans from plastic aluminosilicates to brittle globules, which remain non-deformable during the rolling process, up to yielding pure alumina [28]. Each morphological type of NMI exhibits specific physical and mechanical properties, such as modulus of elasticity (E_{HMI}), tensile strength (σ_u^{NMI}) resulting in diverse SCC.

Fig. 4 illustrates the derived relationships depicting the dependency of SCC on the tensile strength of steel concerning three potential elemental compositions of NMIs, %, along with sizes of 4.0, 5.8 and 7.0 μm:

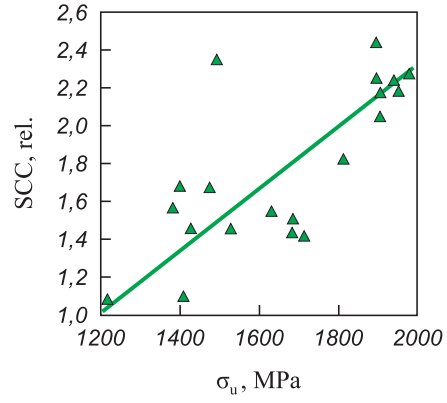

Fig. 3. Dependence of SCC on tensile strength of steel

Рис. 3. Зависимость ККН от временного сопротивления стали

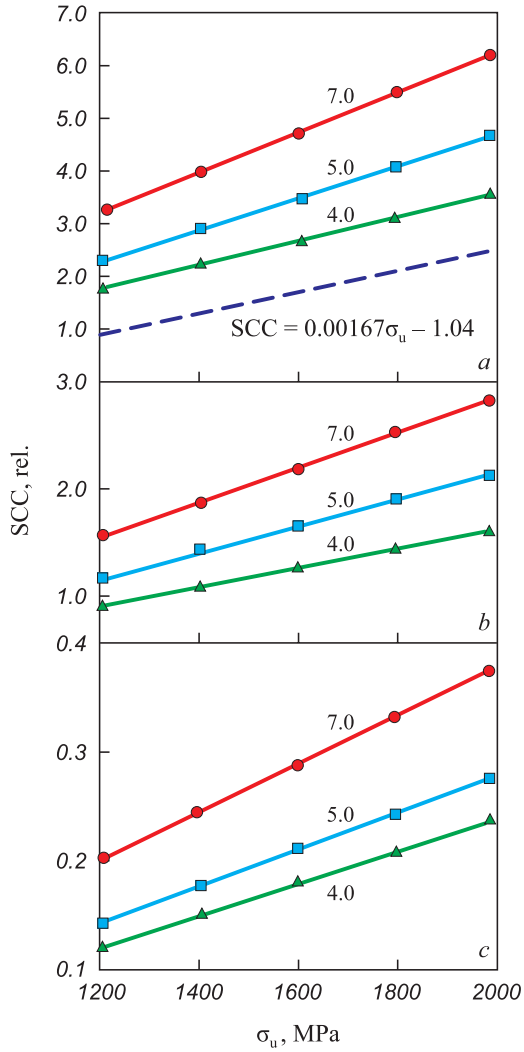

Fig. 4. Calculated dependences of SCC on tensile strength of steel for alumosilicate NMI with different concentrations of SiO_2 and Al_2O_3 oxides in them:
a – 10 % SiO_2, 90 % Al_2O_3, E = 350 hPA;
b – 25 % SiO_2, 75 % Al_2O_3, E = 320 hPA;
c – 80 % SiO_2, 20 % Al_2O_3, E = 100 hPA;
solid lines – calculated values;
dashed line – experimental values;
numbers indicate thickness (diameter) of NMI (μm)

Рис. 4. Расчетные зависимости ККН от временного сопротивления стали для алюмосиликатных НВ с разными концентрациями в них оксидов SiO_2 и Al_2O_3:
a – 10 % SiO_2, 90 % Al_2O_3, E = 350 ГПа;
b – 25 % SiO_2, 75 % Al_2O_3, E = 320 ГПа;
c – 80 % SiO_2, 20 % Al_2O_3, E = 100 ГПа;
сплошные линии – расчетные значения;
штриховая линия – экспериментальные значения;
цифрами обозначена толщина (диаметр) НВ (мкм)

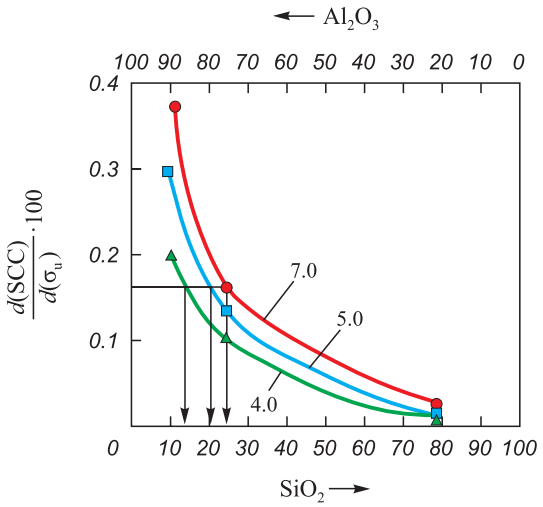

Fig. 5. Dependence of the rate (intensity) of increase in SCC on the ratio of mass fractions of SiO_2 and Al_2O_3 oxides in NMI

Рис. 5. Зависимость скорости (интенсивности) увеличения ККН от соотношения в НВ массовых долей оксидов SiO_2 и Al_2O_3

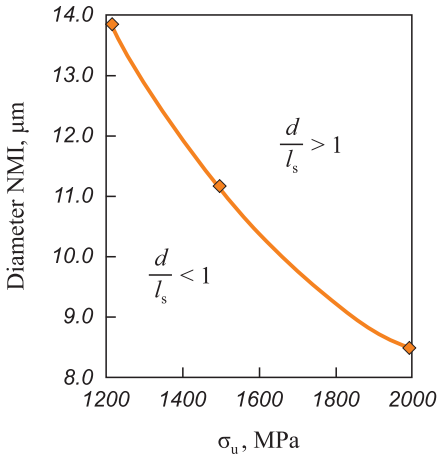

Fig. 6. Dependence of the limit diameter of NMI (60 – 65 % SiO_2; 35 – 40 % Al_2O_3) on tensile strength of steel at $d/l_s = 1$

Рис. 6. Зависимость предельного диаметра НВ (60 – 65 % SiO_2; 35 – 40 % Al_2O_3) от временного сопротивления стали при $d/l_s = 1$

Group	SiO_2	Al_2O_3	E, hPa
1	10	90	350
2	25	75	320
3	80	20	100

Aluminosilicates falling within groups *1* and *2* of high-modulus NMIs, surpassing the typical modulus of elasticity within the MM (with an average value of 205 hPa, as indicated in the Table). Conversely, aluminosilicates categorized under group *3* demonstrate low-modulus traits.

SCC escalates proportionally with the increase in both steel strength and the diameter (or thickness) of the NMI. The rate of this rise in SCC depends on the size and elastic modulus E_{NMI} of the NMI, dictated by the ratio of mass fractions of SiO_2 and Al_2O_3 oxides within the NMI (Fig. 5). It's noteworthy that the average rate of change in SCC, calculated from experimental data using Equation (2), corresponds to analogous indicators for NMIs: 13 % SiO_2; 87 % Al_2O_3 (4.0 μm thick); 20 % SiO_2, 80 % Al_2O_3 (5.0 μm thick); 25 % SiO_2; 75 % Al_2O_3 (7.0 μm thick).

For example, in the context of producing spring grade steels by smelting and deoxidation processes (as indicated in the Table), where diverse high-modulus NMIs are formed, these inclusions significantly impact fatigue indicators. To enhance the steel's fatigue strength limit, it becomes crucial to ensure the formation of NMIs with a modulus of elasticity not exceeding that of MM ($E_{NMI} \le E_{MM}$) and a thickness (d) that does not surpass l_s.

As per [18], achieving involves the formation of NMIs in steel, comprising at least 60 – 65 % SiO_2, with the total content of high-modulus oxides like Al_2O_3, MgO not surpassing 35 – 40 %. These NMIs, when produced under these conditions, exhibit ductility at the heating temperature for metal rolling, allowing for easy deformation, resulting in the formation of thin filaments. For example, during rail rolling, aluminosilicate NMIs are generated within the rail head, measuring approximately 4.0 – 6.0 μm in diameter and having an average length of 40 – 50 μm. Fig. 6 illustrates the calculated maximum diameter (or thickness) for NMIs with the specified chemical composition and various levels of tensile strength within the MM.

Hence, as long as the NMI thickness does not exceed 8.5 μm (maintaining a $d/l_c \le 1$, $E_{NMI}/E_{MM} \approx 1.0$ [18], the SCC remains below 1.0, even with MM strength reaching 2000 MPa. In this context, the fatigue strength of the considered steel must be equal to or exceed the yield strength of the metallic matrix during shear.

Conclusions

To enhance the fatigue endurance of steel, particularly in high-strength conditions, employing aluminum-free metal deoxidation technology during smelting proves beneficial. This approach facilitates the creation of a desirable NMI morphology, ensuring that the SCC remains below 1.0. Achieving a fine-grained structure in steel post heat treatment is feasible by deoxidizing without the inclusion of aluminum, instead incorporating minimal amounts of vanadium, niobium, or titanium.

References / Список литературы

1. Suresh S. *Fatigue of metals*. Cambridge University Press; 2006:701.
2. Nicholas T. *High Cycle Fatigue: A Mechanics of Materials Perspective*. Elsevier; 2006:656.
3. Ishida M. Rolling contact fatigue (RCF) defects of rails in Japanese railways and its mitigation strategies. *Electronic*

Journal of Structural Engineering. 2013;13(1):67–74. https://doi.org/10.56748/ejse.131621

4. Zhong W., Hu J.J., Shen P., Wang C.Y., Lius Q.Y. Experimental investigation between rolling contact fatigue and Wear of high-speed and heavy-haul railway and selection of rail material. *Wear*. 2011;271(9-10):2485–2493.
5. Seo J.-W., Jun H.-K., Kwon S.-J., etc. Rolling contact fatigue and wear of two different rail steels under rolling-sliding contact. *International Journal of Fatigue*. 2016;83:184–194.
6. Kim D., Quagliato L., Park D., Kim N. Lifetime prediction of linear slide rails based on surface abrasion and rolling contact fatigue-induced damage. *Wear*. 2019;420-421:184–194. https://doi.org/10.1016/j.wear.2018.10.015
7. Gromov V.E., Ivanov Yu.F., Vorobiev S.V., Konovalov S.V. *Fatigue of Steels Modified by High Intensity Electron*. Cambridge; 2015:272.
8. Yakovleva T.Yu., Matokhnyuk L.E. Prediction of fatigue characteristics of metals at different loading frequences. *Strength of Materials*. 2004;36(4):442–448. https://doi.org/10.1023/B:STOM.0000041545.08426.7d
9. Marines-Garcia I., Bin X., Bathias C. An understanding of very high cycle fatigue of metals. *International Journal of Fatigue*. 2003;25(9-11):1101–1107. http://doi.org/10.1016/S0142-1123(03)00147-6
10. Mylnikov V.V., Shetulov D.I., Chernyshev E.A. On evaluation of durability criteria in carbon steels. *Metals Technology*. 2010;(2):19–22.
11. Zhao Y., Tan Y., Ji X., Xiang Z., He Y., Xiang S. In situ study of cementite deformation and its fracture mechanism in pearlitic steels. *Materials Science and Engineering: A*. 2018;731:93–101. http://doi.org/10.1016/j.msea.2018.05.114
12. Song R., Ponge D., Raabe D. Mechanical properties of an ultrafine grained C–Mn steel processed by warm deformation and annealing. *Acta Materialia*. 2005;53(18):4881–4792. http://doi.org/10.1016/j.actamat.2005.07.009
13. Calcagnotto M., Adachi Y., Ponge D., Raabe D. Deformation and fracture mechanisms in fine- and ultrafine-grained ferrite/martensite dual-phase steels and the effect of aging. *Acta Materialia*. 2011;59(2):658–670. http://doi.org/10.1016/j.actamat.2010.10.002
14. Kumar B.R., Raabe D. Tensile deformation characteristics of bulk ultrafine-grained austenitic stainless steel produced by thermal cycling. *Scripta Materialia*. 2012; 66(9): 634–637. https://doi.org/10.1016/j.scriptamat.2012.01.052
15. Pavlov V.V., Temlyantsev M.V., Troshkina A.V. On relationship of fatigue parameters with strength properties of steel and the role of non-metallic inclusions. *Problemy chernoi metallurgii i materialovedeniya*. 2020;(2):44–50. (In Russ.).

    Павлов В.В., Темлянцев М.В., Трошкина А.В. О связи усталостных показателей с прочностными свойствами стали и роли неметаллических включений. *Проблемы черной металлургии и материаловедения*. 2020;(2):44–50.
16. Evstratova N.N., Kolnaneets V.G., Sukharnikova V.A. *Materials Science*. Rostov-on-Don: Feniks; 2006:269. (In Russ.).

    Евстратова Н.Н., Компанеец В.Г., Сухарникова В.А. *Материаловедение*. Ростов-на-Дону: Феникс; 2006:269.
17. Ardamasova B.N., Mukhina G.G. *Materials Science*. Moscow: Bauman Moscow State Technical University; 2008:48. (In Russ.).

    Ардамасова Б.Н., Мухина Г.Г. *Материаловедение*. Москва: Изд. МГТУ им. Баумана; 2008:48.
18. Pavlov V.V. Non-Metallic *Inclusions, Fatigue, Contact Fatigue Defects*. Novokuznetsk: SibSIU; 2021:144. (In Russ.).

    Павлов В.В. *Неметаллические включения, усталость, дефекты контактной усталости*. Новокузнецк: ИЦ СибГИУ; 2021:144.
19. *Grade Guide of Steels and Alloys*. Zubchenko A.S. ed. Moscow: Mashinostroenie; 2003:784. (In Russ.).

    Марочник сталей и спалов / Под общ. ред. А.С. Зубченко. Москва: Машиностроение; 2003:784.
20. *Metal Science and Heat Treatment of Steel and Cast Iron. In 3 vols. Vol. 1. Methods of Tests and Research*. Rakhshtadt A.G., Kaputkina L.M., Prokoshkin S.D., Supov A.V. eds. Moscow: Intermet Inzhiniring; 2004:688. (In Russ.).

    Металловедение и термическая обработка стали и чугунов. В 3-х томах. Т. 1. Методы испытаний и исследования / Под общ. ред. А.Г. Рахштадта, Л.М. Капуткиной, С.Д. Прокошкина, А.В. Супова. Москва: Интермет Инжиниринг; 2004:688.
21. *Metal Science and Heat Treatment of Steel and Cast Iron. In 3 vols. Vol. 3. Thermal and Thermomechanical Treatment of Steel and Cast Iron*. Rakhshtadt A.G., Kaputkina L.M., Prokoshkin S.D., Supov A.V. eds. Moscow: Intermet Inzhiniring; 2007:920. (In Russ.).

    Металловедение и термическая обработка стали и чугунов. В 3-х томах. Т. 3. Термическая и термомеханическая обработка стали и чугунов / Под общ. ред. А.Г. Рахштадта, Л.М. Капуткиной, С.Д. Прокошкина, А.В. Супова. Москва: Интермет Инжиниринг; 2007:920.
22. Arzamasov B., Solov'eva T.V., Gerasimov S.A. *Handbook of Structural Materials*. Moscow: Bauman MSTU; 2005:640. (In Russ.).

    Арзамасов Б., Соловьева Т.В., Герасимов С.А. *Справочник по конструкционным материалам*. Москва: МГТУ им. Баумана; 2005:640.
23. Sorokin V.G., etc. *Steels and Alloys. Grade Guide*. Moscow: Intermet inzhiniring; 2001:608. (In Russ.).

    Сорокин В.Г. и др. *Стали и сплавы. Марочник*. Москва: Интермет инжиниринг; 2001:608.
24. Pavlov V.V., Korneva L.V. Interaction of the system "metal matrix – non-metal inclusion" in rail steel. In: *Sci. Reports "Improving the Quality and Operating Conditions of Rails and Rail Fasteners"*. Yekaterinburg; 2010:133–148. (In Russ.).

    Павлов В.В., Корнева Л.В. Взаимодействие системы «металлическая матрица – неметаллическое включение» в рельсовой стали. В кн.: *Научные доклады «Улучшение качества и условий эксплуатации рельсов и рельсовых скреплений»*. Екатеринбург; 2010:133–148.
25. Gubenko S.I. *Non-Metallic Inclusions and Strength of Steels*. Donetsk: ART-PRESS; 2015:468. (In Russ.).

    Губенко С.И. *Неметаллические включения и прочность сталей*. Донецк: АРТ-ПРЕСС; 2015:468.
26. Pavlov V.V. Aluminum-free deoxidation of steel. In: *Sci. Reports "Improving the Quality and Operating Conditions of Rails and Rail Fasteners"*. Sankt-Peterburg;2015:231–240. (In Russ.).

    Павлов В.В. Безалюминевое раскисление стали. В кн.: *Сб. научных докладов «Улучшение качества и условий*

эксплуатации рельсов и рельсовых скреплений». Санкт-Петербург; 2015:231–240.

27. Pavlov V.V., Korneva L.V. Development of a method for assessing the tendency of rail steel to the formation of defects of contact-fatigue origin. In: *Sci. Reports "Improving the Quality and Operating Conditions of Rails and Rail Fasteners"*. Yekaterinburg; 2011:117–137. (In Russ.).

Павлов В.В., Корнева Л.В. Разработка методики оценки склонности рельсовой стали к образованию дефектов контактно-усталостного происхождения. В кн.: *Сб. научных докладов «Улучшение качества и условий эксплуатации рельсов и рельсовых скреплений»*. Екатеринбург; 2011:117–137.

28. Jiang M., Wang X., Chen B., Wang W. Laboratory study on evolution mechanisms of non-metallic inclusions in high strength alloyed steel refined by high basicity slag. *ISIJ International*. 2010;50(1):95–104.
https://doi.org/10.2355/isijinternational.50.95

Information about the Authors / Сведения об авторах

Vyacheslav V. Pavlov, *Deputy Technical Director*, Siberian Mining and Metallurgical Company

Mikhail V. Temlyantsev, *Dr. Sci. (Eng.), Prof., Vice-Rector for Educational Work*, Siberian State Industrial University
ORCID: 0000-0001-7985-5666
E-mail: uchebn_otdel@sibsiu.ru

Vyacheslav V. Bukhmirov, *Dr. Sci. (Eng.), Prof., of the Chair of Theoretical Foundations of Thermal Engineering*, Ivanovo State Power University named after V.I. Lenin
E-mail: buhmirov@tot.ispu.ru

Вячеслав Владимирович Павлов, *заместитель директора по техническим вопросам*, Сибирская горно-металлургическая компания

Михаил Викторович Темлянцев, *д.т.н., профессор, проректор по учебной работе*, Сибирский государственный индустриальный университет
ORCID: 0000-0001-7985-5666
E-mail: uchebn_otdel@sibsiu.ru

Вячеслав Викторович Бухмиров, *д.т.н., профессор, профессор кафедры «Теоретические основы теплотехники»*, Ивановский государственный энергетический университет им. В.И. Ленина
E-mail: buhmirov@tot.ispu.ru

Contribution of the Authors / Вклад авторов

V. V. Pavlov – formation of the article idea, conducting theoretical research, analysis and scientific substantiation of the data obtained, formulation of conclusions.
M. V. Temlyantsev – analysis of the relevance of research on the problem, systematization of information and data in the problem area.

V. V. Bukhmirov – elaboration of the content of sections, selection of references.

В. В. Павлов – создание идеи статьи, проведение теоретических исследований, анализ и научное обоснование полученных данных, формулировка выводов.
М. В. Темлянцев – анализ актуальности исследований проблемы, систематизация сведений и данных в проблемной области.
В. В. Бухмиров – проработка содержания разделов, подбор библиографического списка.

Received 30.03.2023
Revised 03.04.2023
Accepted 10.05.2023

Поступила в редакцию 30.03.2023
После доработки 03.04.2023
Принята к публикации 10.05.2023

UDC 669.162.12:622
DOI 10.17073/0368-0797-2023-5-529-537

Original article
Оригинальная статья

Development of equipment and technology for pelletizing iron ore charge in production of pellets

V. M. Pavlovets

Siberian State Industrial University (42 Kirova Str., Novokuznetsk, Kemerovo Region – Kuzbass 654007, Russian Federation)

pawlowets.victor@yandex.ru

Abstract. New possibilities of pelletizing process in pellet production can improve the production performance. The principles of induced nucleation in the pelletizing technique expand its technological capabilities. The technical indicators of the new pellet production technology and the physical parameters of wet pellets make it possible to increase the metallurgical properties of agglomerated raw materials. The presented technical diagrams reflect the production capabilities of induced nucleation in the processes of forming a sprayed layer (SL) of the charge and its division by various technical devices. The design features and technological modes of the developed technical schemes are implemented on a typical disc pelletizer. Experimental data obtained during implementation of the developed technological schemes make it possible to change the relative values of strength, mass and moisture content of the pellets during pelletizing of the iron ore charge. These parameters can be adjusted during loading of charge, its spraying onto the charge shell of the pelletizer, dividing the sprayed layer of the charge into nuclei and further pelletizing of the nuclei to form a pellet shell. An assessment of these technological schemes led to selection of the most effective solutions based on thermal power spraying of wet charge, taking into account its adhesion, material consumption and complexity of the equipment design. For practical use, we recommend a combined technological scheme for the production of pellets using the induced nucleation technology on the basis of SL formation of a single air-charge jet (ACJ) containing strengthening additives, on a pre-profiled skull and dividing the SL into nuclei by a conical drum equipped with a metal string. At the end of the technological cycle of pellet production, increased porosity with a high proportion of open pores is formed in the central embryonic part of the pellets. The pellets have a low moisture content ($\Theta_W = 0.97$) and a favorable pore structure. In the forecast, they require less energy consumption for their subsequent heat treatment. The technology makes it possible to produce pellets with the required and maximum strength ($\Theta_П \geq 1.0$) 12 – 16 mm in size with higher productivity ($\Theta_М = 0.68$). In the course of experiments, it was found that the technology of preliminary nucleation has high reliability and versatility, and it can be easily introduced into the existing production.

Keywords: iron ore raw materials, equipment and technology of pelletizing, agglomerated metallurgical raw materials, iron ore pellets, thermal power spraying of wet charge, induced nucleation

For citation: Pavlovets V.M. Development of equipment and technology for pelletizing iron ore charge in production of pellets. *Izvestiya. Ferrous Metallurgy*. 2023;66(5):529–537. https://doi.org/10.17073/0368-0797-2023-5-529-537

Особенности развития техники и технологии окомкования железорудной шихты в производстве окатышей

В. М. Павловец

Сибирский государственный индустриальный университет (Россия, 654007, Кемеровская обл. – Кузбасс, Новокузнецк, ул. Кирова, 42)

pawlowets.victor@yandex.ru

Аннотация. Новые возможности процесса окомкования в производстве окатышей позволяют улучшить производственные показатели. Принципы принудительного зародышеобразования в технике окомкования расширяют его технологические возможности. Технические показатели новой технологии производства окатышей и физические параметры влажных окатышей позволяют повысить металлургические свойства окускованного сырья. Представленные технические схемы отражают производственные возможности принудительного зародышеобразования в процессах формирования напыленного слоя (НС) шихты и его деления различными техническими устройствами. Конструктивные особенности и технологические режимы разработанных технических схем реализованы на типичном тарельчатом окомкователе. Опытные данные, полученные при реализации разработанных технологических схем, позволяют изменять относительные величины прочности, массы и влажности окатышей в ходе окомкования железорудной шихты. Эти параметры можно регулировать в ходе загрузки шихты, ее напыления на шихтовый гарнисаж окомкователя, деления напыленного слоя шихты на зародыши и доокомкования зародышей с формированием оболочки окатышей. Оценка указанных технологических схем привела к выбору наиболее эффективных решений, основанных на теплосиловом напылении влажной шихты с учетом процесса ее налипания, материалоемкости и сложности конструктивного оформления оборудования. Для практического использования рекомендована комбинированная технологическая схема

получения окатышей по технологии принудительного зародышеобразования на основе формирования НС одиночной воздушношихтовой струей, содержащей упрочняющие добавки, на предварительно профилированный гарнисаж и деления НС на зародыши коническим барабаном, снабженным металлической струной. В конце технологического цикла производства окатышей в центральной зародышевой части окатышей формируется повышенная пористость с высокой долей открытых пор. Окатыши обладают пониженной влажностью ($\Theta_W = 0{,}97$) и благоприятной поровой структурой. В прогнозе они требуют меньших энергозатрат на их последующую термообработку. Технология позволяет выпускать окатыши необходимой и максимальной прочности размером 12 – 16 мм с более высокой производительностью. В ходе экспериментов установлено, что технология предварительного зародышеобразования обладает высокой надежностью и универсальностью, легко внедряется в действующее производство.

Ключевые слова: железорудное сырье, техника и технология окомкования, окускованное металлургическое сырье, железорудные окатыши, теплосиловое напыление влажной шихты, принудительное зародышеобразование

Для цитирования: Павловец В.М. Особенности развития техники и технологии окомкования железорудной шихты в производстве окатышей. *Известия вузов. Черная металлургия*. 2023;66(5):529–537. https://doi.org/10.17073/0368-0797-2023-5-529-537

Introduction

The process of pelletizing an iron ore charge in the production of pellets represents the initial phase of agglomerating raw materials derived from iron ore. This process facilitates the formation of a wet bulk mass, its primary structuring, and subsequent hardening [1; 2]. The primary objective of pelletization is to create round-shaped pellets possessing maximum possible strength, allowing them to withstand transportation and endure thermal operations without softening. The wet charge forming process in pellet production initiates with nucleation and culminates in the final pelletizing of nuclei. In traditional pellet production technology, impacting the nucleation process using existing technical means without involving auxiliary physical fields proves challenging [3]. However, a recent proposal aims to enhance the functionality of the pelletizing section by employing thermal power spraying of the wet charge onto the pelletizer skull. This method endows it with additional shape-generating and structure-forming functionalities during pellet production [4; 5]. Known as the technology of induced nucleation by spraying and final pelletizing (NSF) of nuclei, it significantly transforms the processes of nucleation and pelletization of the iron ore charge. This technology offers a diverse array of tools to influence pellet structural properties and the parameters of pelletizer production [4 – 6]. According to this technology, the initial stage of raw pellets production involves the formation of a dense sprayed layer (SL) of the charge using an air-charge jet (ACJ) within the idle zone of the rotating disc pelletizer. To create an embryonic mass, the SL within the same pelletizer zone is mechanically divided into solid nuclei, having shapes akin to spherocubes or spheroparallelepipeds. During the subsequent forming stage within the pelletizer's working zone containing lumpy materials, the corners and faces of these nuclei are crumpled to form a round shape. Simultaneously, the nuclei undergo final pelletizing while mixed with moistened charge in a rolling mode, thereby forming the pellet shell [6 – 8]. The central part of two-layer pellets exhibits lower moisture content and is characterized by higher porosity, featuring an increased proportion of open pores. The low moisture content of such raw pellets, coupled with this porosity pattern, mitigates crack formation and significantly reduces the temperature of shock fracture during drying [4; 5]. Consequently, the likelihood of a decrease in strength of annealed pellets during subsequent metallurgical treatment diminishes. Even after undergoing intense firing, the structure of pellets maintains an augmented number of permeable pores open to reducing gases [5]. This specific pellet structure minimizes diffusion limitations during subsequent reduction processes and enhances the reactivity of agglomerated raw materials. Similar structural properties of pellets can also be achieved by utilizing pore-forming biomass [7; 8] or complementary technologies [9 – 11]. Figs. 1 and 2 depict the schematic representation of NSF technology and the macrostructure of the materials involved in wet charge forming. Implementing the production scheme can be readily accomplished within existing sites possessing available manufacturing areas and technical capabilities. The NSF technology has laid the groundwork for various technical solutions [4; 5] that facilitate the control of nucleation processes, pellet formation, and their physical properties. By analyzing the operational processes of nuclei and pellets, one can formulate the general principles governing nucleation and structurization of the lumpy mass within this technology.

The primary aim of this paper is to analyze the technical solutions directed towards equipment and technology development for pelletizing iron ore charge during pellet production based on induced nucleation.

Materials and methods

Fig. 3 display technical diagrams of devices used in pellet production, showcasing different methods of forming the dense SL by spraying the wet charge onto the skull. Meanwhile, Fig. 4 present schematic representations of the diverse methods employed to divide the SL into nuclei within these devices. It's important to note that the author has secured patents from the Russian Federation for the depicted technical schemes (Figs. 3, 4). For the implementation of the pellet production technical schemes, the laboratory semi-industrial disc pelletizer served as the foundational apparatus

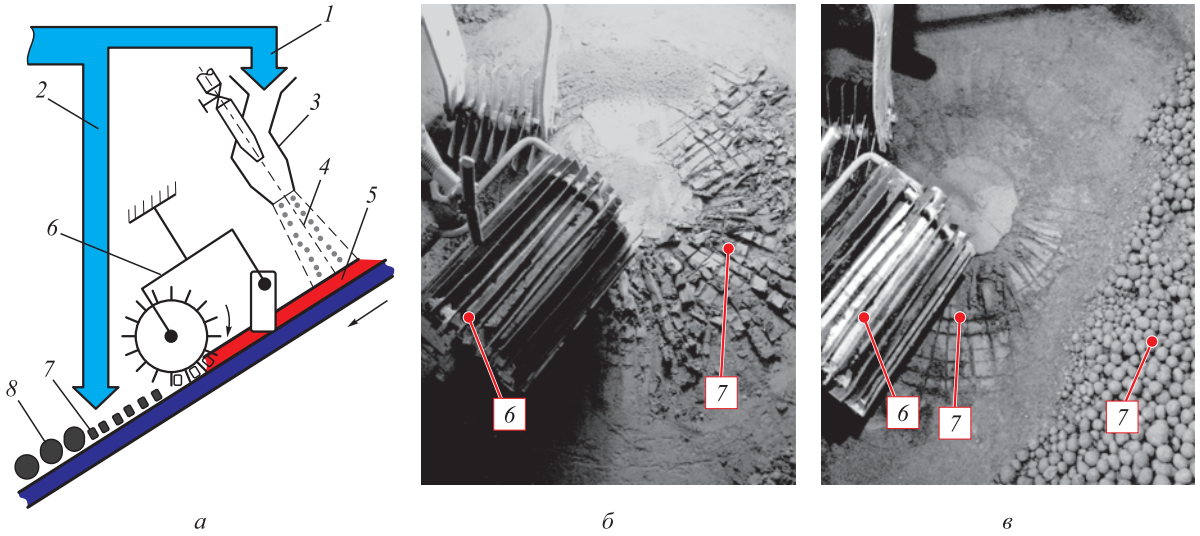

а *б* *в*

Fig. 1. Scheme of wet charge forming into nuclei and pellets (*a*) and appearance of experimental installation based on a disk pelletizer for producing pellets using the NSF technology (nucleation by spraying and final pelletizing of nuclei – *b*, *c*):
1 – charge flow for nucleation; *2* – charge flow for the final pelleting of nucleus; *3* – jet unit; *4* – air-charge jet; *5* – sprayed charge layer; *6* – SL divider, consisting of longitudinal (lamellar knives) and transverse (rotating drum with edges) dividers; *7* – nucleus; *8* – pellets

Рис. 1. Схема формообразования влажной шихты в зародыши и окатыши (*а*) и внешний вид экспериментальной установки на основе тарельчатого окомкователя для получения окатышей по технологии ЗНД (*b*, *c*):
1 – поток шихты для зародышеобразования; *2* – тоже для доокомкования зародышей; *3* – струйный аппарат; *4* – воздушношихтовая струя; *5* – напыленный слой шихты; *6* – делитель НС, состоящий из продольного (пластинчатые ножи) и поперечного (вращающийся барабан с ребрами) делителей; *7* – зародыши; *8* – окатыши

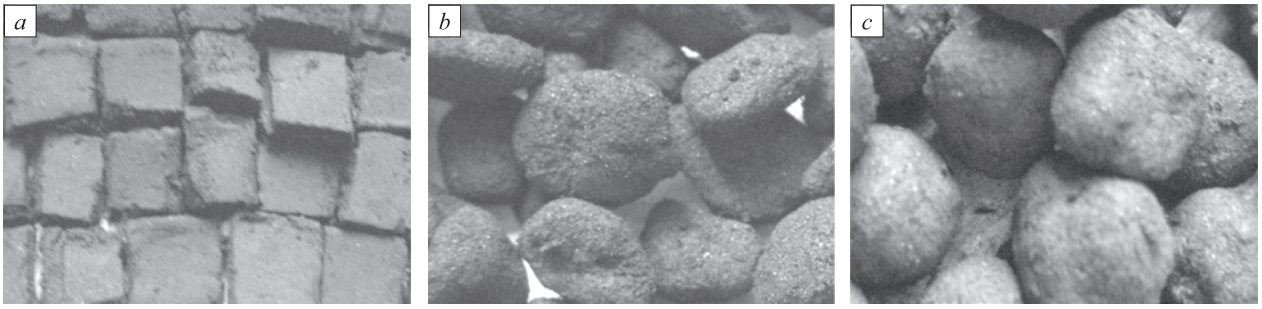

Fig. 2. Appearance of charge materials and sequence of pellets formation from nuclei using NSF technology:
a – fragment of SL divided into nuclei; *b* – nucleus 60 s after final pelletizing; *c* – nucleus 300 s after final pelletizing

Рис. 2. Внешний вид шихтовых материалов и последовательность формирования окатышей из зародышей по технологии ЗНД:
а – фрагмент НС, разделенного на зародыши; *b* и *c* – зародыши через 60 и 300 с после доокомкования соответственно

(diameter 0.62 m, disc inclination angle $\gamma = 45°$, number of revolutions $n = 12$ rpm). The pelletizer is equipped with a jet unit (JU) (diameter $d_{JU} = 0.02$ m, charge flow rate $G_{sh} = 0.03 – 0.04$ kg/s, pressure $P_a = 0.2$ MPa, compressed air flow rate $V_a = 0.6$ m^3/min) and variously designed devices for dividing the SL into nuclei. To implement the multi-jet technical schemes initially, three JUs, each with a diameter of 0.02 m, were utilized, all operating under identical initial conditions and maintaining the same charge flow rate. The wet charge employed in this process consisted of iron-ore concentrate sourced from the Tei deposit ($d_h = 0.068$ mm) and 1 % bentonite. A 5-kg charge was sprayed over a period of 60 s onto the 30 mm thick charge skull (CS) ($\rho_{CS} = 2230$ kg/m^3, $W_{CS} = 8.14$ %) present in the idle zone of the disc, positioned at $\Theta_L = 25$ ($\Theta_L = L/d_{JU}$ – dimensionless distance, $L = 0.5$ m). For the final pelletizing of nuclei and the formation of standard pellets, an additional 5 kg of wet charge were introduced into the pelletizer's working zone. Average strength and moisture content measurements were conducted for all formed materials. The dimensions of the SL were measured (diameter d_{SL}, m and SL height on its axis h_t, m). Subsequently, the embryonic mass and the array of pellets were sieved. The sampling methodology is detailed in [4; 5].

For the technical schemes implementing of various methods of SL formation (Fig. 3), the spraying coefficient C_{SL}, %, was calculated as follows:

$$C_{SL} = \frac{M_{sh} - M_m}{M_{sh}},$$

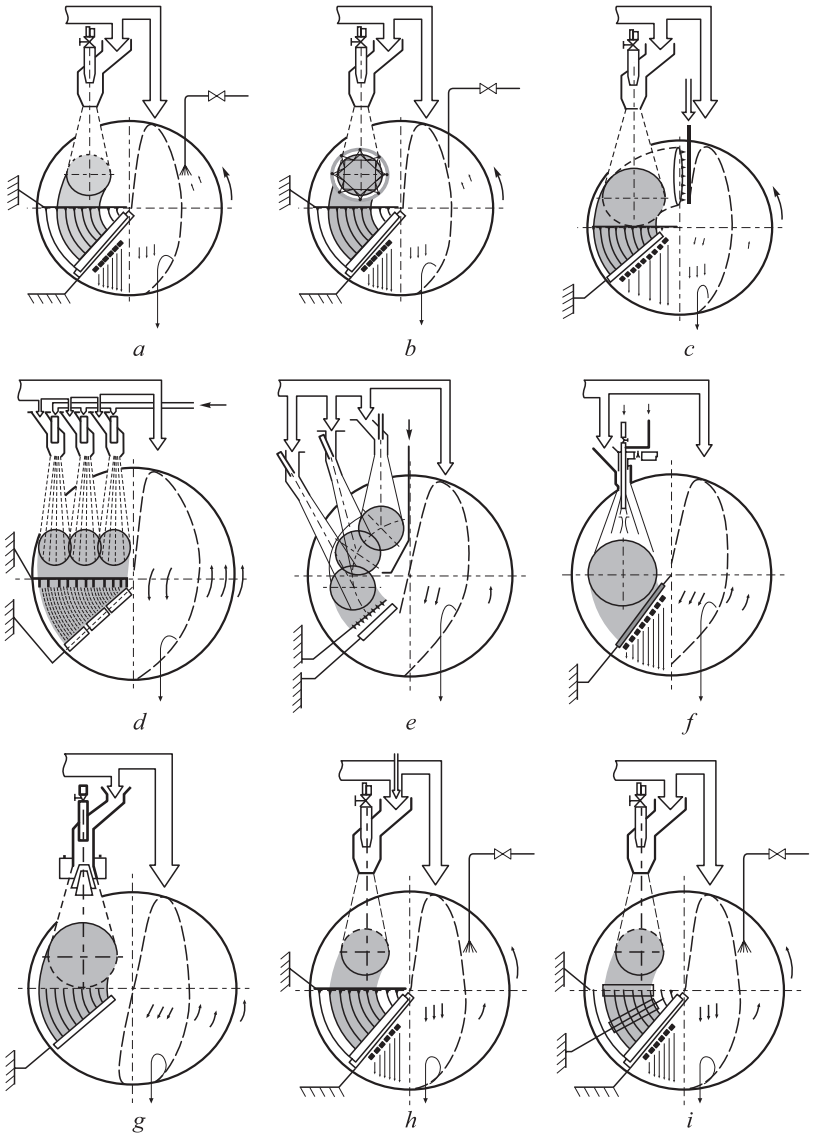

Fig. 3. Technical schemes of SL formation on pelletizer skull:
a – one ACJ; *b* – the same with moistening of the deposition zone; *c* – moistening of the charge skull (CS); *d* – several ACJ with superposition of SL along the radius; *e* – the same with superposition of SL along an arc; *f* – one ACJ with auxiliary air flow; *g* – one ACJ with deflecting nozzles on the path of ACJ; *h* – one ACJ with hardening additives in the charge; *i* – additional compaction of SL with drums

Рис. 3. Технические схемы формирования НС на гарнисаже окомкователя:
a – одной ВШС; *b* – тоже с увлажнением зоны напыления; *c* – увлажнение ШГ; *d* – несколькими ВШС с наложением НС по радиусу; *e* – тоже с наложением НС по дуге; *f* – одной ВШС с вспомогательным потоком воздуха; *g* – одной ВШС с отклоняющими насадками на пути ВШС; *h* – одной ВШС с упрочняющими добавками в шихте; *i* – дополнительное уплотнение НС барабанами

where M_{sh} is the mass of the deposited charge, kg; M_m is the mass of the charge remaining after SL formation, kg.

For the technical schemes implementing various methods of SL division into nuclei (Fig. 4), the fractional composition of the embryonic mass and the nucleation coefficient C_{nucl}, %, were determined using the following formula:

$$C_{nucl} = \frac{M_{nucl}}{M_{sh}} = \frac{M_{sh} - M_m - M_n}{M_{sh}},$$

where M_{nucl} is the mass of nuclei ranging from 2 to 10 mm in size, kg; M_n is the mass of nuclei fines smaller than 2 mm in size, kg.

Multiple experiments were conducted for each technical scheme, enabling the acquisition of average values for the parameters being analyzed. In order to provide a comprehensive assessment of the NSF technology's efficiency and the properties of the SL, nuclei, and pellets, certain experimental outcomes were presented in dimensionless form, as discussed in [4; 5]. The relative strength of the molded materials, denoted as Θ_S, was determined using the equation

$$\Theta_S = \frac{S_{av}}{S_p},$$

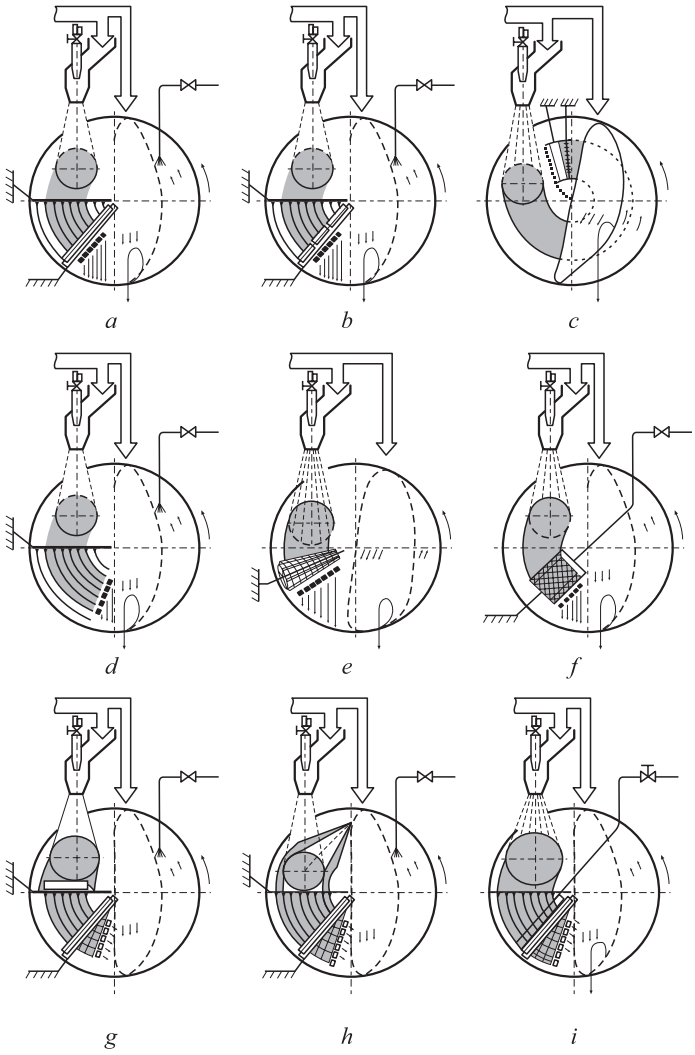

Fig. 4. Technical schemes of charge SL division into nuclei on pelletizer skull with:
a – longitudinal plate knives and drum with transverse ribs; *b* – the same with composite rotating drums; *c* – division of SL by longitudinal plate knives and rotating drum with transverse ribs at outlet from lumpy materials layer; *d* – plow dividers; *e* – conical drum equipped with metal strings; *f* – drum equipped with ribs with semicircular cells; *g* – SL profiling in width and height; *h* – CS profiling; *i* – drum with transverse ribs and system of rods

Рис. 4. Технические схемы деления напыленного слоя шихты на зародыши на гарнисаже окомкователя:
a – продольными пластинчатыми ножами и барабаном с поперечными ребрами; *b* – тоже с составными вращающимися барабанами; *c* – деление НС продольными пластинчатыми ножами и вращающимся барабаном с поперечными ребрами на выходе из слоя комкуемых материалов; *d* – плужковыми делителями; *e* – коническим барабаном, снабженным металлическими струнами; *f* – барабаном, снабженным ребрами с полукруглыми ячейками; *g* – с профилированием НС по ширине и высоте; *h* – с профилированием ШГ; *i* – барабаном с поперечными ребрами и системой стержней

where S_{av} is the average strength of samples from SL, nuclei and pellets, kPa, S_p is the average strength of pellets, 12 – 16 mm in size, kPa, and S_p = 280 kPa.

The relative mass of molded materials (SL, nuclei, and pellets) Θ_M was calculated using the formula

$$\Theta_M = \frac{M_m}{M_t},$$

where M_m is the average mass of molded materials (SL, nuclei, and pellets), kg, M_t is the total mass of the charge used in pellet production, inclusive of the charge fed for the final pelletizing of nuclei in the pelletizer's working zone, kg, M_t = 10 kg.

The relative moisture content of the molded materials Θ_W was evaluated using the equation

$$\Theta_W = \frac{W_{av}}{W_{sh}},$$

where W_{av} is the average moisture content of the samples from SL, nuclei, and pellets, %, W_{sh} is the moisture content of the deposited charge, %, set at W_{sh} = 8.2 %.

The relative duration of the processes involving charge loading, depositing, SL division, and final pelletizing of nuclei, represented as Θ_τ, was calculated using the equation

$$\Theta_\tau = \frac{\tau_i}{\tau_p},$$

where τ_i is the duration encompassing charge loading, depositing, SL division, and final pelletizing of nuclei, s. The time periods for depositing, SL division, and final pelletizing of nuclei were to 15, 5 and 300 s, respectively. Meanwhile τ_p represent the total duration of pelletization, set at $\tau_p = 380$ s.

To determine the characteristics of SL (C_{SL}, Θ_M, Θ_S, Θ_W), formed in various ways (Fig. 3), the pelletizer was operated without dividers throughout the entire spraying period. In order to conduct a comparative analysis of the performance of these diverse technical schemes, we utilized the fundamental scheme (Fig. 3, *a*). This scheme relied on a single JU operation, spraying the wet charge onto an unprepared CS. It is noteworthy that most industrial depositing technologies entail numerous performance requirements concerning spraying devices and techniques, as indicated in [12 – 15].

To calculate the parameters of the embryonic mass (fractional composition, C_{nucl}, Θ_M, Θ_S, Θ_W) acquired via various methods of SL division into nuclei (Fig. 4), the SL divider was utilized on the pelletizer subsequent to SL formation. For a comparative assessment of these technical schemes, we utilized the fundamental scheme (Figs. 1 and 3, *a*), which was additionally equipped with a divider featuring longitudinal (lamellar knives) and transverse (rotating drum with edges) dividers coated with bakelite varnish to prevent charge adhesion (Fig. 4, *a*).

Results and discussion

Fig. 5 illustrates the typical changes in parameters Θ_M, Θ_S, Θ_W during the process of charge formation, which includes charge deposition, SL formation, and its subsequent division into nuclei, followed by pelletization.

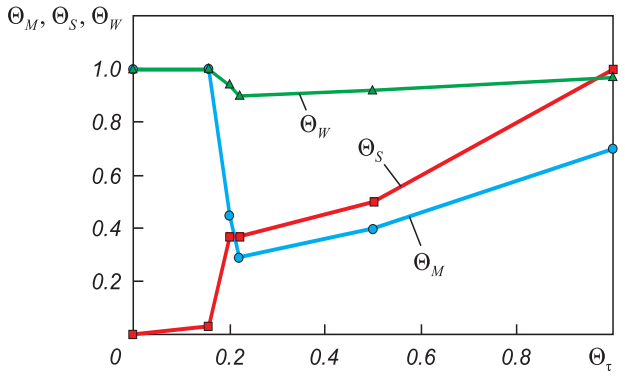

Fig. 5. Kinetics of changes in relative strength Θ_S, mass Θ_M and moisture content Θ_W of materials during charge forming and pellets formation

Рис. 5. Кинетика изменения относительной прочности Θ_S, массы Θ_M и влажности Θ_W материалов в процессе формообразования шихты и формирования окатышей

These trends were observed in the basic spraying scheme (Figs. 3, *a* and 4, *a*). The experimental results are comprehensively presented in Tables 1 and 2. The dependencies obtained from these experiments, as depicted in Fig. 5, allow for the generalization of research outcomes and the identification of potential constraints within the NSF technology. Across all technical schemes detailed in Tables 1 and 2, a consistent observation is the rapid formation of the wet charge, showcasing an average nuclei mass growth rate exceeding 3.0 g/s. This rapid growth is accompanied by an increase in strength ($\Theta_S > 0.39$) and relatively minor mass loss of the formed materials during the stages of charge deposition (up to $\Theta_M = 0.44$) and SL division (up to $\Theta_M = 0.29$) into nuclei (Fig. 5). It has been noted that enhancing the strength of the SL during charge deposition ($\Theta_S > 0.8 – 0.9$) [4; 5] brings it closer to that of the whole pellet. However, this particular regime results in decreased porosity and a reduction in the proportion of open pores in the embryonic part of the pellet, which contradicts the fundamental structurization principles of the NSF technology. The slight increase in nuclei strength during SL division can be attributed to the mechanical compaction of the wet mass facilitated by dividers or supplementary devices. During the final pelletizing phase of the nuclei, both the mass and strength of the pellets increase as the shell forms in the rolling mode. The dehydration process of the SL is closely associated with barodiffusive moisture transfer facilitated by the ACJ, into which the SL and embryonic mass come into contact during the spraying process. The final pelletizing phase of nuclei is accompanied by the growth of parameters Θ_M, Θ_S, Θ_W, includes several stages and extends over a longer dura-

Table 1

Indicators of technical schemes that implement various methods of SL formation

Таблица 1. **Показатели технических схем, реализующих различные способы формирования НС**

The scheme is presented in Fig. 3	Indicators					
	C_{SL}	d_{SL} / d_{JU}	d_{SL} / h_t	Θ_M	Θ_S	Θ_W
a	0.88	10.5	20.5	0.44	0.39	0.96
b	0.95	11.5	21.5	0.46	0.41	0.99
c	0.92	11.5	21.5	0.46	0.42	0.97
d	0.92	29.0	94.0	0.46	0.40	0.96
e	0.91	11.5	21.5	0.46	0.45	0.94
f	0.88	14.5	59.0	0.43	0.36	0.96
h	0.86	15.0	60.0	0.43	0.35	0.96
h	0.86	10.5	20.5	0.45	0.48	0.96
i	0.88	11.5	23.5	0.44	0.45	0.95

Table 2

Indicators of technical schemes that implement various methods of SL division into nuclei

Таблица 2. **Показатели технических схем, реализующих различные способы деления НС на зародыши**

The scheme is presented in Fig. 4	Indicators								
	nuclei fractional composition, mm					A_{nucl}, mm	C_{nucl}	Θ_M	Θ_S
	0 – 2	2 – 4	4 – 6	6 – 10	>10				
a	34.1	18.8	18.2	28.1	0.8	4.34	0.58	0.29	0.42
b	32.5	18.5	20.2	28.4	0.4	4.21	0.61	0.30	0.42
c	33.2	19.5	20.5	26.2	0.6	4.09	0.61	0.30	0.51
d	43.4	22.6	15.4	10.4	8.2	2.71	0.45	0.22	0.41
e	26.1	18.6	24.6	30.2	0.5	4.51	0.69	0.35	0.43
f	25.4	19.3	25.4	29.9	0	4.49	0.58	0.29	0.42
h	15.2	21.3	30.6	32.9	0	5.67	0.62	0.31	0.42
h	12.3	22.2	31.9	33.6	0	6.22	0.67	0.38	0.42
i	32.1	19.8	20.2	26.1	0.8	4.15	0.58	0.29	0.38

tion (300 s), significantly slowing down both the growth rate of mass (to 0.11 g/s) and strength [4; 5]. During this phase, the moisture content of pellets formed in the final pelletizing stage increases due to excessive moistening of the pellet shell. In the majority of technical schemes employing the NSF technology for final pellet production, the focus is on forming the maximum number of pellets sized between 12 to 16 mm ($\Theta_M > 0.7$). These pellets exhibit an average mass growth rate (more than 0.3 g/s), attain the required strength ($\Theta_S = 1.0$), and demonstrate reduced moisture content in their structure ($\Theta_W < 1$). In the central embryonic part of the pellets, this decrease is even greater ($\Theta_W < 0.95$).

An analysis of the efficiency of the reviewed technical schemes would be prudent. The scheme depicted in Fig. 3, *b*, deviates from the basic one by intensively moistening the deposition zone and the SL surface. This alteration allows for an increase in CSL to 0.95 and augmentation of the SL's geometrical dimensions and parameters Θ_M, Θ_S, Θ_W (Table 1). However, the excessive moistening of the SL to $W_{SL} = 0.99W_{sh}$ and, consequently, the nuclei and resultant pellets, prolongs the subsequent drying duration of pellets during the heat treatment stage. Similarly, the scheme illustrated in Fig. 3, *c*, results in similar SL characteristics by premoistening the charge before spraying, differing from the basic solution. The scheme presented in Fig. 3, *d*, enhances the transverse dimensions and maintains a consistent SL thickness by overlapping boundary zones ($\delta = 1.0 – 0.8$, where δ denotes the dimensionless radius of the SL). These SL zones exhibit high porosity and low strength. A similar effect on the spraying process is detailed in [16 – 20], associating control of the dispersed phase flow rate in the JU with variations in the rotation speed of the sprayed base. The scheme displayed in Fig. 3, *e*, is notably more intricate and diverges from the basic scheme by employing successive charge spraying using three JUs, thereby expanding the longitudinal deposition area. This extended exposure of the ACJ to the SL for approximately three times longer increases the SL strength by around 10 – 15 %. It intensifies moisture removal from the SL, maintaining indicator levels Θ_M, Θ_W closely resembling those of the basic scheme. The scheme shown in Fig. 3, *f*, focuses on improving the uniformity of SL thickness by utilizing a single JU operating alongside auxiliary fan-supplied air along the JU axis. This modification results in larger geometric dimensions of the SL due to the expansion angle of the jet increasing to 30°. However, a drawback of this scheme is the reduced strength properties of the SL due to decreased ACJ pressure. The scheme illustrated in Fig. 3, *g*, involves deflecting mechanical devices positioned in the path of the ACJ. This scheme has analogous disadvantages and facilitates the acquisition of SL with characteristics akin to the previously described scheme. The scheme presented in Fig. 3, *h*, deviates from the basic one by enabling the addition of auxiliary materials (strengthening, binding, hard-to-pelletize, and structure-forming additives) to the air-charge jet (ACJ). By introducing a relatively small amount (up to 1 – 2 %) of additives, such as an aqueous solution of liquid glass, into the deposited charge, the SL strength can be augmented by 10 – 15 % [4; 5]. The scheme shown in Fig. 3, *i*, incorporates additional measures beyond ACJ pressure. It employs extra strengthening and profiling (height aligning) loads formed by rotating drums mounted on the SL surface before its division. This approach enhances the SL strength and uniformity of its geometric dimensions. However, it entails increased technical complexity and is characterized by enhanced charge buildup on the metal drums.

The scheme illustrated in Fig. 4, *b*, diverges from the basic one due to the inclusion of composite drums. These composite drums account for the differences in the cir-

cumferential velocities of the SL circumferential velocities easing the division of larger diameter SL. Consequently, this modification leads to a 5 % increase in the strength of the nuclei and a reduction in fines content to 33.2 % (Table 2). The scheme displayed in Fig. 4, *c*, uses the pressure from the layer of materials circulating in the pelletizer's working zone, which possesses substantial height and mass. This pressure aids in hardening the SL, facilitating its division upon exiting the lumpy materials layer [4; 5]. This approach results in a 5 – 10 % increase in nuclei strength while maintaining a relatively uniform fractional composition. The pelletizer divider shown in Fig. 4, *d*, employs a curved plow divider with a simplified structure. It enables the generation of nuclei in various sizes, encompassing a significant amount of fines (0 – 2 mm) at 43.4 %, along with larger pellets exceeding 10 mm. The scheme depicted in Fig. 4, *e*, involves a thin metal string stretched across a conical drum, serving as a divider for SL. This innovative design enables the simultaneous division of SL in both longitudinal and transverse directions, requiring significantly less force. It boasts features such as minimal mass buildup, low metal consumption, and high technological effectiveness [4; 5]. Similar devices are utilized in the ceramic industry for mass division before molding. In Fig. 4, *f*, the SL division scheme incorporates a cylindrical drum with wave-shaped ribs acting as a divider to form pelletized nuclei. To counter increased charge buildup, this scheme implements intensive moistening of the drum ribs before SL division, consequently elevating the moisture content of the nuclei. the SL and charge skull profiling schemes depicted in Fig. 4, *g* and *h*, respectively, ensure a constant thickness of the SL, thereby enhancing the uniformity of the fractional composition and resulting in larger average nuclei size A_{nucl} of 6.22 mm. The SL division scheme in Fig. 4, *i*, employs a divider equipped with a system of rods to create a specialized nuclei structure. However, this configuration results in significantly lower strength values compared to those of the basic scheme.

Considering the characteristics of SL and embryonic mass (Θ_M, Θ_S, Θ_W, Table 1, 2) derived from the implemented technical schemes, along with an evaluation of the technological effectiveness of the devices (such as charge buildup, additional equipment material consumption, design complexity, reliability, and operational stability), a combined technological scheme for pellet production is recommended for practical implementation. This recommended scheme encompasses the induced nucleation NSF technology based on SL formation by a single ACJ (Fig. 3, *a*), enabling the utilization of strengthening additives in the deposited charge (Fig. 3, *h*). In this setup, the material is sprayed onto the pre-profiled charge skull (Fig. 4, *g*), and the SL is divided into nuclei using the conical drum equipped with a metal string (Fig. 4, *e*). Implementing the NSF technology based on these components facilitates the production of pellets characterized by reduced moisture content ($\Theta_W = 0.97$), evenly distributed across the cross-section, achieving necessary and sufficient strength ($\Theta_S \geq 1.0$), favorable pore structure, and a maximum yield of pellets sized between 12 to 16 mm ($\Theta_M = 0.72$). These parameters are much lower when conventional nucleation and pelletization technology is used ($\Theta_W = 1.1$, $\Theta_M = 0.33$) [4; 5]. Based on these findings, it is reasonable to anticipate higher pelletizer performance, along with lower energy consumption for thermal drying of pellets during subsequent heat treatment.

Conclusions

The results of studies investigating the performance of technical schemes based on NSF technology, which enables the control of the nucleation and pelletization processes, were analyzed. General principles governing the nucleation and structurization of lumpy mass within this technology framework have been formulated. We assessed the typical variations in parameters Θ_M, Θ_S, Θ_W during the charge formation and pelletization processes for both the basic scheme and several technical schemes under investigation. Through a comprehensive evaluation considering the indicators of NSF technology and technological effectiveness (e.g., charge buildup level, material consumption of additional equipment, design complexity, reliability, and operational stability), specific technical schemes were appraised, and the most efficient solutions were identified. The recommended combined scheme for pellet production utilizes NSF technology based on SL formation by a single air-charge jet (ACJ), permitting the incorporation of strengthening additives. In this approach, the material is sprayed onto a pre-profiled charge skull, and the SL is divided into nuclei using a conical drum equipped with a metal string. Implementing the NSF technology based on these elements allows for the production of pellets characterized by reduced moisture content ($\Theta_W = 0.97$) evenly distributed across the cross-section, achieving necessary and sufficient strength ($\Theta_S \geq 1.0$) and yielding maximum pellets sized between 12 to 16 mm ($\Theta_M = 0.72$). These findings provide grounds to anticipate enhanced pelletizer performance and reduced energy consumption during subsequent pellet heat treatment.

References / Список литературы

1. Pavlovets V.M. *Pellets in Technology of Metals Extraction from Ores*. Moscow, Vologda: Infra-Ingineriya; 2022:284.

   Павловец В.М. *Окатыши в технологии экстракции металлов из руд*. Москва, Вологда: Инфра-Инженерия; 2022:284.

2. Abzalov V.M., etc. *Physico-Chemical and Thermal Engineering Fundamentals for Iron Ore Pellets Production*. Ekaterinburg: NPVP "TOREX"; 2012:340.

   Абзалов В.М. и др. *Физико-химические и теплотехнические основы производства железорудных окатышей*. Екатеринбург: НПВП «ТОРЕКС»; 2012:340.

3. Yusfin Yu.S., etc. *Production Intensification and Quality Improvement of Pellets*. M.: Metallurgiya; 1994:240.

Юсфин Ю.С. и др. *Интенсификация производства и улучшение качества окатышей*. Москва: Металлургия; 1994:240.

4. Pavlovets V.M. *Expanding the Functionality of Units for Preparing Iron Ore Raw Materials for Metallurgical Smelting*. Moscow, Vologda: Infra-Ingineriya, 2023:328.

Павловец В.М. *Расширение функциональных возможностей агрегатов для подготовки железорудного сырья к металлургической плавке*. Москва, Вологда: Инфра-Инженерия, 2023:328.

5. Pavlovets V.M. *Development of Equipment and Technology for Pelletizing Iron Ore Raw Materials in Metallurgy*. Moscow, Vologda: Infra-Engineering; 2022:336.

Павловец В.М. *Развитие техники и технологии окомкования железорудного сырья в металлургии*. Москва, Вологда: Инфра-Инженерия; 2022:336.

6. Pavlovets V.M. Study of thermal power modes of wet charge spraying intended for induced nucleation. *Izvestiya. Ferrous Metallurgy*. 2009;52(6):9–13.

Павловец В.М. Исследование теплосиловых режимов напыления влажной шихты, предназначенных для принудительного зародышеобразования. *Известия вузов. Черная металлургия*. 2009;52(6):9–13.

7. Iwase K., Higuchi T., Yamamoto T., Murakami T. Design for carbon core pellet toward co-production with sinter. *Tetsu-to-Hagane*. 2021;107(6):483–493. https://doi.org/10.2355/tetsutohagane.TETSU-2020-080

8. Kieush L., Boyko M., Koveria A., Yaholnyk M., Poliakova N. Production of iron ore pellets by utilization of sunflower husks. *Acta Metallurgica Slovaca*. 2021;27(4):167–171. https://doi.org/10.36547/ams.27.4.1052

9. Okeke S.I., Onukwuli O.D. Effect of basicity on metallurgical properties of pellets produced from Itakpe iron ore concentrates. *Discovery and Innovation*. 1999;11(3):170–176. https://doi.org/10.4314/dai.v11i3.15549

10. Frantes K. North American iron mines running flat out to meet domestic and worldwide demand. *Skillings' Mining Review*. 2005;94(7):6–21.

11. *Basics in Mineral Processing*. Metso: Outotec, 2015:752. Available at URL: https://www.metso.com/globalassets/insights/ebooks/mo-basics-in-mineral-processing-handbook_lowres.pdf

12. Goejen J.G., Miller R.A., Brindley W.J., Leissler G.W. *A simulation technique for predicting defects of thermal sprayed coatings: NASA Technical Memorandum TM-106939*, 1995.

13. Hansbo A., Nylén P. Models for the simulation of spray deposition and robot motion optimization in thermal spraying of rotating objects. *Surface and Coatings Technology*. 1999;122(3-4):191–201. https://doi.org/10.1016/S0257-8972(99)00255-8

14. Ensz M.T., Griffith M.L., Reckaway D.E. *Critical issues for functionally graded material deposition by laser engineered net shaping*. Available at URL: http://edge.cs.drexel.edu/GICL/people/schroeder/references/mpif02me.pdf

15. De Los Santos Valladares L., Domínguez A.B., Félix L.L., Kargin J.B., Mukhambetov D.G., Kozlovskiy A.L., Moreno N.O., Santibañez J.F., Cabrera R.C., Barnes C.H.W. Characterization and magnetic properties of hollow α-Fe_2O_3 microspheres obtained by sol gel and spray roasting methods. *Journal of Science: Advanced Materials and Devices*. 2019;4(3):483–491. https://doi.org/10.1016/j.jsamd.2019.07.004

16. Walker W.J., Reed J.S., Verma S.K. Influence of slurry parameters on the characteristics of spray-dried granules. *Journal of the American Ceramic Society*. 1999;82(7):1711–1719.

17. Chen C., Planche M.-P., Deng S., Huang R., Ren Z., Liao H. Strengthened peening effect on metallurgical bonding formation in cold spray additive manufacturing. *Journal of Thermal Spray Technology*. 2019;28:769–779. https://doi.org/10.1007/s11666-019-00854-4

18. Assadi H., Gartner F., Stoltenhoff T., Kreye H. Bonding mechanism in cold gas spraying. *Acta Materialia*. 2003;51(15):4379–4394. https://doi.org/10.1016/S1359-6454(03)00274-X

19. Dorfman M. Thermal spray materials. *AM&P Technical Articles*. 2002;160:49–51.

20. Kasparova M., Houdkova S., Cubrova J. Thermally sprayed coatings for high temperature application. In: *Proceedings of the 21st Int. Conf. on Metallurgy and Materials, Brno, Czech Republic, 23–25.05.2012*. 2012:144–146.

Information about the Author / Сведения об авторе

Viktor M. Pavlovets, *Cand. Sci. (Eng.), Assist. Prof. of the Chair "Thermal Power and Ecology",* Siberian State Industrial University
E-mail: pawlowets.victor@yandex.ru

Виктор Михайлович Павловец, *к.т.н., доцент кафедры теплоэнергетики и экологии,* Сибирский государственный индустриальный университет
E-mail: pawlowets.victor@yandex.ru

Received 11.05.2022
Revised 16.11.2022
Accepted 04.09.2023

Поступила в редакцию 11.05.2022
После доработки 16.11.2022
Принята к публикации 04.09.2023

ECOLOGY AND RATIONAL USE OF NATURAL RESOURCES | ЭКОЛОГИЯ И РАЦИОНАЛЬНОЕ ПРИРОДОПОЛЬЗОВАНИЕ

UDC 631.45:57.042:57.048(470.314)
DOI 10.17073/0368-0797-2023-5-538-543

Original article
Оригинальная статья

Ecomonitoring of sanitary protection zone of metallurgical enterprise: Snow and soil cover

M. A. Zakharova[1], A. S. Vodoleev[1] ✉, O. S. Andreeva[2], K. I. Domnin[1]

[1] **Siberian State Industrial University** (42 Kirova Str., Novokuznetsk, Kemerovo Region – Kuzbass 654007, Russian Federation)
[2] **KUZBASS Humanitarian Pedagogical Institute of Kemerovo State University** (23 Tsiolkovskogo Str., Novokuznetsk, Kemerovo Region – Kuzbass 654041, Russian Federation)

✉ botanic-egf@yandex.ru

Abstract. The paper considers the issues related to monitoring the state of snow and soil cover in the zone of influence of industrial emissions into the atmosphere at the borders of the sanitary protection zone (SPZ) of the metallurgical enterprise JSC "EVRAZ United West Siberian Metallurgical Combine" (JSC EVRAZ ZSMK). Sanitary protection zone is the territory separating enterprises (their buildings and structures) with technological processes that serve as a source of impact on the environment and human health from residential development. SPZ is designed to reduce the impact of all factors beyond its limits to the required hygienic standards, to create a sanitary barrier between industrial and residential buildings. Ecomonitoring provides an objective analysis of depositing spheres (snow, soil) on the territory of the SPZ. The method of chemical laboratory analysis is important for the assessment of primary and secondary air pollution (samples of snow, soils and waters). The results of chemical analysis of snow water showed that the dry residue in meltwater is lower (7 – 8 times) MPC at all sites, the content of chloride ions does not exceed the MPC (350 mg/l), the content of sulfate ions at site *1* is 2 times lower than the MPC, at other sites below the detection limit by the methodology set out in RD 52.04.186 – 89. The content of heavy metals and arsenic in the soil at the SPZ test sites does not exceed the values of the established MPC. Soil analysis showed that the active acidity (*p*H of the water extract) is in the range of 6.30 – 7.40 units, which indicates the absence of technogenic acidification of soils. The content of petroleum products in the selected samples is below the threshold value, which makes it possible to attribute soils at all sites of the SPZ of JSC EVRAZ ZSMK according to the compound under consideration to conditionally pure. The content of benz(a)pyrene in the soil does not exceed the MPC (0.02 mg/kg) at all experimental sites, except site 7. The sulfur content does not exceed the MPC values at all test sites of the SPZ.

Keywords: ecomonitoring, sanitary protection zone, atmospheric air, soil, snow cover, harmful emissions, chemical analysis, MPC, technogenic acidification of soils, heavy metals, benz(a)pyrene

For citation: Zakharova M.A., Vodoleev A.S., Andreeva O.S., Domnin K.I. Ecomonitoring of sanitary protection zone of metallurgical enterprise: Snow and soil cover. *Izvestiya. Ferrous Metallurgy*. 2023;66(5):538–543. https://doi.org/10.17073/0368-0797-2023-5-538-543

Экомониторинг санитарно-защитной зоны металлургического предприятия: снежный и почвенный покровы

М. А. Захарова[1], А. С. Водолеев[1] ✉, О. С. Андреева[2], К. И. Домнин[1]

[1] **Сибирский государственный индустриальный университет** (Россия, 654007, Кемеровская обл. – Кузбасс, Новокузнецк, ул. Кирова, 42)
[2] **Кузбасский гуманитарно-педагогический институт ФГБОУ ВО «Кемеровский государственный университет»** (Россия, 654041, Кемеровская обл. – Кузбасс, Новокузнецк, ул. Циолковского, 23)

✉ botanic-egf@yandex.ru

Аннотация. Рассмотрены вопросы, связанные с мониторингом состояния снежного и почвенного покровов в зоне влияния промышленных выбросов в атмосферный воздух на границах санитарно-защитной зоны (СЗЗ) металлургического предприятия АО «ЕВРАЗ Объединенный Западно-Сибирский металлургический комбинат» (АО «ЕВРАЗ ЗСМК»). Санитарно-защитная зона – территория, отделяющая предприятия (их здания и сооружения) с технологическими процессами, служащими источником воздействия на среду обитания и здоровье человека, от жилой застройки. Территория СЗЗ предназначена для снижения за ее пределами уровня воздействия всех вредных факторов до требуемых гигиенических нормативов, создания санитарно-защитного барьера между промышленной и жилой застройками. Экомониторинг дает объективный анализ депонирующих сфер (снег, почва) на территории СЗЗ. Для оценки первичного (воздушной среды) и вто-

ричного (снежных проб, почв и вод) загрязнений применяется метод химического лабораторного анализа. Результаты химического анализа снеговой воды показали, что сухой остаток в талой воде ниже (в 7 – 8 раз) ПДК на всех площадках, содержание хлорид-ионов не превышает ПДК (350 мг/л), содержание сульфат-ионов на площадке *1* в два раза ниже ПДК, на остальных площадках ниже предела обнаружения методикой, изложенной в РД 52.04.186 – 89. Содержание в почве тяжелых металлов и мышьяка на пробных площадках СЗЗ не превышает ПДК. Почвенный анализ показал, что активная кислотность (*p*H водной вытяжки) находится в пределах 6,3 – 7,4 единиц, что указывает на отсутствие техногенного закисления почв. Содержание нефтепродуктов в отобранных пробах ниже порогового значения, что делает возможным отнести почвы на всех площадках СЗЗ АО «ЕВРАЗ ЗСМК» по рассматриваемому соединению к условно чистым. Содержание бенз(а)пирена в почве не превышает ПДК (0,02 мг/кг) на всех экспериментальных площадках, кроме площадки *7*. Содержание серы не превышает ПДК на всех пробных площадках СЗЗ.

Ключевые слова: экомониторинг, санитарно-защитная зона, атмосферный воздух, почва, снежный покров, вредные выбросы, химический анализ, ПДК, техногенное закисление почв, тяжелые металлы, бенз(а)пирен

Для цитирования: Захарова М.А., Водолеев А.С., Андреева О.С., Домнин К.И. Экомониторинг санитарно-защитной зоны металлургического предприятия: снежный и почвенный покровы. *Известия вузов. Черная металлургия*. 2023;66(5):538–543. https://doi.org/10.17073/0368-0797-2023-5-538-543

Introduction

When evaluating the impact of large industrial enterprises, a crucial consideration involves mitigating the adverse effects on all environmental components. In resource-rich regions such as the Kemerovo Region (Kuzbass), both natural ecosystems and the urban environment, essential for ensuring the population's quality of life, are significantly affected. This study focuses on eco-monitoring within the sanitary protection zone (SPZ) using JSC "EVRAZ United West Siberian Metallurgical Combine" (JSC EVRAZ ZSMK) as a case study. The enterprise in question is situated in close proximity to ten specially protected natural reserves (SPNR) of various levels and categories, notable heritage sites of Kuzbass. Distances to the boundaries of these SPNRs are as follows: 17 km – Uvaly Luchshego regional reserve; 30 km – Chernovoy Naryk regional reserve; 35 km – Kostenkovskie Rocks regional natural monument; 55 km – Kuzedeevsky regional natural monument; 55 km – Kuzedeevo Linden Island federal natural monument; 56 km – Kuznetsky Alatau state nature reserve; 65 km – Karakansky regional reserve; 68 km – Artyshta regional natural monument; 75 km – Belsinsky regional reserve; 83 km – Bochatskiye sopki regional reserve. Preserving these unique natural complexes necessitates compliance with environmental protection requirements, including the establishment of a sanitary protection zone. The primary goal of this zone is to reduce atmospheric air pollution levels to specified emission limits after the enterprises have implemented all necessary measures to eliminate harmful substances.

The objective of the paper is to investigate and analyze the impact of industrial emissions on the environmental status of soil and snow cover within the SPZ of JSC EVRAZ ZSMK.

Background

The set tasks to accomplish this objective were as follows:

– to explore the methods for investigating the soil-ecological condition within the sanitary protection zone;

– to analyze the findings derived from laboratory examinations of the snow cover and soil at the boundaries of the SPZ of JSC EVRAZ ZSMK.

Novokuznetsk is situated in the southern part of the Kemerovo Region within a vast depression amid the floodplains of the Kondoma and Tom' Rivers. It is encircled by the Kuznetsk Alatau and Salair Ridge mountain ranges. The metallurgical plant of JSC EVRAZ ZSMK is situated in the northeastern region of the city. The rationale behind its location was to position the plant in close proximity to energy and raw material sources while maximizing the distance from residential areas within the city. JSC EVRAZ ZSMK falls into the category of first-class enterprises concerning plant capacity, process specifications, as well as the nature and volume of pollutants released into the environment. The sanitary protection zone's radius for first-class metallurgical enterprises is typically 1 km (although in practice, it extends to 5 km), in accordance with SanPiN 2.2.1/2.1.1.1200 – 03[1] regulations. Landscaping involves the use of specialized tree species, constituting at least 50 % of the development footprint.

A modern metallurgical facility comprises various units that have the potential to emit pollutants into the surrounding air. Such emissions are virtually unavoidable. Hence, measures for safeguarding atmospheric air quality have been implemented, encompassing a system designed to ensure air purity and sustain it at levels safe for human life and health [1; 2].

The sanitary protection zone of JSC EVRAZ ZSMK comprises eight designated test sites within the northern industrial hub, each representing distinct soil types:

1 – floodplain granular soil near the Ilyinsky Bridge (east wind);

2 – alluvial meadow soil close to Teleuty Village (northeast wind);

3 – fertile leached chernozem behind Malaya Shchedrukha Village (north wind);

[1] SanPiN 2.2.1/2.1.1.1200 – 03. Sanitary protection zones and sanitary classification of enterprises, structures, and other facilities Sanitary and Epidemiological Rules and Regulations. URL: https://files.stroyinf.ru/Data1/52/52471/index.htm (accessed on: 09.12.2022).

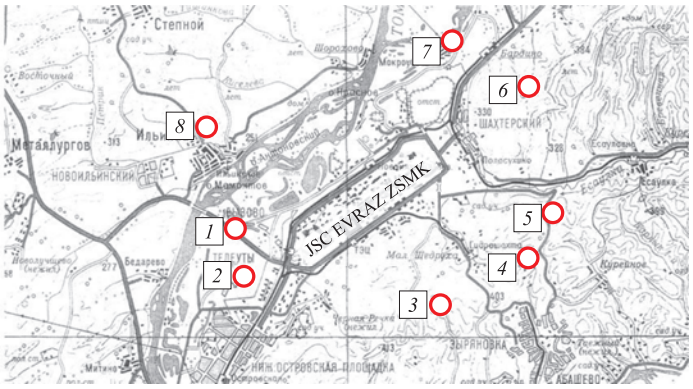

Areas of experimental sites of SPZ of JSC EVRAZ ZSMK

Зоны опытных площадок СЗЗ АО «ЕВРАЗ ЗСМК»

4 – leached chernozem in the area of Yubileynaya mine (north-west wind);

5 – meadow heavy loamy soil along the road to Kuregesh – Esaulovka (west wind);

6 – chernozem meadow heavy loamy soil near the road to Chistogorsk Settlement (south-western wind);

7 – leached moderately deep light loamy chernozem in the vicinity of Mokrousovo Village (south wind);

8 – leached moderately deep light loamy chernozem in the area of Ilyinka Village (southeast wind).

The Figure illustrates the respective areas of these test sites within JSC EVRAZ ZSMK.

The boundaries of the sanitary protection zone of the northern industrial hub extend at distances of 5 km to the north, 3.3 km to the northeast, 3.5 km to the east, 4.1 km to the southeast, 1.8 km to the southwest, 2.6 km to the west, 4 km to the northwest, and 4.2 km to the south from the boundaries of JSC EVRAZ ZSMK industrial site.

The assessment of environmental conditions in major cities and enterprises commonly involves individual environmental components: atmospheric air, surface and groundwater, soil (considering microflora), vegetation cover, and citizen health [3 – 7].

Snow cover, with its high sorption capacity, stands out as an informative indicator for detecting anthropogenic pollution not only in atmospheric precipitation but also in atmospheric air, subsequently affecting water bodies and soils [8].

Snow samples were collected following the guidelines of RD 52.04.186 – 89, utilizing a specific template (pipe) with a cross-sectional area of 50.3 cm^2, reaching from the top of the snow cover to the ground. These samples were then placed in plastic bags and transported to the laboratory for monitoring industrial waste, soils, fuels, and lubricants. In the laboratory, the samples underwent processing and analysis for *p*H, carbonate and bicarbonate content, chlorides, sulfates, dry residue, calcium, magnesium, and dust, in accordance with RD 52.04.186 – 89 procedures.

During the melting period, snowmelt enters water bodies and is categorized as atmospheric runoff[2] [9 – 11]. To assess its condition, regulatory limits established in SanPiN[1, 3, 4] were used as the basis of comparison. The findings of the snow water study are summarized in Table 1.

The data presented indicates that:

– dry residue in snowmelt water across all sites is (7 – 8 times) lower than the MPC;

– chloride ion content does not exceed the MPC (350 mg/l);

– sulfate ion content at site *1* is twice lower than the MPC, while at the other sites, it is below the detection limit outlined in RD 52.04.186 – 89 procedures;

– *p*H values at all sites fall within the normal range, confirming the absence of anthropogenic soil acidification within the SPZ territory.

Soil monitoring was conducted to oversee various soil parameters [12], encompassing data related to [13 – 15]:

– heavy metals such as vanadium, manganese, antimony, nickel, copper, zinc, lead, mercury, cadmium;

– arsenic;

– chemical indicators including *p*H (acidity), benz(a)-pyrene, petroleum products, and sulfur compounds.

Pollution indicators were assessed for eight chemical elements (V, Mn, As, Sb, Ni, Cu, Zn, Pb). Table 2 presents the specifics of soil contamination caused by heavy metals within the confines of the SPZ. The concentration of heavy metals and arsenic at the SPZ test sites remains below the MPC values.

[2] Procedure for arrangement and operation of sanitary protection zones of industrial enterprises. URL: http://www.centreco.ru/szz_6.php (accessed on: 09.12.2022).

[3] SanPiN 1.2.3685 – 21. Hygienic standards and requirements for ensuring safety and (or) harmlessness to humans from environmental factors. URL: https://rkc56.ru/documents/4538 (accessed on: 09.12.2022).

[4] SanPiN 2.1.3684 – 21. Sanitary and epidemiological requirements for the maintenance of the territories of urban and rural settlements, for water bodies, drinking water and drinking water supply, atmospheric air, soils, residential premises, operation of industrial and public premises, organization and conduct of sanitary and anti-epidemic (preventive) measures. URL: http://www.consultant.ru/document/cons_doc_LAW_376166/ (accessed on: 09.12.2022).

Table 1

Результаты анализа снеговой воды

Таблица 1. **Results of analysis of the snow water**

Indicator	MPC, mg/l	Indicator value at the site							
		1	*2*	*3*	*4*	*5*	*6*	*7*	*8*
*p*H	6.5 – 8.5	7.8	7.6	7.6	7.9	7.4	7.6	8.4	7.9
Chlorides	350.0	18.46	19.84	21.3	18.46	21.3	15.62	17.1	18.46
Sulfates	500.0	225.6	bdl	bdl	bdl	bdl	bdl	bdl	bdl
Dry residue	1000.0	126.0	124.0	114.0	110.0	118.0	158.0	22.0	104.0
Ca	–	120.0	100.0	120.0	60.0	80.0	80.0	140.0	100.0
Mg	–	bdl	36.5	bdl	24.3	bdl	bdl	60.8	bdl

N o t e . bdl stands for below the detection limit.

The outcomes from chemical analyses of soils are outlined in Table 3. The active acidity (*p*H of the water extract) ranges between 6.30 and 7.40 units, signifying the absence of technogenic soil acidification. The petroleum product content (PNDF 16.1.41–04) observed in the selected soil samples remains below the threshold value (less than 20 mg/kg). Consequently, soils across all sites can be categorized as conditionally clean concerning this compound. Similarly, the concentration of benz(a)pyrene does not surpass the MPC values (0.02 mg/kg) at all test sites except for site *7*. Additionally, the sulfur content (according to GOST 8606 – 93) does not exceed MPC values of 160 mg/kg.

To assess the degree of soil pollution, the technogenic concentration coefficient K_c is calculated [16]:

$$K_c = K_{tot}/K_{bg},$$

where K_{tot} and K_{bg} are the element contents in the examined soil and in background soil, respectively.

Table 2

Content of heavy metals and arsenic in the soil in boundaries of SPZ

Таблица 2. **Содержание тяжелых металлов и мышьяка в почве в границах СЗЗ**

Site	Content of substances, mg/kg, in soil							
	V	Mn	As	Sb	Ni	Cu	Zn	Pb
1	70	1500	bdl	bdl	50	130	200	50
2	70	1500	bdl	bdl	50	70	200	50
3	70	1500	bdl	bdl	50	100	150	50
4	70	1000	bdl	bdl	30	70	100	50
5	70	1500	bdl	bdl	50	70	200	50
6	70	1000	bdl	bdl	50	70	200	50
7	70	1500	bdl	bdl	50	70	150	50
8	70	1000	bdl	bdl	50	70	150	50
MPC	150	1500	2	4,5	80	132	220	130

When the soil is contaminated by two or more elements, the total pollution index Z_c is calculated as follows:

$$Z_c = \sum_{i=1}^{n} K_c - (n-i),$$

where K_c is the technogenic concentration coefficients that are greater than unity; n is the number of elements with $K_c > 1$.

The level of contamination is categorized as low if Z_c falls within the range of 0 – 16; medium (moderately hazar-

Table 3

Results of chemical analysis of the soil samples

Таблица 3. **Результаты химических анализов почвенных образцов**

Site (sampling points)	Depth of sampling, cm	*p*H of aqueous extract	Benz(a)pyrene, mg/kg, ISO 13877 (MPC = 0.02 mg/kg)
1	0 – 5	7.16	0.0044
	5 – 20	7.40	0.0037
2	5 – 20	7.27	0.0010
3	0 – 5	7.38	0.0021
	5 – 20	7.23	0.0022
4	0 – 5	6.30	0.0033
	5 – 20	6.41	0.0029
5	0 – 5	7.07	0.0010
	5 – 20	7.05	0.0013
6	0 – 5	6.62	<0.0010
	5 – 20	6.53	<0.0010
7	0 – 5	6.91	0.0158
	5 – 20	6.76	0.0197
8	0 – 5	6.44	<0.0010
	5 – 20	5.75	<0.0010

Table 4

Categories of soil chemical contamination

Таблица 4. **Категории химического загрязнения почв**

The site and its location	Metal concentration coefficient							Z_c	Pollution category
	Cd	Cu	Ni	Pb	Zn	As	Hg		
1 – Ilyinsky Bridge area	1.67	1.50	0.82	1.13	1.39	1.88	5.75	14.13	Acceptable
2 – Teleuty Village area	1.67	1.36	0.82	1.04	1.52	1.96	3.13	11.48	Acceptable
3 – Malaya Shchedruha Village area	1.67	1.25	0.94	1.16	1.26	2.50	6.88	15.65	Acceptable
4 – Yubileinaya mine area	1.67	1.14	0.98	0.92	1.27	2.59	8.88	17.44	Moderately hazardous
5 – area of the road to Kurugesh-Esaulovka	1.67	1.28	0.92	0.85	1.26	2.50	8.50	16.98	Moderately hazardous
6 – area of the road to Chistogorsk	1.67	1.17	0.98	0.54	1.37	2.05	7.25	15.03	Acceptable
7 – Mokrousovo Village area	1.67	1.70	1.01	1.08	3.76	1.96	13.88	25.07	Moderately hazardous
8 – Ilyinka Village area	1.67	1.44	0.95	0.67	4.31	1.43	11.00	21.47	Moderately hazardous

dous) if $Z_c = 16 \div 32$; high (hazardous) if $Z_c = 32 \div 128$; very high (extremely hazardous) if $Z_c > 128$.

Table 4 presents the assessment of chemical pollution at the test sites for several elements. The evaluation outcomes can be summarized as follows:

– the total pollution index for sites *1*, *2*, *3*, *6* is less than 16, indicating that soil pollution at these sites falls within the "acceptable" category;

– for sites *4*, *5*, *7*, *8* the integral pollution index ranges between 16 and 32, classifying soil pollution at these sites as "moderately dangerous.

Conclusions

The analysis of snow cover revealed that the concentrations of heavy metals, including arsenic, dry residue in meltwater, chloride ions, and sulfate ions at the test sites within the SPZ of JSC EVRAZ ZSMK, do not surpass the MPC limits. Similarly, in the soil cover at these SPZ test sites, the levels of heavy metals (V, Mn, As, Sb, Ni, Cu, Zn, Pb), arsenic, sulfur, oil products, and *p*H values are within the normal range. The benz(a)pyrene level slightly exceeds the norm at only one out of the eight sites.

The total pollution index categorizes the contamination levels at four out of the eight test sites as "acceptable".

References / Список литературы

1. Turos O.I., Petrosyan A.A., Anan'єva O.V., Kartavtsev O.M. Expanding the possibilities of sanitary and epidemiological expertise in justifying the establishment of size of sanitary protection zone for a ferroalloy enterprise at the risk management stage. *Gigiena naselenikh mists'*. 2013;(61):62–70. (In Ukr.).

   Турос О.І., Петросян А.А., Ананьєва О.В., Картавцев О.М. Розширення можливостей санітарно-епідеміологічної експертизи при обгрунтуванні встановлення розміру санітарно-захисної зони для феросплавного підприємства на етапі управління ризиком. *Гігієна населених місць*. 2013;(61):62–70.
2. Alimbaev T., Mazhitova Zh., Beksultanova C., TentigulKyzy N. Activities of mining and metallurgical industry enterprises of the Republic of Kazakhstan: environmental problems and possible solutions. In: *XIII Int. Sci. and Pract. Conf. "State and Prospects for the Development of Agribusiness – INTERAGROMASH 2020"*. 2020;175:14019. https://doi.org/10.1051/e3sconf/202017514019
3. Casas A., Ferrero G., Tapias J.C., Rivero L., Font X., Viladevall M. Mapping heavy metal pollution of soils affected by metallurgical point-source pollution near Barcelona (Spain). In: *68th European Association of Geoscientists and Engineers Conference and Exhibition incorporating SPE EUROPEC 2006, EAGE 2006: Opportunities in Mature Areas.* 2006;4: 2091–2095. https://doi.org/10.3997/2214-4609.201402202
4. Medvedev M.A., Medvedev A.N., Kolomytseva A. On the use of cluster analysis for interpretation of soil pollution monitoring data obtained near mining enterprise. In: *44th Int. Conf. on Applications of Mathematics in Engineering and Economics*. 2018;2048(1):060016. https://doi.org/10.1063/1.5082131
5. Zhukorskyi O., Nykyforuk O. Assessment of snow cover in sanitary protection zone of pig complexes of different capacities. *Агроекологічний журнал*. 2014;(3):64–69.
6. Brimblecombe P., Lefèvre R.-A. Weathering of materials at Notre-Dame from changes in air pollution and climate in Paris, 1325–2090. *Journal of Cultural Heritage*. 2021;50: 88–94. https://doi.org/10.1016/j.culher.2021.06.007
7. Kozłowski R., Jóźwiak M., Jóźwiak M.A., Rabajczyk A. Chemism of atmospheric precipitation as a consequence of air pollution: The case of Poland's holy cross mountains. *Polish Journal of Environmental Studies*. 2011;20(4):919–924.
8. Pilecka J., Valujeva K., Grinfelde I., Eihe P., Purmalis O. Snow in the cities as an indicator of air pollution caused by traffic. In: *19th Int. Multidisciplinary Sci. GeoConference Surveying Geology and Mining Ecology Management, SGEM, 2019*. 2019;19(4.1):1069–1076. https://doi.org/10.5593/sgem2019/4.1/S19.136
9. Pilecka J., Grinfelde I., Purmalis O., Valujeva K., Ulcugacevs V. The heavy metal deposition in snow: case study of Jelgava city. In: *20th Int. Multidisciplinary Sci. GeoConference Surveying Geology and Mining Ecology Management, SGEM 2020.* 2020;20(4.1):507–514. https://doi.org/10.5593/sgem2020/4.1/s19.063

10. Chen L., Zhi X., Shen Z., Dai Y., Aini G. Comparison between snowmelt-runoff and rainfall-runoff nonpoint source pollution in a typical urban catchment in Beijing, China. *Environmental Science and Pollution Research*. 2018;25(3): 2377–2388. https://doi.org/10.1007/s11356-017-0576-z

11. Rogulya L.I. Snow cover – an indicator of atmospheric pollution. *Molodoi uchenyi*. 2018;(39):48–51. Available at URL: https://moluch.ru/archive/225/52866/ (Accessed: 14.09.2023). (In Russ.).

Рогуля Л.И. Снежный покров – индикатор загрязнения атмосферы. *Молодой ученый*. 2018;(39):48–51. URL: https://moluch.ru/archive/225/52866/ (Дата обращения: 14.09.2023).

12. Bezrukova V.V., Samokhvalova O.A., Il'ina A.S., Khoroshikh P.S., Vorob'eva D.N. Ecomonitoring of snow and soil cover in the boundaries of sanitary protection zone of JSC EVRAZ ZSMK. In: *Science and Youth: Problems, Searches, Solutions. Proceedings of the All-Russ. Sci. Conf. of Students, Postgraduates and Young Scientists, May 14-16, 2019 Novokuznetsk*. SibGIU, 2019; 23(6):342–347. (In Russ.).

Безрукова В.В., Самохвалова О.А., Ильина А.С., Хороших П.С., Воробьева Д.Н. Экомониторинг снежного и почвенного покровов в границах санитарно-защитной зоны АО «ЕВРАЗ ЗСМК». В кн.: *Наука и молодежь: проблемы, поиски, решения. Труды Всероссийской научной конференции студентов, аспирантов и молодых ученых, 14-16 мая 2019 г. Новокузнецк*, ИЦ СибГИУ, 2019;23(6):342–347.

13. Kicińska A. Environmental risk related to presence and mobility of As, Cd and Tl in soils in the vicinity of a metallurgical plant – Long-term observations. *Chemosphere*. 2019;236: 124308. https://doi.org/10.1016/j.chemosphere.2019.07.039

14. Paliulis D., Uselyte I., Couch W. J. Experimental investigations of heavy metals concentrations in the ground of section Kazlu Ruda – Jure. In: *7th Int. Conf. on Environmental Engineering, ICEE 2008 – Conf. Proceedings*. 2008:267–273.

15. Stevanović J., Serbula S.M., Trujić V. Arsenic heavy metals and SO_2 derived in: A mining-metallurgical production process. In: *Hazardous Materials: Types, Risks and Control*. 2011:187–223.

16. Achkasov A.I., Basharkevich I.L., Onishchenko T.L., Pavlova L.N., Revich B.A., Saet Yu.E., Sarkisyan S.Sh., Smirnova R.S., Trefilova N.Ya., Yanin E.P. *Geochemistry of the Environment*. Moscow: Nedra; 1990:335. (In Russ.).

Геохимия окружающей среды / А.И. Ачкасов, И.Л. Башаркевич, Т.Л. Онищенко, Л.Н. Павлова, Б.А. Ревич, Ю.Е. Сает, С.Ш. Саркисян, Р.С. Смирнова, Н.Я. Трефилова, Е.П. Янин. Москва: Недра; 1990:335.

Information about the Authors / Сведения об авторах

Marina A. Zakharova, *Postgraduate of the Chair of Ferrous Metallurgy,* Siberian State Industrial University
E-mail: marina-shentsova@mail.ru

Anatolii S. Vodoleev, *Dr. Sci. (Agr.), Prof. of the Chair "Thermal Power and Ecology"*, Siberian State Industrial University
ORCID: 0009-0003-0081-2797
E-mail: botanik-egf@yandex.ru

Oksana S. Andreeva, *Cand. Sci. (Geogr.), Assist. Prof. of the Chair "Geoecology and Geography"*, Kuzbass Humanitarian and Pedagogical Institute of the Kemerovo State University
E-mail: o_s_a@bk.ru

Konstantin I. Domnin, *Postgraduate of the Chair "Thermal Power and Ecology"*, Siberian State Industrial University
ORCID: 0009-0003-2257-091X
E-mail: domnin_k_i@mail.ru

Марина Александровна Захарова, *аспирант кафедры металлургии черных металлов*, Сибирский государственный индустриальный университет
E-mail: marina-shentsova@mail.ru

Анатолий Сергеевич Водолеев, *д.с-х.н., профессор кафедры теплоэнергетики и экологии*, Сибирский государственный индустриальный университет
ORCID: 0009-0003-0081-2797
E-mail: botanik-egf@yandex.ru

Оксана Сергеевна Андреева, *к.г.н., доцент кафедры геоэкологии и географии*, Кузбасский гуманитарно-педагогический институт Кемеровского государственного университета
E-mail: o_s_a@bk.ru

Константин Игоревич Домнин, *аспирант кафедры теплоэнергетики и экологии*, Сибирский государственный индустриальный университет
ORCID: 0009-0003-2257-091X
E-mail: domnin_k_i@mail.ru

Contribution of the Authors / Вклад авторов

M. A. Zakharova – conducting experimental studies, processing and analysis of the results.
A. S. Vodoleev – formation of the main concept, goals and objectives of the study; writing the text.
O. S. Andreeva – literary review, analysis of experimental data.
K. I. Domnin – processing of the results, data analysis, revision of the text.

М. А. Захарова – проведение экспериментальных исследований, обработка и анализ результатов.
А. С. Водолеев – формирование основной концепции, цели и задач исследования; написание текста рукописи.
О. С. Андреева – обзор публикаций по теме статьи, анализ экспериментальных данных.
К. И. Домнин – обработка результатов, анализ данных, доработка текста.

Received 07.10.2021
Revised 02.06.2023
Accepted 08.06.2023

Поступила в редакцию 07.10.2021
После доработки 02.06.2023
Принята к публикации 08.06.2023

MATERIALS SCIENCE / МАТЕРИАЛОВЕДЕНИЕ

UDC 621.78:669.15-194.56
DOI 10.17073/0368-0797-2023-5-544-553

Original article
Оригинальная статья

Effect of silver and heat treatment on properties of 03Kh17N10M2 austenitic steel wire

A. D. Gorbenko[1, 2], M. A. Kaplan[1], S. V. Konushkin[1], E. O. Nasakina[1], A. S. Baikin[1], K. V. Sergienko[1], A. Yu. Ivannikov[1], Ya. A. Morozova[1, 2], S. A. Oshkukov[3], A. G. Kolmakov[1], M. A. Sevost'yanov[1, 2]

[1] **Baikov Institute of Metallurgy and Materials Science, Russian Academy of Sciences** (49 Leninskii Ave., Moscow 119991, Russian Federation)
[2] **All-Russian Research Institute of Phytopathology** (5 Institut Str., Bol'shie Vyazemy Vil., Odintsovo District, Moscow Region 143050, Russian Federation)
[3] **M.F. Vladimirskii Moscow Regional Research Clinical Institute** (61/2 Shchepkina Str., Moscow 129110, Russian Federation)

artemgorbenk@yandex.ru

Abstract. The article examines the influence of various heat treatments, their temperature, as well as silver alloying on mechanical properties, phase composition and structure of steel wire from chromium-nickel-molybdenum austenitic stainless steel 03Kh17N10M2. Choice of the amount of silver alloying was based on previous studies of the antibacterial effect of modifying medical steels with silver. Since the antibacterial effect was confirmed on several bacterial strains, for the most efficient operation of alloys, it is necessary to determine the best temperature mode for working with them. Steel for the study was smelted and then transformed into wire through rolling, forging and drawing operations. On the obtained wire samples of different diameters with a silver content (0; 0.2 and 0.5 wt. %) mechanical tests were carried out to determine the elongation, yield strength and tensile strength. Various modes and temperatures of heat treatment were tested on wire of different diameters to study their effect on mechanical properties and structure. Microstructure of the wire samples subjected to heat treatment and obtained after drawing was investigated. A phase analysis was also carried out to determine the effect of silver in various quantities on austenitic steel. According to the results of the phase composition analysis, it was concluded that silver reduces the amount of gamma phase in steel, and this effect increases in proportion to the increase in silver amount. This change correlates with a slight drop in the metal ductility. At the same time, there are no significant changes in the strength characteristics and microstructure from the presence of silver.

Keywords: heat treatment, wire, silver, stainless steel, mechanical properties, phase composition

For citation: Gorbenko A.D., Kaplan M.A., Konushkin S.V., Nasakina E.O., Baikin A.S., Sergienko K.V., Ivannikov A.Yu., Morozova Ya.A., Oshkukov S.A., Kolmakov A.G., Sevost'yanov M.A. Effect of silver and heat treatment on properties of 03Kh17N10M2 austenitic steel wire. *Izvestiya. Ferrous Metallurgy*. 2023;66(5):544–553. https://doi.org/10.17073/0368-0797-2023-5-544-553

Влияние серебра и термической обработки на свойства проволоки из аустенитной стали 03Х17Н10М2

А. Д. Горбенко[1, 2], М. А. Каплан[1], С. В. Конушкин[1], Е. О. Насакина[1], А. С. Баикин[1], К. В. Сергиенко[1], А. Ю. Иванников[1], Я. А. Морозова[1, 2], С. А. Ошкуков[3], А. Г. Колмаков[1], М. А. Севостьянов[1, 2]

[1] **Институт металлургии и материаловедения им. А.А. Байкова РАН** (Россия, 119991, Москва, Ленинский пр., 49)
[2] **Всероссийский научно-исследовательский институт фитопатологии** (Россия, 143050, Московская область, Одинцовский район, р.п. Большие Вяземы, ул. Институт, владение 5)
[3] **Московский областной научно-исследовательский клинический институт им. М.Ф. Владимирского** (Россия, 129110, Москва, ул. Щепкина, 61/2)

artemgorbenk@yandex.ru

Аннотация. В статье рассматривается влияние различных термических обработок, их температуры, а также легирования серебром на механические свойства, фазовый состав и структуру проволоки из нержавеющей хромоникельмолибденовой аустенитной стали 03Х17Н10М2. Выбор величины легирования серебром основывался на ранее проведенных исследованиях антибактериального эффекта от модифицирования медицинских сталей серебром. Поскольку антибактериальное воздействие подтверждено на нескольких штаммах бактерий, для наиболее эффективной эксплуатации сплавов требуется определить наилучший температурный режим работы с ними. Сталь для исследования выплавлена и затем через операции прокатки, ковки и волочения преобразована в проволоку. На полученных образцах проволоки разного диаметра с содержанием серебра 0; 0,2 и 0,5 % (по массе) проведены механические испытания для определения относительного удлинения, предела текучести и предела прочности. На проволоке разного диаметра опробованы различные режимы и температуры термических обработок для исследования их влияния на механические свойства и структуру. Исследована микроструктура подвергнутых термической обработке и полученных после волочения образцов проволоки. Также проведен фазовый анализ с целью установления эффекта от присутствия серебра в различных количествах на аустенитную сталь. По результатам исследования фазового состава сделан вывод, что серебро уменьшает количество гамма-фазы в стали, и этот эффект растет пропорционально увеличению доли серебра. Данное изменение коррелирует с небольшим падением пластичности металла. При этом значимых изменений в прочностных характеристиках и микроструктуре от присутствия серебра не наблюдается.

Ключевые слова: термическая обработка, проволока, серебро, нержавеющая сталь, механические свойства, фазовый состав

Для цитирования: Горбенко А.Д., Каплан М.А., Конушкин С.В., Насакина Е.О., Баикин А.С., Сергиенко К.В., Иванников А.Ю., Морозова Я.А., Ошкуков С.А., Колмаков А.Г., Севостьянов М.А. Влияние серебра и термической обработки на свойства проволоки из аустенитной стали 03Х17Н10М2. *Известия вузов. Черная металлургия*. 2023;66(5):544–553. https://doi.org/10.17073/0368-0797-2023-5-544-553

Introduction

Austenitic steels find widespread use in economic sectors where materials necessitate high resistance to corrosion and durability. These sectors include medicine, the food industry, chemical production, among others. This utilization is linked to a specific set of requirements, primarily corrosion resistance and relatively low cost. These steels have gained significant traction in medicine, particularly in applications involving direct and prolonged contact with the human body, such as implantation. This is attributed to their biotolerance and relatively high plasticity [1 – 3].

For short-term implantation, biotolerant materials are employed, meeting the standards set by State Standards GOST, such as high-alloy stainless steels [4; 5]. While they can be utilized in creating long-lasting prostheses [6; 7], current practices involve augmenting these materials with coatings and other methods to enhance biocompatibility [8]. Stainless medical steels exhibit resistance to the aggressive internal environment of the human body and, notably, do not typically induce an immune reaction, barring individual, rare allergic responses to specific components. However, despite the advantages of these materials, the possibility of bacterial infection in the vicinity of the implant cannot be entirely ruled out during operations [9 – 12].

Silver is known for its capability to disrupt bacteria metabolism [13 – 16]. This essential property persists when silver is incorporated into coatings [17; 18] or utilized as a doping component [19 – 21]. Several publications [2; 19] detail the authors' endeavors in producing 03Kh17N10M2 steel with 0.2 and 0.5 % Ag additions, examining these compositions for their antibacterial properties. The research revealed that a mere 0.2 % Ag within the steel composition suffices to suppress detrimental strains of *Pseudomonas marginalis* and *Clavibacter bacteria*. Furthermore, an escalation in silver content resulted in a more pronounced effect. Additionally, these compositions underwent scrutiny to ascertain their mechanical properties and microstructural changes. However, the research focused on materials in the form of ingots and rolled products, while acknowledging the potential use of such steels in wire form or as a workpiece. This could facilitate further utilization in additive manufacturing, welding, or product formation through simple mechanical processing.

This study aimed to determine the mechanical properties of wire fabricated from 03Kh17N10M2 steel (akin in chemical composition to steels employed in medicine and jewelry, such as 316L) with silver additives. The investigation explored the influence of silver on the steel's structure, phase composition, mechanical properties, and the impact of various heat treatment methods on the silver-enhanced steel.

Materials and methods

The smelting of steel took place at the Baikov Institute of Metallurgy and Materials Science, Russian Academy of Sciences. Through a process of triple remelting, chromium-nickel-molybdenum stainless austenitic steel 03Kh17N10M2 was produced, incorporating additional doping with silver. The chemical composition of the resulting alloys is detailed in Table 1. Alloy *1* represents the base composition without the addition of silver, while alloy contains 0.2 % Ag and alloy *3* contains 0.5 % Ag. Further details on the ingot production technology are available in [2].

The cast billets were rolled into 1 mm thick plates using a two-roll mill. Subsequently, the deformed workpieces were rotated by 90° and, through repeated rolling,

Table 1

Compositions of the smelted alloys

Таблица 1. **Составы выплавленных сплавов**

Alloy No.	Content of elements, wt. %									
	C	Cr	Ni	Ag	Si	Mn	Mo	P	S	N
1	0.023	16.75	10.09	0	0.43	1.82	2.05	0.041	0.009	0.073
2	0.023	16.75	10.09	0.2	0.43	1.82	2.05	0.041	0.009	0.073
3	0.023	16.75	10.09	0.5	0.43	1.82	2.05	0.041	0.009	0.073

were shaped into bars measuring 10×10 mm. To achieve a diameter of 2.4 mm, rotational forging was conducted on radial forging machines. This process involved successive changes of strikers, progressing in increments of 1 mm until reaching a 5 mm diameter, at which point the increment was reduced to 0.5 mm. Intermediate heating up to 700 °C was applied during the forging process.

In preparation for subsequent operations and to analyze the impact of various heat treatments (HT) on the properties of the resulting steel bars, a bar with a 2.4 mm diameter underwent different heat treatment processes–annealing, normalization, and quenching – inside a muffle furnace.

Before reducing the diameter further, a scale removal process was performed using a solution of nitric and hydrochloric acids. Subsequently, the bars were lubricated with sodium soap, and a layer of borax was applied as a lubricating agent to enhance adhesion to the steel surface.

The subsequent reduction in diameter to 1 mm was achieved utilizing a drawing machine in an atmospheric environment. The wire underwent processing at a speed of 5 m/min, gradually decreasing in diameter by 0.2 mm per pass, from 2.4 to 1.6 mm. Following this, a two-minute heat treatment at 900 °C was conducted in the furnace to anneal the cold-worked steel. Subsequent wire drawing to reduce the diameter to 1 mm occurred at half the previous steps and speeds: 0.1 mm per pass at a rate of 2.5 m/min.

Fig. 1. Obtained wire with a diameter of 1 mm

Рис. 1. Полученная проволока диаметром 1 мм

Upon achieving the final diameter, the silver-free steel wire underwent heat treatment at temperatures of 900, 950, 1000 and 1050 °C, each for a holding time of 2.5 min (Fig. 1).

Structural examinations were performed on thin sections of the resulting steel samples. These samples were embedded in non-conductive resin, followed by grinding and polishing.

Surface etching was conducted using a composition suitable for high-alloy steels, comprising hydrofluoric, sulfuric, and nitric acids (2, 15 and 5 %, respectively, with the rest being water).

Microstructural analyses were carried out using an Altami MET 5C microscope, resulting in images depicting the wire's structure at two different diameters: 2.4 and 1 mm. Photographic recording was executed in polarized light with maximum brightness.

The phase composition of the resulting steels was investigated through *X*-ray diffraction patterns obtained using CuK_α radiation in a parallel beam geometry. The positional error of reflections during analysis did not exceed 0.01° 2θ. The crystal lattice parameter was adjusted by extrapolation to θ = 90° using the Nelson–Riley method within Origin-2017 software. Microstrain in the crystal lattice of the main phase was determined using the Williamson–Hall method, and the quantitative content of crystalline phases was estimated using the corundum number method.

Mechanical properties of the resulting wires were calculated based on tensile tests conducted on an INSTRON 3382 universal testing machine. The average values were derived from five experiments, determining ultimate strength, yield stress, and relative elongation in accordance with State Standard GOST 1497 – 84, utilizing the software integrated with the testing machine.

Results and discussion

Fig. 2 displays the surface characteristics of sections obtained from bars with a 2.4 mm diameter.

Upon analyzing the microstructure, it can be inferred that the presence of silver did not exhibit a discernible impact on the grain size in both cases.

The materials after drawing are strengthened, heavily deformed throughout the volume of the metal, thereby exhibiting minimal ductility. To enable further processing and to investigate the influence of silver and various heat treatments on the properties of bars composed of steel 03Kh17N10M2, annealing, normalization, and quenching of the resulting bars were conducted. Fig. 3 exhi-

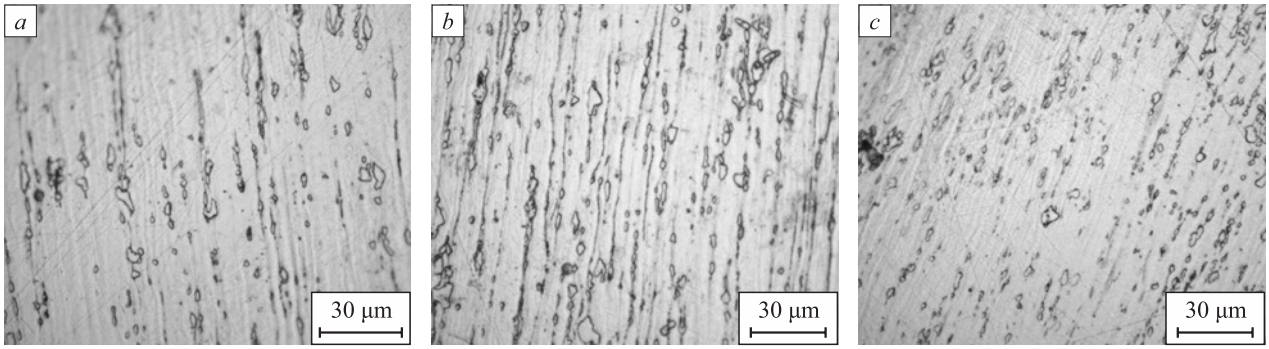

Fig. 2. Microstructure of the bars:
a – 03Kh17N10M2; *b* – 03Kh17N10M2 + 0.2 Ag; *c* – 03Kh17N10M2 + 0.5 Ag

Рис. 2. Микроструктура прутков:
a – 03Х17Н10М2; *b* – 03Х17Н10М2 + 0,2 Ag; *c* – 03Х17Н10М2 + 0,5 Ag

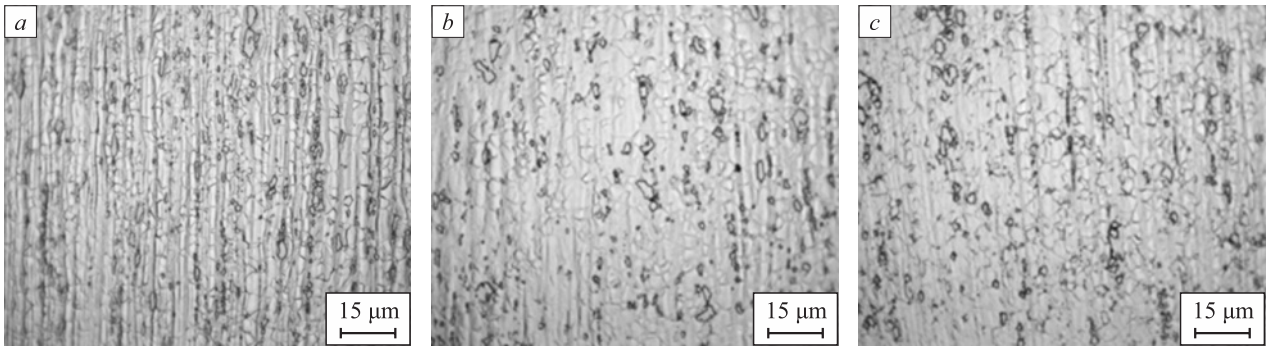

Fig. 3. Microstructure of the bars after normalization at 900 °C (holding time – 2 min):
a – 03Kh17N10M2; *b* – 03Kh17N10M2 + 0.2 Ag; *c* – 03Kh17N10M2 + 0.5 Ag

Рис. 3. Микроструктура прутков после нормализации при 900 °С (выдержка 2 мин):
a – 03Х17Н10М2; *b* – 03Х17Н10М2 + 0,2 Ag; *c* – 03Х17Н10М2 + 0,5 Ag

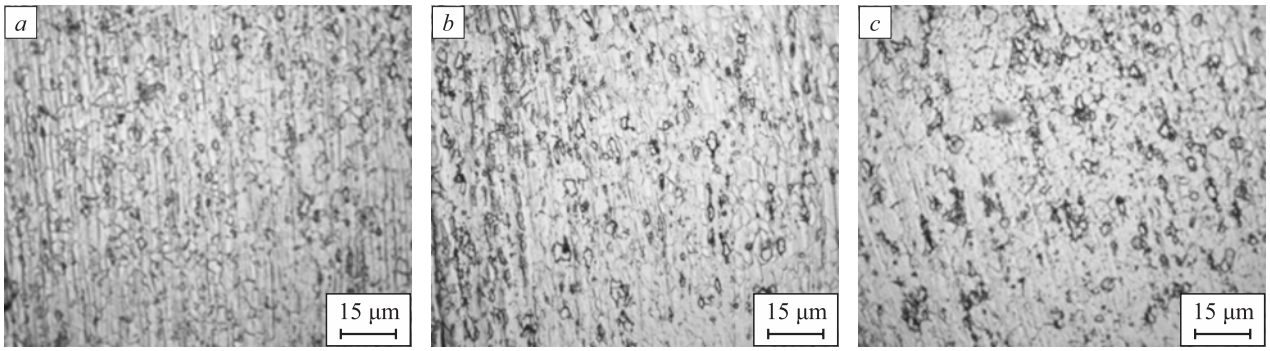

Fig. 4. Microstructure of the bars after annealing at 950 °C (holding time – 2.5 min):
a – 03Kh17N10M2; *b* – 03Kh17N10M2 + 0.2 Ag; *c* – 03Kh17N10M2 + 0.5 Ag

Рис. 4. Микроструктура прутков после отжига при 950 °С (выдержка 2,5 мин):
a – 03Х17Н10М2; *b* – 03Х17Н10М2 + 0,2 Ag; *c* – 03Х17Н10М2 + 0,5 Ag

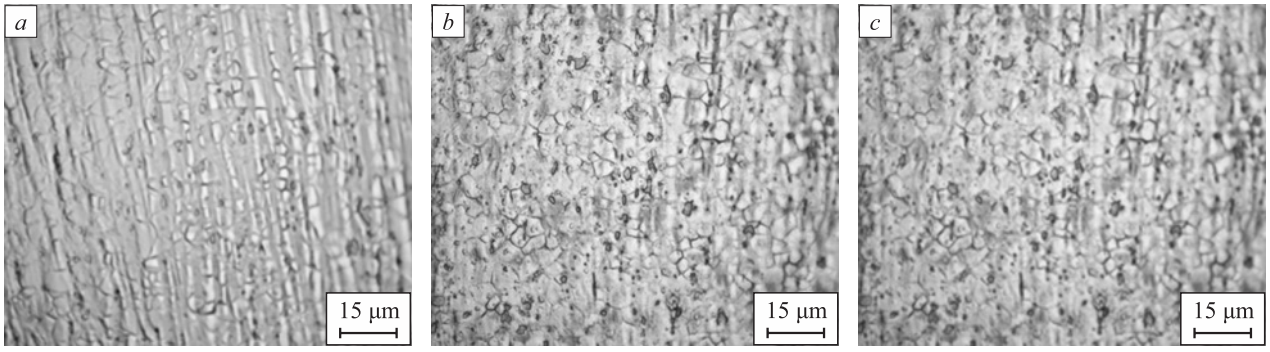

Fig. 5. Microstructure of the bars after quenching at 950 °C (holding time – 2.5 min):
a – 03Kh17N10M2; *b* – 03Kh17N10M2 + 0.2 Ag; *c* – 03Kh17N10M2 + 0.5 Ag

Рис. 5. Микроструктура прутков после закалки 950 °С (выдержка 2,5 мин):
a – 03Х17Н10М2; *b* – 03Х17Н10М2 + 0,2 Ag; *c* – 03Х17Н10М2 + 0,5 Ag

bits images of three alloys post-normalization at 900 °C, while Fig. 4 showcases the microstructure subsequent to annealing at 950 °C. Fig. 5 demonstrates the microstructure following quenching at 950 °C.

Following heat treatments, the wire materials undergo recrystallization, leading to the formation of a fine-grained structure with grain sizes ranging from 3 to 6 μm.

Upon quenching, an equiaxed and finely dispersed austenite structure becomes apparent. The presence of banding suggests that recrystallization was incomplete before the samples experienced accelerated cooling. Samples cooled in a furnace displayed grains with a more uniform shape than those cooled in water. Interestingly, annealed samples exhibited superior etchability when contrasted with quenched ones. Samples normalized at 900 °C exhibited similar microstructures to those subjected to the quenching process.

The microstructures of all compositions, regardless of the presence of silver, exhibit no significant differences from each other. This indicates that microdoping does not yield discernible microstructural changes.

Mechanical properties of steels from melts *1* to *3* were evaluated after undergoing various heat treatments, with a summary of the test results presented in Table 2.

Heat treatment of bars with a 2.4 mm diameter consistently results in a notable increase in ductility, which is essential for alleviating cold-working and producing wire of smaller diameters. Notably, the most pronounced

Table 2

Mechanical properties of a bar with diameter of 2.4 mm, depending on the sample composition and heat treatment

Таблица 2. **Механические свойства прутка диаметром 2,4 мм в зависимости от химического состава образца и термической обработки**

Material and heat treatment	Relative elongation, %	Yield stress, MPa	Ultimate strength, MPa
1 (03Kh17N10M2) after drawing	12 ± 1	243 ± 3	1026 ± 10
1 + normalization 900 °C, 2 min	31 ± 1	454 ± 5	760 ± 8
1 + annealing 950 °C, 2.5 min	33 ± 2	423 ± 4	738 ± 7
1 + quenching 950 °C, 2.5 min	53 ± 2	311 ± 3	691 ± 7
2 (03Kh17N10M2 + 0.2 % Ag) after drawing	10 ± 1	177 ± 3	974 ± 8
2 + normalization 900 °C, 2 min	42 ± 2	365 ± 4	721 ± 7
2 + annealing 950 °C, 2.5 min	28 ± 1	346 ± 3	667 ± 7
2 + quenching 950 °C, 2.5 min	35 ± 2	295 ± 3	645 ± 5
3 (03Kh17N10M2 + 0.5 % Ag) after drawing	3 ± 1	276 ± 3	900 ± 9
3 + normalization 900 °C, 2 min	30 ± 1	336 ± 4	672 ± 6
3 + annealing 950 °C, 2.5 min	31 ± 1	394 ± 5	714 ± 7
3 + quenching 950 °C, 2.5 min	45 ± 2	293 ± 4	680 ± 6

Table 3

Phase composition and parameters of the crystal lattice of 1 mm wire samples *1 – 3*

Таблица 3. **Фазовый состав и параметры кристаллической решетки проволоки диаметром 1 мм образцов *1 – 3***

Composition	Crystal lattice parameters, Å	Phase composition	Volumetric fraction, %	Weight fraction, %
1 (03Kh17N10M2)	3.59442 ± 0.00008	γ-Fe	85.3 ± 0.1	85.6 ± 0.1
	2.87512 ± 0.00011	α-Fe	13.8 ± 0.1	13.5 ± 0.1
	8.81800	σ-NiCr	0.9 ± 0.1	0.8 ± 0.1
	4.57800			
2 (03Kh17N10M2 + 0.2 % Ag)	3.59488 ± 0.00009	γ-Fe	82.9 ± 0.2	83.3 ± 0.2
	2.87552 ± 0.00012	α-Fe	15.8 ± 0.1	15.5 ± 0.1
	8.81800	σ-NiCr	1.3 ± 0.1	1.3 ± 0.1
	4.57800			
3 (03Kh17N10M2 + 0.5 % Ag)	3.59497 ± 0.00008	γ-Fe	74.2 ± 0.1	74.7 ± 0.1
	2.87599 ± 0.00008	α-Fe	24.1 ± 0.1	23.7 ± 0.1
	8.80994 ± 0.00165	σ-NiCr	1.7 ± 0.1	1.6 ± 0.1
	4.59121 ± 0.00165			

effect was observed in the case of 03Kh17N10M2 without the addition of silver, wherein quenching facilitated achieving a relative elongation of over 50 %. The influence of silver on the mechanical properties was marginal, resulting in a slight reduction in ductility. Consequently, quenching was deemed the most suitable method for preparing the wire for further drawing to a 1 mm diameter.

To delve deeper into the impact of silver, *X*-ray phase analysis was conducted on the wires with a 1 mm diameter. The phase composition data for the wires are outlined in Table 3 and depicted in Figs. 6, 7.

The analysis of the phase composition revealed a decrease in the γ-Fe fraction and an increase in α-Fe and σ-NiCr from wire composition *1* to composition *3*. This denotes a ferrite-forming effect attributed to silver in the stainless steel composition. The escalation in silver content correlates with an increase in the α-Fe and σ-NiCr phases. The presence of ferrite results from significant plastic deformation during wire drawing, and it remains unaltered since the steel's content of austenitizing elements (such as carbon, manganese, and nickel) is relatively low. Considering potential applications involving the produced wire in its current form, heat treatment might be advisable to achieve a single-phase structure.

Fig. 8 displays the microstructure of the wires utilized in the phase analysis, highlighting the hardening effect post-drawing.

Table 4 presents the mechanical properties of the resulting wires from compositions *1 – 3* after being drawn to a 1 mm diameter.

Comparing the mechanical properties of the original composition wire with the alloyed compositions, it was observed that the wire with the addition of silver demonstrated similar mechanical characteristics.

Samples of strain-hardened wire with a 1 mm diameter were subjected to heat treatments at temperatures of 900, 950, 1000, 1050 °C, each for a duration of 2.5 min. The results of mechanical tests conducted on the material after these heat treatments are summarized in Table 5.

It has been observed that as the heating temperature for hardening increases, ductility also increases while strength decreases. This phenomenon occurs due to a reduction in the density of dislocations and an increase in grain size within the material. The choice of cooling medium (air or water) exhibits a similar effect

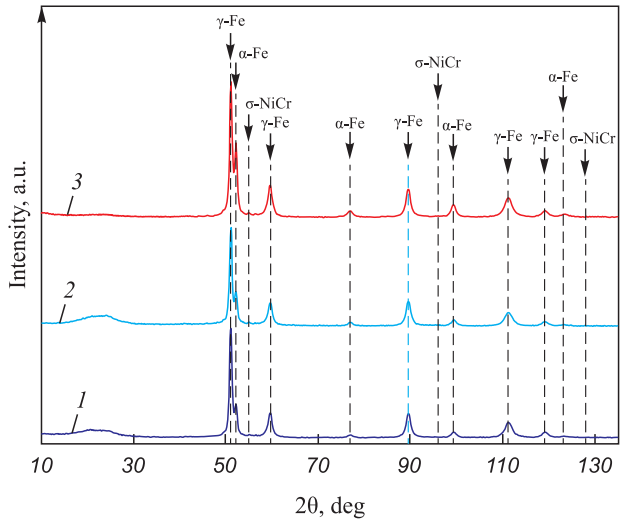

Fig. 6. Diffractogram with the results of phase analysis

Рис. 6. Дифрактограмма с результатами фазового анализа

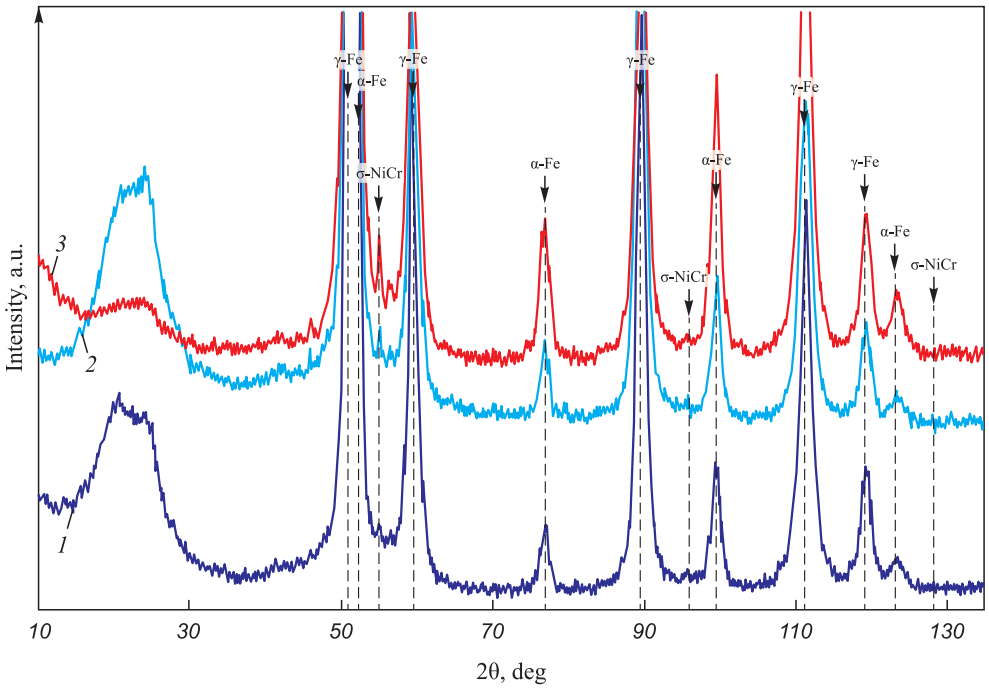

Fig. 7. Enlarged diffractogram with the results of phase analysis

Рис. 7. Увеличенная дифрактограмма с результатами фазового анализа

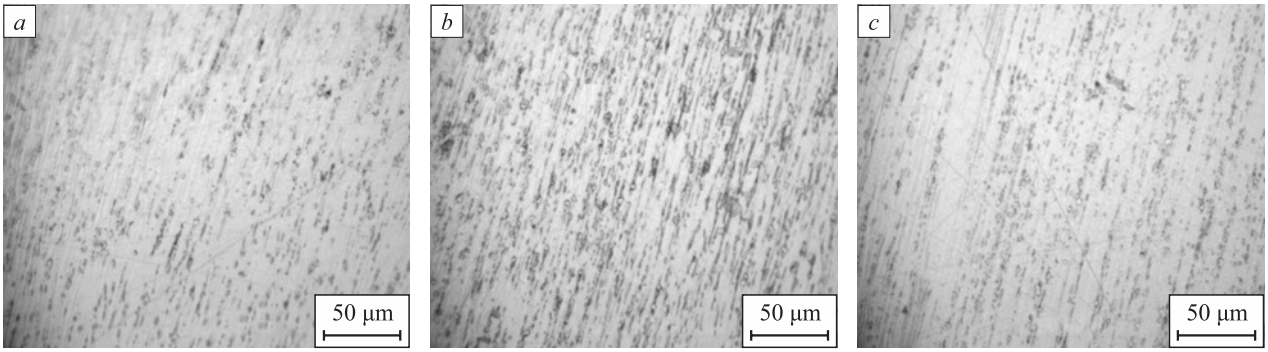

Fig. 8. Microstructure of the wires with a diameter of 1 mm obtained on optical microscope *1* (*a*), *2* (*b*), *3* (*c*)

Рис. 8. Микроструктура проволок диаметром 1 мм, полученная при волочении из сталей марок *1* (*a*), *2* (*b*), *3* (*c*)

on the mechanical properties owing to the relatively small diameter of the wire.

The acquired data aligns with established recommendations for the heat treatment of chromium-nickel-molybdenum steels. Furthermore, the results from mechanical tests conducted on bars, despite the inclusion of silver in the steel composition, do not demonstrate any anomalous findings. Notably, the observed ferrite-forming effect

Table 4

Mechanical properties of wires with diameter of 1 mm

Таблица 4. **Механические свойства проволок диаметром 1 мм**

Composition	Relative elongation, %	Yield stress, MPa	Ultimate strength, MPa
1 (03Kh17N10M2)	2.1 ± 0.3	1018 ± 8	1356 ± 8
2 (03Kh17N10M2 + 0.2 % Ag)	1.5 ± 0.3	1207 ± 9	1648 ± 10
3 (03Kh17N10M2 + 0.5 % Ag)	1.2 ± 0.2	1280 ± 9	1636 ± 10

Table 5

. **Mechanical properties of the wire with composition *1* and diameter, depending on heat treatment (cooling in air or water)**

Таблица 5. **Механические свойства проволоки состава *1* диаметром 1 мм в зависимости от термической обработки (охлаждение на воздухе или в воде)**

Heat treatment	Relative elongation, %	Yield stress, MPa	Ultimate strength, MPa
900 °C, 2 min, air	51.5 ± 1.3	399 ± 5	802 ± 7
950 °C, 2 min, air	52.1 ± 1.4	371 ± 4	765 ± 7
1000 °C, 2 min, air	55.7 ± 1.5	325 ± 3	738 ± 6
1050 °C, 2 min, air	61.4 ± 1.8	311 ± 3	707 ± 6
900 °C, 2 min, water	52.3 ± 1.4	386 ± 5	792 ± 7
950 °C, 2 min, water	54.6 ± 1.5	344 ± 4	766 ± 7
1000 °C, 2 min, water	58.0 ± 1.8	320 ± 3	739 ± 6
1050 °C, 2 min, water	66.7 ± 1.9	319 ± 3	713 ± 6

of silver, as identified through *X*-ray phase analysis, corresponds with findings in prior research [20]. In the mentioned study, the addition of 0.2 % Ag to 2205 DSS steel resulted in a 1.1 % increase in the ferrite phase content. However, in the case of steel 03Kh17N10M2, this effect was more than two times greater, measuring at 2.3 %. This disparity is likely due to the initial disparity in the ferrite phase content between 2205 DSS steel, which inherently had a significantly higher amount of ferrite phase, and 03Kh17N10M2 steel.

Conclusions

The investigation into the mechanical properties of wires made of austenitic stainless steel 03Kh17N10M2, both without and with silver additions of 0.2 and 0.5 %, revealed a slight reduction in ductility and an increase in strength due to silver doping. Furthermore, the escalation in silver content induced a shift in the phase composition, characterized by a decrease in the γ-phase and an increase in the α-phase and σ-phase. Specifically, the addition of 0.5 % Ag resulted in an 11.1 % decrease in the austenite fraction.

Post-heat treatments, irrespective of wire chemical composition and diameter, recrystallization occurred, fostering the development of a fine-grained structure with grain sizes ranging from 3 to 6 μm.

Interestingly, quenching the resulting 1 mm diameter wire in both air and water yielded similar outcomes. This suggests that for products made from steels with examined compositions, quenching up to a diameter of 1 mm can be effectively executed in air. However, when dealing with diameters larger than 2 mm, the type of heat treatment yields significant variations in mechanical properties.

References / Список литературы

1. Chen Q., Thouas G.A. Metallic implant biomaterials. *Materials Science and Engineering: R: Reports*. 2015;87:1–57. https://doi.org/10.1016/j.mser.2014.10.001
2. Kolmakov A.G., Ivannikov A.Yu., Kaplan M.A., Kirsankin A.A., Sevost'yanov M.A. Corrosion-resistant steels in additive manufacturing. *Izvestiya. Ferrous Metallurgy*. 2021;64(9):619–650. (In Russ.). https://doi.org/10.17073/0368-0797-2021-9-619-650

   Колмаков А.Г., Иванников А.Ю., Каплан М.А., Кирсанкин А.А., Севостьянов М.А. Коррозионностойкие стали в аддитивном производстве. *Известия вузов. Черная металлургия*. 2021;64(9):619–650. https://doi.org/10.17073/0368-0797-2021-9-619-650
3. Kaplan M.A., Ivannikov A.Yu., Konushkin S.V., etc. Investigation of the structure, mechanical and antibacterial properties of corrosion-resistant steel alloyed with silver and titanium. *Reports of the Russian Academy of Sciences. Chemistry, Materials Sciences*. 2022;502(2):41–49. (In Russ.). https://doi.org/10.31857/S268695352201006X

   Каплан М.А., Иванников А.Ю., Конушкин С.В., и др. Исследование структуры, механических и антибактериальных свойств коррозионностойкой стали, легированной серебром и титаном. *Доклады Российской академии наук. Химия, науки о материалах*. 2022;502(2):41–49. https://doi.org/10.31857/S268695352201006X
4. *State standard R 51148-98. Medical products. Requirements for samples and documentation submitted for toxicological, sanitary and chemical tests, sterility and pyrogenicity tests*. Moscow: Izd-vo standartov; 05.05.1998:17. (In Russ.).

   ГОСТ Р 51148-98. Изделия медицинские. Требования к образцам и документации, представляемым на токсикологические, санитарно-химические испытания, испытания на стерильность и пирогенность. Москва: Издательство стандартов; 05.05.1998:17.
5. *State standard 30208-94. Surgical instruments. Metal materials. Part 1: Stainless steel*. Moscow: Izd-vo standartov; 01.10.2002:7. (In Russ.).

ГОСТ 30208-94. Инструменты хирургические. Металлические материалы. Часть 1: Нержавеющая сталь. Москва: Издательство стандартов; 01.10.2002:7.

6. Zardiackas L.D. Stainless steels for implants. *Wiley Encyclopedia of Biomedical Engineering*. 2006:1–9. https://doi.org/10.1002/9780471740360.ebs1136
7. Dick J.C., Bourgeault C.A. Notch sensitivity of titanium alloy, commercially pure titanium, and stainless steel spinal implants. *Spine*. 2001;26(15):1668–1672. https://doi.org/10.1097/00007632-200108010-00008
8. Khosravi F., Nouri Khorasani S., Khalili S., etc. Development of a highly proliferated bilayer coating on 316L stainless steel implants. *Polymers*. 2020;12(5):1022. https://doi.org/10.3390/polym12051022
9. Rogers B.A., Little N.J. Surgical site infection with methicillin-resistant Staphylococcus aureus after primary total hip replacement. *The Bone & Joint Journal*. 2008; 90-B(11):1537–1538. https://doi.org/10.1302/0301-620X.90B11.21242
10. Arciola C.R., Campoccia D., Montanaro L. Implant infections: adhesion, biofilm formation and immune evasion. *Nature Reviews Microbiology*. 2018;16(7):397–409. https://doi.org/10.1038/s41579-018-0019-y
11. Filipović U., Dahmane R.G., Ghannouchi S., Zore A., Bohinc K. Bacterial adhesion on orthopedic implants. *Advances in Colloid and Interface Science*. 2020;283:102228. https://doi.org/10.1016/j.cis.2020.102228
12. Arciola C.R., An Y.H., Campoccia D., Donati M.E., Montanaro L. Etiology of implant orthopedic infections: A survey on 1027 clinical isolates. *The International Journal of Artificial Organs*. 2005;28(11):1091–1100. https://doi.org/10.1177/039139880502801106
13. Rai M.K., Deshmukh S.D., Ingle A.P., Gade A.K. Silver nanoparticles: the powerful nanoweapon against multidrug-resistant bacteria. *Journal of Applied Microbiology*. 2012;112(5):841–852. https://doi.org/10.1111/j.1365-2672.2012.05253.x
14. Morones J.R., Elechiguerra J.L., Camacho A., Holt K., Kouri J.B., Ramírez J.T., Yacaman M.J. The bactericidal effect of silver nanoparticles. *Nanotechnology*. 2005;16(10):2346. https://doi.org/10.1088/0957-4484/16/10/059
15. Baker C., Pradhan A., Pakstis L., Pochan D.J., Shah S.I. Synthesis and antibacterial properties of silver nanoparticles. *Journal of Nanoscience and Nanotechnology*. 2005;5(2): 244–249. https://doi.org/10.1166/JNN.2005.034
16. Yamanaka M., Hara K., Kudo J. Bactericidal actions of a silver ion solution on Escherichia coli, studied by energy-filtering transmission electron microscopy and proteomic analysis. *Applied and Environmental Microbiology*. 2005;71(11):7589–7593. https://doi.org/10.1128/AEM.71.11.7589-7593.2005
17. Mirzaee M., Vaezi M., Palizdar Y. Synthesis and characterization of silver doped hydroxyapatite nanocomposite coatings and evaluation of their antibacterial and corrosion resistance properties in simulated body fluid. *Materials Science and Engineering: C*. 2016;69:675–684. https://doi.org/10.1016/j.msec.2016.07.057
18. Gobi S.K., Sudhakar T., Karthik Al., etc. Silver-calcia stabilized zirconia nanocomposite coated medical grade stainless steel as potential bioimplants. *Surfaces and Interfaces*. 2021;24:101086. https://doi.org/10.1016/j.surfin.2021.101086
19. Kaplan M.A., Gorbenko A.D., Ivannikov A.Y., etc. Investigation of antibacterial properties of corrosion-resistant 316L steel alloyed with 0.2 wt.% and 0.5 wt.% Ag. *Materials.* 2023;16(1):319. https://doi.org/10.3390/ma16010319
20. Yang S.M., Chen Y.C., Pan Y.T., Lin D.Y. Effect of silver on microstructure and antibacterial property of 2205 duplex stainless steel. *Materials Science and Engineering: C*. 2016;63:376–383. https://doi.org/10.1016/j.msec.2016.03.014
21. Gong P., Li H., He X., Wang K., Hu J., Tan W., Zhang S., Yang X. Preparation and antibacterial activity of Fe_3O_4@Ag nanoparticles. *Nanotechnology*. 2007;18(28):285604. https://doi.org/10.1088/0957-4484/18/28/285604

Information about the Authors / Сведения об авторах

Artem D. Gorbenko, *Research Engineer*, Baikov Institute of Metallurgy and Materials Science, Russian Academy of Sciences; *Research Engineer*, All-Russian Research Institute of Phytopathology
E-mail: artemgorbenk@yandex.ru

Mikhail A. Kaplan, *Junior Researcher*, Baikov Institute of Metallurgy and Materials Science, Russian Academy of Sciences
ORCID: 0000-0002-8635-0719
E-mail: mkaplan@imet.ac.ru

Sergei V. Konushkin, *Junior Researcher*, Baikov Institute of Metallurgy and Materials Science, Russian Academy of Sciences
ORCID: 0000-0002-9574-1957
E-mail: venev.55@mail.ru

Elena O. Nasakina, *Senior Researcher*, Baikov Institute of Metallurgy and Materials Science, Russian Academy of Sciences
ORCID: 0000-0002-0783-1558
E-mail: nacakina@mail.ru

Aleksandr S. Baikin, *Research Associate*, Baikov Institute of Metallurgy and Materials Science, Russian Academy of Sciences
E-mail: baikinas@mail.ru

Артем Дмитриевич Горбенко, *инженер-исследователь*, Институт металлургии и материаловедения им. А.А. Байкова РАН; *инженер-исследователь*, Всероссийский научно-исследовательский институт фитопатологии
E-mail: artemgorbenk@yandex.ru

Михаил Александрович Каплан, *младший научный сотрудник*, Институт металлургии и материаловедения им. А.А. Байкова РАН
ORCID: 0000-0002-8635-0719
E-mail: mkaplan@imet.ac.ru

Сергей Викторович Конушкин, *младший научный сотрудник*, Институт металлургии и материаловедения им. А.А. Байкова РАН
ORCID: 0000-0002-9574-1957
E-mail: venev.55@mail.ru

Елена Олеговна Насакина, *старший научный сотрудник*, Институт металлургии и материаловедения им. А.А. Байкова РАН
ORCID: 0000-0002-0783-1558
E-mail: nacakina@mail.ru

Александр Сергеевич Баикин, *научный сотрудник*, Институт металлургии и материаловедения им. А.А. Байкова РАН
E-mail: baikinas@mail.ru

Konstantin V. Sergienko, *Junior Researcher*, Baikov Institute of Metallurgy and Materials Science, Russian Academy of Sciences
E-mail: shulf@yandex.ru

Aleksandr Yu. Ivannikov, *Cand. Sci. (Eng.), Senior Researcher*, Baikov Institute of Metallurgy and Materials Science, Russian Academy of Sciences
ORCID: 0000-0003-1113-391X
E-mail: aivannikov@imet.ac.ru

Yaroslava A. Morozova, *Research Engineer*, Baikov Institute of Metallurgy and Materials Science, Russian Academy of Sciences; *Research Engineer*, All-Russian Research Institute of Phytopathology
E-mail: yasya12987@gmail.com

Sergei A. Oshkukov, *Cand. Sci. (Medical), Senior Researcher*, M. F. Vladimirskii Moscow Regional Research Clinical Institute
E-mail: sergey0687@mail.ru

Aleksei G. Kolmakov, *Corresponding Member of RAS, Dr. Sci. (Eng.), Head of the Laboratory*, Baikov Institute of Metallurgy and Materials Science, Russian Academy of Sciences
ORCID: 0000-0002-4907-951X
E-mail: akolmakov@imet.ac.ru

Mikhail A. Sevost'yanov, *Cand. Sci. (Eng.), Leading Researcher*, Baikov Institute of Metallurgy and Materials Science, Russian Academy of Sciences; *Head of the Center*, All-Russian Research Institute of Phytopathology
ORCID: 0000-0003-2652-8711
E-mail: msevostyanov@imet.ac.ru

Константин Владимирович Сергиенко, *младший научный сотрудник,* Институт металлургии и материаловедения им. А.А. Байкова РАН
E-mail: shulf@yandex.ru

Александр Юрьевич Иванников, *к.т.н., старший научный сотрудник,* Институт металлургии и материаловедения им. А.А. Байкова РАН
ORCID: 0000-0003-1113-391X
E-mail: aivannikov@imet.ac.ru

Ярослава Анатольевна Морозова, *инженер-исследователь,* Институт металлургии и материаловедения им. А.А. Байкова РАН; *инженер-исследователь*, Всероссийский научно-исследовательский институт фитопатологии
E-mail: yasya12987@gmail.com

Сергей Александрович Ошкуков, *к.мед.н., старший научный сотрудник*, Московский областной научно-исследовательский клинический институт им. М. Ф. Владимирского
E-mail: sergey0687@mail.ru

Алексей Георгиевич Колмаков, *член-корреспондент РАН, д.т.н., заведующий лабораторией*, Институт металлургии и материаловедения им. А.А. Байкова РАН
ORCID: 0000-0002-4907-951X
E-mail: akolmakov@imet.ac.ru

Михаил Анатольевич Севостьянов, *к.т.н, ведущий научный сотрудник*, Институт металлургии и материаловедения им. А.А. Байкова РАН; *руководитель центра*, Всероссийский научно-исследовательский институт фитопатологии
ORCID: 0000-0003-2652-8711
E-mail: msevostyanov@imet.ac.ru

Contribution of the Authors / Вклад авторов

A. D. Gorbenko – writing of the text, processing of the results.
M. A. Kaplan – conducting the research.
S. V. Konushkin – modes testing, obtaining the wire.
E. O. Nasakina – consultation in research and writing the article.

A. S. Baikin – conducting phase analysis.
K. V. Sergienko – processing of test results.
A. Yu. Ivannikov – conducting heat treatment.
Ya. A. Morozova – study of the wire structure.
S. A. Oshkukov – study of the wire mechanical properties.
A. G. Kolmakov – finalization of the text, correction of conclusions.
M. A. Sevostyanov – scientific guidance, article editing.

А. Д. Горбенко – подготовка текста статьи, обработка результатов.
М. А. Каплан – проведение исследований.
С. В. Конушкин – отработка режимов, получение проволоки.
Е. О. Насакина – консультация в исследованиях и написании работы.
А. С. Баикин – проведение фазового анализа.
К. В. Сергиенко – обработка результатов испытаний.
А. Ю. Иванников – проведение термической обработки.
Я. А. Морозова – исследование структуры проволоки.
С. А. Ошкуков – исследование механических свойств проволоки.
А. Г. Колмаков – доработка текста, корректировка выводов.
М. А. Севостьянов – научное руководство, редактура статьи.

Received 07.04.2023
Revised 05.05.2023
Accepted 28.08.2023

Поступила в редакцию 07.04.2023
После доработки 05.05.2023
Принята к публикации 28.08.2023

MATERIALS SCIENCE / МАТЕРИАЛОВЕДЕНИЕ

UDC 669.15:621.78
DOI 10.17073/0368-0797-2023-5-554-563

Original article
Оригинальная статья

Preservation conditions of hot work hardening in die steel with regulated austenitic transformation during exploitation

A. A. Kruglyakov[1], S. O. Rogachev[2, 3] ✉, P. Yu. Sokolov[2], D. V. Priupolin[2]

[1] **Scientific Production Association WBH** (106 b Friedrichstrasse, Berlin D-10117, Germany)
[2] **National University of Science and Technology "MISIS"** (4 Leninskii Ave., Moscow 119049, Russian Federation)
[3] **Baikov Institute of Metallurgy and Materials Science, Russian Academy of Sciences** (49 Leninskii Ave., Moscow 119334, Russian Federation)

✉ csaap@mail.ru

Abstract. Die steels with regulated austenitic transformation during exploitation (RATE steels) are a new class of tungsten-free steels for hot forming at operating temperatures up to 750 – 800 °C. High durability of the pressing tool and its long service life are ensured by the ability of these steels to preservation of hot work hardening. This circumstance distinguishes RATE steels from traditional alloy steels, which are prone to softening at high temperatures. However, the temperature ranges for the preservation of hot hardening in RATE steels was not systematically studied, which makes it difficult to use a pressing tool more efficiently. In this paper, we study the mechanical behavior of RATE die steel during thermo-mechanical treatment in a wide temperature range, including the stage of preliminary deformation at lower temperatures and the stage of main deformation at higher temperatures corresponding to operating temperatures of the pressing tool. The thermo-mechanical treatment was carried out using a hardening-deformation dilatometer DIL 805 A/D according to the compression mode. We obtained the true stress-strain curves and determined the mechanical characteristics and strain hardening index. Size of the former austenite grain in the steel structure after thermo-mechanical treatment was measured. The temperature-force conditions for enhancing hot hardening or stabilizing hot hardening, or softening, were established. It is shown that the hardening achieved at the stage of preliminary deformation at a temperature of 450 °C is enhanced at the stage of main deformation at temperatures in the range from 550 to 800 °C, while in this temperature range the tendency to increase hot hardening is weakened.

Keywords: RATE steels, die steels, hot deformation, hot work hardening, austenite

Acknowledgements: The study of the structure was carried out using the equipment of the Center for Collective Use "Materials Science and Metallurgy" with the financial support of the Ministry of Science and Higher Education of the Russian Federation (agreement No. 075-15-2021-696).
The authors express their gratitude to Khatkevich V.M. for advice on the study organization.

For citation: Kruglyakov A.A., Rogachev S.O., Sokolov P.Yu., Priupolin D.V. Preservation conditions of hot work hardening in die steel with regulated austenitic transformation during exploitation. *Izvestiya. Ferrous Metallurgy*. 2023;66(5):554–563.
https://doi.org/10.17073/0368-0797-2023-5-554-563

Условия сохранения горячего наклепа в штамповой стали с регулируемым аустенитным превращением при эксплуатации

А. А. Кругляков[1], С. О. Рогачев[2, 3] ✉, П. Ю. Соколов[2], Д. В. Приуполин[2]

[1] **Научно-коммерческая фирма WBH** (Германия, D-10117, Берлин, Фридрихштрассе, 106 Б)
[2] **Национальный исследовательский технологический университет «МИСИС»** (Россия, 119049, Москва, Ленинский пр., 4)
[3] **Институт металлургии и материаловедения им. А.А. Байкова РАН** (Россия, 119334, Москва, Ленинский пр., 49)

✉ csaap@mail.ru

Аннотация. Штамповые стали с регулируемым аустенитным превращением при эксплуатации (РАПЭ) – новый класс безвольфрамовых сталей для горячей обработки давлением при рабочих температурах до 750 – 800 °С. Высокая стойкость прессового инструмента и его длительный ресурс обеспечиваются за счет способности этих сталей сохранять горячее деформационное упрочнение (горячий наклеп). Это обстоятельство отличает стали с РАПЭ от традиционных легированных сталей, склонных к разупрочнению при высоких температурах. Однако температурные диапазоны проявления горячего упрочнения в сталях с РАПЭ систематически не изучены, что

затрудняет более эффективное использование штампового инструмента. В данной работе изучено механическое поведение штамповой стали с РАПЭ при термомеханической обработке в широком диапазоне температур, включающей этап предварительной деформации при более низких температурах и этап основной деформации при более высоких температурах, соответствующих температурам эксплуатации прессового инструмента. Термомеханическую обработку проводили на закалочно-деформационном дилатометре DIL 805 A/D по схеме сжатия. Получены истинные диаграммы деформации, определены механические характеристики и показатель деформационного упрочнения. Измерен размер бывшего зерна аустенита в структуре стали после термомеханической обработки. Авторы установили температурно-силовые условия, в которых сталь демонстрирует усиление и стабилизацию горячего упрочнения, либо разупрочнение. Показано, что достигнутое на этапе предварительной деформации при температуре 450 °С упрочнение усиливается на этапе основной деформации при температурах в интервале от 550 до 800 °С, при этом в указанном температурном интервале склонность к усилению горячего упрочнения ослабевает.

Ключевые слова: стали с РАПЭ, штамповые стали, горячая деформация, горячий наклеп, аустенит

Благодарности: Исследование структуры выполнено с использованием оборудования ЦКП «Материаловедение и металлургия» при финансовой поддержке Министерства науки и высшего образования РФ (соглашение № 075-15-2021-696).
Авторы выражают благодарность к.т.н. Хаткевичу В.М. за советы в организации исследования.

Для цитирования: Кругляков А.А., Рогачев С.О., Соколов П.Ю., Приуполин Д.В. Условия сохранения горячего наклепа в штамповой стали с регулируемым аустенитным превращением при эксплуатации. *Известия вузов. Черная металлургия*. 2023;66(5):554–563.
https://doi.org/10.17073/0368-0797-2023-5-554-563

Introduction

The heat resistance of α-iron-based steels at temperatures around 690 – 700 °C is considered ultimate. Consequently, the most heat-resistant die steels, such as 5Kh3V3MFS, 3Kh2V8F (also known as DIN: X30WCrV9-3, AISI/SAE: H21 or H21A), 4Kh2V5MF, and 4Kh2V4FS, which boast high tungsten content, are typically limited to operating temperatures during hot pressing up to 660 – 680 °C [1 – 3]. Tungsten-free steels like 70Kh3G2FTR or 4Kh5MGFS have even lower operating temperatures [4; 5]. While the operating temperatures of austenitic steels are somewhat higher, their manufacturability is notably low [6 – 8].

In the 1980s, A.D. Ozerskii and A.A. Kruglyakov pioneered the development of die steels featuring a controlled austenitic transformation during exploitation, (RATE steels). These were tungsten-free steels primarily composed of α-iron, designed for high-pressure hot working at operating temperatures reaching up to 750 – 800 °C [9 – 11]. The exceptional durability of these press tools and their extended service life stem from the steels' capability to maintain hot strain hardening, also known as hot work hardening [12; 13]. This quality distinguishes RATE steels from conventional alloy steels, which are susceptible to softening under high-temperature conditions. The primary cause of this softening lies in the onset of recovery processes and dynamic recrystallization [14 – 16]. As a consequence, there is a notable alteration in the shape of stress-strain curves at elevated temperatures [17; 18].

The inclination towards hot work hardening in RATE steels underwent experimental scrutiny through thermomechanical treatment, involving initial deformation at a lower temperature followed by subsequent deformation at a higher temperature [19 – 21]. The hardening level attained during the preliminary deformation stage was not only sustained but further augmented during the main deformation phase. However, these studies confined the preliminary deformation temperature to 450 °C and the main deformation temperature to 750 °C. Consequently, the temperature ranges conducive to showcasing hot hardening in such steels have not been comprehensively explored. This is a crucial aspect in determining pre-hardening temperatures for the die and operational temperatures that ensure optimal and prolonged die tool performance.

This study aims to investigate the impact of hot deformation temperature on the manifestation of hot hardening in RATE die steel, focusing on a medium-carbon Fe – C – Si – Cr – Ni – Mn – Mo – V – Ti – Nb steel as an illustrative example.

Materials and methods

In this study, RATE die steel, specifically of the 4Kh2N3M2G4FTBS type [22], was utilized subsequent to a softening heat treatment, resulting in an approximate hardness of ~34 HRC.

Thermomechanical treatment (TMT) was conducted using cylindrical samples measuring 10 mm in height and 5 mm in diameter on a DIL 805 A/D hardening-deformation dilatometer. The TMT process comprised the following sequential stages:

– austenitization at 1150 °C for 15 min;

– a 15 min holding period and preliminary plastic deformation at a temperature range of 400 – 500 °C (in intervals of 50 °C);

– a 15 min holding period and main plastic deformation at a temperature range of 550 – 850 °C (in intervals of 50 °C).

After TMT, the samples underwent free cooling (~10 °C/s).

The layout of the TMT protocol is represented in Fig. 1.

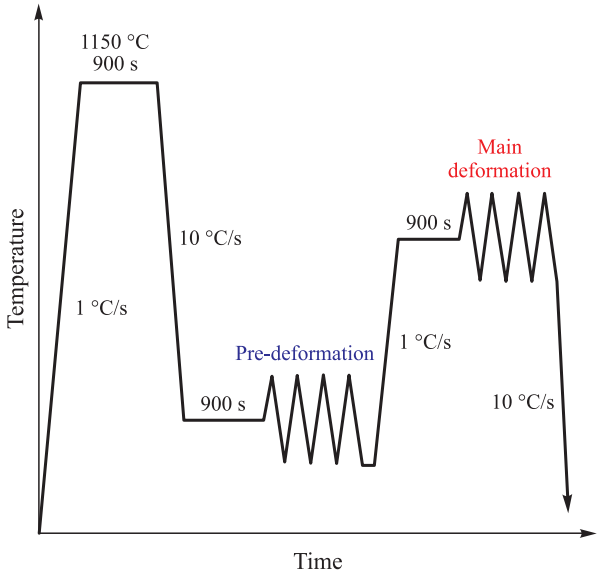

Fig. 1. Thermo-mechanical treatment diagram

Рис. 1. Диаграмма термомеханической обработки

The deformation process was carried out according to a compression sequence involving five cycles, with each cycle involving deformation within the range of 1 – 2 % and a deformation rate set at 1 – 2 %, rate: 0.1 s^{-1}). Process curves capturing "true stress – true deformation" coordinates were recorded throughout the deformation sequences.

The strain hardening index n was calculated utilizing the equation $S = Ke^n$, where S is the true stress; K is the coefficient, and e is the true deformation.

Microstructural analysis of polished sections involved etching in a 5 % aqueous solution of nitric acid. The resulting microstructure was examined using an NIM-100 optical microscope at a magnification of 200x. The grain size was determined from the microstructure images obtained by employing the secant method.

Microhardness was assessed using the Vickers method with a Micromet 5101 Buehler instrument. The experimental parameters were as follows: a load of 300 g, load application time of 10 s, and microscope magnification set at 500x. Measurements were conducted on transverse polished sections of samples subsequent to TMT in two distinct zones: at the periphery and at the center of the sample.

Results and discussion

The mechanical characteristics of the RATE steel during TMT with varying temperatures for preliminary deformation and a consistent temperature for the main deformation are detailed in Table 1, while the strain curves are visually represented in Fig. 2. Similar to earlier investigations [19; 20], multiple plastic deformations at 450 °C led to a notable strengthening of the steel: the maximum cycle stress (S_{max}) escalated from the initial range of 248 – 263 to 441 – 467 MPa (1.8 times). This achieved level of hardening remained steady during the first cycle of main deformation at 750 °C and further increased across the subsequent four cycles: S_{max} rose to 517 – 523 MPa (1.1 times). Altering the temperature within the preliminary deformation stage from 400 to 500 °C exerted a marginal influ-

Table 1

Mechanical characteristics of RATE steel during TMT with varying pre-deformation temperature

Таблица 1. **Механические характеристики стали с РАПЭ при ТМО с варьированием температуры предварительной деформации**

Deformation	Preliminary					Main				
Temperature	400 °C					750 °C				
Cycle, No.	1	2	3	4	5	6	7	8	9	10
S, MPa	263	326	379	425	467	471	486	498	508	517
e	0.019	0.018	0.018	0.017	0.016	0.016	0.016	0.015	0.015	0.012
n	0.37					0.06				
Temperature	450 °C					750 °C				
S, MPa	250	312	364	409	450	474	493	502	511	518
e	0.019	0.019	0.017	0.017	0.017	0.016	0.016	0.015	0.015	0.014
n	0.38					0.06				
Temperature	500 °C					750 °C				
S, MPa	248	308	358	402	441	486	500	510	517	523
e	0.019	0.018	0.018	0.017	0.017	0.015	0.015	0.015	0.014	0.012
n	0.37					0.04				

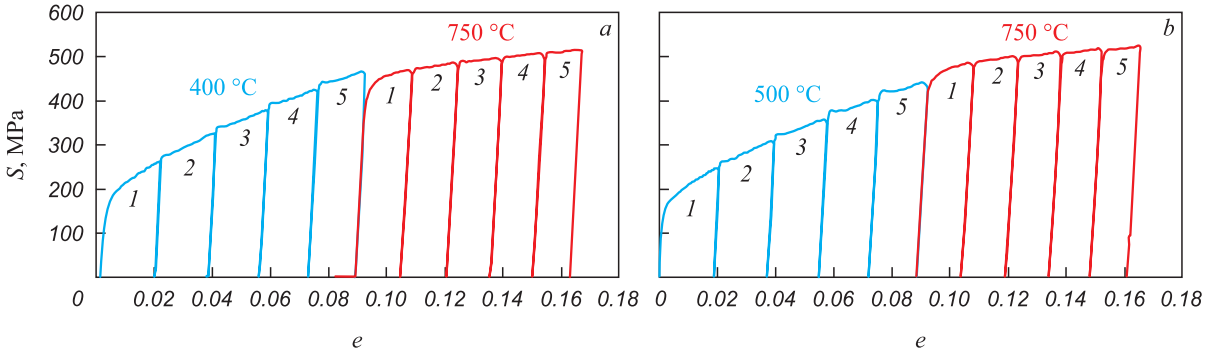

Fig. 2. Stress-strain curves of RATE steel during TMT with varying pre-deformation temperature 400 (*a*) and 500 °C (*b*)

Рис. 2. Кривые деформации стали с РАПЭ при ТМО с варьированием температуры предварительной деформации 400 (*a*) и 500 °C (*b*)

Table 2

Mechanical characteristics of RATE steel during TMT with varying the main deformation temperature

Таблица 2. **Механические характеристики стали с РАПЭ при ТМО с варьированием температуры основной деформации**

Deformation	Preliminary					Main				
Temperature	450 °C					550 °C				
Cycle, No.	1	2	3	4	5	6	7	8	9	10
S, MPa	252	313	363	408	449	445	478	512	541	569
e	0.019	0.019	0.018	0.017	0.017	0.016	0.016	0.015	0.015	0.014
n	0.37					0.16				
Temperature	450 °C					600 °C				
S, MPa	242	303	354	398	438	420	445	485	513	537
e	0.019	0.018	0.018	0.017	0.017	0.016	0.015	0.015	0.014	0.012
n	0.38					0.16				
Temperature	450 °C					650 °C				
S, MPa	254	316	368	414	452	439	474	504	530	552
e	0.019	0.019	0.018	0.018	0.017	0.016	0.016	0.015	0.015	0.013
n	0.37					0.15				
Temperature	450 °C					700 °C				
S, MPa	245	305	355	398	438	454	477	501	521	537
e	0.019	0.019	0.019	0.019	0.018	0.017	0.017	0.017	0.016	0.014
n	0.36					0.11				
Temperature	450 °C					750 °C				
S, MPa	250	312	364	409	450	474	493	502	511	518
e	0.019	0.019	0.017	0.017	0.017	0.016	0.016	0.015	0.015	0.014
n	0.38					0.06				
Temperature	450 °C					800 °C				
S, MPa	254	315	367	410	449	442	449	449	451	451
e	0.019	0.018	0.017	0.017	0.017	0.015	0.015	0.015	0.014	0.013
n	0.37					0.01				
Temperature	450 °C					850 °C				
S, MPa	246	303	352	395	436	368	373	375	377	378
e	0.019	0.018	0.017	0.017	0.017	0.017	0.017	0.016	0.016	0.014
n	0.37					0.02				

ence on the hardening level, both during preliminary and main deformations. At equivalent degrees of deformation, the maximum stress disparity was no more than 6 %. However, this difference diminished as the degree of primary deformation increased. The heightened hardening observed in the first cycle of main deformation, compared to the fifth cycle of preliminary deformation, was most pronounced (10 %) when the preliminary deformation temperature was set at 500 °C.

The mechanical characteristics of the RATE steel during TMT at a constant temperature for preliminary deformation while varying the temperature of the primary deformation are summarized in Table 2, with corresponding strain curves presented in Fig. 3.

The achieved level of hardening during the preliminary deformation stage at a temperature of 450 °C demonstrates intensification during the main deformation phase at temperatures ranging from 550 to 750 °C. Specifically, at 550 °C, S_{max} increases to 569 MPa (a 27 % increase), while at 750 °C, it reaches 518 MPa (a 15 % rise). Notably, as the temperature of the main deformation escalates from 550 to 750 °C, the propensity for hot

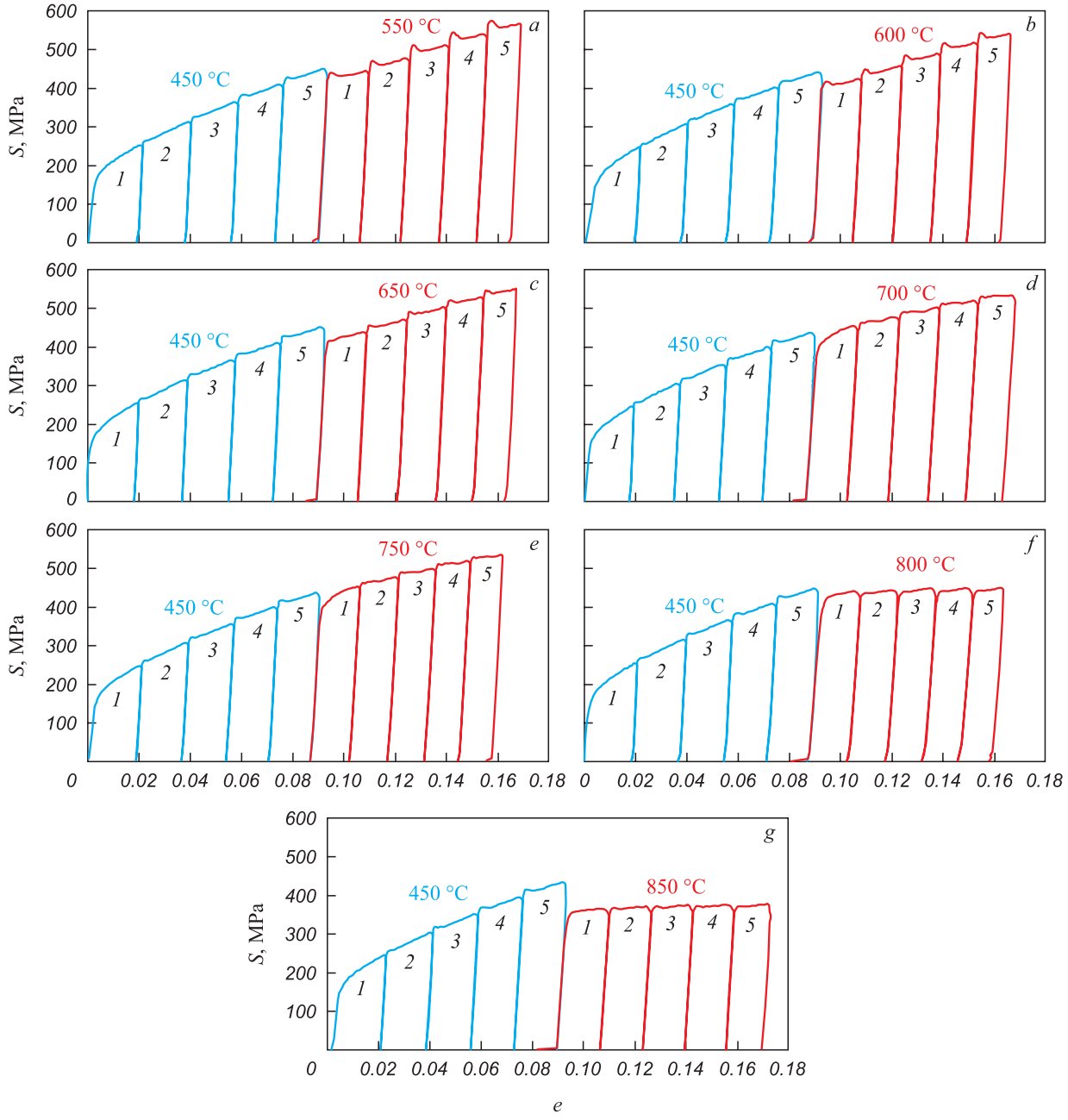

Fig. 3. Stress-strain curves of RATE steel during TMT with varying the main deformation temperature, °C:
a – 550; *b* – 600; *c* – 650; *d* – 700; *e* – 750; *f* – 800; *g* – 850

Рис. 3. Кривые деформации стали с РАПЭ при ТМО с варьированием температуры основной деформации, °C:
a – 550; *b* – 600; *c* – 650; *d* – 700; *e* – 750; *f* – 800; *g* – 850

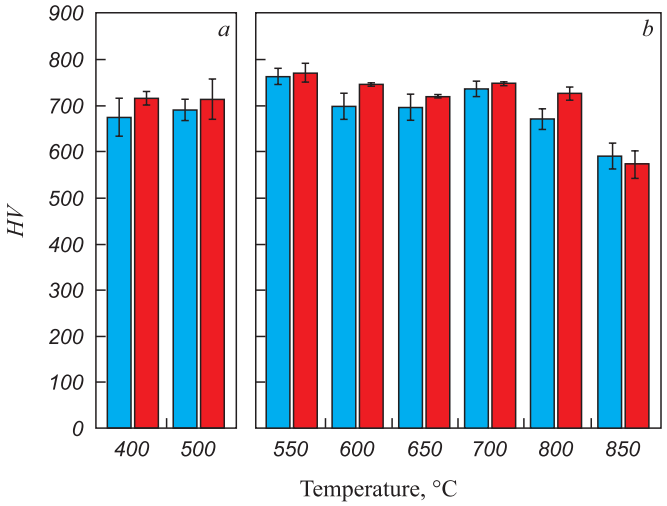

Fig. 4. Dependence of RATE steel microhardness on temperature of preliminary (*a*) and main (*b*) deformation:
■ – periphery; ■ – center

Рис. 4. Зависимость микротвердости стали с РАПЭ от температуры предварительной (*a*) и основной (*b*) деформации:
■ – периферия; ■ – центр

hardening diminishes, indicated by a decrease in the strain hardening index '*n*' from 0.16 to 0.06. Further elevating the temperature of the main deformation to 800 °C does not yield an additional increase in hot hardening; instead, it stabilizes at S_{max} levels of around 450 MPa (n = 0.01). Eventually, with a subsequent increase in the temperature of the main deformation to 850 °C, some softening of the steel becomes apparent: S_{max} in the initial deformation cycle drops to 368 MPa (a 20 % decrease), maintaining this level across the subsequent four deformation cycles (n = 0.02). It's crucial to highlight that even at 850 °C, the S_{max} values surpass those observed during the initial hardening cycles at 450 °C. Remarkably, the strength level of the RATE steel at 850 °C exceeds that of high-alloy 10Cr–10Ni–5Mo–2Cu steel (under comparable degrees of deformation and loading rates) [23].

The microhardness of the RATE steel after TMT and cooling to room temperature mainly correlates with the level of hot hardening after the main deformation (Fig. 4). Consequently, following preliminary deformation within the range of 400 – 500 °C and subsequent cooling, the microhardness remains constant at approximately 700 HV. After cooling from main deformation temperatures spanning 550 – 800 °C, a minor decreasing trend in microhardness is observed, ranging from 770 to 700 HV. After main deformation at a temperature of 850 °C, the microhardness sharply drops to 580 HV. The disparity in microhardness between the sample's center and its periphery is negligible.

Fig. 5 illustrates the microstructure, specifically the former austenite grain of the RATE steel after TMT, varying the temperature of preliminary deformation,

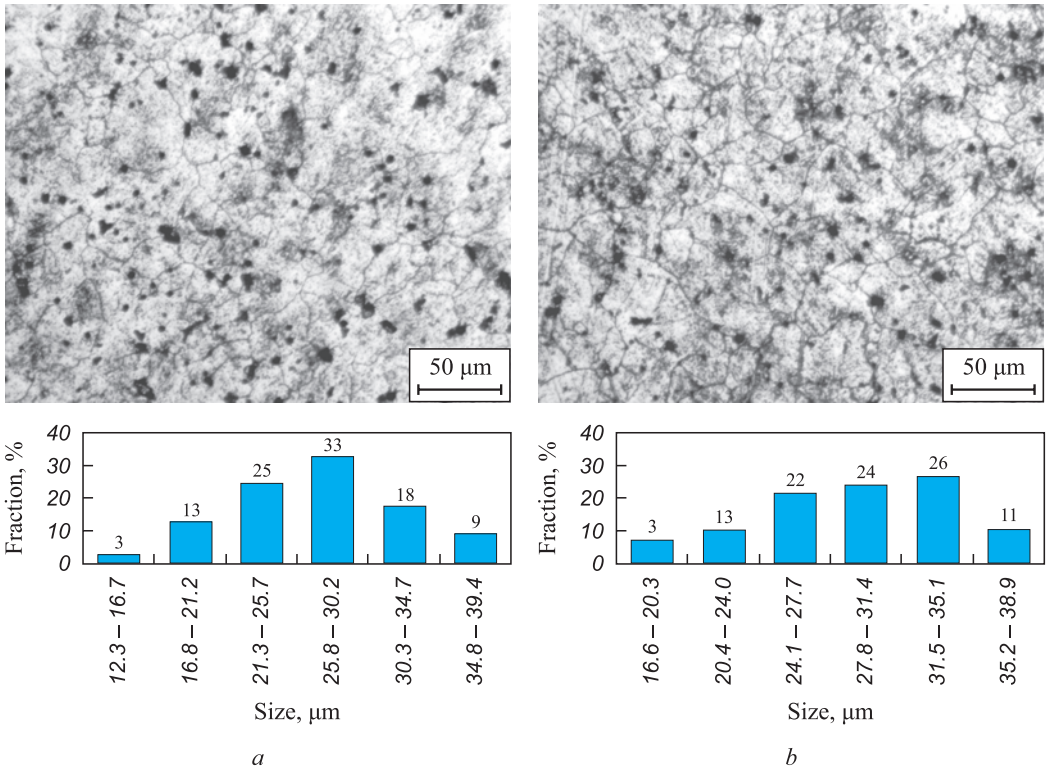

Fig. 5. Former austenite grain in the structure of RATE steel after TMT with varying pre-deformation temperature 400 (*a*) and 500 °C (*b*)

Рис. 5. Бывшее зерно аустенита в структуре стали с РАПЭ после ТМО с варьированием температуры предварительной деформации 400 (*a*) и 500 °C (*b*)

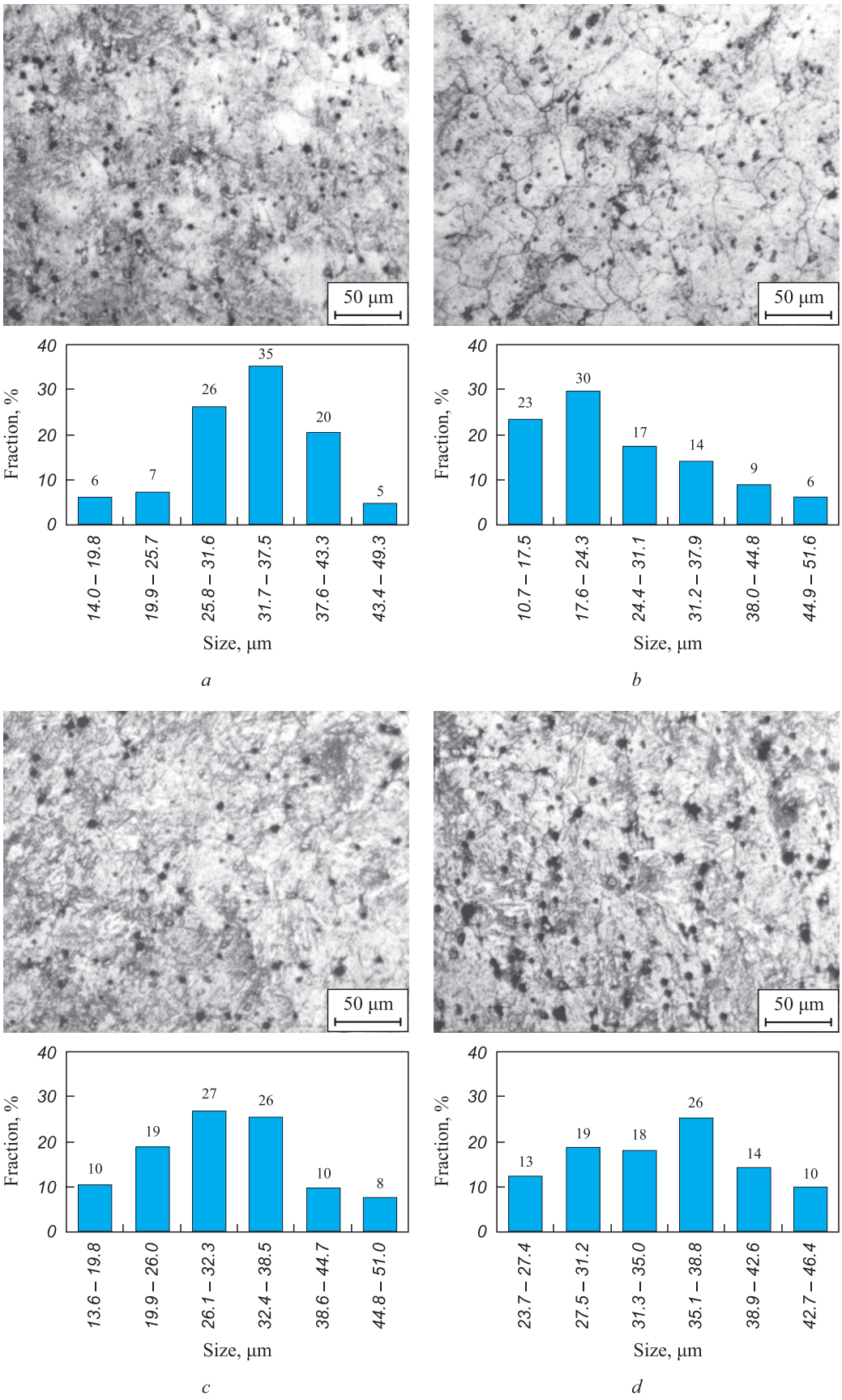

Fig. 6. Former austenite grain in the structure of RATE steel after TMT with varying the main deformation temperature, °C:
a – 550; *b* – 750; *c* – 800; *d* – 850

Рис. 6. Бывшее зерно аустенита в структуре стали с РАПЭ после ТМО с варьированием температуры основной деформации, °С:
a – 550; *b* – 750; *c* – 800; *d* – 850

Table 3

Size of the former austenite grain in the structure of RATE steel after TMT with varying pre-deformation temperature

Таблица 3. **Размер бывшего зерна аустенита в структуре стали с РАПЭ после ТМО с варьированием температуры предварительной деформации**

Pre-deformation temperature, °C	400	500
Minimum grain size, μm	12	17
Maximum grain size, μm	39	39
Average grain size, μm	27 ± 6	29 ± 5

Table 4

Size of the former austenite grain in the structure of RATE steel after TMT with varying the main deformation temperature

Таблица 4. **Размер бывшего зерна аустенита в структуре стали с РАПЭ после ТМО с варьированием температуры основной деформации**

Main deformation temperature, °C	550	600	650	700	750	800	850
Minimum grain size, μm	17	16	12	11	14	14	16
Maximum grain size, μm	38	36	34	52	49	51	48
Average grain size, μm	29 ± 5	25 ± 5	22 ± 5	26 ± 8	33 ± 7	31 ± 8	35 ± 6

and cooling to room temperature, alongside histograms depicting grain size distribution.

Table 3 provides the former austenite grain size after TMT, showcasing that an increase in the preliminary deformation temperature from 400 to 500 °C doesn't influence the former austenite grain's size, which averages around 28 μm, aligning with 7 points according to State Standard GOST 5639–82.

Fig. 6 illustrates the microstructure, particularly the former austenite grain of the RATE steel after TMT, while varying the temperature of the main deformation and subsequent cooling to room temperature. Additionally, histograms representing grain size distribution are provided.

Table 4 presents the former austenite grain size following TMT at various main deformation temperatures. The data reveals a slight inclination towards an increase in the former austenite grain size from 29 to 35 μm as the main deformation temperature escalates from 550 to 850 °C. This progression aligns with 7 points according to State Standard GOST 5639–82.

Conclusions

The rise in preliminary deformation temperature from 400 to 500 °C minimally impacts the strengthening of steel with RATE at both the preliminary and main deformation stages at a constant temperature of 750 °C.

At a constant preliminary deformation temperature of 450 °C, the level of hardening achieved intensifies during the main deformation stage within the range of 550 to 750 °C. However, this strain hardening tendency weakens with rising temperatures. Further elevation of the main deformation temperature to 800 °C results in a stabilized strengthened state. Subsequently, a marginal softening is observed up to 850 °C.

Increasing the preliminary deformation temperature from 400 to 500 °C at a constant main deformation temperature of 750 °C does not significantly alter the size of the former austenite grain, which averages around 28 μm. Conversely, a subtle increase in the former austenite grain size from 29 to 35 μm is noted when the main deformation temperature rises from 550 to 850 °C, while maintaining a constant preliminary deformation temperature of 450 °C.

The findings suggest that RATE steel demonstrates efficient performance across a broad range of tool heating temperatures, spanning from 550 to 800 °C. Notably, even at a heating temperature of 850 °C, the steel retains a considerably high strength margin of 380 MPa.

References / Список литературы

1. Gorbatyuk S.M., Morozova I.G., Naumova M.G. Development of the working model of production reindustrialization of die steel heat treatment. *Izvestiya. Ferrous Metallurgy*. 2017; 60(5):410–415. https://doi.org/10.17073/0368-0797-2017-5-410-415

Горбатюк С.М., Морозова И.Г., Наумова М.Г. Разработка рабочей модели процесса реиндустриализации производства термической обработки штамповых сталей. *Известия вузов. Черная металлургия*. 2017; 60(5):410–415. https://doi.org/10.17073/0368-0797-2017-5-410-415

2. Ozerski A.D., Kruglyakov A.A. *Die Steel with Regulated Austenitic Transformation during Exploitation*. Leningrad: LDNTP; 1988:28. (In Russ.).

Озерский А.Д., Кругляков А.А. *Штамповые стали с регулируемым аустенитным превращением при эксплуатации*. Ленинград: ЛДНТП; 1988:28.

3. Poznyak L.A. *Tool Steels*. Kyiv: Naukova Dumka; 1996:488. (In Russ.).

Позняк Л.А. *Инструментальные стали*. Киев: Наукова думка; 1996:488.

4. Orlov Yu.G., Dudetskaya L.R. *Materials and Technologies for the Production of Cast Die Tools*. Minsk, Belarus: Navuka; 2010:171. (In Russ.).

Орлов Ю.Г., Дудецкая Л.Р. *Материалы и технологии изготовления литого штампового инструмента*. Минск: Беларуская навука; 2010:171.

5. Kruglyakov A.A. Effect of alloying elements on the hardening of die steels in the austenitic state during high-temperature plastic deformation. *Russian Metallurgy (Metally)*. 2019;2019(10):1096-1101. https://doi.org/10.1134/S0036029519100343

Кругляков А.А. Влияние легирующих элементов на упрочнение штамповых сталей в аустенитном состоянии при высокотемпературной пластической деформации. *Деформация и разрушение материалов*. 2019;(3):28–32. https://doi.org/10.31044/1814-4632-2019-3-28-32

6. Kruglyakov A.A., Nikulin S.A. Structure and features of strain hardening of die steels with controlled austenite transformation. *Deformatsiya i razrushenie materialov*. 2014;(11):23-25. (In Russ.).

Кругляков А.А., Никулин С.А. Структура и особенности деформационного упрочнения штамповых сталей с регулируемым аустенитным превращением. *Деформация и разрушение материалов*. 2014;(11):23–25.

7. Loginov Yu.N., Inatovich Yu.V. *Tools for Metal Pressing*. Yekaterinburg: Ural. Gos. Univ.; 2014:224. (In Russ.).

Логинов Ю.Н., Инатович Ю.В. *Инструмент для прессования металлов*. Екатеринбург: Издательство Уральского университета; 2014:224.

8. Fedulov V.N. Influence of quantitative alloying of tool steels for hot deformation on their hardening level. *Lit'e i metallurgiya.* 2015;(3):123–131. (In Russ.).

Федулов В.Н. Влияние количественного легирования инструментальных сталей для горячего деформирования на уровень их упрочнения. *Литье и металлургия*. 2015;(3):123–131.

9. Krylova S.E., Kletsova O.A., Gryzunov V.I., Fot A.P., Tavtilov I.Sh. Effect of heat treatment on the structure and properties of die steel 70Kh3G2FTR. *Metal Science and Heat Treatment*. 2017;59(10):4–10. https://doi.org/10.1007/s11041-018-0198-1

Крылова С.Е., Клецова О.А., Грызунов В.И., Фот А.П., Тавтилов И.Ш. Влияние термической обработки на структуру и свойства штамповой стали 70Х3Г2ФТР. *Металловедение и термическая обработка металлов*. 2017;(10):4–10.

10. Wang L., Li H., Li G., Tang Z., Ma M. Microstructural evolution and flow behavior of 2205 and 2507 duplex stainless steel during double pass hot compressive deformation. *Chinese Journal of Materials Research*. 2016;30(12):888–896. https://doi.org/10.11901/1005.3093.2016.410

11. Fomina O.V. Structure formation of high strength nitrogen-bearing steel under hot deformation. *Izvestiya. Ferrous Metallurgy*. 2017;60(3):216–222. (In Russ.). https://doi.org/10.17073/0368-0797-2017-3-216-222

Фомина О.В. Формирование структуры высокопрочной азотсодержащей стали в процессе горячей деформации. *Известия вузов. Черная металлургия*. 2017;60(3):216–222. https://doi.org/10.17073/0368-0797-2017-3-216-222

12. Alimi A., Fajoui J., Kchaou M., Branchu S., Elleuch R., Jacquemin F. Multi-scale hot working tool damage (X40CrMoV5-1) analysis in relation to the forging process. *Engineering Failure Analysis*. 2016;62:142–155. https://doi.org/10.1016/j.engfailanal.2015.11.031

13. Llanos L., Pereda B., Lopez B., Rodriguez-Ibabe J.M. Hot deformation and static softening behavior of vanadium microalloyed high manganese austenitic steels. *Materials Science and Engineering: A*. 2016;651:358–369. https://doi.org/10.1016/j.msea.2015.10.123

14. Petković R.A., Luton M.J., Jonas J.J. Recovery and recrystallization of carbon steel between intervals of hot working. *Canadian Metallurgical Quarterly*. 1975;14(2):137–145. https://doi.org/10.1179/000844375795050201

15. Graetz K., Miessen C., Gottstein G. Analysis of steady-state dynamic recrystallization. *Acta Materialia*. 2014;67:58–66. https://doi.org/10.1016/j.actamat.2013.12.005

16. Sakai T., Belyakov A., Kaibyshev R., Miura H., Jonas J.J. Dynamic and post-dynamic recrystallization under hot, cold and severe plastic deformation conditions. *Progress in Materials Science*. 2014;60:130–207. https://doi.org/10.1016/j.pmatsci.2013.09.002

17. Giordani E.J., Jorge Jr. A.M., Balancin O. Proportion of recovery and recrystallization during interpass times at high temperatures on a Nb- and N-bearing austenitic stainless steel biomaterial. *Scripta Materialia*. 2006;55(8):743–746. https://doi.org/10.1016/j.scriptamat.2006.05.015

18. Souza R.C., Silva E.S., Jorge Jr. A.M., Cabrera J.M., Balancin O. Dynamic recovery and dynamic recrystallization competition on a Nb- and N-bearing austenitic stainless steel biomaterial: Influence of strain rate and temperature. *Materials Science and Engineering: A*. 2013;582:96–107. https://doi.org/10.1016/j.msea.2013.06.037

19. Krugljakow A.A., Nikulin S.A., Rogachev S.O., Nguyen H.X., Lebedeva N.V., Panova G.A. Hot-hardening phenomenon in die steel during thermomechanical processing. *Materials Letters*. 2020;266:127475. https://doi.org/10.1016/j.matlet.2020.127475

20. Krugljakow A.A., Rogachev S.O., Lebedeva N.V., Sokolov P.Yu., Arsenkin A.M., Khatkevich V.M. On the nature of hot work hardening phenomenon in die steel with regulated austenitic transformation during exploitation. *Materials Science and Engineering: A*. 2022;833:142548. https://doi.org/10.1016/j.msea.2021.142548

21. Lebedeva N.V., Panova G.A., Kruglyakov A.A., Rogachev S.O. *Method for hardening treatment of tool from die steels*. Patent no. 2776893 RU. Publ. 28.07.2022. (In Russ.).

Пат. 2776893 RU. *Способ упрочняющей обработки инструмента из штамповых сталей* / Н.В. Лебедева, Г.А. Панова, А.А. Кругляков, С.О. Рогачев; опубл. 28.07.2022.

22. Nikulin S.A., Kruglyakov A.A., Rogachev S.O., Panova G.A., Lebedeva N.V. *Die steel*. Patent no. 2744584 RU. Publ. 11.03.2021. (In Russ.).

Пат. 2744584 RU. *Штамповая сталь* / С.А. Никулин, А.А. Кругляков, С.О. Рогачев, Г.А. Панова, Н.В. Лебедева; опубл. 11.03.2021.

23. Abbasi S.M., Shokuhfar A. Prediction of hot deformation behaviour of 10Cr–10Ni–5Mo–2Cu steel. *Materials Letters*. 2007;61(11–12):2523–2526. https://doi.org/10.1016/j.matlet.2006.09.050

Information about the Authors / Сведения об авторах

Aleksandr A. Kruglyakov, *Cand. Sci. (Eng.), General Director,* Scientific Production Association WBH
E-mail: dr.a.krugljakow@t-online.de

Stanislav O. Rogachev, *Cand. Sci. (Eng.), Assist. Prof. of the Chair "Metallography and Physics of Strength"*, National University of Science and Technology "MISIS"; *Research Associate*, Baikov Institute of Metallurgy and Materials Science, Russian Academy of Sciences
ORCID: 0000-0001-7769-7748
E-mail: csaap@mail.ru

Pavel Yu. Sokolov, *Senior Lecturer*, National University of Science and Technology "MISIS"
E-mail: sokolov@misis.ru

Denis V. Priupolin, *Student,* National University of Science and Technology "MISIS"
E-mail: dpriupolin@gmail.com

Александр Аркадьевич Кругляков, *к.т.н., генеральный директор,* Научно-коммерческая фирма WBH
E-mail: dr.a.krugljakow@t-online.de

Станислав Олегович Рогачев, *к.т.н., доцент кафедры металловедения и физики прочности,* Национальный исследовательский технологический университет «МИСИС»; *научный сотрудник,* Институт металлургии и материаловедения им. А.А. Байкова РАН
ORCID: 0000-0001-7769-7748
E-mail: csaap@mail.ru

Павел Юрьевич Соколов, *старший преподаватель,* Национальный исследовательский технологический университет «МИСИС»
E-mail: sokolov@misis.ru

Денис Викторович Приуполин, *студент,* Национальный исследовательский технологический университет «МИСИС»
E-mail: dpriupolin@gmail.com

Contribution of the Authors / Вклад авторов

A. A. Kruglyakov – conceptualization, formulation of conclusions.

S. O. Rogachev – scientific guidance, writing the text.
P. Yu. Sokolov – investigation, calculations.
D. V. Priupolin – investigation, calculations.

А. А. Кругляков – формирование основной концепции, формулирование выводов.
С. О. Рогачев – научное руководство, подготовка текста статьи.
П. Ю. Соколов – проведение расчетов.
Д. В. Приуполин – проведение расчетов.

Received 15.03.2023
Revised 22.04.2023
Accepted 24.08.2023

Поступила в редакцию 15.03.2023
После доработки 22.04.2023
Принята к публикации 24.08.2023

MATERIALS SCIENCE / МАТЕРИАЛОВЕДЕНИЕ

UDC 004.852
DOI 10.17073/0368-0797-2023-5-564-570

Original article
Оригинальная статья

Structural changes in the melt of a heat-resistant nickel alloy as phase transition of the second order

O. B. Mil'der[1], D. A. Tarasov[1], A. G. Tyagunov[1], V. S. Tsepelev[1], V. V. V'yukhin[1], A. L. Levonyan[2], O. V. Anoshina[3]

[1] **Ural Federal University named after the first President of Russia B.N. Yeltsin** (19 Mira Str., Yekaterinburg 620002, Russian Federation)
[2] **National Polytechnic University of Armenia** (105 Teryan Str., Yerevan 0009, Armenia)
[3] **Russian State Professional Pedagogical University** (11 Mashinostroitelei Str., Yekaterinburg 620012, Russian Federation)

anoshina@inbox.ru

Abstract. Information about the behavior of melts of the high-temperature nickel alloys is the basis for creating new smelting technologies that significantly increase the service properties of metal products, as well as solve a number of technological problems. The results of numerous studies indicate structural changes occurring in various metal melts under the influence of temperature and time. For many years, there has been a scientific discussion about the nature of these phenomena, and a common opinion was formulated on a number of issues. Structural changes in metallic liquids are presented as a second-order phase transition, where a liquid of higher density is replaced by a liquid of lower density. These transformations in the structures of liquid metals are called liquid-liquid transition (LLT). Studies of the structure-sensitive properties of melts of the heat-resistant nickel alloys also reveal structural changes that irreversibly transform the melt into a microhomogeneous state. The research results presented in this article confirmed that structural changes in melts of the high-temperature nickel alloys are also a second-order phase transition, as evidenced by the breakage of atomic microgroups, uniform redistribution of alloying elements, and the formation of new clusters characterized by smaller sizes and greater chemical homogeneity. Therefore, these changes can be characterized as LLT, while this does not contradict the previously substantiated quasi-crystalline model of the microinhomogeneous state of liquid heat-resistant nickel alloys.

Keywords: melt, nickel alloy, structure, irreversible change, phase transition, temperature, homogeneity

For citation: Mil'der O.B., Tarasov D.A., Tyagunov A.G., Tsepelev V.S., V'yukhin V.V., Levonyan A.L., Anoshina O.V. Structural changes in the melt of a heat-resistant nickel alloy as phase transition of the second order. *Izvestiya. Ferrous Metallurgy*. 2023;66(5):564–570. https://doi.org/10.17073/0368-0797-2023-5-564-570

Структурные изменения расплава жаропрочного никелевого сплава как фазовый переход второго рода

О. Б. Мильдер[1], Д. А. Тарасов[1], А. Г. Тягунов[1], В .С. Цепелев[1], В. В. Вьюхин[1], А. Л. Левонян[2], О. В. Аношина[3]

[1] **Уральский федеральный университет имени первого Президента России Б.Н. Ельцина** (Россия, 620002, Екатеринбург, ул. Мира, 19)
[2] **Национальный политехнический университет Армении** (Армения, 0009, Ереван, ул. Теряна, 105)
[3] **Российский государственный профессионально-педагогический университет** (Россия, 620012, Екатеринбург, ул. Машиностроителей, 11)

anoshina@inbox.ru

Аннотация. Информация о поведении расплавов жаропрочных никелевых сплавов является основой для создания новых технологий плавки, позволяющих значительно повысить эксплуатационные свойства металлопродукции, а также решить ряд технологических задач. Результаты многочисленных исследований свидетельствуют о структурных изменениях, происходящих в расплавах различных металлов под влиянием температуры и времени. На протяжении многих лет ведется научная дискуссия о природе этих явлений, по ряду вопросов сформулировано общее мнение. Структурные изменения в металлических жидкостях представляются как фазовый переход второго

рода, при котором жидкость большей плотности заменяется жидкостью меньшей плотности. Эти превращения в структурах жидких металлов называют переходом жидкость – жидкость (LLT). Исследования структурно-чувствительных свойств расплавов жаропрочных никелевых сплавов также выявляют структурные изменения, необратимо переводящие расплав в микрогомогенное состояние. Результаты исследований, представленные в данной работе, подтвердили, что структурные изменения в расплавах жаропрочных никелевых сплавов также являются фазовым переходом второго рода. Об этом свидетельствуют разрывы атомных микрогруппировок, равномерное перераспределение легирующих элементов и образование новых кластеров, характеризующихся меньшими размерами и большей химической однородностью. Поэтому данные изменения можно характеризовать как LLT, что не противоречит ранее обоснованной квазикристаллической модели микронеоднородного состояния жидких жаропрочных никелевых сплавов.

Ключевые слова: расплав, никелевый сплав, структура, необратимое изменение, фазовый переход, температура, однородность

Для цитирования: Мильдер О.Б., Тарасов Д.А., Тягунов А.Г., Цепелев В.С., Вьюхин В.В., Левонян А.Л., Аношина О.В. Структурные изменения расплава жаропрочного никелевого сплава как фазовый переход второго рода. *Известия вузов. Черная металлургия*. 2023; 66(5):564–570. https://doi.org/10.17073/0368-0797-2023-5-564-570

Introduction

An important aspect in enhancing the properties of metal products rests in the preparation of the melts for crystallization, contingent upon attaining an equilibrium state within a broad temperature range. The existence of a non-equilibrium melt, slightly above the liquidus temperature, can be explained by the residual presence of solid structures. This phenomenon is comprehended through the lens of a quasicrystalline model portraying a micro-inhomogeneous state, depicted as an array of atomic microgroups (clusters) of varying sizes, coupled with an irregular distribution of alloying elements. As the temperature of the melt rises during heating, the structural transformations take place. Consequently, the melt attains a state of equilibrium, characterized by microhomogeneity, sustained until the onset of crystallization. This transformation yields advantageous casting structures and substantially enhances the material's functional properties. This thermal treatment of melt finds extensive industrial utility and is denoted as thermal time treatment (TTT) or high-temperature melt treatment (HTMT) [1].

Multi-component heat-resistant nickel compositions are used in manufacturing the most critical components of gas turbine engines designed to operate under high-temperature and tensile stress conditions. The chemical composition comprises up to 22 alloying elements: C, Cr, Co, Mo, W, Al, Ti, Nb, B, Fe, Y, Zr, Ta, Re, Ru, V, Ce, La, Mn, Mg, Hf, Si, and may also contain challenging-to-remove impurities such as S, Si, P, and dissolved gases O, N. However, at the metallurgical production stage, several challenges emerge, including defects, low yield, and complexities in utilizing waste materials. The application of HTMT for heat-resistant nickel alloys has substantially addressed these issues and notably improved the quality of metal products [2].

The development of HTMT procedures for heat-resistant nickel alloys is rooted in an in-depth examination of structural changes occurring in melts during heating. A proposed quasicrystalline model delineates a micro-inhomogeneous state for melts of heat-resistant nickel alloys [1]: liquid heat-resistant nickel alloys comprise atomic microgroups exhibiting a stoichiometric composition akin to the primary strengthening γ′-phase $Ni_3(Al, Ti)$. The act of heating or prolonged isothermal holding of a metallic liquid facilitates the transformation of melts into a homogeneous and microhomogeneous state across an extensive temperature range. This transformation is irreversible and persists until the initiation of solid structure formation. For most investigated metallic materials, such structural changes represent a second-order phase transition, known as a liquid–liquid transition (LLT) [3; 4]. Post-restructuring, a stable metallic liquid emerges, comprising homogeneous atomic microgroups characterized by smaller radii, altered interatomic distances, or modified coordination numbers [3; 4].

Experimental evidence supports the structural modifications observed in the metal melts of heat-resistant nickel alloys [3 – 5]. Given the ongoing debate surrounding the mechanism underlying these changes in nickel-based alloys, this study aims to ascertain whether the structural alterations occurring during the heating of nickel compositions align with a second-order phase transition.

Experimental

The heat-resistant nickel alloy ZhS6U was selected as the test material due to its frequent industrial usage. The melting composition is detailed in Table.

According to the Landau phenomenological theory [6], second-order phase transitions are characterized by the continuity of state changes without any release or absorption of latent energy.

Differential Thermal Analysis (DTA) stands as the primary method for detecting the presence of latent energy release or absorption in a process. Fig. 1 displays DTA curves acquired during the heating (*1*) and subsequent cooling (*2*) of the ZhS6U alloy. These curve patterns are typical for a majority of heat-resistant nickel alloy grades.

The arrows in the figures indicate the solidus temperature (t_S) and liquidus temperature (t_L). Within the temperature range of 1250 to 1350 °C, distinct thermal effects related to both the melting (*1*) and subsequent crystallization (*2*)

Melting chemical composition of ZhS6U heat-resistant nickel alloy sample, at. %

Плавочный химический состав образца жаропрочного никелевого сплава ЖС6У, % (ат.)

C	Cr	Co	Mo	W	Al	Ti	Nb	B	Fe	Zr	S	Si	Mn	P	Ni
0.18	9.0	9.8	1.5	10.3	5.4	2.6	1.0	0.025	0.5	0.04	0.015	0.5	0.5	0.015	base.

of the studied alloy were identified. Above the liquidus temperature, the DTA curves exhibit a horizontal line, indicating a complete absence of heat absorption or release over an extended temperature range. The experimental findings strongly suggest the absence of latent heat during the structural changes in the liquid heat-resistant alloy.

For this investigation, the electrical resistivity method was chosen due to its high sensitivity in studying structural alterations in melts of heat-resistant nickel alloys [2]. Further details regarding this technique are available in [7]. Polytherms $\rho = f(t)$ (Fig. 2) and isotherms $\rho = f(\tau)$ (Fig. 3) of the considered alloy were analyzed.

The curves $\rho = f(t)$ obtained during both heating and subsequent cooling of the ZhS6U melt exhibit a characteristic pattern observed in most liquid heat-resistant nickel compositions [2; 5]. The heating polytherm reveals a non-monotonic change in electrical resistivity, featuring specific points denoted as t_{an} and t_k. Between these points, an interval with an anomalous increase in electrical resistivity is observed. Another characteristic of electrical resistivity polytherms in heat-resistant nickel alloys is the phenomenon of hysteresis, showcasing a discrepancy between the heating and cooling branches.

To discern the nature of structural alterations occurring in the ZhS6U melt within the temperature range below t_k, measurements of electrical resistivity were conducted during isothermal holding at temperatures of 1417, 1448, and 1479 °C. The observed electrical resistance was recorded at intervals of 300 s (5 min).

Based on the experimental findings, it was observed that during the duration of isothermal exposures, the electrical resistivity consistently rose until reaching a peak (Fig. 3), following which its sensitivity to time diminished. Moreover, higher holding temperatures resulted in a shorter duration for the melt to reach its peak resistivity.

Results and discussion

The behavior of the $\rho = f(t)$ function and the positioning of points t_{an} and t_k explanation through the quasi-chemical model of the micro-inhomogeneous state in heat-resistant nickel alloys [1]: upon immediate melting, the structure of the ZhS6U melt exhibits homogeneity but retains a micro-inhomogeneous nature. It comprises dynamic clusters of varying sizes and uneven distribution of atoms from the alloy's chemical composition. With rising temperatures, a transition occurs toward a state of enhanced homogeneity and microhomogeneity, characterized by more uniform sizes and compositions of atomic associations. The cooling polytherms of samples preheated to temperatures exceeding t_k exhibit linearity, signifying that structural changes persist during cooling across an extensive temperature range. This suggests that the melt approaches a more equilibrium state before the onset of solidification.

The Drude's theory proposes an equation defining the electrical conductivity of metals as follows

$$\frac{1}{\rho} = \sigma = \frac{ne^2\tau_m}{m}, \qquad (1)$$

where n is the concentration of all electrons per unit volume (considered as the concentration of conduction

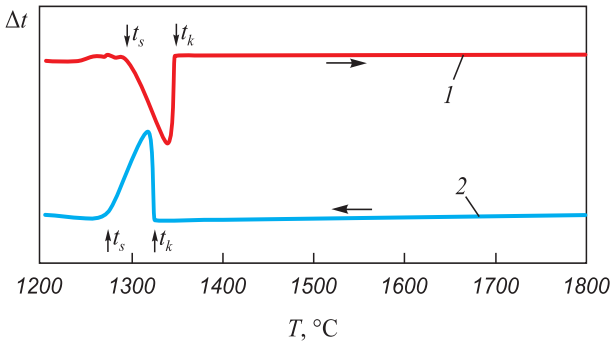

Fig. 1. DTA curves of ZhS6U alloy:
1 – during heating; *2* – during cooling

Рис. 1. ДТА кривые сплава ЖС6У:
1 – при нагреве; *2* – при охлаждении

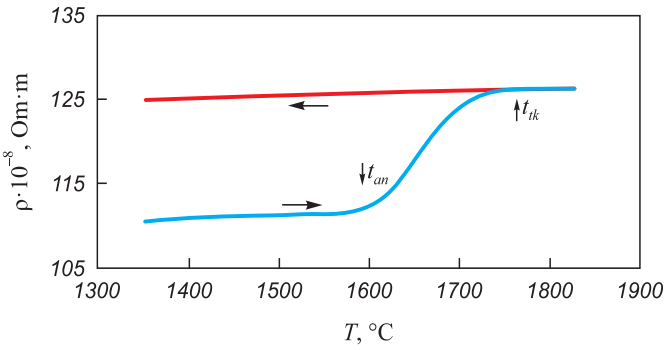

Fig. 2. Electrical resistivity polytherms of ZhS6U alloy during heating and cooling

Рис. 2. Политермы удельного электросопротивления исследуемого сплава ЖС6У при нагреве и охлаждении

electrons in contemporary models), while τ_m is the average free travel time.

In modern models, the equation retains its formal structure; however, the interpretation of the included parameters evolves [8]. Notably, the only parameter correlated with the nonlinear rise in electrical resistivity is the average free travel time. This nonlinear increase in electrical resistivity (equivalently, decrease in electrical conductivity) is attributed to a heightened presence of scattering centers.

The phenomenon of hysteresis in the physical properties of melts (Fig. 2), characterized by a discrepancy between the forward and reverse branches, has been extensively detailed by several researchers [9 – 12]. These studies emphasize the irreversibility of changes occurring in the melt over a broad temperature range.

Analysis of the experimental data illustrated in Fig. 3 reveals that the time constant diminishes with escalating temperatures during isothermal holding, indicating a relationship described by $\theta = f(t)$. Additionally, an empirical regularity emerged:

$$(t - t_{liq})\theta = \text{const}, \quad (2)$$

where t is the temperature of isothermal holding, while t_{liq} is the liquidus point.

By formally approaching the time constant towards zero, we can approximate the temperature at which the vast majority of clusters undergo dissolution, signifying the temperature t_k corresponding to the transition of the metallic liquid into a microhomogeneous state.

Consequently, structural transformations within the metallic liquid transpire not only during the process of heating to temperature t_k, but also as a consequence of prolonged time exposures. In essence, the decay of clusters occurs not solely due to alterations in the system's thermodynamic parameters (polytherm) but also when these parameters remain fixed (isotherm). This observation underscores the continuum of the ongoing process, a characteristic indicative of a second-order phase transition, as previously noted.

Parallel results concerning relaxation during extended exposures have been reported by other researchers [13 – 15].

Given that the second-order LLT phase transition exhibits both thermodynamic and structural characteristics, the provided thermodynamic rationale allows us to infer the mechanism of structural modifications in the ZhS6U melt. Upon immediate melting, the melt assumes a micro-inhomogeneous state, characterized by clusters of varying sizes and an uneven distribution of chemical elements. Subsequent heating and/or isothermal holding induce a second-order LLT phase transition within the melt: the original structure of the metallic liquid is replaced by a similar structure possessing a lower density. This transition involves the breakdown of cluster formations, a uniform redistribution of atoms, and the formation of new clusters with smaller sizes. The rise in electrical resistivity also indicates an increase in the number of atomic microgroups. These structural changes are irreversible, as evidenced by the disparity between the cooling polytherm and the heating polytherm. The resultant structural state demonstrates stability and microhomogeneity, validated by the absence of extremities in the cooling polytherm.

These observations align with the findings of authors in [16], who also affirm that the stability of cluster sizes in each phase region signifies a microhomogeneous state.

Moreover, the works by authors in [17 – 20] echo similar conclusions. They further highlight a notable sharp decrease in lattice parameter and coordination number with increasing temperature, contributing significantly to the observed increase in electrical resistivity.

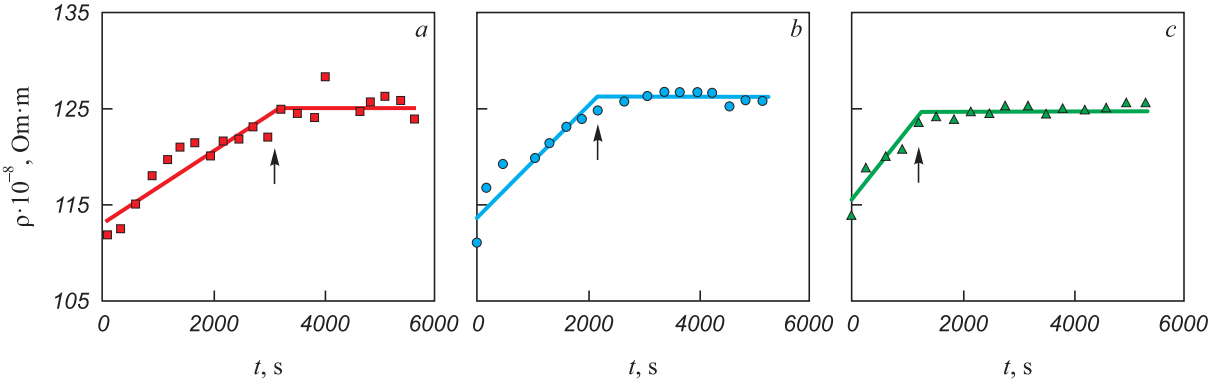

Fig. 3. Electrical resistivity isotherms of ZhS6U melt obtained at temperatures, °C: 1417 (*a*); 1448 (*b*); 1479 (*c*).
Arrows indicate the time of completion of structural changes in the melt

Рис. 3. Изотермы удельного электросопротивления расплава ЖС6У, полученные при температурах, °С: 1417 (*a*); 1448 (*b*); 1479 (*c*).
Стрелками указано время завершения структурных изменений расплава

Conclusions

Investigations on the heat-resistant nickel alloy ZhS6U reveal that when subjected to heating or isothermal holding, the alloy undergoes structural transformations, transitioning into a microhomogeneous state across an extensive temperature range. The delineated boundaries of these structural alterations on the electrical resistivity polytherms of the melt are denoted as t_{an} and t_k indicating irreversible changes.

The experimentally derived time constant, describing the process of structural modifications in the nickel-based melt during fixed thermodynamic parameters (isothermal holding), substantiates that these changes correspond to a second-order LLT phase transition.

The presented thermodynamic evidence elucidates the nature of structural changes in the melt of the heat-resistant nickel alloy, indicating a thermal-temporal effect referred to as the liquid-liquid transformation (LLT). Prior to LLT, the melt comprises clusters of varying sizes and configurations of atoms. During the LLT phase, atomic microgroups disintegrate, leading to a uniform redistribution of alloying elements, consequently forming new clusters characterized by reduced sizes and enhanced chemical homogeneity.

These findings align with the quasicrystalline theory of the microinhomogeneous state of metallic liquids, serving as an extension and not contradicting its principles.

References / Список литературы

1. Baum B.A. *Metallic Liquids*. Moscow: Nauka; 1979:120. (In Russ.).

   Баум Б.А. *Металлические жидкости*. Москва: Наука; 1979:120.

2. Efimov V.E. Influence of temperature-time treatment of Ni_3Al based intermetallic alloys on their phase composition and heat resistance. In: *Aviation Materials and Technologies. High Heat-Resistant Materials for Modern and Advanced Gas Turbine Engines and Advanced Technologies for their Production*. Moscow: VIAM; 2003:79–92. (In Russ.).

   Ефимов В.Е. Влияние температурно-временной обработки интерметаллидных сплавов на основе Ni_3Al на их фазовый состав и жаропрочность. *Авиационные материалы и технологии. Выпуск «Высокожаропрочные материалы для современных и перспективных газотурбинных двигателей и прогрессивные технологии их производства»*. Москва: ВИАМ; 2003:79–92.

3. Nikolaev B.V., Tyagunov G.V., Baum B.A., Baryshev E.E., Larionov V.N., Khlystov V.N., Buler T.P., Pechatnikov M.I. Influence of melt preparation on structure and properties of Ni_3Al based intermetallic alloy. *Metally*. 1991;(1):104–110. (In Russ.).

   Николаев Б.В., Тягунов Г.В., Баум Б.А., Барышев Е.Е., Ларионов В.Н., Хлыстов В.Н., Булер Т.П., Печатников М.И. Влияние подготовки расплава на структуру и свойства интерметаллидного сплава на основе Ni_3Al. *Металлы*. 1991;(1):104–110.

4. Zu F.-Q. Temperature-induced liquid-liquid transition in metallic melts: A brief review on the new physical phenomenon. *Metals*. 2015;5(1):395–417. https://doi.org/10.3390/met5010395

5. Buntushkin V.P., Efimov V.E., Nikolaev V.V. Influence of mycoadditives on critical melt temperature and heat resistance of a casting alloy based on Ni_3Al intermetallic compound. *Metally*. 1995;(3):60-69. (In Russ.).

   Бунтушкин В.П., Ефимов В.Е., Николаев В.В. Влияние микродобавок на критическую температуру расплава и жаропрочность литейного сплава на основе интерметаллида Ni_3Al. *Металлы*. 1995;(3):60–69.

6. Landau L.D., Lifshits E.M. *Theoretical Physics. Statistical Physics. Part I. Vol. V*. Moscow: Nauka; 1976:584. (In Russ.).

   Ландау Л.Д., Лифшиц Е.М. *Теоретическая физика. Статистическая физика. Часть I. Т. V*. Москва: Наука; 1976:584.

7. Tyagunov G.V., Baum B.A., Tsepelev V.S., Tyagunov A.G. Measurement of resistivity by the method of rotating magnetic field. *Zavodskaya laboratoriya. Diagnostika materialov*. 2003;69(2):35–37. (In Russ.).

   Тягунов Г.В., Баум Б.А, Цепелев В.С., Тягунов А.Г. Измерение удельного электросопротивления методом вращающегося магнитного поля. *Заводская лаборатория. Диагностика материалов*. 2003;69(2):35–37.

8. Blakemore J.S. *Solid State Physics*. Cambridge University Press;1985, 506. https://doi.org/10.1017/CBO9781139167871

   Блейкмор Дж. *Физика твердого тела*. Москва: Мир; 1988:608.

9. Tsepelev V.S., Konashkov V.V., Baum B.A. *Properties of Metal Melts. Part 1*. Yekaterinburg: USTU-UPI; 2008:358. (In Russ.).

   Цепелев В.С., Конашков В.В., Баум Б.А. *Свойства металлических расплавов. Часть 1*. Екатеринбург: УГТУ-УПИ; 2008:358.

10. Tsepelev V.S., Konashkov V.V., Baum B.A. *Properties of Metal Melts. Part 2*. Yekaterinburg. USTU-UPI; 2008:383. (In Russ.).

    Цепелев В.С., Конашков В.В., Баум Б.А. *Свойства металлических расплавов. Часть 2*. Екатеринбург; УГТУ-УПИ; 2008:383.

11. Ri Kh., Ri E.Kh., Khimukhin S.N., Ri V.E., Zernova T.S., Knyazev G.A. Influence of thermal treatment on structure formation and properties of aluminum alloys. *Vestnik TOGU*. 2013;(2(29)):137–144. (In Russ.).

    Ри Х., Ри Э.Х., Химухин С.Н., Ри В.Э., Зернова Т.С., Князев Г.А. Тепловые воздействия на структурообразование и свойства алюминиевых сплавов. *Вестник ТОГУ*. 2013;(2(29)):137–144.

12. Li Y., Chen W., Dong B., Zhou S. Effects of metalloid content on viscosity of Fe-Si-B-P-C alloy melt. *Journal of Non-Crystalline Solids*. 2018;490:31–34. https://doi.org/10.1016/j.jnoncrysol.2018.03.042

13. Lad'yanov V.I., Lagunov S.V., Pakhomov S.V. On oscillating relaxation processes in nonequilibrium metal melts after melting. *Metally*. 1998;(5):20–23. (In Russ.).

Ладьянов В.И., Лагунов С.В., Пахомов С.В. Об осциллирующих релаксационных процессах в неравновесных металлических расплавах после плавления. *Металлы*. 1998;(5):20–23.

14. Vasin M.G., Lad'yanov V.I., Bovin V.P. On the mechanism of nonmonotonic relaxation processes in metal melts. *Metally*. 2000;(5):27–32. (In Russ.).

    Васин М.Г., Ладьянов В.И., Бовин В.П. О механизме немонотонных релаксационных процессов в металлических расплавах. *Металлы*. 2000;(5):27–32.
15. Kolotukhin E.V., Tyagunov G.V., Nikolaev B.V., Baum B.A. On kinetic mode of relaxation of the structure of a multicomponent metal melt. *Journal of Physical Chemistry*. 1989;63(4):1118–1121. (In Russ.).

    Колотухин Э.В., Тягунов Г.В., Николаев Б.В., Баум Б.А. О кинетическом режиме процесса релаксации структуры многокомпонентного металлического расплава. *ЖФК*. 1989;63(4):1118–1121.
16. Wang L., Bian X.F., Liu J.T. Discontinuous structural phase transition of liquid metal and alloys. *Physics Letters A*. 2004;326(5-6):429–435. https://doi.org/10.1016/j.physleta.2004.04.052
17. Borovykh M.A., Chikova O.A., Tsepelev V.S., V'yukhin V.V. Effect of heat treatment conditions on electrical resistivity of 35KhGF molten steel. *Izvestiya. Ferrous Metallurgy*. 2018;61(3):237–243. (In Russ.). https://doi.org/10.17073/0368-0797-2018-3-237-243

    Боровых М.А., Чикова О.А., Цепелев В.С., Вьюхин В.В. О влиянии режима термообработки на удельное электросопротивление расплава стали 35ХГФ. *Известия вузов. Черная Металлургия*. 2018;61(3):237–243. (In Russ.). https://doi.org/10.17073/0368-0797-2018-3-237-243
18. Popel P.S., Sidorov V.E. Microheterogeneity of liquid metallic solutions and its influence on the structure and properties of rapidly quenched alloys. *Materials Science and Engineering: A*. 1997:226–228:237–244. https://doi.org/10.1016/S0921-5093(96)10624-9
19. Su H., Wang H., Zhang J., Guo M., Liu L., Fu H. Influence of melt superheating treatment on solidification characteristics and rupture life of a third-generation Ni-based single-crystal superalloy. *Metallurgical and Materials Transactions B*. 2018;49(4):1537–1546. https://doi.org/10.1007/s11663-018-1256-1
20. Wang L.N., Sun X.F., Guan H.R. Effect of melt heat treatment on MC carbide formation in nickel-based superalloy K465. *Results in Physics*. 2017;7:2111–2117. https://doi.org/10.1016/j.rinp.2017.06.020

Information about the Authors / Сведения об авторах

Oleg B. Mil'der, *Cand. Sci. (Phys.–Math.), Assist. Prof.,* Ural Federal University named after the first President of Russia B.N. Yeltsin
ORCID: 0000-0001-7828-032X
E-mail: o.b.milder@urfu.ru

Dmitrii A. Tarasov, *Cand. Sci. (Eng.), Assist. Prof.,* Ural Federal University named after the first President of Russia B.N. Yeltsin
ORCID: 0000-0001-6911-8371
E-mail: d.a.tarasov@urfu.ru

Andrei G. Tyagunov, *Cand. Sci. (Eng.), Assist. Prof.,* Ural Federal University named after the first President of Russia B.N. Yeltsin
ORCID: 0000-0001-8129-9726
E-mail: AG.Tyagunov@urfu.ru

Vladimir S. Tsepelev, *Dr. Sci. (Eng.), Prof., Director of the Research Center of Physics of Metallic Liquids,* Ural Federal University named after the first President of Russia B.N. Yeltsin
ORCID: 0000-0003-4195-9042
E-mail: v.s.tsepelev@urfu.ru

Vladimir V. V'yukhin, *Research Associate of the Research Center of Physics of Metallic Liquids,* Ural Federal University named after the first President of Russia B.N. Yeltsin
ORCID: 0000-0002-0772-8155
E-mail: v.v.vyukhin@urfu.ru

Aik L. Levonyan, *Cand. Sci. (Eng.), Assist. Prof.,* National Polytechnic University of Armenia
ORCID: 0009-0006-3003-8781
E-mail: hayk_levonyan@mail.ru

Ol'ga V. Anoshina, *Cand. Sci. (Phys.–Math.), Assist. Prof.,* Russian State Professional Pedagogical University
ORCID: 0000-0003-0563-8217
E-mail: anoshina@inbox.ru

Олег Борисович Мильдер, *к.ф.-м.н., доцент*, Уральский федеральный университет имени первого Президента России Б.Н. Ельцина
ORCID: 0000-0001-7828-032X
E-mail: o.b.milder@urfu.ru

Дмитрий Александрович Тарасов, *к.т.н., доцент*, Уральский федеральный университет имени первого Президента России Б.Н. Ельцина
ORCID: 0000-0001-6911-8371
E-mail: d.a.tarasov@urfu.ru

Андрей Геннадиевич Тягунов, *к.т.н., доцент*, Уральский федеральный университет имени первого Президента России Б.Н. Ельцина
ORCID: 0000-0001-8129-9726
E-mail: AG.Tyagunov@urfu.ru

Владимир Степанович Цепелев, *д.т.н., профессор, директор Исследовательского центра физики металлических жидкостей,* Уральский федеральный университет имени первого Президента России Б.Н. Ельцина
ORCID: 0000-0003-4195-9042
E-mail: v.s.tsepelev@urfu.ru

Владимир Викторович Вьюхин, *научный сотрудник Исследовательского центра физики металлических жидкостей*, Уральский федеральный университет имени первого Президента России Б.Н. Ельцина
ORCID: 0000-0002-0772-8155
E-mail: v.v.vyukhin@urfu.ru

Айк Левонович Левонян, *к.т.н., доцент*, Национальный политехнический университет Армении
ORCID: 0009-0006-3003-8781
E-mail: hayk_levonyan@mail.ru

Ольга Владимировна Аношина, *к.ф.-м.н., доцент*, Российский государственный профессионально-педагогический университет
ORCID: 0000-0003-0563-8217
E-mail: anoshina@inbox.ru

Contribution of the Authors

O. B. Mil'der – development of the idea, theoretical justification, writing the text.
D. A. Tarasov – development of the idea, theoretical justification, analysis.
A. G. Tyagunov – writing the text, conducting an experiment, analysis.

V .S. Tsepelev – development of the idea, theoretical justification.
V. V. V'yukhin – conducting an experiment, analysis.
A. L. Levonyan – conducting an experiment, theoretical justification, analysis.
O. V. Anoshina – writing the text, laboratory support, editing.

Вклад авторов

О. Б. Мильдер – разработка идеи, теоретическое обоснование, написание текста.
Д. А. Тарасов – разработка идеи, теоретическое обоснование, выполнение анализа.
А. Г. Тягунов – написание текста, проведение эксперимента, выполнение анализа.
В. С. Цепелев – разработка идеи, теоретическое обоснование.
В. В. Вьюхин – проведение эксперимента, выполнение анализа.
А. Л. Левонян – проведение эксперимента, теоретическое обоснование, выполнение анализа.
О. В. Аношина – написание текста, лабораторное сопровождение, редактирование.

Received 12.04.2023
Revised 24.08.2023
Accepted 30.09.2023

Поступила в редакцию 12.04.2023
После доработки 24.08.2023
Принята к публикации 30.09.2023

MATERIALS SCIENCE / МАТЕРИАЛОВЕДЕНИЕ

UDC 669.018
DOI 10.17073/0368-0797-2023-5-571-579

Original article
Оригинальная статья

Effect of retained austenite on mechanical properties of steel with 15 % Cr

I. Yu. Pyshmintsev, S. M. Bityukov, A. A. Gusev

LLC "Research Center TMK" (5 Bol'shoi Blvd.., Skolkovo, Moscow 143026, Russian Federation)

gusev.a@tmk-group.com

Abstract. The paper considers the study of influence of retained austenite on the mechanical properties of steel of the austenite-martensitic class based on 15 % Cr after various heat treatment. Significant amount of retained austenite remains in the steel microstructure after quenching and subsequent tempering or heating in the intercritical temperature range that makes difficult to achieve a high yield strength. Destabilization of retained austenite with subsequent transformation into newly formed martensite is provided by multi-stage heat treatment which includes quenching, heating in the intercritical temperature range or above the A_{C3} point and final tempering. It was established that retained austenite remains in the microstructure of two-phase steel and has the form of blocks and thin layers located in the inter-lath space. Tensile testing of steel based on 15 % Cr showed that multi-stage heat treatment provides a high-strength condition corresponding to strength groups Q125 and Q135. A comparative analysis of deformation behavior of semi-austenitic steel in various states indicates that the beginning of the martensitic transformation after the final tempering shifts into the elastic region during tension and leads to the formation of stress-assisted martensite. It was determined that block-shaped retained austenite in steel with 15 % Cr predominantly undergoes martensitic transformation during tensile and impact tests at a subzero temperature. This is supposed to be the reason for the noticeably lower impact toughness of semi-austenitic steel with 15 % Cr compared to martensitic steel with 13 % Cr at equal strength.

Keywords: stainless high-strength steels, semi-austenitic steels, heat treatment, hardening, tempering, martensite, retained austenite, impact toughness, phase composition, X-ray microanalysis, transmission electron microscopy, electron backscatter diffraction

For citation: Pyshmintsev I.Yu., Bityukov S.M., Gusev A.A. Effect of retained austenite on mechanical properties of steel with 15 % Cr. *Izvestiya. Ferrous Metallurgy*. 2023;66(5):571–579. https://doi.org/10.17073/0368-0797-2023-5-571-579

Влияние остаточного аустенита на механические свойства стали с 15 % Cr

И. Ю. Пышминцев, С. М. Битюков, А. А. Гусев

ООО «Исследовательский центр ТМК» (Россия, 143026, Москва, Инновационный Центр Сколково, Большой бульвар, 5)

gusev.a@tmk-group.com

Аннотация. Исследованы особенности влияния остаточного аустенита на механические свойства стали аустенитно-мартенситного класса с 15 % Cr после различных режимов термической обработки. По окончании нагрева под закалку и последующего отпуска или нагрева в межкритический интервал температур в микроструктуре стали сохраняется значительное количество остаточного аустенита, что затрудняет достижение высокого предела текучести. Дестабилизация остаточного аустенита с последующим превращением в «свежий» мартенсит обеспечивается за счет многоступенчатой термической обработки, включающей закалку, нагрев в межкритический интервал температур или выше точки A_{C3} и заключительный отпуск. Установлено, что сохранившийся в микроструктуре двухфазной стали остаточный аустенит имеет форму блоков и тонких прослоек, расположенных в межреечном пространстве. Испытание на растяжение стали с 15 % Cr показало, что многоступенчатая термообработка обеспечивает высокопрочное состояние, соответствующее группам прочности Q125 и Q135. Сравнительный анализ характера деформации аустенитно-мартенситной стали в различных состояниях свидетельствует о смещении начала мартенситного превращения при растяжении после заключительного отпуска в упругую область с образованием мартенсита напряжения. Для стали с 15 % Cr установлена ограниченная деформационная устойчивость остаточного аустенита блочной формы, преимущественно претерпевающего мартенситное превращение при испытаниях на растяжение и удар при отрицательной температуре. Предположительно, этим обусловлена заметно меньшая ударная вязкость аустенитно-мартенситной стали с 15 % Cr по сравнению со сталью мартенситного класса с 13 % Cr при равной прочности.

Ключевые слова: нержавеющие высокопрочные стали, стали переходного класса, термическая обработка, закалка, отпуск, мартенсит, остаточный аустенит, ударная вязкость, фазовый состав, микрорентгеноспектральный анализ, просвечивающая электронная микроскопия, дифракция обратного рассеяния электронов

Для цитирования: Пышминцев И.Ю., Битюков С.М., Гусев А.А. Влияние остаточного аустенита на механические свойства стали с 15 % Cr. *Известия вузов. Черная металлургия*. 2023;66(5):571–579. https://doi.org/10.17073/0368-0797-2023-5-571-579

Introduction

Low-carbon complex alloy steels containing 13 % chromium [1] have proven themselves as corrosion-resistant, high-strength materials used in pipe products within the oil, gas, and energy industries. However, the ongoing exploration of deep deposits (exceeding 4000 m) with elevated CO_2 levels, alongside the development of projects for CO_2 capture, utilization, and disposal via absorption wells, necessitates enhanced corrosion resistance in steels. This enhancement can be achieved by augmenting the chromium composition. However, an increase in chromium content may potentially prompt the formation of δ ferrite within the steel's microstructure. This formation adversely affects its visco-plastic properties at both room temperature and sub-zero temperatures, as well as its manufacturability during hot deformation [2]. The emergence of δ ferrite in the steel can be circumvented by introducing austenite-forming elements, such as nickel. Nonetheless, a combined elevation in the levels of chromium and nickel notably lowers the temperature at which martensitic transformation commences, shifting the steel from the martensitic class to the transitional (austenitic–martensitic) class [3 – 6]. Steels classified within the transitional category maintain high strength. However, due to the presence of retained austenite in the martensitic matrix, they exhibit increased ductility and deformability at low temperatures [7 – 11].

The heat treatment of transition class steels involves several operations, starting with quenching at a temperature sufficient to dissolve chromium-based carbides. The next operation aims to convert the majority of austenite into martensite [2; 3; 5]. Various techniques, including cold treatment, are employed to achieve the most comprehensive transformation. However, employing this method in the production of pipe products is deemed impractical.

An alternative approach involves intermediate heating above the Ac_3 point, facilitating the controlled release of carbides and consequently elevating the martensitic transformation temperature. The selection of heating temperature is determined by the carbon content and dopants, potentially reaching 780 – 800 °C for steel grade 08Kh17N5M3 [2].

The final tempering process aims to mitigate internal stresses that arise during the formation of "fresh" (untempered) martensite, thereby enhancing ductility and strengthening the material [3; 7].

In high-strength steels, retained austenite typically manifests as blocks or thin layers [12 – 15]. Block austenite in low-alloy high-strength steels exhibits a heightened concentration of carbon, situated adjacent to softer ferrite regions. Conversely, thin layers of austenite are enveloped by hard bainite or martensite laths [14; 16; 17]. Block austenite tends to possess low stability, making it susceptible to undergoing martensitic transformation during deformation [12; 13; 17 – 19]. Thin layers of austenite exhibit greater stability due to the influence of the surrounding lath microstructure of martensite or bainite, impeding the $\gamma \rightarrow \alpha$ transformation and creating a "shielding" effect [17; 20 – 22].

The purpose of this research is to investigate the influence exerted by the quantity and morphology of retained austenite on the mechanical properties of 13 and 15 % chromium steel as well as on achievement of strength properties for the Q125 strength category (σ_u not less than 931 MPa; $\sigma_{0.65}$ not less than 862 MPa) and Q135 strength category ($\sigma_u \geq 1000$ MPa; $\sigma_{0.65} \geq 930$ MPa) in accordance with State Standard GOST 31446 – 2017.

Materials and methods

The investigation focused on two steels containing 13 and 15 % Cr (Table 1) exhibiting compositions typical for such materials [23 – 25]. Following smelting in a laboratory vacuum induction furnace and subsequent casting, the ingots were heated to 1180 – 1200 °C, maintaining a homogenizing hold.

Further processing involved hot rolling the ingots into 16 mm diameter rods using a universal mill, implemented in three passes, with a finishing temperature of at least 850 °C. The rods were then air-cooled to reach a temperature of 20 °C. Subsequent tempering of the rods occurred at 620 °C for 1 h.

Austenitization of the steels was conducted in an LH 30/13 electric furnace, with a 30 min hold followed by air cooling. For steel *1*, the heating temperature for hardening was 980 °C, whereas for steel *2*, it ranged from 900 to 1020 °C. Subsequent heating in the temperature range of 530 to 760 °C was carried out in an electric furnace LAC PP 40/85 for durations of 1 to 2 h, followed

Table 1

Chemical composition of the studied steels, %

Таблица 1. **Химический состав исследуемых сталей, %**

Steel No.	C	Si	Mn	S	P	Cr	Ni	Mo
1	0.08	0.23	0.43	0.007	0.013	12.7	4.2	1.1
2	0.08	0.37	0.42	0.005	0.007	15.2	6.5	2.2

by air cooling. To attain the mechanical properties corresponding to strength groups Q125 and Q135, steel *1* underwent tempering at 560 °C for 1.5 h.

The phase composition analysis of the steels was conducted using a Bruker *X*-ray diffractometer, model D8 ADVANCE, using a cobalt anode. For microstructural examination, a JSM-IT500 scanning electron microscope (SEM) equipped with an inverted electron backscattering diffraction detector (EBSD), and a JEOL JEM-2100Plus transmission electron microscope (TEM) featuring a Bruker XFlash 6TI60 energy-dispersive spectrometer were employed. Chemical etching of SEM samples was performed using the Vilella reagent. TEM foils were prepared from 0.5 mm thick blanks, achieving a final thickness of approximately 100 nm through mechanical thinning and electrolytic polishing at a temperature of –22 °C.

Tensile mechanical properties were determined according to State Standard GOST 1497 – 84, using cylindrical five-fold samples with a diameter of 6 mm on an MTS Insight universal testing machine. The yield stress was determined at full elongation under a load of 0.65 % in accordance with State Standard GOST 31446 – 2017. The strain rate during the tension was set at $1.67 \cdot 10^{-3}$ s^{-1}.

Impact bending tests, as per State Standard GOST 9454 – 78, were carried out using a Zwick RKP-450 pendulum impact tester on samples featuring a *V* notch measuring 55×10×10 mm at a temperature of –40 °C.

Table 2

Influence of hardening temperature on steel *2* phase composition

Таблица 2. **Влияние температуры нагрева под закалку на фазовый состав стали *2***

Temperature of heating for quenching, °C	900	930	960	990	1020
Contain of retained austenite, %	20.9	32.2	38.6	53.6	55.5

Results and discussion

The Potak–Sagalevich structural diagram [2] was employed to determine the phase composition of the steels, offering a more precise evaluation of phase ratios compared to the Scheffler diagram [2]. Steel *1* exhibited a wholly martensitic structure based on the calculated chromium equivalents for ferrite and martensite formation, while steel *2* fell within the austenitic-martensitic classification, displaying an even distribution of structural components. *X*-ray structural phase analysis in the quenched state revealed negligible austenite presence of no more than 1 % in steel *1*. Conversely, steel *2* exhibited varying austenite amounts from 20.9 to 55.5 % with increasing heating temperatures for quenching (Table 2).

Quenching steel *2* from 960 °C aimed to diminish retained austenite and dissolve a significant portion of carbides [26]. Subsequent high tempering within the temperature range of 530 to 590 °C resulted in a marginal reduction in retained austenite content, leading to a lower yield stress (as detailed in Table 3).

Elevated heating within the intercritical temperature region (ICR) up to 680 °C notably destabilized retained austenite, thereby augmenting the yield stress. However, the emergence of "fresh" martensite during cooling noticeably decreased the relative elongation.

The microstructure of steel *2* following high tempering at 590 °C showcased decomposition products of martensite and retained austenite (Fig. 1, *a*), while heating in the ICR at 680 °C revealed clusters of "fresh" martensite (Fig. 1, *b*).

Additionally, the microstructure of steel *2* post-quenching and high tempering contained chromium and molybdenum-based carbides primarily situated in the grain boundary regions (Fig. 2), categorized as carbides of the $Me_{23}C_6$ type.

Given that the yield stress did not meet the necessary criteria for strength groups Q125 and Q135 following

Table 3

Influence of heat treatment on phase composition and mechanical properties of the studied steels

Таблица 3. **Влияние режимов термической обработки на фазовый состав и механические свойства исследуемых сталей**

Steel No.	Heat treatment mode, °C		γ_{ret}, %	σ_u, MPa	$\sigma_{0.65}$, MPa	δ, %
	quenching	tempering				
1	980 (0.5 h)	560 (1.5 h)	0.2	968 – 1053	924 – 956	17 – 19
2	960 (0.5 h)	530 (1.5 h)	36.1	1137 – 1148	596 – 659	20
		560 (1.5 h)	30.6	1120	757 – 779	20
		590 (1.5 h)	29.8	1078 – 1090	810 – 833	20 – 21
		Heating in ICR 680 (1.5 h)	25.4	1072 – 1075	824 – 841	14 – 16

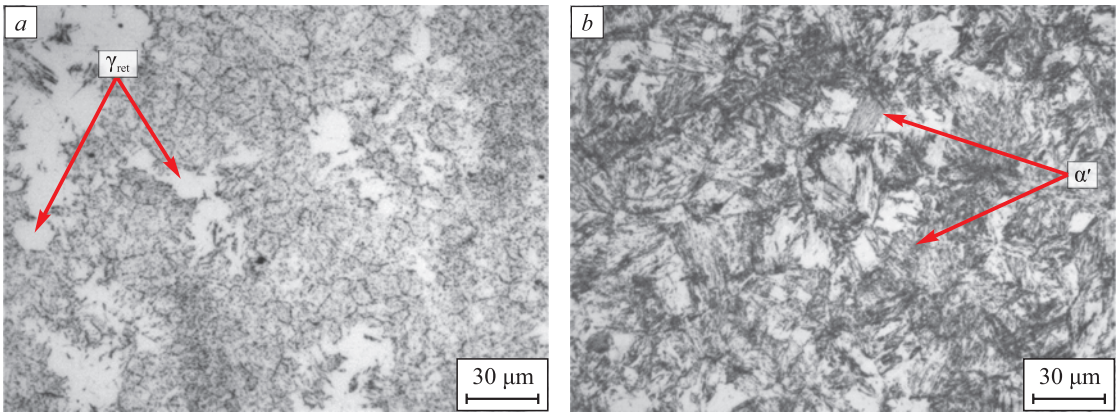

Fig. 1. Microstructure of steel *2* after hardening (960 °C) and tempering at 590 °C (*a*) or heat at 680 °C (*б*); γ_{ret} – retained austenite; α′ – newly formed lath martensite

Рис. 1. Микроструктура стали *2* после закалки от 960 °C и отпуска при 590 °C (*a*) и нагрева при 680 °C (*b*): γ_{ret} – остаточный аустенит; α′ – «свежий» мартенсит

the aforementioned heat treatments, steel *2* underwent a multi-stage heat treatment process. This involved hardening from 1020 °C with subsequent air cooling, followed by heating at 760 °C and tempering at 530 °C. Heating at 760 °C induced a reduction in the gamma solid solution in carbon through carbide precipitation and destabilization of austenite. The final tempering phase aimed to alleviate internal stresses by decomposing fresh martensite, thereby enhancing both plasticity and yield stress (Table 4).

The heating of steel *2* at 760 °C results in the precipitation of carbides exhibiting an equiaxed shape, with sizes ranging between 20 to 150 nm (see Fig. 3). These carbides align with the highly tempered state ($Me_{23}C_6$), wherein some chromium atoms are substituted by molybdenum.

An analysis of the phase composition of steel *2* after heating at 760 °C using EBSD revealed a well-defined

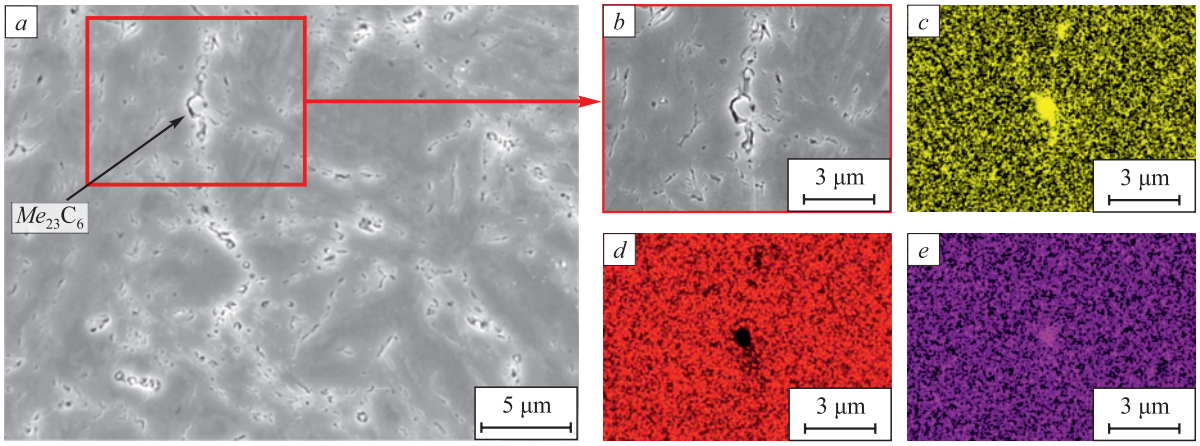

Fig. 2. Microstructure (*a*, *b*) of steel *2* after hardening (960 °C) and tempering (590 °C) and distribution of chemical elements: Cr (*c*), Fe (*d*), Mo (*e*)

Рис. 2. Микроструктура стали *2* после закалки от 960 °C и отпуска при 590 °C (*a*, *b*) с распределением химических элементов по структурным составляющим: Cr (*c*), Fe (*d*), Mo (*e*)

Table 4

Influence of multistage heat treatment on phase composition and mechanical properties of steel *2*

Таблица 4. **Влияние многоступенчатой термической обработки на фазовый состав и механические свойства стали *2***

Heat treatment mode, °C		γ_{ret}, %	σ_u, MPa	$\sigma_{0.65}$, MPa	δ, %
Quenching 1020 (0.5 h)	Heating 760 (2 h)	12.2	1119 – 1143	765 – 782	15 – 16
	Heating 760 (2 h) + tempering 530 (1 h)	10.7	1069 – 1075	959 – 974	19 – 21

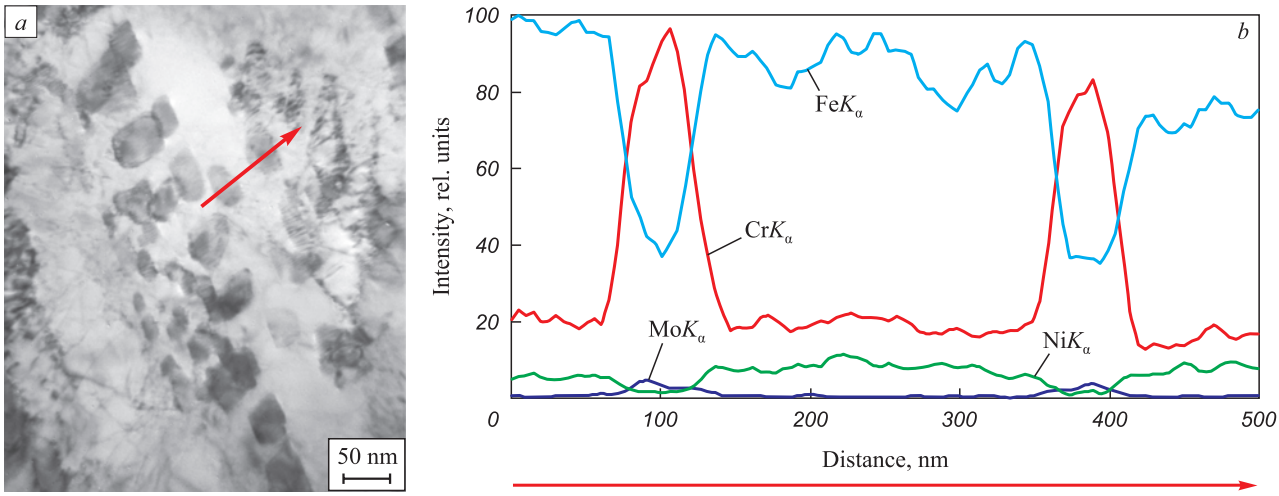

Fig. 3. Bright-field image (*a*) and composition (*b*) of carbides in microstructure of steel *2* after hardening from 1020 °C and heating at 760 °C

Рис. 3. Светлопольное изображение (*a*) и состав (*b*) отмеченных стрелкой карбидов в микроструктуре стали *2* после закалки от 1020 °C и нагрева при 760 °C

substructure comprising packets of lath "fresh" martensite (α′) and retained austenite (Fig. 4). The retained austenite manifests in block-like structures (γ_{bl}) and interlayers (γ_{il}) interspersed among martensite laths.

Comparative EBSD analysis demonstrated that the final tempering at 530 °C facilitates additional $Me_{23}C_6$ carbides formation, increasing their fraction on the phase map from 1.7 to 2.2 %. Thermo-Calc thermodynamic calculations [26] also support this elevation in carbide fraction at 530 °C. Simultaneously, the fraction of retained austenite diminishes by 1.5 %.

To assess the strengthening mechanisms in the austenitic–martensitic steel, the Orowan relation was applied, considering spherical incoherent non-cut particles uniformly dispersed within a homogeneous microstructure [27]. The contribution of carbides released during the final tempering in the multi-stage heat treatment was estimated using the equation

$$\sigma_t = \frac{10^{-6} Gb}{r} \sqrt[3]{\frac{4\pi}{3f}},$$

where G is the shear modulus (assumed to be $75 \cdot 10^9$ Pa for high-alloy martensitic steels); b is the Burgers vector (considered to be $2.49 \cdot 10^{-10}$ m); r is the average particle radius (estimated at 40 nm); f is the calculated dimensionless fraction of carbide particles assuming complete separation (based on the full stoichiometry of the carbide $(Cr_{21}Mo_2)C_6$ taken as 0.003. The maximum possible contribution of dispersed particles does not exceed ~45 MPa.

A comparative analysis of the austenitic–martensitic steel behavior during tensile testing at various stages of heat treatment (Fig. 5, curve *1*) demonstrates that after quenching from 1020 °C and heating at 760 °C, a pronounced strain hardening occurs, attributed to the partial transformation of retained austenite into deformation martensite. Subsequent tempering at 530 °C results in

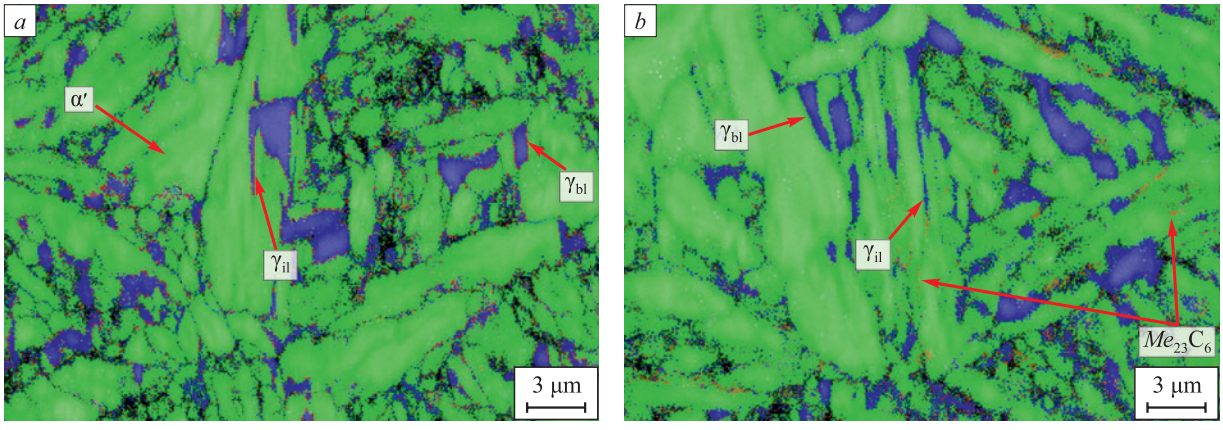

Fig. 4. Phase map of steel *2* microstructure after heating at 760 °C (*a*) and subsequent tempering at 530 °C (*b*)

Рис. 4. Фазовая карта микроструктуры стали *2* после нагрева при 760 °C (*a*) и последующего отпуска при 530 °C (*b*)

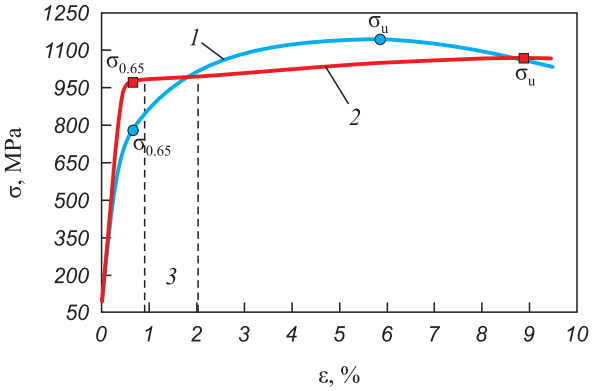

Fig. 5. Section of tensile stress-deformation diagram of steel *2* in various states:
1 – heating at 760 °C; *2* – subsequent tempering at 530 °C; *3* – yield plateau

Рис. 5. Участок диаграммы растяжения разрывного образца стали *2* в различных состояниях:
1 – нагрев при 760 °С; *2* – последующий отпуск при 530 °С; *3* – площадка текучести

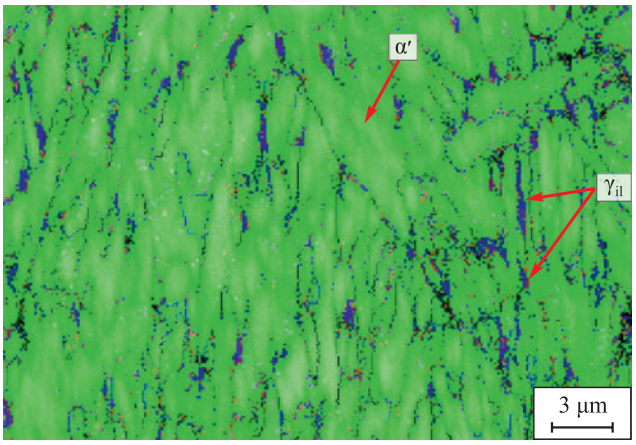

Fig. 6. Phase map of proportional elongation zone of steel *2* tensile sample after hardening from 1020 °C, heating at 760 °C and tempering at 530 °C

Рис. 6. Фазовая карта микроструктуры разрывного образца стали *2* на участке равномерного удлинения после закалки от 1020 °С, нагрева при 760 °С и отпуска при 530 °С

a noteworthy increase in the yield strength, forming a plateau, accompanied by a reduction in the impact of strain hardening (curve *2*).

X-ray structural phase analysis conducted on the region exhibiting uniform elongation in a tensile-tested sample post-multi-stage heat treatment unveiled a decrease in the proportion of retained austenite from 10.7 to 5.3 %. Examination of the phase map within this region, along a longitudinal section, revealed that austenite predominantly exists in the form of interlath layers (Fig. 6). This suggests a prevailing transformation of retained austenite into a block-like morphology during deformation.

During the final tempering at 530 °C, there was an additional precipitation of carbides, resulting in reduced carbon content within the gamma solid solution. This reduction in carbon content diminished the stability of retained austenite, leading to its partial transformation into martensite upon subsequent cooling (refer to Table 4). This likely caused a shift in the initiation of martensitic transformation of retained austenite during tension towards the region of elastic deformation. Consequently, stress martensite formation ensued, resulting in a notable increase in the yield stress. The presence of a yield plateau indicates the occurrence of plastic deformation attributed to local slip and martensitic transformation, a characteristic feature observed in steels exhibiting transformation-induced plasticity (TIP steels) [28]. If the formation of martensite during tension primarily arises from the martensitic transformation of austenite with block morphology, localized shear is facilitated by more stable layers of austenite, along which rigid martensite laths can glide [14; 17].

Testing of the steels for impact bending at a temperature of –40 °C was carried out after heat treatment, following the outlined procedures in Table. 5. The examined steels exhibited high impact toughness, meeting the requirements for operation in cold macroclimatic conditions.

The notably lower impact toughness observed in the austenitic-martensitic steel with 15 % Cr compared to the martensitic steel with 13 % Cr, despite similar strengths, could be attributed to the limited deformation stability of block austenite. This notion is supported by the phase composition data, indicating a decrease in the fraction of retained austenite in steel *2* near the fracture surface after the impact test, dropping from 10.7 to 8.2 %. The phase map of the austenitic-martensitic

Table 5

Impact toughness of the studied steels

Таблица 5. **Ударная вязкость исследуемых сталей**

Steel No.	Heat treatment mode	Impact toughness $KCV^{-40\ °C}$, J/cm^2
1	Quenching at 980 °C (0.5 h) + tempering at 560 °C (1.5 h)	136 ± 6
2	Quenching at 1020 °C (0.5 h) + heating at 760 °C (2 h) + tempering at 530 °C (1 h)	84 ± 5

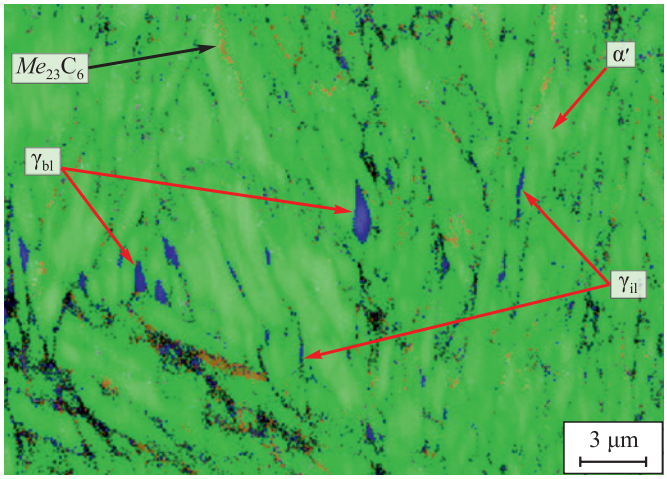

Fig. 7. Phase map of microstructure near the fracture surface of steel *2* impact sample after hardening from 1020 °C, heating at 760 °C and tempering at 530 °C

Рис. 7. Фазовая карта микроструктуры вблизи поверхности излома ударного образца стали *2* после закалки от 1020 °C, нагрева при 760 °C и отпуска при 530 °C

steel (Fig. 7) illustrates a significant reduction in the fraction of block morphology of retained austenite, likely due to the partial γ → α′ transformation.

The computed impact toughness effect of retained austenite, represented as stable interlayers, according to the results of linear approximation [29], shows an insignificant impact when its concentration is below 10 %. The reduction observed in the impact toughness of steel *2* might also be linked to the liberation of carbide phase particles, which negatively impact the resistance against the propagation of brittle cracks [6; 30].

Conclusions

The investigation reveals that quenching of 15 % chromium steel, characterized by a high nickel and molybdenum content, coupled with tempering in the temperature range of 530 to 590 °C, does not yield a high yield stress due to incomplete martensitic transformation and the retention of a considerable quantity of retained austenite (ranging from 30 to 36 %). Even heating the austenitic-martensitic steel in ICR to 680 °C did not meet the desired performance criteria.

However, employing a multi-stage heat treatment procedure involving hardening from 1020 °C, intermediate heating at 760 °C, and final tempering at 530 °C proved effective in reducing the quantity of retained austenite and ensuring mechanical properties aligned with strength groups Q125 and Q135. The precipitation of dispersed $Me_{23}C_6$ carbides (chromium and molybdenum-based) and a reduction in the carbon content within the retained austenite after heating and subsequent tempering led to a decrease its content to 10.7 %.

Post multi-stage heat treatment, retained austenite appears in the microstructure as blocks and interlayers situated between martensite laths. Static tensile testing and subsequent structural-phase analysis unveiled the low stability of block-shaped austenite, which undergoes martensitic transformation under deformation.

It is presumed that the reduction in carbon content within the gamma solid solution due to the final tempering at 530 °C shifted the process of martensitic transformation of retained austenite during static tension into the elastic deformation region. This leads to the formation of stress assisted martensite and a significant increase in the yield stress. Due to the stability of the inter-lath layers of retained austenite, enabling local sliding of surrounding laths, this steel exhibits higher relative elongation compared to martensitic steel with 13 % Cr.

The limited deformation stability of block-shaped retained austenite appears to underlie the reduced impact toughness when contrasted with steel possessing a homogeneous martensitic microstructure.

References / Список литературы

1. *ANSI/API Spec 5CRA. Specification for corrosion-resistant alloy seamless tubes for use as casing, tubing, and coupling stoc*. American Petroleum Institute; 2010:100.
2. Potak Ya.M. *High-Strength Steels*. Moscow: Metallurgiya; 1972:208. (In Russ.).

   Потак Я.М. *Высокопрочные стали*. Москва: Металлургия; 1972:208.
3. Pickering F.B. *Physical Metallurgy and the Design of Steels*. Applied Science Publishers; 1978:275.

   Пикеринг Ф.Б. *Физическое металловедение и разработка сталей*. Москва: Металлургия; 1982:182.
4. Pomerantseva S.I., Voznesenskaya N.M., Tarasenko LV., Lashchevskii V.B., High-strength corrosion-resistant semi-austenitic steels VNS-5 and SN-3. *Voprosy aviatsionnoi nauki i tekhniki. Aviatsionnye materialy*. 1986;(High-strength steels):65–72. (In Russ.).

   Померанцева С.И., Вознесенская Н.М., Тарасенко Л.В., Лащевский В.Б. Высокопрочные коррозионностойкие стали переходного аустенитно-мартенситного класса ВНС-5 и СН-3. *Вопросы авиационной науки и техники. Авиационные материалы*. 1986; (№ Высокопрочные стали):65–72.
5. Potak Ya.M., Sachkov V.V., Popova L.S., Lavrov V.I. Stainless steel Kh16N6 (SN-2A, EP288) of transition class with high viscosity. *Metal Science and Heat Treatment*. 1968;(11):4–7. (In Russ.).

   Потак Я.М., Сачков В.В., Попова Л.С., Лавров В.И. Нержавеющая сталь Х16Н6 (СН-2А, ЭП288) переходного класса с высокой вязкостью. *Металловедение и термическая обработка металлов*. 1968;(11):4–7.
6. Voznesenskaya N.M., Petrakov A.F., Kablov E.N., Shal'kevich A.B. High-strength corrosion-resistant steels of austenitic-martensitic class. *Metal Science and Heat Treatment*. 2002;(7):34–37. (In Russ.).

Вознесенская Н.М., Петраков А.Ф., Каблов Е.Н., Шалькевич А.Б. Высокопрочные коррозионностойкие стали аустенито-мартенситного класса. *Металловедение и термическая обработка металлов*. 2002;(7):34–37.

7. Pomerantseva S.I., Voznesenskaya N.M., Lashchevskii V.B., Gurvich L.Ya. Effect of heating at 400-450°C on the stress corrosion cracking resistance of welded joints of high-strength stainless steels. *Voprosy aviatsionnoi nauki i tekhniki. Aviatsionnye materialy*. 1988;(Corrosion and protection of metallic materials and structures):22–26. (In Russ.).

Померанцева С.И., Вознесенская Н.М., Лащевский В.Б., Гурвич Л.Я. Влияние нагревов при 400-450 °С на сопротивление коррозионному растрескиванию сварных соединений высокопрочных нержавеющих сталей. *Вопросы авиационной науки и техники. Авиационные материалы*. 1988;(№ Коррозия и защита металлических материалов и конструкций):22–26.

8. Voznesenskaya N.M., Lashchevskii V.B., Gurvich L.Ya., Krivov N.A., Ermolin P.A. Increasing the resistance to corrosion cracking of stamped parts made of steel 08Kh17N5M3. *Voprosy aviatsionnoi nauki i tekhniki. Aviatsionnye materialy.* 1988;(no. Corrosion and protection of metallic materials and structures):15–21. (In Russ.).

Вознесенская Н.М., Лащевский В.Б., Гурвич Л.Я., Кривов Н.А., Ермолин П.А. Повышение сопротивления коррозионному растрескиванию штампованных деталей из стали 08Х17Н5М3. *Вопросы авиационной науки и техники. Авиационные материалы.* 1988;(№ Коррозия и защита металлических материалов и конструкций):15–21.

9. Petrakov A.F., Kozlovskaya V.I., Savinkov R.A., Trantsevich Ya.V. Effect of hydrogen on the properties of corrosion-resistant chromium-nickel steels at room and cryogenic temperatures. *Voprosy aviatsionnoi nauki i tekhniki. Aviatsionnye materialy*. 1985;(3):15–21. (In Russ.).

Петраков А.Ф., Козловская В.И., Савинков Р.А., Транцевич Я.В. Влияние водорода на свойства коррозионностойких хромоникелевых сталей при комнатной и криогенных температурах. *Вопросы авиационной науки и техники. Авиационные материалы*. 1985;(3):15–21.

10. Makhneva T.M., Dement'ev V.B. Phase composition of VNS2 steel undergone to intensive plastic deformation after hardening and aging in a closed volume. *Vestnik IZhGTU*. 2009;(4):54–58. (In Russ.).

Махнева Т.М., Дементьев В.Б. Фазовый состав подвергнутой интенсивной пластической деформации стали марки ВНС2 после закалки и старения в замкнутом объеме. *Вестник ИжГТУ*. 2009;(4):54–58.

11. Gromov V.I., Voznesenskaya N.M., Pokrovskaya N.G., Tonysheva O.A. High-strength constructional and corrosion-resistant steels developed by VIAM for aviation engineering. *Aviatsionnye materialy i tekhnologii*. 2017;(S):159–174. (In Russ.). https://doi.org/10.18577/2071-9140-2017-0-S-159-174

Громов В.И., Вознесенская Н.М., Покровская Н.Г., Тонышева О.А. Высокопрочные конструкционные и коррозионностойкие стали ФГУП «ВИАМ» для изделий авиационной техники. *Авиационные материалы и технологии*. 2017;(S):159–174. https://doi.org/10.18577/2071-9140-2017-0-S-159-174

12. Wong A. Modelling the stability and transformation kinetics of retained austenite in steels. *Materials Science and Technology*. 2022;38(11):676–688. http://dx.doi.org/10.1080/02670836.2022.2063539

13. Xiong X.C., Chen B., Huang M.X., Wang J.F., Wang L. The effect of morphology on the stability of retained austenite in a quenched and partitioned steel. *Scripta Materialia*. 2013;68(5):321–324. http://dx.doi.org/10.1016/j.scriptamat.2012.11.003

14. Yang K., Ding W., Liu S., Li W., Jin X. Dominating role of film-like carbon-enriched austenite for the simultaneous improvement of strength and toughness in low-carbon steel. *Steel Research International*. 2021;92(2):2000344. https://doi.org/10.1002/srin.202000344

15. Ghazvinloo H.R., Honarbakhsh-Raouf A., Borhami E. Morphological characteristics of retained austenite in 0.362C–1.38Si–1.24Mn steel processed by one-step quenching and partitioning. *Metallurgist*. 2016;60:758–764. https://doi.org/10.1007/s11015-016-0363-y

16. Narasimha Rao B.V., Thomas G. Structure-property relations and the design of Fe-4Cr-C base structural steels for high strength and toughness. *Metallurgical Transactions A*. 1980;11:441–457. https://doi.org/10.1007/bf02654568

17. Maresca F., Kouznetsova V.G., Geers M.G.D. On the role of interlath retained austenite in the deformation of lath martensite. *Modelling and Simulation in Materials Science and Engineering*. 2014;21:21. https://doi.org/10.1088/0965-0393/22/4/045011

18. Liu W., Zhang B., Zhao A., Guo H., Sun S. Control of morphology and dimension of blocky retained austenite in medium-carbon steel. *Material Research Express*. 2018;6(1):10. https://doi.org/10.1088/2053-1591/aae561

19. Liu W., Liang J., Liang Y., Zhang B., Zhao A. A study of blocky retained austenite and properties under variously heat-treated ultra-fine bainitic steel. *Material Research Express*. 2019;6(10):15. https://doi.org/10.1088/2053-1591/ab3937

20. Lu X., Yang Z., Qian D., Lan J., Hua L. Effect of martensite pre-quenching on bainite transformation kinetics, martensite/bainite duplex microstructures, mechanical properties and retained austenite stability of GCr15 bearing steel. *Journal of Materials Research and Technology*. 2021;15:2429–2438. https://doi.org/10.1016/j.jmrt.2021.09.070

21. Xiao H., Zhao G., Xu D., Cheng Y., Bao S. Effect of microstructure morphology of Q&P steel on carbon and manganese partitioning and stability of retained austenite. *Metals*. 2022;12(10):1613. https://doi.org/10.3390/met12101613

22. Yi H.L., Chen P., Bhadeshia H.K.D.H. Optimizing the morphology and stability of retained austenite in a d-TRIP steel. *Metallurgical and Materials Transactions A*. 2014;45:3512–3518. https://doi.org/10.1007/s11661-014-2267-4

23. Dragunov Yu.G., Zubchenko A.S., Kashirskii Yu.V. *Grade Guide of Steels and Alloys*. Moscow. 2014, 1216 p. (In Russ.).

Драгунов Ю.Г., Зубченко А.С., Каширский Ю.В. *Марочник сталей и сплавов. 4-е изд. перераб. и доп*. Москва; 2014:1216.

24. Cao L., Anderko A., Gui F., Sridhar N. Localized corrosion of corrosion resistant alloys in H_2S-containing environments. *Corrosion*. 2016;72(5):636–654. https://doi.org/10.5006/2016

25. Kimura M., Tamari T., Shimamoto K. High Cr stainless steel OCTG with high strength and superior corrosion resistance. *JFE Technical Report*. 2005;(9):7–12.

26. Pumpyanskii D.A., Pyshmintsev I.Yu., Bityukov S.M., Gervas'ev M.A., Gusev A.A. Features of microstructure, phase composition and strengthening capability of stainless steels with 13 – 17% Cr. *Izvestiya. Ferrous Metallurgy*. 2022;65(9):644–653. (In Russ.).
https://doi.org/10.17073/0368-0797-2022-9-644-653

Пумпянский Д.А., Пышминцев И.Ю., Битюков С.М., Гервасьев М.А., Гусев А.А. Особенности микроструктуры, фазового состава и возможности упрочнения нержавеющих сталей с 13 – 17 % Cr. *Известия вузов. Черная металлургия*. 2022;65(9):644–653.
https://doi.org/10.17073/0368-0797-2022-9-644-653

27. Shtremel M.A. *Strength of Alloys. Part II. Deformation*. Moscow: MISIS; 1997:527. (In Russ.).

Штремель М.А. *Прочность сплавов. Часть II. Деформация*. Москва: МИСИС; 1997:527.

28. Gervasyev M.A., Estemirova S.K., Mushnikov A.N., Sharapova V.A., Gusev A.A., Bashirova M.A., Mushnikov A.N. Changes in the phase composition of high-manganese steels during tensile deformation. *The Physics of Metals and Metallography*. 2022;(1):32–36.
https://doi.org/10.31857/S0015323022010053

Гервасьев М.А., Эстемирова С.Х., Мушников А.Н., Шарапова В.А., Гусев А.А., Баширова М.А. Изменение фазового состава высокомарганцевых сталей при растяжении. *Физика металлов и металловедение*. 2022;(1):35–39. https://doi.org/10.31857/S0015323022010053

29. Nakagawa H., Miyazaki T. Effect of retained austenite on the microstructure and mechanical properties of martensitic precipitation hardening stainless steel. *Journal of Materials Science*. 1999;34:3901–3908.
https://doi.org/10.1023/A:1004626907367

30. Pyshmintsev I.Yu., Smirnov M.A., Laev K.A., Khramkov E.V., Alyutin D.M. Properties of high-chromium corrosion-resistant steels exposed to high-temperature thermomechanical treatment. *Vestnik Magnitogorskogo gosudarstvennogo tehnitseskogo universiteta im. G.I. Nosova*. 2015;(3):78–82. (In Russ.).

Пышминцев И.Ю., Смирнов М.А., Лаев К.А., Храмков Е.В., Алютин Д.М. Свойства высокохромистых коррозионностойких сталей, подвергнутых высокотемпературной термомеханической обработке. *Вестник МГТУ им. Г. И. Носова*. 2015;(3):78–82.

Information about the Authors / Сведения об авторах

Igor' Yu. Pyshmintsev, *Dr. Sci. (Eng.), Prof., General Director*, LLC "TMK R&D"
E-mail: PyshmintsevIU@tmk-group.com

Sergei M. Bityukov, *Cand. Sci. (Eng.), Head of the Laboratory*, LLC "TMK R&D"
E-mail: BitiukoySM@tmk-group.com

Aleksei A. Gusev, *Junior Researcher*, LLC "TMK R&D"
E-mail: GusevAA1@tmk-group.com

Игорь Юрьевич Пышминцев, *д.т.н., профессор, генеральный директор,* ООО «ИЦ ТМК»
E-mail: PyshmintsevIU@tmk-group.com

Сергей Михайлович Битюков, *к.т.н., заведующий лабораторией,* ООО «ИЦ ТМК»
E-mail: BitiukoySM@tmk-group.com

Алексей Антонович Гусев, *младший научный сотрудник,* ООО «ИЦ ТМК»
E-mail: GusevAA1@tmk-group.com

Contribution of the Authors / Вклад авторов

I. Yu. Pyshmintsev – substantiation of the research concept, planning of the experiments, analysis of literary and experimental data, interpretation of the research results, formation of the conclusions, editing and revision of the manuscript

S. M. Bityukov – planning of the experiments, analysis of experimental data, interpretation and generalization of the research results, formation of the conclusions, editing and revision of the manuscript

A. A. Gusev – search and analysis of literary data, conducting experimental studies (sample preparation, heat treatment, metallography, diffraction research), analysis of experimental data, interpretation of the research results; formation of the conclusions; design, editing and revision of the manuscript.

И. Ю. Пышминцев – обоснование концепции и планирование исследований, разработка программы экспериментальных исследований, анализ данных литературы, анализ экспериментальных данных, интерпретация результатов исследования, формулировка выводов, редактирование и переработка рукописи.

С. М. Битюков – планирование исследований, разработка программы экспериментальных исследований, анализ экспериментальных данных, интерпретация и обобщение результатов исследования, формулировка выводов, редактирование и переработка рукописи.

А. А. Гусев – сбор и анализ данных литературы, проведение экспериментальных исследований (подготовка проб образцов, термообработка, металлография и дифрактография), анализ экспериментальных данных, интерпретация результатов исследования, формулировка выводов, оформление, редактирование и переработка рукописи.

Received 20.07.2023
Revised 05.09.2023
Accepted 11.09.2023

Поступила в редакцию 20.07.2023
После доработки 05.09.2023
Принята к публикации 11.09.2023

MATERIALS SCIENCE / МАТЕРИАЛОВЕДЕНИЕ

UDC 669:539.381.296
DOI 10.17073/0368-0797-2023-5-580-586

Original article
Оригинальная статья

Effect of heat treatment on deformation inhomogeneity of carbon steel / stainless steel bimetal

S. P. Buyakova[1], K. N. Kayurov[2], S. A. Barannikova[1]

[1] **Institute of Strength Physics and Materials Science, Siberian Branch of the Russian Academy of Sciences** (2/4 Akademicheskii Ave., Tomsk 634055, Russian Federation)
[2] **Scientific Production Enterprise of Geophysical Equipment "LUCH"** (34 2nd Yurginskaya Str., Novosibirsk 630051, Russian Federation)

sbuyakova@ispms.ru

Abstract. The work is devoted to the study of the effect of annealing on mechanical properties and inhomogeneity of plastic deformation of a bimetallic plate made of stainless / carbon steel with the dimensions of the working part 50×7×2 mm. To develop laser technology for producing bimetals of various compositions, the contact zone of two dissimilar steels is of greatest interest. Since the performance characteristics of the entire product as a whole depend on the structure and properties of this zone, interaction of the components of the bimetal in the process of its manufacture leads to appearance of heterogeneity of various types near the interface and in the volumes adjacent to it. The research material was obtained by laser cladding of wire AISI 304 stainless steel on a plate of low-carbon steel St3. Bimetallic samples were subjected to vacuum heating at a temperature of 700 °C at various times from 2 to 8 h. The use of data on the distributions of local strains by the speckle photography method made it possible to consider the process of plastic flow in the initial section of tension diagram and to establish the effect of annealing temperature on plastic strain localization during mechanical tests. For a quantitative assessment of deformation inhomogeneity in the main and cladding layers, we used spatiotemporal distributions of local elongations and the corresponding values of the variation coefficient. It was established that the level of deformation inhomogeneity of microvolumes at the interface during tension is higher than that of the bimetal main layers. With increase in the annealing time, increase in the variation coefficient in the joint zone is noted, which is more significant on the stainless steel side, and this increases the probability of microcracks initiation. The increased level of deformation inhomogeneity of microvolumes of the cladding layer carburized zone is contingent on the increased localization of deformation in nearby microvolumes due to structural heterogeneity.

Keywords: plastic deformation, localization, bimetal, low carbon steel, stainless steel

Acknowledgements: The work was performed within the framework of the complex project "Organization of high-tech production of rotary controlled systems for opening complex formations and drilling wells with a large deviation from the vertical in difficult geological conditions, in the Arctic" (grant agreement No. 075-11-2022-019 dated April 06, 2022), the financial support of the Ministry of Science and Education of the Russian Federation (decree of the Government of the Russian Federation dated 09.04.2010 No. 218).

For citation: Buyakova S.P., Kayurov K.N., Barannikova S.A. Effect of heat treatment on deformation inhomogeneity of carbon steel/stainless steel bimetal. *Izvestiya. Ferrous Metallurgy*. 2023;66(5):580–586. https://doi.org/10.17073/0368-0797-2023-5-580-586

О влиянии нагрева на неоднородность деформации биметалла углеродистая сталь – нержавеющая сталь

С. П. Буякова[1], К. Н. Каюров[2], С. А. Баранникова[1]

[1] **Институт физики прочности и материаловедения Сибирского отделения РАН** (Россия, 634055, Томск, пр. Академический, 2/4)
[2] **Научно-производственное предприятие геофизической аппаратуры «ЛУЧ»** (Россия, 630051, Новосибирск, ул. 2-я Юргинская, 34)

sbuyakova@ispms.ru

Аннотация. Работа посвящена изучению влияния отжига на механические свойства и неоднородность пластической деформации биметаллической пластины из нержавеющей/углеродистой сталей с размерами рабочей части 50×7×2 мм. Для отработки лазерной технологии получения биметаллов различных композиций наибольший интерес представляет изучение зоны контакта двух разнородных сталей. Поскольку от структуры и свойств данной зоны зависят эксплуатационные характеристики всего изделия в целом, взаимодействие

составляющих биметалла в процессе его изготовления приводит к возникновению неоднородности различных видов вблизи границы раздела и в объемах, прилегающих к ней. Материал исследований получали методом лазерной наплавки проволоки нержавеющей стали AISI 304 на пластину из низкоуглеродистой стали Ст3. Биметаллические образцы с наплавкой подвергали вакуумному нагреву при температуре 700 °С в течение различного времени (от 2 до 8 ч). Использование данных о распределениях локальных деформаций методом спекл-фотографии позволило рассмотреть процесс пластического течения на начальном участке диаграммы растяжения и установить влияние температуры отжига на локализацию пластической деформации в процессе механических испытаний. Для количественной оценки неоднородности деформации в основном и плакирующем слоях использовали пространственно-временные распределения локальных удлинений и соответствующие величины коэффициента вариации. Установлено, что уровень неоднородности деформации микрообъемов на интерфейсе в процессе растяжения выше, чем основных слоев биметалла. С увеличением времени отжига отмечается повышение значений коэффициента вариации в зоне соединения, более значительное со стороны нержавеющей стали, что увеличивает вероятность зарождения микротрещин. Повышенный уровень неоднородности деформации микрообъемов науглероженной зоны плакирующего слоя обусловлен усилением локализации деформации в близлежащих микрообъемах из-за структурной неоднородности.

Ключевые слова: пластическая деформация, локализация, биметаллы, низкоуглеродистая сталь, нержавеющая сталь

Благодарности: Работа выполнена в рамках комплексного проекта «Организация высокотехнологичного производства роторных управляемых систем для вскрытия сложных пластов и бурения скважин с большим отходом от вертикали в сложных геологических условиях, Арктике» (соглашение о предоставлении субсидии от 6 апреля 2022 № 075-11-2022-019), реализуемого Институтом физики прочности и материаловедения Сибирского отделения РАН при финансовой поддержке Минобрнауки России в рамках постановления Правительства РФ от 09.04.2010 № 218.

Для цитирования: Буякова С.П., Каюров К.Н., Баранникова С.А. Влияние термической обработки на неоднородность деформации биметалла углеродистая сталь – нержавеющая сталь. *Известия вузов. Черная металлургия*. 2023;66(5):580–586. https://doi.org/10.17073/0368-0797-2023-5-580-586

Introduction

To effectively handle materials within power-generating or oil refining equipment subjected to simultaneous mechanical loading and high temperatures, it is imperative to develop novel methods for evaluating their performance [1]. These methods should comprehensively consider the influence stemming from various structural and mechanical inhomogeneities [2 – 4]. Despite their high strength, bimetallic materials are particularly susceptible to delamination at their interfaces. Defects like delamination may arise during the manufacturing and operational phases of bimetallic materials, thereby somewhat restricting their industrial applications [5 – 8]. The unevenness of deformation in bimetallic composites during rolling is contingent upon several factors, including the disparity in deformation resistances between components, initial layer thicknesses, stacking sequence, parameters within the deformation zone, and the magnitude of contact friction forces and tangential stresses at the interface [9 – 12]. This deformation irregularity within bimetallic composites detrimentally affects the rolling process and the resultant bimetal properties. It leads to the accumulation of significant residual stresses, which, in turn, can induce bimetal delamination, bending, warping, and the fracturing of harder layers [13 – 16].

An exceptionally promising domain for advancing laser cladding technology using high-performance lasers lies in leveraging cladding materials presented in solid and powder metal strips [17; 18]. The primary motivation driving the shift from conventional coating methods (thermal spraying and arc surfacing) toward laser-based techniques is the superior quality of the coatings produced. This superiority stems from the reduced mixing coefficient between the clad material and the substrate, along with heightened adhesion characteristics [19].

Given that the processes occurring in the vicinity of the interface during laser cladding can significantly influence material properties [20], the objective of this study was to examine the influence of temperature-time factors on the inhomogenity of plastic deformation in bimetallic plates.

Materials and methods

The investigation focused on studying the deformation inhomogeneity of a bimetal comprising low-carbon steel St3 and AISI 304 stainless steel, achieved through laser cladding. The St3 low-carbon steel plate measured approximately 6 mm in thickness, while the AISI 304 stainless steel formed a clad layer of about 1 mm thickness. The laser cladding process, using filler wire, was conducted on plates composed of low-carbon steel St3 at the experimental facility of the Institute of Strength Physics and Materials Science of the Siberian Branch of the RAS. The application of the laser cladding technique involved introducing filler wire into the laser impact zone using a standard arc torch and a semi-automatic welding machine PDGO-601. In this particular laser cladding setup, AISI 304 stainless steel filler wire with a diameter of 1.0 mm served as the material for the clad layer. Employing the fiber laser LS-15, boasting a capacity of 15 kW, facilitated a productivity range of 130 – 170 g/min, resulting in deposited beads measuring 0.8 – 1.5 mm in width. To ensure the creation of a uniform monolithic coating, cladding parameters were meticulously selected based on established technological modes. These included specific settings for scanning width (approximately 30 mm), laser output power (4 kW), and speed (65 mm/min). The scanning process was executed using the “triangular” mode at a frequency of 25 Hz. Upon metallographic examination of cross-

sections and XRD (*X*-ray diffraction) analysis, it was observed that none of the samples exhibited pores, cracks, or unmelted powder particles.

When subjected to heating, bimetals composed of distinct chemical compositions display variations in the rate and direction of diffusion for carbon and alloying elements, contingent upon the temperature of heating [3]. Following heat treatment (conducted via vacuum heating up to 700 °C and holding for durations of 2, 4, 6 and 8 h), the distribution of chemical elements within the steel layers of the bimetallic plate was analyzed. This examination was performed using the LEO EVO 50 scanning electron microscope (Carl Zeiss, Germany), equipped with an Oxford Instruments attachment for *X*-ray dispersive micro-analysis. These analyses were conducted at the NANOTECH Center for Collective Use, part of the ISPMS SB RAS. Microhardness measurements were carried out using the PMT-3 microhardness tester, following the methodology outlined in GOST 9450 – 76.

During mechanical uniaxial tensile tests performed on flat samples measuring 50×7×2 mm, the deformation fields were recorded using the Walter+Bai LFM-125 testing machine. The deformation rate was set at $6.67 \cdot 10^{-5}$ s^{-1} and tests were conducted at room temperature. These tests simultaneously employed an adapted speckle photography technique, as detailed in [21 – 23], to capture the deformation fields. In analyzing the plastic distortion tensor, the local elongation along the direction of the sample's tensile axis εxx is often considered the most natural component for visualization and analysis. Shear and rotational components exhibit more intricate distributions, rendering them less convenient for analysis. The distributions obtained through these techniques reflect local deformation increments rather than integral values from the commencement of the loading process. Fig. 1, *a* illustrates a typical distribution of local deformations $\varepsilon_{xx}(x, y)$ within the sample subsequent to laser cladding, where the total tensile deformation measures 0.01. This data presentation elucidates that post-yield point, plastic deformation becomes localized within specific zones of the sample, while other material volumes exhibit minimal deformation at the given increment. To quantitatively assess the degree of deformation inhomogenity across various layers of the bimetal (substrate and cladding), the coefficient of variation of local deformations ε_{xx} was employed. This coefficient is calculated as the ratio of the standard deviation to the arithmetic mean *n* of measurements:

$$\nu = \frac{\sqrt{\frac{1}{n}\sum_{i=1}^{n}\left(\langle\varepsilon_{xx}\rangle - \varepsilon_{xx_i}\right)^2}}{\langle\varepsilon_{xx}\rangle},$$

where $\langle\varepsilon_{xx}\rangle = \frac{\sum_{1}^{n}\varepsilon_{xx_i}}{n}$.

When $\nu > 0.4$ it is considered that the distribution of local elongations ε_{xx} within the sample demonstrates a substantial level of inhomogenity $\langle\varepsilon_{xx}\rangle$ rendering the value not representative [24].

Results and discussion

The hardness observed within the junction zone of the bimetal was notably higher compared to the hardness measured in both the substrate and the surfacing areas outside this zone (Fig. 1, *b*). Following heat treatment, as the heating duration increased, the average

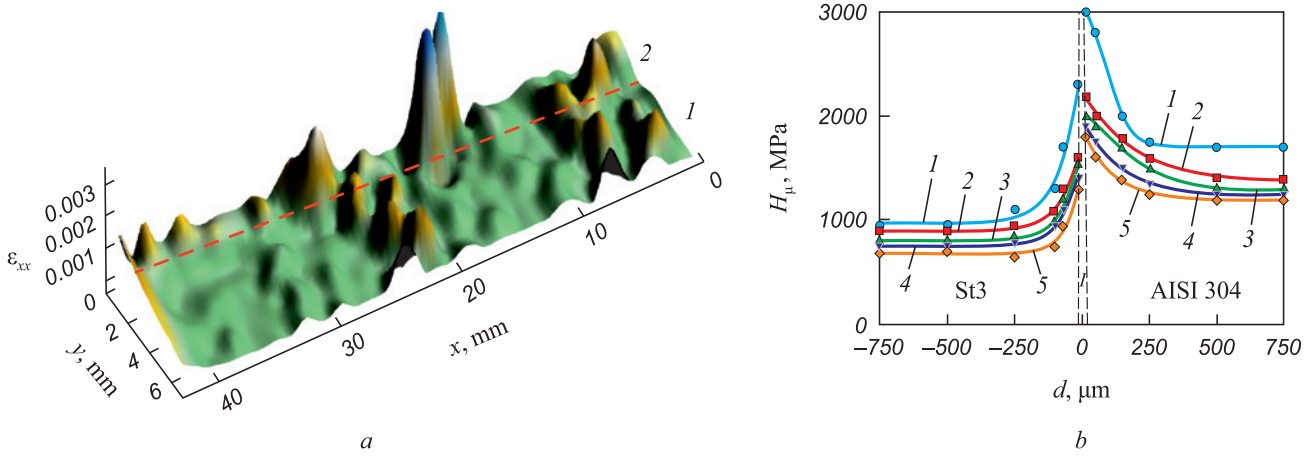

Fig. 1. Distribution of local deformations ε_{xx} in the substrate (*1*) and surfacing (*2*) at the initial stage of plastic flow (*a*) and the change in microhardness along the width of the sample (*b*) after laser surfacing (*1*) and after heat treatment at 2 (*2*), 4 (*3*), 6 (*4*) and 8 h (*5*) (dotted line (*I*) marks the junction zone)

Рис. 1. Распределение локальных деформаций ε_{xx} в подложке (*1*) и наплавке (*2*) на начальной стадии пластического течения (*a*) и изменение микротвердости по ширине образца (*b*) после лазерной наплавки (*1*) и после термической обработки в течение 2 (*2*), 4 (*3*), 6 (*4*) и 8 ч (*5*) (пунктирной линией (*I*) отмечена зона соединения)

hardness levels observed in the substrate and surfacing decreased significantly. However, the hardening gradient between the two types of steels near the junction zone remained consistent.

Fig. 2 illustrates the influence of heating duration on the distribution of fundamental elements (iron, chromium, nickel, manganese) across the thickness of the sample.

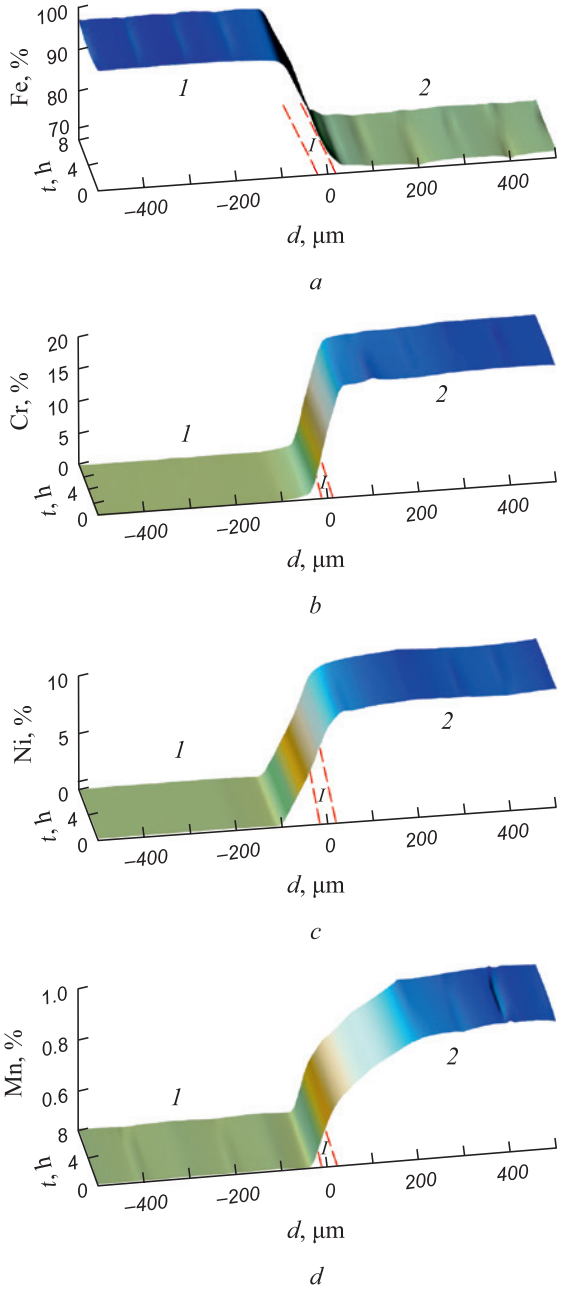

Fig. 2. Effect of annealing time on distribution of iron (*a*), chromium (*b*), nickel (*c*) and manganese (*d*) over the thickness of the sample:
1 – low-carbon steel; *2* – stainless steel;
I – transition layer in the junction zone

Рис. 2. Влияние времени отжига на распределение железа (*a*), хрома (*b*), никеля (*c*) и марганца (*d*) по толщине образца:
1 – низкоуглеродистая сталь; *2* – нержавеющая сталь;
I – переходный слой в зоне соединения

The depicted data indicates that the impact of heating remains insignificant for each of the steel types when compared to their initial states without heat treatment.

The bimetal consists of low-carbon and stainless steel, with a distinct transition layer (*I*) between them. Within this transitional zone, the concentrations of iron, chromium, nickel, and manganese exhibit a linear variation. The diffusion depth of chromium and nickel into the base layer of low-carbon steel extends up to 20 μm. During the heating process, alloying elements diffuse from the austenitic (stainless) steel into the carbon (pearlitic) steel, while carbon diffuses in the opposite direction.

In Fig. 3, *a*, the impact of heating duration on the distribution of carbon throughout the sample thickness is depicted.

Within the span from carbon steel to stainless steel, the distribution of carbon content manifests in distinct layers: following the transition layer (*I*), there exist decarburized (*II*) and supercarburized (*III*) layers. The thickness

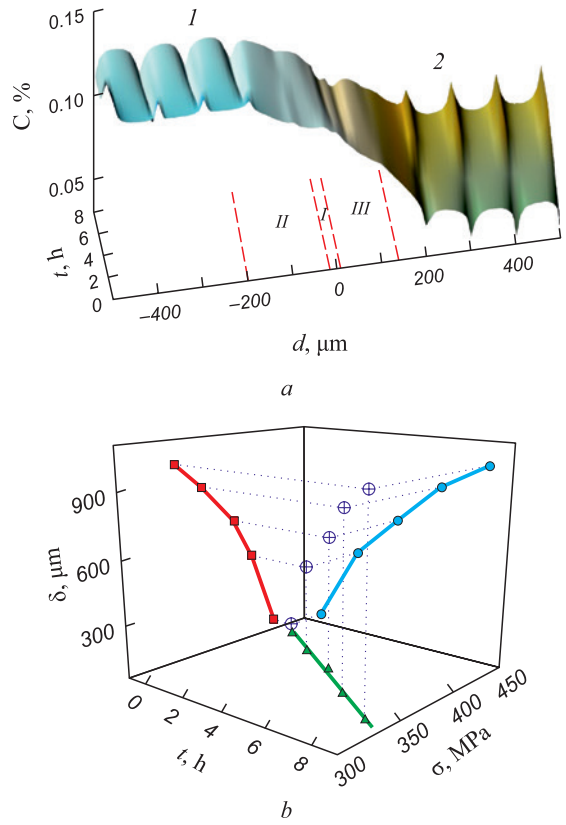

Fig. 3. Carbon distribution over the thickness of the surfaced sample (*a*), depth of decarburization δ of the base layer and tensile strength σ of the bimetal depending on annealing duration *t* (*b*):
1 – low-carbon steel; *2* – stainless steel;
I – transition layer in the junction zone

Рис. 3. Распределение углерода по толщине образца с наплавкой (*a*), а также глубина обезуглероживания δ основного слоя и предел прочности σ биметалла в зависимости от длительности отжига *t* (*b*):
1 – низкоуглеродистая сталь; *2* – нержавеющая сталь;
I – переходный слой в зоне соединения

of these layers varies in response to the duration of heating. With prolonged annealing periods, the expanding decarburized ferrite zone on the carbon steel side exhibits reduced strength characteristics. Consequently, this contributes to a decrease in the tensile strength of the bimetal (Fig. 3, *b*). The process of chromium diffusion from the austenitic phase and carbon diffusion in the opposite direction results in the formation of a thin carbide layer on the carbon steel side.

The structural and chemical inhomogeneities near the substrate and cladded layer interface play an important role in shaping the nature of plastic deformation around the transition zone. Ensuring compatibility of deformations at the bimetal interface necessitates an equivalent deformation of metal microvolumes adjoining the interface. Consequently, the levels of deformation inhomogeneity within these microvolumes at the interface layers, as assessed by the coefficient of variation of local deformations ν, are expected to be uniform. By meeting these conditions, the stress conditions within these regions become more intricate.

Fig. 4 illustrates the impact of heat treatment on the changes in the coefficient of variation (ν), which serves as an indicator of the degree of deformation inhomogeneity near the transition zone of the bimetal during the initial stages of deformation. In the bimetal state subsequent to laser cladding, notable differences in the levels of deformation inhomogenity are observed among the microvolumes in the boundary zones of the stainless and carbon steel sides, nearly twofold (Fig. 4, curve *1*). The reduced level of deformation heterogeneity is characteristic of the microvolumes in the decarburized zone,

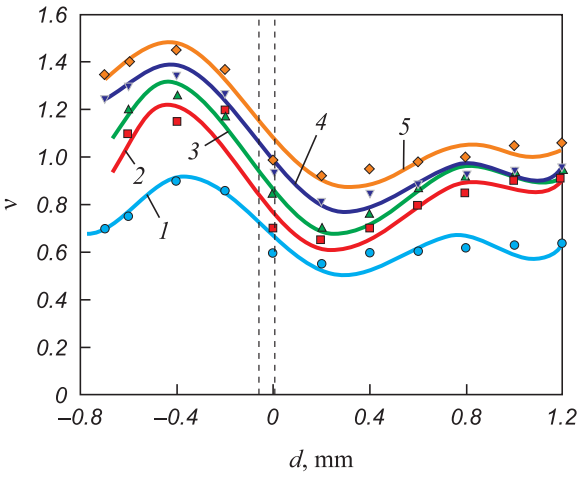

Fig. 4. Change in the level of inhomogeneity of deformation ν by thickness of the sample layers at the initial stage of plastic flow in the state after laser surfacing (*1*) and after annealing at 2 (*2*), 4 (*3*), 6 (*4*) and 8 h (*5*)

Рис. 4. Изменение уровня неоднородности деформации ν по толщине слоев образца на начальной стадии пластического течения в состоянии после лазерной наплавки (*1*) и после отжига в течение 2 (*2*), 4 (*3*), 6 (*4*) и 8 ч (*5*)

directly adjacent to the interface, as well as in the state post-cladding (Fig. 4, curve *1*). The existence of a carbide interlayer leads to the emergence of microcracks and a more non-uniform distribution of local deformations within the carburized layer of austenitic steel, with a total deformation of ε = 0.01. Research outlined in [23] demonstrates that at the bimetal's yield point, the Lüders band originating in the main St3 steel layer can act as a "wedge" in accordance with the Barenblatt wedging model [25], potentially initiating cracks in the cladding layer. Due to heightened local stresses at the interface, the Lüders band contributes to the formation of martensitic α′-phase and the emergence of isolated zones of localized deformation in the clad layer during the initial phase of plastic flow.

After heat treatment, with increasing annealing duration (Fig. 4, curves *2* – *5*), the coefficients of variation of deformation inhomogeneity in the substrate and the cladded metal notably escalate. Even after prolonged annealing, the two steels near the junction zone still exhibit distinct levels of deformation inhomogeneity. Statistical analysis utilizing the double *t*-criterion method [24] indicates a "significant" difference in the coefficients of variation of deformation heterogeneity between the substrate and the deposited metal.

This study underscores the influence of structural inhomogeneity near the layer interface on the distribution of local deformations when subjecting the bimetal obtained by laser cladding to uniaxial tension. The nature of deformation inhomogeneity in the transition zone and the primary layers varies, potentially impacting the properties of bimetal products. To maintain or prevent a decrease in the mechanical properties of bimetals composed of carbon steel and stainless steel, manufacturing should adhere to technological modes that ensure minimal levels of deformation inhomogeneity within microvolumes at the transition zone.

Conclusions

The bimetal obtained through laser cladding exhibits a considerable increase in hardness within the junction zone. Subsequent heating up to 700 °C, with holding durations ranging from 2 to 8 h, does not diminish the hardening gradient. This lack of reduction is attributed to the formation of a carbide interlayer due to the diffusion of components.

The heat treatment process results in the growth of a decarburized layer on the carbon steel side and a subsequent reduction in the tensile strength of the bimetal.

Elevated values of the coefficient of variation of local deformations within the carburized layer of the cladded metal are linked to heightened concentration of deformations, stemming from the presence of chromium carbides

and microcracks. Prolonged annealing durations further escalate the coefficients of variation of deformation inhomogeneity within both the substrate and the cladded metal.

References / Список литературы

1. Khodadad Motarjemi A., Koçak M., Ventzke V. Mechanical and fracture characterization of a bi-material steel plate. *International Journal of Pressure Vessels and Piping*. 2002;79(3):181–191. https://doi.org/10.1016/S0308-0161(02)00012-1
2. Gao X., Jiang Z., Wei D., Jiao S., Chen D., Xu J., Zhang X., Gong D. Effects of temperature and strain rate on microstructure and mechanical properties of high chromium cast iron/low carbon steel bimetal prepared by hot diffusion-compression bonding. *Materials and Design*. 2014;63:650–657. https://doi.org/10.1016/j.matdes.2014.06.067
3. Zasukha P.F., Korshchikov V.D., Bukhvalov O.B., Ershov A.A. *Bimetallic Rolling*. Moscow: Metallurgiya1971: 264. (In Russ.).

   Биметаллический прокат / П.Ф. Засуха, В.Д. Корщиков, О.Б. Бухвалов, А.А. Ершов. Москва: Металлургия; 1971:264.
4. Akramifard H.R., Mirzadeh H., Parsa M.H. Estimating interface bonding strength in clad sheets based on tensile test results. *Materials and Design*. 2014;64:307–309. https://doi.org/10.1016/j.matdes.2014.07.066
5. Li L., Nagai K., Yin F. Progress in cold roll bonding of metals. *Science and Technology of Advanced Materials*. 2008;9(2):023001. http://doi.org/10.1088/1468-6996/9/2/023001
6. Li Z., Zhao J., Jia F., Zhang Q., Liang X., Jiao S., Jiang Z. Analysis of bending characteristics of bimetal steel composite. *International Journal of Mechanical Sciences*. 2018;148:272–283. https://doi.org/10.1016/j.ijmecsci.2018.08.032
7. DebRoy T., Wei H.L., Zuback J.S., Mukherjee T., Elmer J.W., Milewski J.O., Beese A.M., Wilson-Heid A., De A., Zhang W. Additive manufacturing of metallic components – Process, structure and properties. *Progress in Materials Science*. 2018;92:112–224. https://doi.org/10.1016/j.pmatsci.2017.10.001
8. Hinojos A., Mireles J., Reichardt A., Frigola P., Hosemann P., Murr L.E., Wicker R.B. Joining of Inconel 718 and 316 Stainless Steel using electron beam melting additive manufacturing technology. *Materials and Design*. 2016;94:17–27. http://doi.org/10.1016/j.matdes.2016.01.041
9. Dhib Z., Guermazi N., Ktari A., Gasperini M., Haddar N. Mechanical bonding properties and interfacial morphologies of austenitic stainless steel clad plates. *Materials Science and Engineering: A*. 2017;696:374–386. https://doi.org/10.1016/j.msea.2017.04.080
10. Li Z., Lin Y.C., Zhang L., Jia F., Jiang Z., Jiao S. Investigation of compact tensile and fracture mechanical properties of a duplex stainless steel bimetal composite with the interfacial zone. *Journal of Materials Research and Technology*. 2022;19:809–820. https://doi.org/10.1016/j.jmrt.2022.05.085
11. Li Z., Zhao J., Jia F., Liang X., Zhang Q., Yuan X., Jiao S., Jiang Z. Interfacial characteristics and mechanical properties of duplex stainless steel bimetal composite by heat treatment. *Materials Science and Engineering: A*. 2020;787:139513. http://doi.org/10.1016/j.msea.2020.139513
12. Li L., Niu X., Han B., Song L., Li X. Microstructure and properties of laser cladding coating at the end of L415/316L bimetal composite pipe. *International Journal of Pressure Vessels and Piping*. 2022;195:104568. https://doi.org/10.1016/j.ijpvp.2021.104568
13. Chen N., Ali Khan H., Wan Z., Lippert J., Sun H., Shang S.-L., Liu Z.-K., Li J. Microstructural characteristics and crack formation in additively manufactured bimetal material of 316L stainless steel and Inconel 625. *Additive Manufacturing*. 2020;32:101037. https://doi.org/10.1016/j.addma.2020.101037
14. Li Z., Zhao J., Jia F., Lu Y., Liang X., Yuan X., Jiao S., Zhou C., Jiang Z. Hot deformation behaviour and interfacial characteristics of bimetal composite at elevated temperatures. *Intermetallics*. 2020;125:106893. http://doi.org/10.1016/j.intermet.2020.106893
15. Li Z., Zhao J., Jia F., Lu Y., Zhang Q., Jiao S., Jiang Z. Analysis of flow behaviour and strain partitioning mechanism of bimetal composite under hot tensile conditions. *International Journal of Mechanical Sciences*. 2020;169:105317. https://doi.org/10.1016/j.ijmecsci.2019.105317
16. Fudzii T., Dzako M. *Mechanics of Composite Materials Destruction*. Moscow: Mir, 1982:232. (In Russ.).

   Фудзии Т., Дзако М. *Механика разрушения композиционных материалов*. Москва: Мир: 1982:232.
17. Biryukov V., Tatarkin D., Khriptovich E., Fishkov A. Development of technologies and equipment for laser strengthening and melting of mills and machine parts. *Stankoinstrument*. 2017;9:42–47. (In Russ.). http://dx.doi.org/10.22184/24999407.2017.9.4.42.47

   Бирюков В., Татаркин Д., Хриптович Е., Фишков А. Разработка технологий и оборудования для лазерного упрочнения и наплавки деталей станков и машин. *Станкоинструмент*. 2017;009(4):42–47. http://dx.doi.org/10.22184/24999407.2017.9.4.42.47
18. Bandyopadhyay A., Heer B. Additive manufacturing of multi-material structures. *Materials Science and Engineering: R: Reports*. 2018;129:1–16. https://doi.org/10.1016/j.mser.2018.04.001
19. Xi W., Song B., Zhao Y., Yu T., Wang J. Geometry and dilution rate analysis and prediction of laser cladding. *The International Journal of Advanced Manufacturing Technology*. 2019;103: 4695–4702. https://doi.org/10.1007/s00170-019-03932-7
20. Kwiecień M., Kopyściański M., Błoniarz R., Muszka K., Majta J. Influence of deformation conditions on the inhomogeneity of plastic flow of structurally graded bimetal systems. *Procedia Manufacturing*. 2018;15:1649–1655. https://doi.org/10.1016/j.promfg.2018.07.272
21. Barannikova S.A., Kosinov D.A., Zuev L.B., Gromov V.E., Konovalov S.V. Hydrogen effect on macrolocalization of plastic deformation of low carbon steel. *Izvestiya. Ferrous Metallurgy*. 2016;59(12):891–895. (In Russ.). https://doi.org/10.17073/0368-0797-2016-12-891-895

   Баранникова С.А., Косинов Д.А., Зуев Л.Б., Громов В.Е., Коновалов С.В. Влияние водорода на макролокализацию пластической деформации низкоуглеродистой стали. *Известия вузов. Черная металлургия*. 2016;59(12):891–895. https://doi.org/10.17073/0368-0797-2016-12-891-895

22. Danilov V.I., Barannikova S.A., Zuev L.B. Autowaves of localized deformation at initial stages of plastic flow of single crystals. *Zhurnal tekhnicheskoi fiziki*. 2003;73(11): 69–75. (In Russ.).

Данилов В.И., Баранникова С.А., Зуев Л.Б. Автоволны локализованной деформации на начальных стадиях пластического течения монокристаллов. *Журнал технической физики*. 2003;73(11):69–75.

23. Barannikova S.A., Li Yu.V. Development kinetics of the plastic wave front at the metal interface. *Russian Physics Journal*. 2020;63(5):731–737.
https://doi.org/10.1007/s11182-020-02091-7

Баранникова С.А., Ли Ю.В. Кинетика развития фронтов пластического течения на границе раздела металлов. *Известия вузов. Физика*. 2020;63(5):19–24.
https://doi.org/10.17223/00213411/63/5/19

24. Mendenhall W.M., Sincich T.L. *Statistics for Engineering and the Sciences*. New York: Chapman and Hall/CRC; 2016:1182.
https://doi.org/10.1201/b19628

25. Barenblatt G.I. The mathematical theory of equilibrium cracks in brittle fracture. *Advances in Applied Mechanics*. 1962;7:55–129.
https://doi.org/10.1016/S0065-2156(08)70121-2

Information about the Authors / Сведения об авторах

Svetlana P. Buyakova, *Dr. Sci. (Eng.), Chief Researcher, Head of the Laboratory of Physical Mesomechanics and Non-Destructive Testing,* Institute of Strength Physics and Materials Science, Siberian Branch of the Russian Academy of Sciences
ORCID: 0000-0002-6315-2541
E-mail: sbuyakova@ispms.ru

Konstantin N. Kayurov, *General Director,* Scientific Production Enterprise of Geophysical Equipment "LUCH"
ORCID: 0000-0001-9545-5400
E-mail: kayurov@looch.ru

Svetlana A. Barannikova, *Dr. Sci. (Phys.–Math.), Leading Researcher of the Laboratory of Strength Physics,* Institute of Strength Physics and Materials Science, Siberian Branch of the Russian Academy of Sciences
ORCID: 0000-0001-5010-9969
E-mail: bsa@ispms.ru

Светлана Петровна Буякова, *д.т.н., главный научный сотрудник, заведующий лабораторией физической мезомеханики и неразрушающих методов контроля,* Институт физики прочности и материаловедения Сибирского отделения РАН
ORCID: 0000-0002-6315-2541
E-mail: sbuyakova@ispms.ru

Константин Николаевич Каюров, *генеральный директор,* Научно-производственное предприятие геофизической аппаратуры «ЛУЧ»
ORCID: 0000-0001-9545-5400
E-mail: kayurov@looch.ru

Светлана Александровна Баранникова, *д.ф.-м.н., ведущий научный сотрудник лаборатории физики прочности,* Институт физики прочности и материаловедения Сибирского отделения РАН
ORCID: 0000-0001-5010-9969
E-mail: bsa@ispms.ru

Contribution of the Authors / Вклад авторов

S. P. Buyakova – formulation of the concept, literary review, analysis of the results.
K. N. Kayurov – selection of laser cladding modes, discussion of the results.
S. A. Barannikova – conducting studies of mechanical characteristics and localization of deformation, discussion of the results, writing the text.

С. П. Буякова – формулирование концепции работы, обзор литературы, анализ результатов.
К. Н. Каюров – подбор режимов лазерной наплавки, обсуждение результатов.
С. А. Баранникова – проведение исследований механических характеристик и локализации деформации, обсуждение результатов, написание текста статьи.

Received 09.03.2023
Revised 20.04.2023
Accepted 10.05.2023

Поступила в редакцию 09.03.2023
После доработки 20.04.2023
Принята к публикации 10.05.2023

Materials science / Материаловедение

UDC 536.425:539.25:539.351
DOI 10.17073/0368-0797-2023-5-587-593

Original article
Оригинальная статья

Formation of the gradient of structural-phase states of high-speed steel during surfacing. Part 1. Solving the Stefan problem with two movable boundaries

S. A. Nevskii[1], L. P. Bashchenko[1], O. A. Peregudov[2]

[1] **Siberian State Industrial University** (42 Kirova Str., Novokuznetsk, Kemerovo Region – Kuzbass 654007, Russian Federation)
[2] **Omsk State Technical University** (11 Mira Ave., Omsk 644050, Russian Federation)

nevskiy.sergei@yandex.ru

Abstract. The article considers theoretical study of solidification of the binary iron–tungsten system at a tungsten content of 18 wt. %. Such tungsten content is typical for heat-resistant alloys used in plasma-arc surfacing on the rolls surface. The axisymmetric Stefan thermal problem is solved for two movable cylindrical boundaries that separate three regions. In region *1*, the melt is at the melting point; in region *2*, the substance is in a two–phase state, and in region *3* – a solid. The liquidus temperature was set at the interface of regions *1* and *2*, and the solidus temperature – at the interface of regions *2* and *3*. At these boundaries, a condition for the heat flows balance was given, from which a system of kinetic equations was obtained. This system was solved by numerical methods, without hypothesizing that the fronts of phase transformations move according to the law $R \sim t^{1/2}$. Solution of the system of kinetic equations shows that the solidus boundary moves almost linearly. The liquidus boundary moves according to the parabolic law. For regions of the micrometer range in size, the processes of phase transformations take place in a time of about 5 ns, whereas for regions of the order of 10 μm in size – in a time of about 50 ms. Dependences of temperature fields on the radial coordinate at various points in time show that with increasing time, the dimensions of region *2* decrease, and as soon as coordinates of the liquidus and solidus boundaries become close, thecrystallization process stops. Further development of the model consists in taking into account the rotation of one of the media. The results obtained will serve as a material for the study of the Mullins-Sekerka two-front instability.

Keywords: iron – tungsten system, the Stefan problem, equation of thermal conductivity, moving boundaries of phase transformations

Acknowledgements: The research was supported by the Russian Science Foundation (grant No. 23-19-00186, https://rscf.ru/project/23-19-00186).

For citation: Nevskii S.A., Bashchenko L.P., Peregudov O.A. Formation of the gradient of structural-phase states of high-speed steel during surfacing. Part 1. Solving the Stefan problem with two movable boundaries. *Izvestiya. Ferrous Metallurgy*. 2023;66(5):587–593.
https://doi.org/10.17073/0368-0797-2023-5-587-593

Формирование градиента структурно-фазовых состояний быстрорежущей стали при наплавке. Часть 1. Решение задачи Стефана с двумя подвижными границами

С. А. Невский[1], Л. П. Бащенко[1], О. А. Перегудов[2]

[1] **Сибирский государственный индустриальный университет** (Россия, 654007, Кемеровская обл. – Кузбасс, Новокузнецк, ул. Кирова, 42)
[2] **Омский государственный технический университет** (Россия, 644050, Омск, пр. Мира, 11)

nevskiy.sergei@yandex.ru

Аннотация. Теоретически рассматривается процесс затвердевания бинарной системы железо – вольфрам при содержании вольфрама 18 % (по массе). Такое содержание вольфрама характерно для теплостойкого сплава, который применяется в процессах плазменно-дуговой наплавки на поверхность валков. Решается осесимметричная тепловая задача Стефана для двух подвижных цилиндрических границ, которые разделяют три области. В области *1* расплав находится при температуре плавления, в области *2* вещество находится в двухфазном состоянии, а в области *3* – твердое тело. На границе раздела областей *1* и *2* задается температура ликвидуса, а на границе раздела *2* и *3* –

температура солидуса. На данных границах задается условие баланса тепловых потоков, из которого получена система кинетических уравнений. Эту систему решали численными методами, при этом не выдвигались гипотезы о том, что фронты фазовых превращений движутся по закону $R \sim t^{1/2}$. Решение системы кинетических уравнений показывает, что граница солидуса движется практически по линейному закону. Граница ликвидуса перемещается по параболическому закону. Для областей микрометрового диапазона по размерам процессы фазовых превращений протекают за время порядка 5 нс, тогда как для областей размерами порядка 10 мкм – за время около 50 мкс. Зависимости температурных полей от радиальной координаты в различные моменты времени показывают, что с увеличением времени размеры области *2* уменьшаются, и, как только значения координат границ ликвидуса и солидуса становятся близкими, процесс кристаллизации останавливается. Дальнейшее развитие модели заключается в учете вращения одной из сред. Полученные результаты послужат материалом для исследования двухфронтовой неустойчивости Маллинза-Секерки.

Ключевые слова: система железо – вольфрам, задача Стефана, уравнение теплопроводности, подвижные границы фазовых превращений

Благодарности: Исследование выполнено при финансовой поддержке Российского научного фонда (грант № 23-19-00186), https://rscf.ru/project/23-19-00186).

Для цитирования: Невский С.А., Бащенко Л.П., Перегудов О.А. Формирование градиента структурно-фазовых состояний быстрорежущей стали при наплавке. Часть 1. Решение задачи Стефана с двумя подвижными границами. *Известия вузов. Черная металлургия*. 2023;66(5):587–593. *https://doi.org/10.17073/0368-0797-2023-5-587-593*

Introduction

The methods involving plasma surfacing of different wear-resistant materials are commonly employed for the restoration or repair of forming rolls [1]. Among the surfacing materials, there is a specific interest in heat-resistant iron-based alloys with elevated tungsten levels (approximately 17 – 18 %) and carbon content (0.76 – 0.82 %), renowned for their high hardness and exceptional wear resistance [2]. To prevent the formation of cold cracks during the application of coatings made from such alloys, pre-heating and controlled slow cooling of the parts are utilized [3]. However, post this treatment, the coatings exhibit reduced hardness and wear resistance. A complex heat treatment process (involving annealing, hardening, and tempering) becomes necessary to enhance these properties. Yet, this significantly restricts the potential applications of these considered alloys [4]. Hence, finding plasma surfacing methods for heat-resistant alloys that circumvent crack formation while preserving high mechanical and tribological properties without the need for additional thermal treatments is crucial. Addressing this challenge requires an understanding of the mechanisms governing the formation of gradient structural-phase states in materials during surfacing. The crystallization processes of the materials play a pivotal role in shaping these states [5], ultimately determining the resulting structure and hence, the mechanical properties achieved during the surfacing process.

Currently, numerous papers [5 – 10] expound upon mechanisms and models pertaining to the crystallization of materials on surfaces of various geometries. Depending on the external factors such as cooling rate, rotation speed, ambient temperature, degree of supercooling, among others, the resulting structure can manifest as cellular, dendritic, or a combination of both structures concurrently [5; 6]. One of the main mechanisms driving their formation, as proposed in [7; 8], involves the instability of the crystallization front induced by the temperature decrease during the phase transition, caused by the expulsion of impurities into the melt and the phenomenon of solutal undercooling. Hence, the configuration of the interfacial boundary significantly influences the impurity distribution within the crystal [9]. The central consensus across all theories of morphological stability is that when a specific balance between temperature and concentration gradients is reached, the crystallization front becomes unstable to minor perturbations [10]. Consequently, intricate structural-phase states emerge, facilitating particle nucleation on dissolved impurities. This leads to the creation of an extended phase transition region preceding the crystallization front [11]. Notably, the models outlined in [5 – 11] solely consider the displacement of phase transition boundaries, disregarding the displacement of melt heating boundaries. Typically, it is assumed that this boundary either maintains a stabilized temperature distribution or extends infinitely [12; 13]. Recognizing the outcomes of resolving the thermal problem, where the heating boundary is not considered infinitely large [14], reveals that the growth rate of particles accelerates in comparison to scenarios where this aspect is disregarded. Consequently, in the development of mathematical models concerning the impact of plasma on material structure, it becomes imperative to consider not only the displacement of phase transition boundaries but also the shifting boundaries of heating. In the quest to understand the mechanisms governing the formation of gradient structures and phase compositions in heat-resistant alloys during plasma surfacing on rotating rolls, integrating the concepts associated with the emergence and progression of the Mullins–Sekerka instability [15] becomes crucial. Analyzing this instability aids in determining the conditions for the onset of these states, taking into consideration the shifts in the heating boundary. This instability is studied through several stages: initially determining the nature of interface perturbations and evaluating the impact of its curvature on the liquidus temperature. Subsequently, calculations are performed for the temperature and concentration fields within

the solid and liquid phases. This analysis includes identifying the dependency of the perturbation growth rate on the conditions existing at the phase transition boundary.

The focal point of this paper revolves around resolving the thermal and diffusion Stefan problem involving two movable boundaries. This approach facilitates the monitoring of material solidification kinetics. Unlike conventional studies [16 – 18] that rely on the assumption of crystal growth being directly proportional to $t^{1/2}$ this hypothesis is deliberately avoided in this investigation. Instead, the evolution of crystal growth over time is tracked by solving a system of kinetic equations derived from temperature and substance balance conditions at the phase transition boundaries.

Research methodology (setting up a problem)

Let us examine the process of directional solidification along the spatial axis r in a cylindrical front. Fig. 1 illustrates the geometry of the problem.

The initial phase occupies the region $R_2(t) < r < +\infty$ (where t represents time) and maintains a temperature of T_0. When the temperature T^{**} is attained, the second phase forms, which occupies the region $R_1(t) < r < R_2(t)$. At temperature T^*, the third phase emerges within the region $0 < r < R_1(t)$. Let us formulate the thermal conductivity equation for each of these distinct regions:

$$\begin{gathered}\frac{\partial T_1}{\partial t} = \chi_1\left[\frac{1}{r}\frac{\partial}{\partial r}\left(r\frac{\partial T_1}{\partial r}\right)\right],\ R_2(t) < r < +\infty;\\ \frac{\partial T_2}{\partial t} = \chi_2\left[\frac{1}{r}\frac{\partial}{\partial r}\left(r\frac{\partial T_2}{\partial r}\right)\right],\ R_1(t) < r < R_2(t);\\ \frac{\partial T_3}{\partial t} = \chi_3\left[\frac{1}{r}\frac{\partial}{\partial r}\left(r\frac{\partial T_3}{\partial r}\right)\right],\ 0 < r < R_1(t),\end{gathered} \tag{1}$$

where χ_1 and χ_2, χ_3 are thermal diffusivity coefficients in regions *1 – 3*.

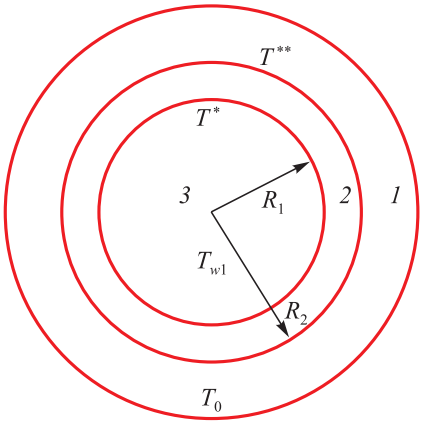

Fig. 1. Diagram of the problem geometry

Рис. 1. Схема геометрии задачи

The shift in phase transition boundaries is determined based on the balance conditions of temperature and heat flows, as expressed by equations (2):

$$\begin{gathered}T_3 = T_2 = T^*,\ r = R_1(t);\\ -\lambda_3\frac{\partial T_3}{\partial r} + \lambda_2\frac{\partial T_2}{\partial r} = \Delta H_1\frac{dR_1}{dt},\ r = R_1(t);\\ T_2 = T_1 = T^{**},\ r = R_2(t);\\ \lambda_1\frac{\partial T_1}{\partial r} - \lambda_2\frac{\partial T_2}{\partial r} = \Delta H_2\frac{dR_2}{dt},\ r = R_2(t),\end{gathered} \tag{2}$$

where λ_1 and λ_2, λ_3 are thermal conductivity coefficients in the regions *1 – 3*; ΔH_1 and ΔH_2 represent the volumetric heat of phase transformations.

At $r \to 0$, the temperature is T_{w1}, and at $r \to \infty$, the temperature is T_0. The initial conditions are defined as

$$T_2(r,\ 0) = T_0;\ R_1(0) = R_0;\ R_2(0) = R_0^*, \tag{3}$$

where R_0 and R_0^* are the initial radii of the phase transition boundaries.

The solution of this system of equations (1) – (3) is determined as follows

$$T_i(r,\ t) = A_i + B_i E_i\left(\frac{r^2}{4\chi_i t}\right), \tag{4}$$

where A_i, B_i are arbitrary constants; $E_i(z)$ is an integral exponent; $i = 1 \div 3$.

Applying the boundary conditions (2) and initial conditions (3) to formula (4), the resulting solution is as follows:

$$\begin{gathered}T_1(r,\ t) = T_0 - \left(T_0 - T^{**}\right)\frac{E_i\left(\frac{r^2}{4\chi_1 t}\right)}{E_i\left(\frac{R_2^2}{4\chi_1 t}\right)},\\ R_2(t) < r < +\infty;\\ T_2(r,\ t) = \left[T^{**}E_i\left(\frac{R_1^2}{4\chi_2 t}\right) - T^*E_i\left(\frac{R_2^2}{4\chi_2 t}\right) + \left(T^* - T^{**}\right)\times\right.\\ \left.\times E_i\left(\frac{r^2}{4\chi_2 t}\right)\right]\Big/\left[E_i\left(\frac{R_1}{4\chi_2 t}\right) - E_i\left(\frac{R_2}{4\chi_2 t}\right)\right],\\ R_1(t) < r < R_2(t);\\ T_3(r,\ t) = \left[T^*E_i\left(\frac{R^2}{4\chi_3 t}\right) - T_{w1}E_i\left(\frac{R_1^2}{4\chi_3 t}\right) - \left(T^* - T_{w1}\right)\times\right.\\ \left.\times E_i\left(\frac{r^2}{4\chi_3 t}\right)\right]\Big/\left[E_i\left(\frac{R^2}{4\chi_3 t}\right) - E_i\left(\frac{R_1^2}{4\chi_3 t}\right)\right],\\ 0 < r < R_1(t).\end{gathered} \tag{5}$$

The parameter R, introduced to prevent divergence at $r \to 0$, is assigned a value of 10^{-8} m to eliminate the singularity at this point in the radial coordinate.

Results and discussion

As equation (5) is integrated into the heat balance equations at the boundaries of phase transitions, the resulting kinetic equations are as follows:

$$\frac{dR_1}{dt} = \frac{\left[F_1 \exp\left(-\frac{R_1^2}{4\chi_1 t}\right)\right] - \left[F_2 \exp\left(-\frac{R_1^2}{4\chi_3 t}\right)\right]}{R_1\left[E_i\left(\frac{R_1^2}{4\chi_2 t}\right) - E_i\left(\frac{R_2^2}{4\chi_2 t}\right)\right]};$$

$$\frac{dR_2}{dt} = \frac{G_1 \exp\left(-\frac{R_2^2}{4\chi_2 t}\right)}{R_2\left[E_i\left(\frac{R_1^2}{4\chi_2 t}\right) - E_i\left(\frac{R_2^2}{4\chi_2 t}\right)\right]} - \frac{G_2 \exp\left(-\frac{R_2^2}{4\chi_1 t}\right)}{R_2\left[E_i\left(\frac{R_2^2}{4\chi_1 t}\right)\right]}; \quad (6)$$

$$F_1 = \frac{2\left(T^{**} - T^*\right)\lambda_2}{\Delta H_1}; \; F_2 = \frac{2\left(T^* - T_{w1}\right)\lambda_3}{\Delta H_1};$$

$$G_1 = \frac{2\left(T^* - T^{**}\right)\lambda_2}{\Delta H_2}; \; G_2 = \frac{2\left(T_0 - T^{**}\right)\lambda_1}{\Delta H_2}.$$

The system (6) of ordinary differential equations is resolved using the high-order Runge-Kutta method. To simplify the mathematical computations, non-dimensional variables $\tilde{R}_i = \frac{R}{R_0}$ and $\tau = t\frac{\chi_1}{R_0^2}$ (where τ is nondimensional time) were employed. Given that as at $t \to 0$, the function $E_i \frac{R_i^2}{4\chi t} \to 0$, the initial time value was set to 10^{-9} s. The characteristics of the investigated material, specifically, iron – tungsten system, are outlined in the table provided.

Characteristics of the iron – tungsten system

Характеристики системы железо – вольфрам

Material characteristics	Designation	Value
Melt temperature, K	T_{w1}	1811
Specific heat of fusion, kJ/kg	ΔH	270
Density, kg/m^3	ρ_1	6980
Thermal conductivity of material, W/(m·K)		
in region *1*	λ_1	39
in region *2*	λ_2	35
in region *3*	λ_3	35
Thermal diffusivity of material, m^2/s		
in region *1*	χ_1	$6.8 \cdot 10^{-6}$
in region *2*	χ_2	$6.9 \cdot 10^{-6}$
in region *3*	χ_3	$6.9 \cdot 10^{-6}$

In region *1*, the initial melt temperature was set at $T_0 = 1811$ K. At the R_2 boundary, the liquidus temperature T^{**} is 1806 K, while at the R_1 boundary, the solidus temperature T^* is 1803 K. These temperatures were determined based on the state diagram [19] for an 18 wt. % tungsten content. The temperature T_{w1} was assumed to be lower than T^* and measured at 1790 K. It was considered that $\chi_2 = \chi_3$ and $\lambda_2 = \lambda_3$, along with $\Delta H_1 = \Delta H_2$. Fig. 2 displays the dependencies of the interface movements. At $R_0 = 1$ μm, the boundary coordinate R_1 exhibits nearly linear growth until $\tau = 0.028$ (4.4118 ns), while R_2 demonstrates non-monotonic changes, decreasing after $\tau > 0.028$ (4.4118 ns). For $R_0 = 10$ μm, a similar trend is observed yet the crystallization process takes place over a longer duration of 41.176 μs.

The results suggest that with a reduction in the size of nuclei, the duration of their steady growth significantly decreases by almost four orders of magnitude. The abrupt decline in the radial coordinate R_2 may indicate instability in the crystallization front, potentially due to interfacial surface tension and supercooling effects. The rapidity of the crystallization process in smaller regions is attributed to a high surface energy, which aims to decrease through size growth and interface configuration changes. In Fig. 3, the temperature dependencies plotted against the non-dimensional radial coordinate illustrate a notable trend: as time progresses, region *2* demonstrates a reduction in size (represented by curves *2* and *3*), while conversely, region *3*, displays growth.

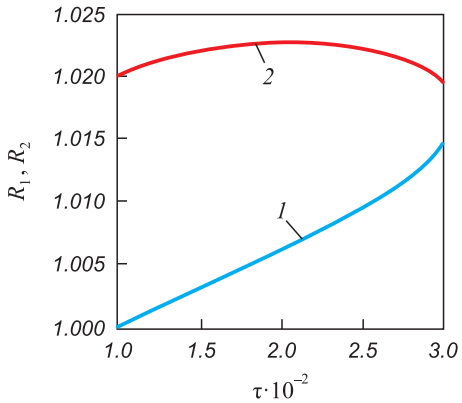

Fig. 2. Dependences of radial coordinates of crystallization front on time at $T_{w1} = 1790$ K, $T^* = 1803$ K, $T^{**} = 1806$ K, $T_0 = 1811$ K, $R_0 = 1$ μm:
1 – boundary of transition between phases *1* and *2*;
2 – boundary of transition between phases *2* and *3*

Рис. 2. Зависимости радиальных координат фронта кристаллизации от времени при $T_{w1} = 1790$ K, $T^* = 1803$ K, $T^{**} = 1806$ K, $T_0 = 1811$ K, $R_0 = 1$ мкм:
1 – граница перехода между фазами *1* и *2*;
2 – граница перехода между фазами *2* и *3*

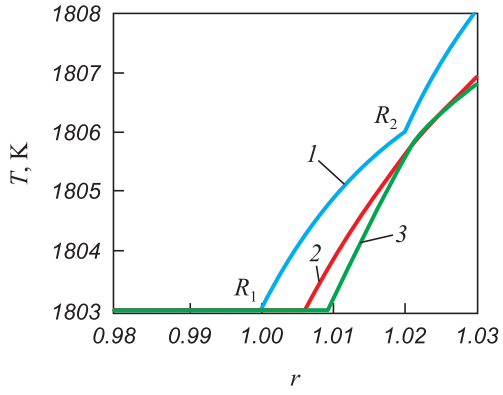

Fig. 3. Temperature dependences on the coordinate at different time points at T_{w1} = 1790 K, T^* = 1803 K, T^{**} = 1806 K, T_0 = 1811 K, R_0 = 1 μm: *1* – τ = 0.01; *2* – τ = 0.02; *3* – τ = 0.025

Рис. 3. Зависимости температуры от координаты в различные моменты времени при T_{w1} = 1790 K, T^* = 1803 K, T^{**} = 1806 K, T_0 = 1811 K, R_0 = 1 мкм: *1* – τ = 0,01; *2* – τ = 0,02; *3* – τ = 0,025

In the scenario where T_0 = 1790 K, T^{**} = 1803 K, T^* = 1803 K and T_{w1} = 1811 K (Fig. 4). The coordinates of the phase transition boundaries exhibit a reduction (Fig. 4, *a*), with R_1 decreasing linearly while R_2 follows a parabolic trajectory. Temperature dependences (Fig. 4, *b*) indicate a similar trend to the previous case, wherein regions *2* and *3* (curves *2* and *3*) experience a decrease in size.

Conclusions

The theoretical investigation of the crystallization process within the iron – tungsten system, conducted by solving kinetic equations, revealed intriguing behavior. Specifically, it was observed that the movement of the liquidus boundary R_2 follows a descending parabolic trajectory, contrary to the expected $R \sim t^{1/2}$ law, whereas the solidus boundary R_1 exhibits almost linear movement. Upon reaching a certain time threshold, the convergence of these boundaries occurs, indicating either the cessation of the crystallization process or the onset of crystallization front instability. The temperature dependencies derived from this study will serve as a foundational framework for further exploration of this observed instability. As the model progresses and adapts to simulate the plasma-arc surfacing process of rolls, future iterations will consider factors such as the rotation of one of the media involved and a more precise incorporation of the concentration of alloying elements.

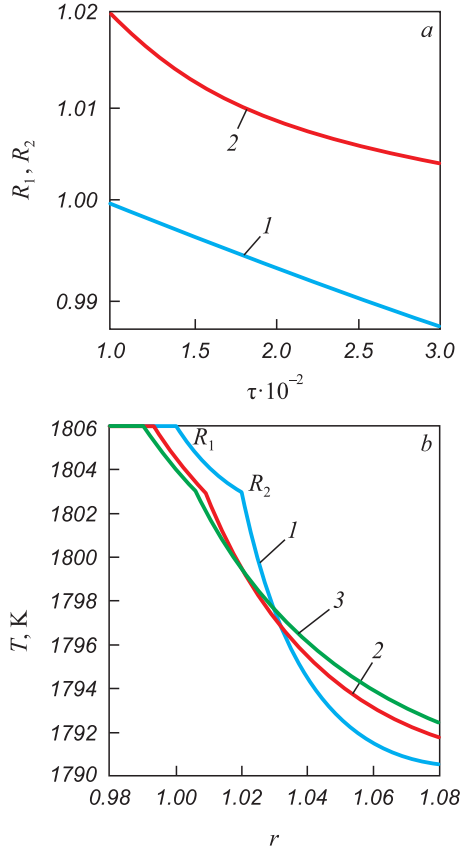

Fig. 4. Calculation results for T_{w1} = 1811 K, T^* = 1806 K, T^{**} = 1803 K, T_0 = 1790 K, R_0 = 1 μm: *a* – dependences of the radial coordinates of the crystallization front on time (*1* – boundary of transition between phases *1* and *2*; *2* – boundary of transition between phases *2* and *3*); *b* – temperature dependences on the coordinate at different time (*1* – τ = 0.01; *2* – τ = 0.02; *3* – τ = 0.025)

Рис. 4. Результаты вычислений при T_{w1} = 1811 K, T^* = 1806 K, T^{**} = 1803 K, T_0 = 1790 K, R_0 = 1 мкм: *a* – зависимости радиальных координат фронта кристаллизации от времени (*1* – граница перехода между фазами *1* и *2*; *2* – граница перехода между фазами *2* и *3*); *b* – зависимости температуры от координаты в различные моменты времени (*1* – τ = 0,01; *2* – τ = 0,02; *3* – τ = 0,025)

References / Список литературы

1. Sosnin N.A., Ermakov S.A., Topolyanskii P.A. *Plasma Technologies. A Guide for Engineers*. SPb.: izd. Politekhnicheskogo un-ta; 2013;406. (In Russ.).
Соснин Н.А., Ермаков С.А., Тополянский П.А. *Плазменные технологии. Руководство для инженеров*. СПб.: изд. Политехнического ун-та; 2013;406.
2. Damon J., Schüßler P., Mühl F., Dietrich S., Schulze V. Short-time induction heat treatment of high speed steel AISI M2: Laboratory proof of concept and application-related component tests. *Materials & Design*. 2023;230:111991. https://doi.org/10.1016/j.matdes.2023.111991
3. Park G.-W., Shin S., Kim J.-Y., Koo Y.-M., Lee W., Lee K.-A., Park S.S., Jeon J.B. Analysis of solidification microstructure and cracking mechanism of a matrix high-speed steel deposited using directed-energy deposition. *Journal of Alloys and Compounds*. 2022;907:164523. https://doi.org/10.1016/j.jallcom.2022.164523
4. Malushin N.N., Romanov D.A., Kovalev A.P., Osetkovskii V.L., Bashchenko L.P. Structural-phase state of a heat-resistant alloy of high hardness formed by plasma surfacing in nitrogen medium and high-temperature tempering. *Izvestiya*

vuzov. Fizika. 2019;62(10(742)):106–111. (In Russ.).
https://doi.org/10.17223/00213411/62/10/106

Малушин Н.Н., Романов Д.А., Ковалев А.П., Осетковский В.Л., Бащенко Л.П. Структурно-фазовое состояние теплостойкого сплава высокой твердости, сформированного плазменной наплавкой в среде азота и высокотемпературным отпуском. *Известия вузов. Физика*. 2019;62(10(742)):106–111.
https://doi.org/10.17223/00213411/62/10/106

5. Aleksandrov D.V., Aleksandrova I.V., Ivanov A.A., Malygin A.P., Nizovtseva I.G. Nonlinear analysis of the stability of solidification with a mushy zone. *Russian Metallurgy (Metally)*. 2014;2014(8):606–617.
https://doi.org/10.1134/S0036029514080035

Александров Д.В., Александрова И.В., Иванов А.А., Малыгин А.П., Низовцева И.Г. Нелинейный анализ устойчивости затвердевания с областью фазового перехода. *Расплавы*. 2014;(2)27–40.

6. Aleksandrov D.V., Aleksandrova I.V., Ivanov A.A., Starodumov I.O., Toropova L.V. Directional solidification with a two-phase zone taking into account the dependence of liquid phase density on temperature and impurity concentration. *Rasplavy*. 2020;(1):37–45. (In Russ.).
https://doi.org/10.31857/S0235010620010028

Александров Д.В., Александрова И.В., Иванов А.А., Стародумов И.О., Торопова Л.В. Направленное затвердевание с двухфазной зоной с учетом зависимости плотности жидкой фазы от температуры и концентрации примеси. *Расплавы*. 2020;(1):37–45.
https://doi.org/10.31857/S0235010620010028

7. Alexandrov D.V., Toropova L.V. The role of incoming flow on crystallization of undercooled liquids with a two-phase layer. *Scientific Reports*. 2022;12:17857.
https://doi.org/10.1038/s41598-022-22786-w

8. Worster M.G. Natural convection in a mushy layer. *Journal of Fluid Mechanics*. 1991;224:335–359.
https://doi.org/10.1017/S0022112091001787

9. Lahiri A., Choudhury A. Theoretical and numerical investigation of diffusive instabilities in multicomponent alloys. *Journal of Crystal Growth*. 2017;459:1–12.
http://dx.doi.org/10.1016/j.jcrysgro.2016.11.046

10. Sekerka R.F. Morphological stability. *Journal of Crystal Growth*. 1968;3-4:71–81.
https://doi.org/10.1016/0022-0248(68)90102-4

11. Alexandrov D.V. Solidification with a quasiequilibrium mushy region: exact analytical solution of nonlinear model. *Journal of Crystal Growth*. 2001;222(4):816–821.
https://doi.org/10.1016/S0022-0248(00)00960-X

12. Elsaid A., Helal S.M. Moving Taylor series for solving one-dimensional one-phase Stefan problem. *Alexandria Engineering Journal*. 2022;61(9):7121–7128.
https://doi.org/10.1016/j.aej.2021.12.055

13. Lykov A.V. *Theory of Thermal Conductivity*. Moscow: Vysshaya shkola; 1967;599. (In Russ.).

Лыков А.В. *Теория теплопроводности*. Москва: Высшая школа; 1967;599.

14. Sergeev S.A. Mathematical modeling of unsteady thermal conductivity of spherical particle crystallization in a melt with moving boundaries. *Issledovano v Rossii*. 2003;(6):664–672.

Сергеев С.А. Математическое моделирование нестационарной теплопроводности кристаллизации частицы сферической формы в расплаве с движущимися границами. *Исследовано в России*. 2003;6:664–672.

15. Chen M.W., Wang Z.D. The evolution and morphological stability of a particle in a binary alloy melt. *Journal of Crystal Growth*. 2023;607:127113.
https://doi.org/10.1016/j.jcrysgro.2023.127113

16. Formalev V.F., Rabinskii L.N. On a Stefan-type problem with two unsteadily moving boundaries of phase transformations. *Izvestiya RAN. Energetika*. 2014;(4):74–81. (In Russ.).

Формалев В.Ф., Рабинский Л.Н. О задаче типа Стефана с двумя нестационарно подвижными границами фазовых превращений. *Известия РАН. Энергетика*. 2014;(4):74–81.

17. Kartashov E.M. Analytical methods for solving boundary value problems of unsteady thermal conductivity in regions with moving boundaries. *Engineering and Physics Journal*. 2001;74(2):171–195.

Карташов Э.М. Аналитические методы решения краевых задач нестационарной теплопроводности в областях с движущимися границами. *Инженерно-физический журнал*. 2001;74(2):171–195.

18. Carslaw H.S., Jaeger J.C. *Conduction of Heat in Solids*. London: Oxford University Press; 1947.

Карслоу Г., Егер Д. *Теплопроводность твердых тел*. Москва: Наука; 1964;488.

19. Lyakishev N.P. *State Diagrams of Double Metal Systems*. In 3 vols. Vol. 2. Moscow: Mashinostroenie; 1997;1024. (In Russ.).

Лякишев Н.П. *Диаграммы состояния двойных металлических систем*. В 3 т. Т. 2. Москва: Машиностроение; 1997;1024.

20. Chen M.-W., Wang Y., Guo H. The effect of anisotropic surface tension on interfacial evolution of a particle in the binary alloy melt. *Journal of Crystal Growth*. 2019;510:32–39.
https://doi.org/10.1016/j.jcrysgro.2018.12.032

Information about the Authors | Сведения об авторах

Sergei A. Nevskii, *Dr. Sci. (Eng.), Assist. Prof. of the Chair of Natural Sciences named after Professor V.M. Finkel,* Siberian State Industrial University
ORCID: 0000-0001-7032-9029
E-mail: nevskiy_sa@physics.sibsiu.ru

Lyudmila P. Bashchenko, *Cand. Sci. (Eng.), Assist. Prof. of the Chair "Thermal Power and Ecology",* Siberian State Industrial University
ORCID: 0000-0003-1878-909X
E-mail: luda.baschenko@gmail.com

Сергей Андреевич Невский, *д.т.н., доцент кафедры естественнонаучных дисциплин им. профессора В.М. Финкеля,* Сибирский государственный индустриальный университет
ORCID: 0000-0001-7032-9029
E-mail: nevskiy_sa@physics.sibsiu.ru

Людмила Петровна Бащенко, *к.т.н., доцент кафедры теплоэнергетики и экологии,* Сибирский государственный индустриальный университет
ORCID: 0000-0003-1878-909X
E-mail: luda.baschenko@gmail.com

Oleg A. Peregudov, *Cand. Sci. (Eng.), Vice-Rector for Youth Policy and Educational Activities,* Omsk State Technical University
ORCID: 0000-0001-5154-5498
E-mail: Olegomgtu@mail.ru

Олег Александрович Перегудов, *к.т.н., проректор по молодежной политике и воспитательной деятельности,* Омский государственный технический университет
ORCID: 0000-0001-5154-5498
E-mail: Olegomgtu@mail.ru

Contribution of the Authors / Вклад авторов

S. A. Nevskii – statement of the problem, development of a model of the section boundaries movement, discussion of the results.
L. P. Bashchenko – calculations, discussion of the results, design of the article.
O. A. Peregudov – discussion of the results, analysis of literary sources on the Stefan problem.

С. А. Невский – постановка задачи, разработка модели движения границ раздела, обсуждение результатов.
Л. П. Бащенко – проведение расчетов, обсуждение результатов, оформление статьи.
О. А. Перегудов – обсуждение результатов, анализ литературных источников по задаче Стефана.

Received 19.06.2023
Revised 27.06.2023
Accepted 28.06.2023

Поступила в редакцию 19.06.2023
После доработки 27.06.2023
Принята к публикации 28.06.2023

MATERIALS SCIENCE / МАТЕРИАЛОВЕДЕНИЕ

UDC 669.017:620.193.4
DOI 10.17073/0368-0797-2023-5-594-596

Short report
Краткое сообщение

On limited possibility of using Al_2O_3 and Al–Zn for corrosion protection of GdTbDyHoSc and GdTbDyHoY alloys in a salt mist chamber

B. R. Gel'chinskii[1], N. I. Il'inykh[1, 2] ✉, E. V. Ignat'eva[1]

[1] **Institute of Metallurgy, Ural Branch of the Russian Academy of Sciences** (101 Amundsena Str., Yekaterinburg 620016, Russian Federation)
[2] **South Ural State University** (76 Lenina Ave., Chelyabinsk 454080, Russian Federation)

✉ ninail@bk.ru

Abstract. Nowadays high-entropy alloys (HEAs) with a hexagonal close packed structure consisting of rare-earth metals (REM) are of particular interest. In this work, we investigated the possibility of using of Al_2O_3 and Al:Zn (1:1) as a protective coatings for REM HEAs GdTbDyHoSc and GdTbDyHoY. The REM HEAs samples were synthesized from metals of purity ≥99.9 % by melting in an electric arc furnace under Ar atmosphere (99.99 %). The samples were coated by supersonic plasma spraying. Corrosion resistance was determined in a salt mist chamber for 48 h. It was found that for all studied samples corrosive effect in conditions of salt mist leads to degradation of the base material of the alloy. Samples coated with Al:Zn (1:1) under salt mist conditions showed less resistance than samples coated with Al_2O_3 due to the chemical interaction between aluminum and sodium chloride solution.

Keywords: corrosion, protective coatings, corrosion resistance, limitation of use, high-entropy alloy (HEA), rare-earth metal (REM)

Acknowledgements: The work was supported by the Russian Science Foundation (grant No. 21-43-00015) using the equipment of the Center for Collective Use "Ural-M".

For citation: Gel'chinskii B.R., Il'inykh N.I., Ignat'eva E.V. On limited possibility of using Al_2O_3 and Al–Zn for corrosion protection of GdTbDyHoSc and GdTbDyHoY alloys in a salt mist chamber. *Izvestiya. Ferrous Metallurgy*. 2023;66(5):594–596. https://doi.org/10.17073/0368-0797-2023-5-594-596

Об ограниченной возможности использования Al_2O_3 и Al–Zn для защиты от коррозии в камере соляного тумана сплавов GdTbDyHoSc и GdTbDyHoY

Б. Р. Гельчинский[1], Н. И. Ильиных[1, 2] ✉, Е. В. Игнатьева[1]

[1] **Институт металлургии Уральского отделения РАН** (Россия, 620016, Екатеринбург, ул. Амундсена, 101)
[2] **Южно-Уральский государственный университет** (Россия, 454080, Челябинск, пр. Ленина, 76)

✉ ninail@bk.ru

Аннотация. В настоящее время особый интерес представляют высокоэнтропийные сплавы (ВЭС) с гексагональной плотноупакованной структурой, состоящие из редкоземельных (РЗМ) элементов. В работе проведено исследование возможности Al_2O_3 и Al:Zn (1:1) играть роль защитных покрытий для ВЭС РЗМ GdTbDyHoSc и GdTbDyHoY. Образцы ВЭС РЗМ синтезированы из металлов чистотой ≥99,9 % расплавлением в электродуговой печи в атмосфере Ar (99,99 %). Покрытия на образцы наносились методом сверхзвукового плазменного напыления. Коррозионную стойкость определяли в камере соляного тумана в течение 48 ч. Установлено, что для всех исследованных образцов коррозионное воздействие в условиях соляного тумана приводит к деградации основного материала сплава. Образцы с покрытием Al:Zn (1:1) в условиях соляного тумана показывают меньшую стойкость, чем образцы с покрытием из Al_2O_3 вследствие имеющего место химического взаимодействия между алюминием и раствором хлорида натрия.

Ключевые слова: коррозия, защитные покрытия, коррозионная стойкость, ограничение применения, ВЭС, РЗМ

Благодарности: Работа выполнена при поддержке Российского научного фонда (грант № 21-43-00015) с использованием оборудования ЦКП «Урал-М».

Для цитирования: Гельчинский Б.Р., Ильиных Н.И., Игнатьева Е.В. Об ограниченной возможности использования Al_2O_3 и Al–Zn для защиты от коррозии в камере соляного тумана сплавов GdTbDyHoSc и GdTbDyHoY. *Известия вузов. Черная металлургия*. 2023;66(5): 594–596. https://doi.org/10.17073/0368-0797-2023-5-594-596

The hypothesis regarding the potential formation of high-entropy alloys (HEA) featuring a hexagonal close-packed (HCP) structure comprising rare earth (RE) elements was initially proposed in [1]. Building upon this assumption, Japanese scientists [2] pioneered the development and production of equiatomic alloys such as YGdTbDyLu and GdTbDyTmLu, showcasing a singular-phase HCP structure. Subsequently, HoDyYGdTb HEAs were fabricated through arc melting [3]. Research indicates that these alloys also exhibit an HCP structure, showcasing macroscopic and microscopic homogeneity without peculiarities related to compositional changes, secondary phase separation, dendrite formation, and similar phenomena. Further investigations substantiated the HCP structure within these alloys [4]. In [5], the authors successfully synthesized multiple pure HCP REM (rare earth metal) alloys devoid of any second-phase, examining their mechanical properties and the reinforcing impact of the solid solution.

Rare-earth metals (REM) possess similar atomic sizes and crystal structures, enabling them to form homogeneous solid solutions. Despite garnering considerable interest within the scientific community, REM HEAs remain relatively understudied materials to date. It is postulated that by combining magnetic rare earth metals with non-magnetic elements like yttrium or scandium, each with distinct atomic radii, it becomes possible to create materials with varying densities of defects in their crystal structures. This approach allows for a comprehensive examination of the role played by the size factor in the structure formation of REM HEAs and their resulting functional characteristics.

These alloys exhibit high chemical reactivity, thus necessitating either a specialized working environment or additional surface protection against both chemical and, in certain cases, electrochemical corrosion.

The investigation aimed to explore the viability of using Al_2O_3 and Al:Zn (1:1) as protective coatings for HEA compositions comprising rare-earth metals like GdTbDyHoSc and GdTbDyHoY. The synthesis of samples involved melting metals with a purity level of ≥99.9 % in a Centorr Vacuum and Industries 5SA arc furnace within an Ar environment of 99.99 % [6]. To apply coatings onto the samples, supersonic plasma spraying methodology was employed [7]. Corrosion resistance tests were conducted in a Q-FOG, SSP60 salt mist chamber for 48 h.

Conclusions

It has been confirmed that exposure to salt mist conditions results in the degradation of the base material of the alloy across all examined samples. Findings indicate that when samples were coated with Al_2O_3 under salt mist conditions, the destructive process occurred through localized surface activation, leading to the formation of pitting corrosion. Interestingly, a substantial portion of the coating on the base material persisted concurrently. This occurrence can be attributed to the interaction between Al_2O_3 and the NaCl solution, enabling temporary protection of the rare-earth alloy under salt mist conditions, albeit for a limited duration. Samples coated with Al:Zn (1:1) demonstrated lower resistance compared to those coated with Al_2O_3 under salt mist conditions. This reduced resistance is attributable to the chemical interaction between aluminum and the sodium chloride solution, exacerbated by the considerable difference in the standard electrode potentials of the system components.

References / Список литературы

1. Zhang Y., Zuo T.T., Tang Z., Gao M.C., Dahmen K.A., Liaw P.K., Lu Z.P. Microstructures and properties of high-entropy alloys. *Progress in Materials Science*. 2014;61:1–93. https://doi.org/10.1016/j.pmatsci.2013.10.001
2. Takeuchi K., Amiya T., Wada K., Yubuta W., Zhang W. High-entropy alloys with a hexagonal close-packed structure designed by equi-atomic alloy strategy and binary phase diagrams. *JOM*. 2014;66:1984–1992. https://doi.org/10.1007/s11837-014-1085-x
3. Feuerbacher M., Heidelmann M., Thomas C. Hexagonal high-entropy alloys. *Materials Research Letters*. 2014;3(1):1–6. https://doi.org/10.1080/21663831.2014.951493
4. Lužnik J., Koželj P., Vrtnik S., Jelen A., Jagličić Z., Meden A., Feuerbacher M., Dolinšek J. Complex magnetism of Ho-Dy-Y-Gd-Tb hexagonal high-entropy alloy. *Physical Review B*. 2015;92:224201. https://doi.org/10.1103/PhysRevB.92.224201
5. Zhao Y.J., Qiao J.W., Ma S.G., Gao M.C., Yang H.J., Chen M.W., Zhang Y. A hexagonal close-packed high-entropy alloy: The effect of entropy. *Materials & Design*. 2016;96: 10–15. https://doi.org/10.1016/j.matdes.2016.01.149
6. Uporov S.A., Ehstemirova S.Kh., Sterkhov E.V., Zaitseva P.V., Skryl'nik M.Yu., Shunyaev K.Yu., Rempel' A.A. Features of crystallization, structure, and thermal stability of high-entropy GdTbDyHoSc and GdTbDyHoY alloys. *Rasplavy*. 2022;(5):443–453.

Упоров С.А., Эстемирова С.Х., Стерхов Е.В., Зайцева П.В., Скрыльник М.Ю., Шуняев К.Ю., Ремпель А.А. Особенности кристаллизации, структуры и термической стабильности высокоэнтропийных сплавов GdTbDyHoSc и GdTbDyHoY. *Расплавы*. 2022;(5):443–453.

7. Ilinykh S.A., Sarsadskih K.I., Chusov S.A., Korolev O.A., Achmetshin S.M., Krashaninin V.A. The study of powder coatings based on Al and Ni, obtained by supersonic plasma spraying. *Journal of Physics: Conference Series*. 2019;1281: 012027. https://doi.org/10.1088/1742-6596/1281/1/012027

Information about the Authors

Boris R. Gel'chinskii, *Dr. Sci. (Phys.–Math.), Prof., Head of the Science Department*, Institute of Metallurgy, Ural Branch of the Russian Academy of Sciences
ORCID: 0000-0001-5964-5477
E-mail: brg47@list.ru

Nina I. Il'inykh, *Cand. Sci. (Phys.-Math.), Senior Researcher*, Institute of Metallurgy, Ural Branch of the Russian Academy of Sciences; *Senior Researcher*, South Ural State University
ORCID: 0000-0003-3357-0133
E-mail: ninail@bk.ru

Elena V. Ignat'eva, *Research Associate*, Institute of Metallurgy, Ural Branch of the Russian Academy of Sciences
ORCID: 0000-0003-4406-3380
E-mail: l.ig_a@mail.ru

Сведения об авторах

Борис Рафаилович Гельчинский, *д.ф.-м.н., профессор, руководитель научного отдела*, Институт металлургии Уральского отделения РАН
ORCID: 0000-0001-5964-5477
E-mail: brg47@list.ru

Нина Иосифовна Ильиных, *к.ф.-м.н., старший научный сотрудник*, Институт металлургии Уральского отделения РАН; *старший научный сотрудник*, Южно-Уральский государственный университет
ORCID: 0000-0003-3357-0133
E-mail: ninail@bk.ru

Елена Викторовна Игнатьева, *научный сотрудник*, Институт металлургии Уральского отделения РАН
ORCID: 0000-0003-4406-3380
E-mail: l.ig_a@mail.ru

Contribution of the Authors

B. R. Gel'chinskii – conceptualization of the work, discussion of the results, editing the text.
N. I. Il'inykh – finding and analyzing of literary data, discussion of the results, writing and editing the text.

E. V. Ignat'eva – investigation of the materials' properties, discussion of the results.

Вклад авторов

Б. Р. Гельчинский – формирование концепции работы, обсуждение результатов, редактирование текста.
Н. И. Ильиных – поиск и анализ литературных данных, исследование свойств материалов, обсуждение результатов, написание и редактирование текста.
Е. В. Игнатьева – исследование свойств материалов, обсуждение результатов.

Received 22.09.2023
Revised 26.09.2023
Accepted 04.10.2023

Поступила в редакцию 22.09.2023
После доработки 26.09.2023
Принята к публикации 04.10.2023

PHYSICO-CHEMICAL BASICS OF METALLURGICAL PROCESSES / ФИЗИКО-ХИМИЧЕСКИЕ ОСНОВЫ МЕТАЛЛУРГИЧЕСКИХ ПРОЦЕССОВ

UDC 669.046.582.5
DOI 10.17073/0368-0797-2023-5-597-603

Original article
Оригинальная статья

Effect of boric anhydride on viscosity of slags used in electric melting of metallized siderite concentrate

A. S. Vusikhis[1], L. I. Leont'ev[1, 2, 3], M. A. Mikheenkov[1]

[1] **Institute of Metallurgy, Ural Branch of the Russian Academy of Science** (101 Amundsena Str., Yekaterinburg 620016, Russian Federation)
[2] **National University of Science and Technology "MISIS"** (4 Leninskii Ave., Moscow 119049, Russian Federation)
[3] **Scientific Council on Metallurgy and Metal Science of Russian Academy of Sciences (Department of Chemistry and Material Sciences)** (32a Leninskii Ave., Moscow 119991, Russian Federation)

vas58@mail.ru

Abstract. The Bakal deposit located in the Southern Urals near the city of Bakal, Chelyabinsk region, is one of the largest deposits of carbonate iron ores (siderites). The total deposit of siderites is about 1 billion tons. They are not in demand among metallurgists because of their low iron content and high magnesium content. At the same time, the Urals metallurgical enterprises are suffering from shortage of iron ore raw materials including steelmaking ore raw materials. The high purity of siderites in terms of phosphorus and non-ferrous metals makes it possible to use methods of coke-free metallurgy for their processing. Pyrometallurgical processing of siderites including their reduction roasting in a rotary furnace followed by grinding and magnetic separation allows obtaining a concentrate to be used as a steelmaking raw material having metallization degree above 90 % and a waste rock content under 3 – 7 %. Calculations showed that the costs of electricity used for melting scrap metal and metallized siderite concentrate containing 30 % of waste rock and loaded into the furnace at temperatures above 1000 °C are close. We propose a siderite processing method including reduction of the initial ore in a rotary furnace, and melting of resulting metallized concentrate hot loaded (at temperatures above 1000 °C) into a furnace. The empty rock of metallized siderite concentrate contains a large percentage of magnesium oxide that makes it refractory. To obtain liquid slag, it is proposed to add boric anhydride in the form of colemanite. To assess the B_2O_3 effect on melting of the metallized siderite oxide phase in the process of electric melting, studies on the viscosity correlation of the magnesian steelmaking slag containing B_2O_3 with temperature and its composition were carried out. It was found that at the discharge temperature (1600 °C) the resulting magnesia slag with the ratio of MgO/SiO_2 in the initial siderite equaling to 0.75 – 1.25 has a low viscosity (less than 3.65 P).

Keywords: iron ore raw materials, Bakal siderites, ore processing, roasting, metallization, viscosity, slag, colemanite, boron oxide

Acknowledgements: The work was supported by the Russian Science Foundation, project No. 22-29-00400.

For citation: Vusikhis A.S., Leont'ev L.I., Mikheenkov M.A. Effect of boric anhydride on viscosity of slags used in electric melting of metallized siderite concentrate. *Izvestiya. Ferrous Metallurgy*. 2023;66(5):597–603. https://doi.org/10.17073/0368-0797-2023-5-597-603

Влияние борного ангидрида на вязкость шлаков электроплавки металлизованного сидеритового концентрата

А. С. Вусихис[1], Л. И. Леонтьев[1, 2, 3], М. А. Михеенков[1]

[1] **Институт металлургии Уральского отделения РАН** (Россия, 620016, Екатеринбург, ул. Амундсена, 101)
[2] **Национальный исследовательский технологический университет «МИСИС»** (Россия, 119049, Москва, Ленинский пр., 4)
[3] **Президиум РАН** (Россия, 119991, Москва, Ленинский пр., 32а)

vas58@mail.ru

Аннотация. Бакальское месторождение, расположенное на Южном Урале вблизи города Бакал Челябинской области, является одним из крупнейших месторождений карбонатных железных руд (сидеритов). Общие запасы сидеритов составляют около 1 млрд т. Они не пользуются спросом у металлургов из-за низкого содержания железа и высокого содержания магния. В то же время металлургические предприятия Урала испытывают дефицит железорудного сырья, в том числе сталеплавильного. Высокая чистота сидеритов по фосфору и цветным металлам позволяет использовать для их переработки методы бескоксовой металлургии. Пирометаллургическое обогащение сидеритов, включающее

их восстановительный обжиг во вращающейся печи с последующим измельчением и магнитной сепарацией, позволяет получить концентрат со степенью металлизации более 90 % и содержанием пустой породы менее 3 – 7 %, пригодный в качестве сырья для сталеплавильного производства. Расчеты показали, что затраты электроэнергии на плавку металлического лома и металлизованного сидеритового концентрата, содержащего 30 % пустой породы, и загружаемого в печь при температуре выше 1000 °С, близки. Предложен способ переработки сидеритов, включающий восстановление исходной руды во вращающейся печи и плавку получаемого металлизованного концентрата, в горячем виде (при температуре выше 1000 °С) загружаемого в сталеплавильную печь. Пустая порода металлизованного сидеритового концентрата содержит большое количество оксида магния, что делает ее тугоплавкой. Для получения жидкого шлака предложено использовать добавку борного ангидрида в виде колеманита. Для оценки влияния B_2O_3 на плавление оксидной фазы металлизованного сидерита в процессе электроплавки проведены исследования корреляции вязкости магнезиального сталеплавильного шлака, содержащего B_2O_3, с температурой и его составом. Обнаружено, что при температуре выпуска (1600 °С) образующийся магнезиальный шлак обладает низкой вязкостью (менее 3,65 Пз) при соотношении MgO/SiO_2 в исходном сидерите, равном 0,75 – 1,25.

Ключевые слова: железорудное сырье, бакальские сидериты, обогащение руды, обжиг, металлизация, вязкость, шлак, колеманит, оксид бора

Благодарности: Работа выполнена при поддержке Российского научного фонда по проекту № 22-29-00400.

Для цитирования: Вусихис А.С., Леонтьев Л.И., Михеенков М.А. Влияние борного ангидрида на вязкость шлаков электроплавки металлизованного сидеритового концентрата. *Известия вузов. Черная металлургия*. 2023;66(5):597–603.
https://doi.org/10.17073/0368-0797-2023-5-597-603

Introduction

Carbonate (siderite) iron ore deposits span across various regions worldwide, including Austria, Bulgaria, Great Britain, Germany, Poland (Europe); China, Russia, Japan (Asia); Algeria (Africa); USA, Canada, Colombia (America), and numerous other countries [1 – 10]. Presently, the sole metallurgical process employing siderite ores is blast furnace smelting. Before loading into the furnace, siderites undergo enrichment, utilizing various methods depending on the ore's composition: gravity, flotation, magnetic separation, electrostatic separation, and roasting-magnetic techniques. One of the largest known deposits of siderite ore globally is the Bakal deposit, situated near the city of Bakal in the Chelyabinsk Oblast, located in the Southern Urals. The total reserves of siderites in this deposit are estimated to be around 1 billion tons [11; 12]. However, due to their low quality – characterized by low iron content and high magnesium oxide content – siderites are in minimal demand among blast furnace metallurgists. Extraction of the ore falls significantly short of the potential yield based on mining and geological conditions. This shortage exacerbates the scarcity of raw materials faced by the metallurgical industry in the Urals, particularly for steelmaking.

Bakal siderites stand out due to their manganese content, reaching up to 2 %, low phosphorus content (less than 0.02 %), and the absence of non-ferrous metals like copper and zinc. These characteristics render them valuable raw materials for the production of high-quality steels using coke-free metallurgy methods [13; 14].

The methods utilized for direct iron production rely heavily on the quality of the iron ore raw materials employed. The recovery process of high-grade concentrates containing a minimum of 70 % iron is executed in various units such as shaft furnaces, retorts, among others. This procedure aims to achieve a metallization level surpassing 90 % using a specialized gas mixture [15]. For the treatment of low-grade ores, prevalent methods involve their metallization through solid reducing agents in rotary kilns, subsequently followed by the separation of waste rock via grinding and magnetic separation [16]. Extensive research indicates that through the pyrometallurgical enrichment of siderite ores [11; 12], a concentrate boasting over 90 % metallization can be attained. This concentrate, with a waste rock content ranging from 3 to 7 %, proves suitable for steelmaking purposes [17]. In order to facilitate the reduction process at temperatures between 1300 and 1350 °C, the easily fusible waste rock, predominantly composed of quartz-clay shale [19], necessitates prior removal. This removal can be achieved through gravity concentration in heavy suspensions [10], polygradient magnetic separation, or the *X*-ray radiometric method.

The comparison of energy intensity between smelting scrap metal in an electric furnace and smelting metalized siderite concentrate, heated to 1000 °C, containing approximately 30 % waste rock, revealed similar energy consumption per ton of iron in both scenarios. This similarity suggests the feasibility of a smelting technology for metalized siderite concentrate, acquired through pyrometallurgical enrichment in a rotary furnace, without the intermediary stages of grinding and magnetic separation. However, it's crucial to consider that the high magnesium oxide content in the oxide phase of the concentrate will result in the formation of slag during the melting process with a considerably high melting point. This particular characteristic of the slag formation renders the proposed technology inefficient.

The addition of boric anhydride (B_2O_3) to slag is recognized for its capacity to lower the melting temperature of the slag [20]. To assess the impact of B_2O_3 on the melting behavior of the oxide phase of metalized siderite during the electric melting process, research focused on examining the correlation between the viscosity of magnesia steelmaking slag – incorporating B_2O_3 – and its temperature alongside composition.

Table 1

Chemical composition of the initial mixtures

Таблица 1. **Химический состав исходных смесей**

Mixture No.	Content, %						
	SiO_2/MgO	FeO	SiO_2	Al_2O_3	CaO	MgO	MnO
1	0.50	10.0	24.0	4.0	7.0	48.0	7.0
2	0.75	10.0	30.9	4.0	7.0	41.1	7.0
3	1.00	10.0	36.0	4.0	7.0	36.0	7.0
4	1.25	10.0	40.0	4.0	7.0	32.0	7.0

Materials and methods

A vibrating viscometer, utilizing damped oscillations and computerized data processing, was employed for the viscosity study [21].

The proportion of various oxides (iron, calcium, aluminum, manganese) in siderites shows slight variation depending on their location. However, the ratio between silicon oxide and magnesium oxide can fluctuate from 0.5 to 1.25 [11; 12]. Consequently, to examine the viscosity of pure oxides, initial mixtures were formulated. These mixtures replicated the composition of the oxide phase found in a metallized siderite concentrate with a metallization degree of 95 %. The compositions maintained a constant proportion of most oxides while adjusting the SiO_2/MgO ratio within the range of 0.5 to 1.25 (Table 1). These mixtures were supplemented with a material – previously molten and crushed – with a composition closely resembling calcined colemanite. This material contained 8 % SiO_2, 34 % CaO, 4 % MgO and 54 % B_2O_3. It was added at ratios equivalent to 10, 15, and 20 % of its fraction in the charge. This corresponds to 60, 90 and 120 kg of raw colemanite (L.O.I. 30 %) per ton of metallized siderite concentrate. The chemical composition of the examined slags is detailed in Table 2.

The research involved forming tablets from mixtures mirroring the slag compositions under investigation. These tablets were placed in molybdenum crucibles, heated in a resistance electric furnace up to 1600 °C, and subsequently, the viscosity was measured.

The analysis revealed that slags *1 – 3*, featuring a SiO_2/MgO ratio of 0.5, exhibited heterogeneity at temperatures below 1600 °C. In the other slags, distinct regions of high and low-temperature viscosity were observed. Within the high-temperature region, viscosity remained below 3.65 P. As the temperature decreased, viscosity showed a slight increase. However, in the low-temperature region, the change in viscosity was more pronounced. An elevation in the SiO_2/MgO ratio and the addition of colemanite to the mixture led to an increase in B_2O_3 content in the slag and consequently lowered the temperature at which viscosity transitioned to the high-temperature region. The results of these measurements are depicted in Fig. 1.

To analyze the slag viscosities corresponding to the transition from the low-temperature to high-temperature regions, and the respective transition temperatures, experimental design methods were employed [22]. An orthogonal design 2^3 was used, with the SiO_2/MgO ratio as the first factor and the colemanite fraction in the charge as the second factor. The experimental plan

Table 2

Chemical composition of the studied slags

Таблица 2. **Химический состав исследуемых шлаков**

Slag No.	SiO_2/ MgO	Fraction of colemanite, %	Content, %						
			FeO	SiO_2	Al_2O_3	CaO	MgO	MnO	B_2O_3
1	0.50	10.0	9.1	22.5	3.7	9.5	44.0	6.4	4.9
2	0.50	15.0	8.7	21.9	3.5	10.5	42.3	6.1	7.0
3	0.50	20.0	8.3	21.3	3.4	11.5	40.7	5.8	8.9
4	0.75	10.0	9.1	28.8	3.7	9.5	37.7	6.4	4.9
5	0.75	15.0	8.7	27.9	3.5	10.5	36.3	6.1	7.0
6	0.75	20.0	8.3	27.1	3.4	11.5	34.9	5.8	8.9
7	1.00	10.0	9.1	33.5	3.7	9.5	33.1	6.4	4.9
8	1.00	15.0	8.7	32.3	3.5	10.5	31.8	6.1	7.0
9	1.00	20.0	8.3	31.3	3.4	11.5	30.7	5.8	8.9
10	1.25	10.0	9.1	37.1	3.7	9.5	29.5	6.4	4.9
11	1.25	15.0	8.7	35.8	3.5	10.5	28.3	6.1	7.0
12	1.25	20.0	8.3	34.7	3.4	11.5	27.3	5.8	8.9

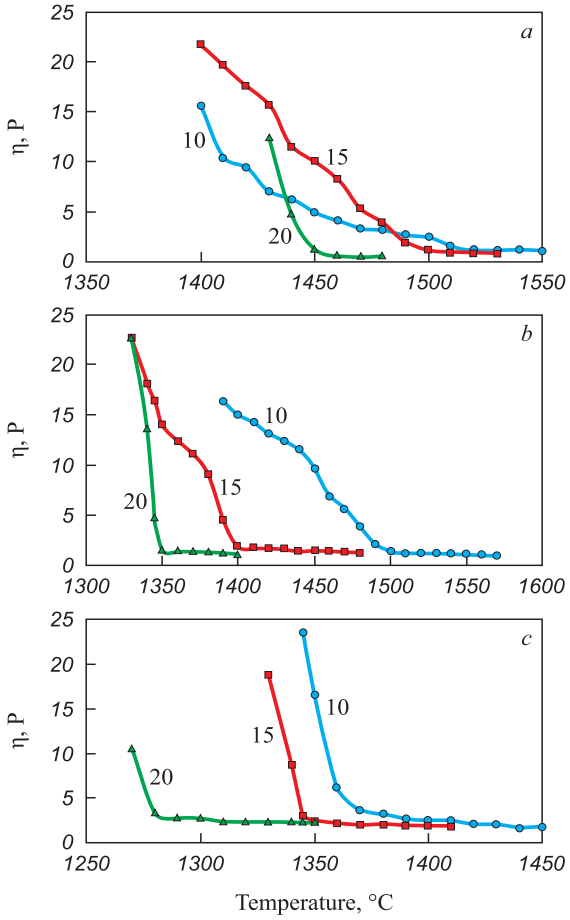

Fig. 1. Change in viscosity of steelmaking slag depending on temperature (numbers near curves – percentage of colemanite) at SiO_2/MgO: 0.75 (*a*); 1.00 (*b*); 1.25 (*c*)

Рис. 1 Изменение вязкости сталеплавильного шлака в зависимости от температуры (цифры у кривых – процент колеманита) при SiO_2/MgO: 0,75 (*a*); 1,00 (*b*); 1,25 (*c*)

Table 3

Plan of the experiment and its results

Таблица 3. **План проведения эксперимента и его результаты**

Test No.	SiO_2/MgO	Fraction of colemanite, wt. %	Temperature, °C	Viscosity, P
1	0.75	10	1520	1.64
2	0.75	15	1500	1.24
3	0.75	20	1450	1.30
4	1.00	10	1500	1.43
5	1.00	15	1400	1.85
6	1.00	20	1350	1.50
7	1.25	10	1370	3.23
8	1.25	15	1345	2.24
9	1.25	20	1280	3.65
10	1.00	15	1400	1.85

and its outcomes are detailed in Table 3 and presented graphically in Figs. 2 – 4.

Fig. 2 provides an overview of the response function depicting slag viscosity and the temperature at which the desired viscosity is achieved, in relation to the SiO_2/MgO ratio and colemanite content.

Fig. 3 shows isolines representing equivalent slag viscosities and the respective temperatures required to achieve those viscosities, contingent on the SiO_2/MgO ratio and colemanite content.

The analysis depicted in Figs. 2 and 3 elucidates the profound impact of the SiO_2/MgO ratio and colemanite content on viscosity. Point *A* in Fig. 3 marks the minimum slag viscosity, attained with a SiO_2/MgO ratio of 0.78 and a colemanite content of 17 %. At a consistent SiO_2/MgO ratio, an increase in colemanite content results in a decrease in the temperature needed to achieve the desired viscosity. For instance, the tem-

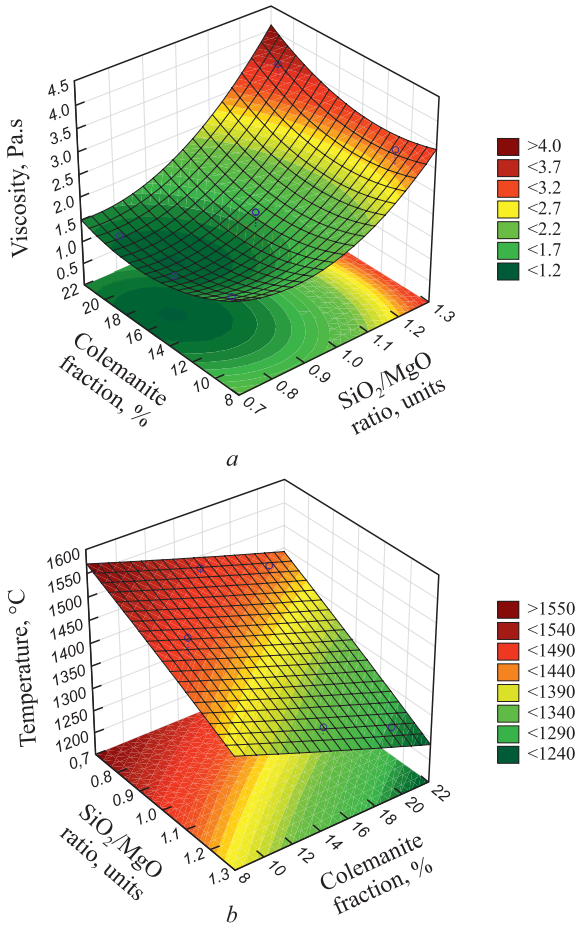

Fig. 2. General view of slag viscosity response function (*a*) and equal temperature at which the required viscosity is achieved (*b*), depending on SiO_2/MgO ratio and proportion of colemanite in the charge

Рис. 2. Общий вид функции отклика вязкости шлака (*a*) и равной температуры, при которой достигается требуемая вязкость (*b*), в зависимости от соотношения SiO_2/MgO и доли колеманита в шихте

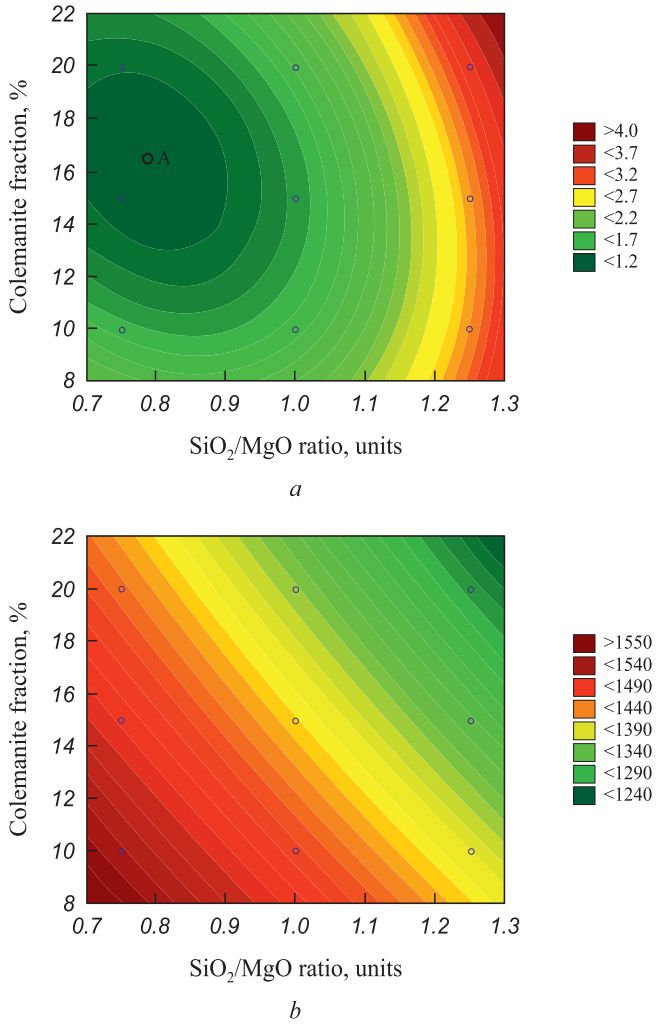

Fig. 3. Isolines of equal slag viscosity (*a*) and equal temperature at which the required viscosity is achieved (*b*), depending on SiO_2/MgO ratio and proportion of colemanite in the charge

Рис. 3. Изолинии равной вязкости шлака (*a*) и равной температуры, при которой достигается требуемая вязкость (*b*), в зависимости от соотношения SiO_2/MgO и доли колеманита в шихте

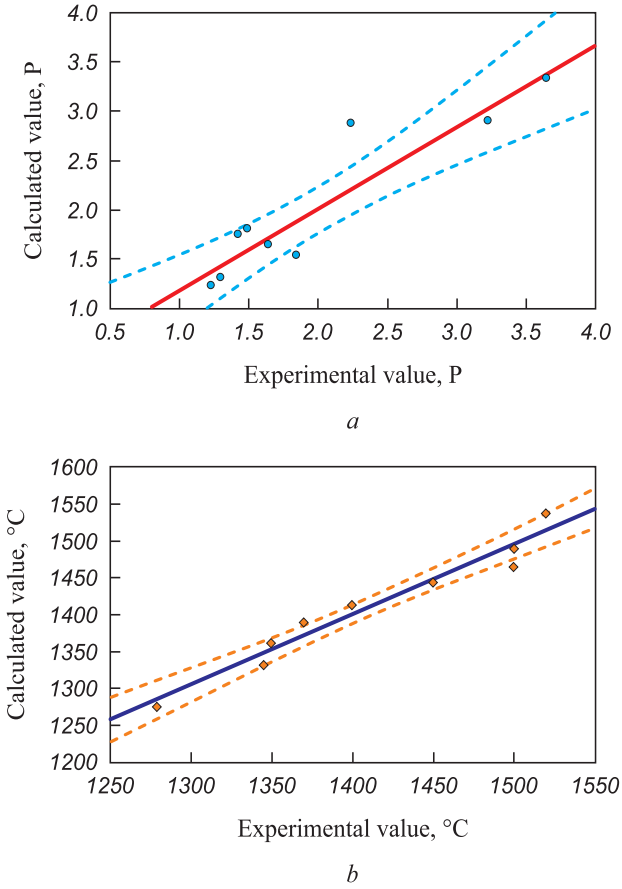

Fig. 4. Correlation diagram of experimental and calculated values of viscosity (*a*) and temperature (*b*)

Рис. 4. Диаграмма корреляции экспериментальных и расчетных значений вязкости (*a*) и температуры (*b*)

perature required to achieve the minimum viscosity with a SiO_2/MgO ratio of 0.78 and a 17 % colemanite content is 1460 °C.

Using the STATISTICA software [24], the experimental results were processed, enabling the calculation of regression equations describing the behavior of the response function (viscosity (*1*) and temperature (*2*)) based on the main factors:

$$\eta = 10.93 - 15.58x + 8.3x^2 - 0.4y + 0.009y^2 + 0.15xy; \quad (1)$$

$$T = 1801.7 - 199.5x - 28.6x^2 - 7.19y + 0.03y^2 - 4.0xy, \quad (2)$$

where x is the SiO_2/MgO ratio, units; y is the colemanite content, wt. %.

Fig. 4 illustrates the comparison between experimental and calculated values of viscosity and temperature to evaluate the model's adequacy determined by the regression equation. The results, assessed via correlation of experimental and calculated data, are visually represented in this figure. The data analysis demonstrates that the regression equation effectively describes the experimental findings. Most of the experimental data points fall within the confidence interval demarcated by the reliability ellipse.

The findings confirm that when the SiO_2/MgO ratio stands at 0.5, the inclusion of colemanite does not yield favorable outcomes. Below temperatures of 1600 °C, the slag retains heterogeneity, impeding the smelting of metallized siderite in electric furnaces. Conversely, in slags featuring a SiO_2/MgO ratio surpassing 0.75, a high-temperature region with viscosity measuring less than 3.65 P is evident. This corresponds to temperatures exceeding 1520 °C, with colemanite fractions ranging from 10 to 20 %. The transition temperature from high to low-temperature regions can be managed by altering both the SiO_2/MgO ratio and the colemanite fraction. Specifically, achieving the same transition temperature involves concurrently increasing the SiO_2/MgO ratio while decreasing the colemanite fraction.

Conclusions

Lump siderite concentrate, reduced to a metallization degree of 95 % in a rotary kiln and loaded into an electric furnace at hot temperatures (above 1000 °C), supplemented with raw colemanite additives within the range of 60 – 120 kg per ton of concentrate, can undergo melting. This process yields a metal-semi-product at outlet temperatures around 1600 °C, suitable for subsequent steel production. Simultaneously, it results in the formation of a homogeneous magnesia slag exhibiting low viscosity (below 3.65 P). This occurs specifically when the original siderite boasts an MgO/SiO_2 ratio ranging from 0.75 to 1.25.

References / Список литературы

1. Frimmel H. Strontium isotopic evidence for the origin of siderite, ankerite and magnesite mineralizations in the Eastern Alps. *Mineralium Deposita*. 1988;23(4):268–275. https://doi.org/10.1007/BF00206407
2. Pohl W. Comparative geology of magnesite deposits and occurrences. In: *Magnesite. Geology, Mineralogy, Geochemistry, Formation of Mg-Carbonates*. Moeller P. ed. Monogr. Ser. Mineral Deposits. 1989;28:1–13.
3. Jonkov J., Mochev D., Grigorova I., Nishkov I. Siderite ore physical separation and reverse flotation. *Journal of Mining and Metallurgy A: Mining*. 2012;48:23–37.
4. Boch R., Wang X., Kluge T., etc. Aragonite–calcite veins of the 'Erzberg' iron ore deposit (Austria): Environmental implications from young fractures. *Sedimentology*. 2019;66(4):604–635. https://doi.org/10.1111/sed.12500
5. Min L., Zhiming C., Qiying C. The role of organic matter in the formation of siderite from Xuanlong area, Hebei Province. *Chinese Journal of Geochemistry*. 1997;16: 86–94. https://doi.org/10.1007/BF02843376
6. Bai S., Wen S., Liu D., Zhang W., Xian Y. Catalyzing carbothermic reduction of siderite ore with high content of phosphorus by adding sodium. *ISIJ International*. 2011;51(10): 1601–1607. https://doi.org/10.2355/isijinternational.51.1601
7. Shikazono N. Composition of siderite and the environments of formation of vein-type deposits in Japan. *Economic Geology*.1977;72(4):632–641. https://doi.org/10.2113/gsecongeo.72.4.632
8. Palinkas S.S., Spangenberg J.E., Palinkas L.A. Organic and inorganic geochemistry of Ljubija siderite deposits, NW Bosnia and Herzegovina. *Mineralium Deposita*. 2009;44: 893–913. https://doi.org/10.1007/s00126-009-0249-z
9. Rudmin M.A., Kalinina N.A., Maximov P.N. Formation of siderite in marine ooidal ironstones on example of Bakchar Deposit (Western Siberia). In: *Proceedings of the X Int. Siberian Early Career Geoscientists Conf. Novosibirsk State University*; 2022:79–80.
10. Zhunev A.G., Yur'ev B.P., Blank M.E. Intensification of roasting and agglomeration of siderite ores. *Ferrous Metallurgy. Bulletin of Scientific, Technical and Economic Information*. 1988;(3):2–13. (In Russ.).

    Жунев А.Г., Юрьев Б.П., Бланк М.Э. Интенсификация процессов обжига и агломерации сидеритовых руд. *Черная металлургия. Бюллетень научно-технической информации*. 1988;(3):2–13.
11. Yur'ev B.P., Melamud S.G., Spirin N.A., Shatsillo V.V. *Technological and Thermal Engineering Bases of Siderite Ore Preparation for Metallurgical Processing: Monograph*. Yekaterinburg: Den' RA; 2016:428. (In Russ.).

    Технологические и теплотехнические основы подготовки сидеритовых руд к металлургическим переделам. Монография / Б.П. Юрьев, С.Г. Меламуд, Н.А. Спирин, В.В. Шацилло. Екатеринбург: День РА; 2016:428.
12. Vusikhis A. S., Leont'ev L. I. *The Use of Siderite Ores in Production of Iron and Steel: Monograph*. Moscow, Vologda: Infra-Inzheneriya; 2022:116. (In Russ.).

    Вусихис А.С., Леонтьев Л.И. *Применение сидеритовых руд при производстве чугуна и стали. Монография*. Москва; Вологда: Инфра-Инженерия; 2022:116.
13. Lapteva A. Coke-free metallurgy: Resources, state, prospects. *Metally Evrazii*. 2012;(2):9–23. (In Russ.).

    Лаптева А. Бескоксовая металлургия: ресурсы, состояние, перспективы. *Металлы Евразии*. 2012;(2):9–23.
14. Kirichenko I.S., Aleksakhin A.V. Development of global and domestic production of direct reduced iron. *Molodoi uchenyi*. 2016;(2):85-90. (In Russ.).

    Кириченко И.С., Алексахин А.В., Развитие мирового и отечественного производства железа прямого восстановления. *Молодой ученый*. 2016;(2):85–90.
15. Timoshpol'skii V.I., Trusova I.A., Plyushchevskii I.N., Korneev S.V. Prospects for the production and use of metallized raw materials to obtain high-quality steel grades. Message 1. Analysis of modern schemes for obtaining metallized raw materials. *Lit'e i metallurgiya*. 2009;(50):134–138. (In Russ.).

    Тимошпольский В.И., Трусова И.А., Плющевский И.Н., Корнеев С.В. Перспективы производства и использования металлизованного сырья для получения высококачественных марок стали. Сообщение 1. Анализ современных схем получения металлизованного сырья. *Литье и металлургия*. 2009;1(50):134–138.
16. Kurunov I.F., Savchuk N.A. *State and Prospects of Direct Metallurgy of Iron*. Moscow: Chermetinformatsiya; 2002:186. (In Russ.).

    Курунов И.Ф., Савчук Н.А. *Состояние и перспективы бездоменной металлургии железа*. Москва: Черметинформация; 2002:198.
17. Gimmel'farb A.I., Nemenov A.M., Tarasov B.E. *Metallization and Electric Smelting of Iron Ore Raw Materials*. Moscow: Metallurgiya; 1981:152. (In Russ.).

    Гиммельфарб А.И., Неменов А.М., Тарасов Б.Е. *Металлизация и электроплавка железорудного сырья*. Москва: Металлургия; 1981:152.
18. Yur'ev B.P., Sheshukov O.Yu., Dudko V.A. Elaboration of an environmentally appropriate technology of siderite ores concentration. *Ferrous Metallurgy. Bulletin of Scientific, Technical and Economic Information*. 2019;75(8):923–929. (In Russ.). https://doi.org/10.32339/0135-5910-2019-8-923-929

    Юрьев Б.П., Шешуков О.Ю., Дудко В.А. Разработка экологически чистой технологии обогащения сидеритовых руд. *Черная металлургия. Бюллетень научно-технической и экономической информации*. 2019;75(8):923–929. https://doi.org/10.32339/0135-5910-2019-8-923-929

19. Akhlyustina A.I., Zhukovskii G.V., Kvaskov A.P. Technological classification of iron ores of the Bakal deposit. *Trudy "Uralmekhanobr"*. 1972;(18):37–43. (In Russ.).

Ахлюстина А.И., Жуковский Г.В., Кваскова А.П. Технологическая классификация железных руд Бакальского месторождения. *Труды «Уралмеханобр»*. 1972;18: 37–43.

20. Ren Sh., Zhang J., Wu L., Fu W., Rao J. Influence of B_2O_3 on viscosity of high Ti-bearing blast furnace slag. *ISIJ International*. 2012;52(6):984–991. https://doi.org/10.1051/metal/2016038

21. Vusikhis A.S., Selivanov E.N., Dmitriev A.N., Chentsov V.P., Ryabov V.V. Structure sensitive properties of system B_2O_3–CaO melts. *Defect and Diffusion Forum*. 2020;400:186–192. https://doi.org/10.4028/www.scientific.net/DDF.400.186

22. Kuprienko N.V., Ponomareva O.A., Tikhonov D.V. *Statistics. Distribution Analysis Methods. Selective Observation: Tutorial*. St. Petersburg: Izd-vo Politekhn. un-ta; 2009:138. (In Russ.).

Куприенко Н.В., Пономарева О.А., Тихонов Д.В. *Статистика. Методы анализа распределений. Выборочное наблюдение: Учебное пособие*. Санкт-Петербург: Издательство Политехнического университета; 2009:138.

Information about the Authors / Сведения об авторах

Aleksandr S. Vusikhis, *Cand. Sci. (Eng.), Senior Researcher of the Laboratory of Pyrometallurgy of Non-Ferrous Metals*, Institute of Metallurgy, Ural Branch of the Russian Academy of Science
ORCID: 0000-0002-6395-0834
E-mail: vas58@mail.ru

Leopol'd I. Leont'ev, *Academician, Adviser*, Russian Academy of Sciences, *Dr. Sci. (Eng.), Prof.*, National University of Science and Technology "MISIS", *Chief Researcher*, Institute of Metallurgy, Ural Branch of the Russian Academy of Science
ORCID: 0000-0002-4343-914X
E-mail: leo@presidium.ras.ru

Mikhail A. Mikheenkov, *Dr. Sci. (Eng.), Senior Researcher of the Laboratory "Pyrometallurgy of Ferrous Metals"*, Institute of Metallurgy, Ural Branch of the Russian Academy of Science
E-mail: silast@mail.ru

Александр Семенович Вусихис, *к.т.н., старший научный сотрудник лаборатории пирометаллургии цветных металлов*, Институт металлургии Уральского отделения РАН
ORCID: 0000-0002-6395-0834
E-mail: vas58@mail.ru

Леопольд Игоревич Леонтьев, *академик, советник*, Президиум РАН, *д.т.н., профессор*, Национальный исследовательский технологический университет «МИСИС», *главный научный сотрудник*, Институт металлургии Уральского отделения РАН
ORCID: 0000-0002-4343-914X
E-mail: leo@presidium.ras.ru

Михаил Аркадьевич Михеенков, *д.т.н., старший научный сотрудник лаборатории пирометаллургии черных металлов*, Институт металлургии УрО РАН
E-mail: silast@mail.ru

Contribution of the Authors / Вклад авторов

A. S. Vusikhis – setting the research problem, calculations, writing the text, forming conclusions, conducting experiments.

L. I. Leont'ev – scientific guidance, analysis of the research results, editing.
M. A. Mikheenkov – calculations.

А. С. Вусихис – постановка задачи исследования, проведение расчетов, подготовка текста, формирование выводов, проведение экспериментов.
Л. И. Леонтьев – научное руководство, анализ результатов исследований, редактирование статьи.
М. А. Михеенков – проведение расчетов.

Received 28.08.2023
Revised 31.08.2023
Accepted 04.09.2023

Поступила в редакцию 28.08.2023
После доработки 31.08.2023
Принята к публикации 04.09.2023

PHYSICO-CHEMICAL BASICS OF METALLURGICAL PROCESSES / ФИЗИКО-ХИМИЧЕСКИЕ ОСНОВЫ МЕТАЛЛУРГИЧЕСКИХ ПРОЦЕССОВ

UDC 669.19: 661.96
DOI 10.17073/0368-0797-2023-5-604-609

Original article
Оригинальная статья

Effect of hydrogen on nickel oxide reduction on the surface of nozzle blade of a gas turbine unit

D. D. Fomina, V. Z. Poilov, A. N. Gallyamov

Perm National Research Polytechnic University (29 Komsomolskii Ave., Perm 614990, Russian Federation)

Fomina97@yandex.ru

Abstract. Currently, there is a growing interest in the use of hydrogen in the composition of fuel mixtures for turbojet engines and gas turbine units (GTU). The effect of hydrogen on heat-resistant nickel alloys of gas turbine blades has been little studied. In this regard, this work is devoted to studying the effect of hydrogen on nickel oxide reduction on the surface of the nozzle blade of a gas turbine engine. Hydrogen is a good reducing agent. Therefore, this article discusses the effects of hydrogen under various conditions with metal oxides, and methods of metal oxides reduction on the surface of the blades of a gas turbine engine. The thermodynamics of the interaction of aluminum, titanium, nickel and tungsten oxides with hydrogen fluoride and reactions of fluoride with hydrogen was investigated in the temperature range 273 – 1373 K. It was established that the interaction of aluminum oxide with hydrogen fluoride occurs in the temperature range from 273 to 1073 K, titanium oxide with hydrogen fluoride – from 273 to 373 K, nickel oxide with hydrogen fluoride – from 273 to 873 K. In this case, of the resulting fluorides, only nickel fluoride interacts with hydrogen at temperatures above 673 K. Hydrogen interacts with nickel oxide throughout the entire temperature range, and with tungsten oxide at temperatures above 1173 K. We studied the effect of hydrogen on heat-resistant nickel alloys of gas turbine blades subjected to preliminary fluorination and not treated with fluorine compounds. Nickel oxide reduction with hydrogen proceeds better after the preliminary fluorination process. In this case, particles 2 – 5 μm in size containing 90.16 % Ni are formed on the surface of the blade sample. Without fluorination, this process at 1223 K and duration of 1 h does not occur.

Keywords: hydrogen, reduction properties, surface cleaning, nozzle blades, heat-resistant nickel alloys, gas turbine unit, hydrogen fluoride, Dayton process

Acknowledgements: The results were obtained during the implementation of the state assignment of the Ministry of Science and Higher Education of the Russian Federation (project FSNM-2023-0004).

For citation: Fomina D.D., Poilov V.Z., Gallyamov A.N. Effect of hydrogen on nickel oxide reduction on the surface of nozzle blade of a gas turbine unit. *Izvestiya. Ferrous Metallurgy*. 2023;66(5):604–609. https://doi.org/10.17073/0368-0797-2023-5-604-609

Влияние водорода на восстановление оксида никеля на поверхности сопловой лопатки газотурбинной установки

Д. Д. Фомина, В. З. Пойлов, А. Н. Галлямов

Пермский национальный исследовательский политехнический университет (Россия, 614990, Пермь, Комсомольский пр., 29)

Fomina97@yandex.ru

Аннотация. В настоящее время растет интерес к использованию водорода в составе топливных смесей для турбореактивных двигателей и газотурбинных установок. Воздействие водорода на жаропрочные никелевые сплавы лопаток газотурбинных установок мало изучено. Данная работа посвящена исследованию влияния водорода на восстановление оксида никеля на поверхности сопловой лопатки газотурбинных установок. Рассмотрено взаимодействие водорода при различных условиях с оксидами металлов, способы восстановления оксидов металлов на поверхности лопаток газотурбинного двигателя. Термодинамика реакций взаимодействия оксидов алюминия, титана, никеля и вольфрама с фтороводородом и реакций фторидов с водородом изучена в диапазоне температур 273 – 1373 К. Установлено, что взаимодействие оксида алюминия с фтороводородом протекает в диапазоне температур от 273 до 1073 К, оксида титана с фтороводородом – от 273 до 373 К, оксида никеля с фтороводородом – от 273 до 873 К. При этом из образовавшихся фторидов с водородом реагирует только фторид никеля при температурах выше 673 К. Водород во всем интервале температур взаимодействует с оксидом никеля, а с оксидом вольфрама – при температурах выше 1173 К. Изучены особенности

воздействия водорода на жаропрочные никелевые сплавы лопаток газотурбинных установок, подвергнутых предварительному фторированию и не обработанных соединениями фтора. Установлено, что восстановление оксида никеля водородом лучше протекает после процесса предварительного фторирования. При этом на поверхности образца лопатки образуются частицы размером 2 – 5 мкм, содержащие 90,16 % Ni. Без фторирования процесс восстановления оксида никеля водородом при температуре 1223 К и длительности 1 ч не происходит.

Ключевые слова: водород, восстановительные свойства, очистка поверхности, сопловые лопатки, жаропрочные никелевые сплавы, газотурбинная установка, фтористый водород, Дейтон-процесс

Благодарности: Результаты получены при выполнении государственного задания Министерства науки и высшего образования Российской Федерации на выполнение фундаментальных научных исследований (проект FSNM-2023-0004).

Для цитирования: Фомина Д.Д., Пойлов В.З., Галлямов А.Н. Влияние водорода на восстановление оксида никеля на поверхности сопловой лопатки газотурбинной установки. *Известия вузов. Черная металлургия*. 2023;66(5):604–609.
https://doi.org/10.17073/0368-0797-2023-5-604-609

Introduction

Hydrogen finds extensive application across chemical, power generation, and metallurgical industries as a versatile fuel, effectively curbing carbon dioxide emissions into the atmosphere. It serves as an energy reservoir, a chemical reagent for synthesizing organic compounds, and a potent reducing agent, among other roles. Although hydrogen is typically chemically inert, its reactivity amplifies, especially when subjected to heat. Under these conditions, molecular hydrogen engages in chemical interactions with various metals, non-metals, and complex compounds. The heightened chemical activity of hydrogen, influenced by additional factors, stems from the partial formation of atomic hydrogen, significantly more reactive than its molecular counterpart. Notably, hydrogen proves to be an exceptional agent for reducing metal oxides into metals. Both atomic and molecular hydrogen can carry out reducing functions [1 – 3].

Atomic hydrogen interacts with the surfaces of solids upon heat absorption, necessitating consideration of different substances' propensity to interact with hydrogen atoms. The recombination of hydrogen atoms occurs most efficiently due to the catalytic effects of metals, with activity decreasing in the following order: Pt > Pd > W > Fe > Cr > Ag > Cu > Pb.

Additionally, the recombination of hydrogen atoms (involving the capture of a free electron by an ion) occurs on the surfaces of oxides such as MgO, CaO, BaO, Al_2O_3, Cr_2O_3 [4].

An important aspect involves exposing the surface of a metal covered with an oxide film to molecular hydrogen, thereby eliminating this film by reducing the oxides to their metallic state. This study delves into the impact of hydrogen on the surfaces of alloy components used in gas turbine unit (GTU) blades, examining both theoretical implications and practical application.

The effectiveness of hydrogen's reducing capabilities is detailed in [5], wherein the authors explore the reduction of various metal oxides. Atomic hydrogen, generated on a heated tungsten catalyst, is employed for the reduction process. The study revealed that oxides of Cu, Ru, Nb, Mo, Rh, Pd, Ir and Pt can be reduced by atomic hydrogen at a substrate temperature of 313 K.

Studies conducted in [6; 7] investigated the extraction processes of nickel from serpentine and limonite ores through leaching at elevated temperatures and pH = 13, followed by the reduction of nickel salts using hydrogen. Exploring the use of hydrogen plasma [8], generated via inductive radio frequency glow discharge at 27.12 MHz and 700 W RF generator power, at a density of $1 – 3^{(10 – 15)}$ m^{-3} within hydrogen pressures ranging from 0.05 to 50 Pa, holds significance for copper oxide reduction. Researchers in [9] similarly employed the reduction process in H_2 plasma for phosphide synthesis. Remarkably, high efficiency was attained in hydrogen plasma due to hydrogen's heightened reactivity in reduction processes.

The ability to reduce iron (III) oxide in a hydrogen-rich atmosphere has been investigated, revealing that an insufficient supply of hydrogen impedes the completion of the reduction process [10]. Additionally, hydrogen plays a crucial role in restoring cathode materials within lithium-ion batteries [11]

In examining methods for cleaning nozzle blades as outlined in [12; 13], the reducing properties of hydrogen are leveraged in a stage aimed at cleansing the surface of gas turbine engine (GTE) blades from metal oxides, using elemental fluorine [14; 15]. This method is employed to clean damaged metal parts composed of a heat-resistant nickel alloy containing microcracks, facilitating part repair via soldering. Elemental fluorine acts as an intermediary reagent, eliminating metal oxides from heat-resistant nickel alloys and forming metal fluorides with the alloy components. The source of elemental fluorine originates from the products resulting from the thermal decomposition of fluorocarbon resin. Subsequently, the reduction of metal fluorides is carried out using hydrogen at elevated temperatures.

The treated part exhibits a surface layer devoid of oxides. It has been noted that the surface contains trace amounts of titanium and aluminum, enhancing the ease of soldering the part.

The patents [16; 17] outline a process involving the exposure of a part to an atmosphere containing carbon, oxygen (in the form of carbon monoxide), hydrogen, and fluorine (C – O – H – F). Initially, these patents detail the decomposition process of polytetrafluoroethylene (PTFE), resulting in the formation of tetrafluoroethylene monomer, which subsequently reacts with hydrogen, producing hydrogen fluoride.

Distinguishing themselves from [14; 15], patents [16; 17] operate within a distinct temperature range of 973 – 1073 K, with a duration of 4 h within this gas environment. During this phase, metal fluorides are generated. In a subsequent step, hydrogen is applied to the part's surface within a temperature range of 1223 – 1373 K.

Existing publications lack an assessment of the efficiency in reducing metal oxides of heat-resistant nickel alloys solely subjected to prior fluorination and not treated with fluorine compounds. Therefore, this study aims to elucidate the characteristics of the process involved in reducing metal oxides of heat-resistant nickel alloys with hydrogen subsequent to preliminary fluorination and in the absence of further treatment with fluorine compounds.

Thermodynamic analysis results

Thermodynamic analysis of fluorination

The thermodynamic analysis conducted involved the examination of the interaction between aluminum, titanium, nickel, and tungsten oxides with hydrogen fluoride, as well as the subsequent reaction of fluorides with hydrogen. The following thermodynamic characteristics pertain to the reducing potential of hydrogen during its interaction with the oxide film present on the surface of the heat-resistant nickel alloy GTU. Presented here are the primary reactions that may occur during these processes, along with enthalpy and entropy values obtained from the reference book [18].

$$Al_2O_3 + 6HF_{(g)} = 2AlF_3 + 3H_2O; \quad (1)$$

$$TiO_2 + 4HF_{(g)} = TiF_4 + 2H_2O; \quad (2)$$

$$NiO + 2HF_{(g)} = NiF_2 + H_2O; \quad (3)$$

$$WO_3 + 6HF_{(g)} = WF_{6(g)} + 3H_2O. \quad (4)$$

The examination of the Gibbs energy of reactions (1) – (4) indicates specific temperature ranges for interactions between aluminum oxide and hydrogen fluoride (273 to 1073 K), titanium oxide and hydrogen fluoride (273 to 373 K), and nickel oxide and hydrogen fluoride (273 to 873 K), as confirmed by their respective negative Gibbs energy values. Notably, the reaction between tungsten oxide and hydrogen fluoride does not occur.

It's noted that above 873 K, aluminum fluoride sublimates from the surface of the GTE blade. A similar sublimation phenomenon occurs when titanium fluoride is heated to temperatures higher than 353 K [19].

Thermodynamic analysis of metal fluoride-hydrogen reactions

The interaction of metal fluorides with hydrogen can proceed according to the following reactions

$$2AlF_3 + 3H_2 = 2Al + 6HF; \quad (5)$$

$$TiF_4 + 2H_2 = Ti + 4HF; \quad (6)$$

$$NiF_2 + H_2 = Ni + 2HF. \quad (7)$$

Analysis of the Gibbs energy indicates that reactions (5) and (6) do not occur as their corresponding Gibbs energy values are positive. Additionally, the reduction of nickel fluoride (7) takes place at temperatures equal to or higher than 673 K.

Thermodynamic analysis of metal oxides-hydrogen reactions

The interaction of metal oxides with hydrogen can proceed according to the following reactions

$$Al_2O_3 + 3H_{2(g)} = 2Al + 3H_2O_{(g)}; \quad (8)$$

$$TiO_2 + 2H_{2(g)} = Ti + 2H_2O_{(g)}; \quad (9)$$

$$NiO + H_{2(g)} = Ni + H_2O_{(g)}; \quad (10)$$

$$WO_3 + 3H_{2(g)} = W + 3H_2O_{(g)}. \quad (11)$$

Analyzing the Gibbs energy of reactions (8) – (11) reveals that hydrogen reduces nickel oxide across the entire temperature range under consideration. Additionally, tungsten oxide reacts with hydrogen at temperatures exceeding 1173 K. This aligns with existing literature data1, which specifies that the reduction process of tungsten anhydride takes place in a hydrogen flow with moisture content not exceeding 2 g/m^3 and oxygen content not surpassing 0.4 vol. %.

Experimental

The study utilized a gas turbine engine nozzle blade provided by Perm Motors JSC as the subject of investigation.

[1] *Reduction of higher oxide of tungsten metal with hydrogen*. URL: https://stal-kom.ru/vosstanovleniye-vodorodom-vysshego-oksida-metalla-vol-frama/ (Accessed on: 03.03.2023).

Potassium bifluoride served as the source to generate hydrogen fluoride and facilitate the surface fluorination process. Thermal decomposition of potassium bifluoride occurred at temperatures exceeding 1023 K within a single-zone tube furnace manufactured by Protherm furnaces company. The fluorination process was conducted at a temperature of 1023 K for a duration of 2 h within an oxygen-free environment. To achieve this, the reactor underwent purging with argon, which was purified to eliminate traces of oxygen using copper chips and titanium sponge at temperatures up to 1073 K. After fluorination, the sample surface underwent reduction by hydrogen supplied from a hydrogen generator. This reduction process occurred at a temperature of 1223 K for a duration of 1 h. Subsequently, the sample was cooled to room temperature in an oxygen-free environment. The surface analysis of the sample was conducted using an S-3400N electron scanning microscope manufactured by HITACHI, Japan, equipped with an attachment from Bruker (Germany) for *X*-ray spectral and *X*-ray fluorescence analyses.

Results and discussion

The description provides an analysis of the blade surface post-fluorination and hydrogen reduction, illustrated in Fig. 1, highlighting the presence of small white-colored inclusions indicative of nickel particles. At a higher magnification (Fig. 2), the spherical nature of these nickel particles becomes apparent.

The composition analysis depicted in Fig. 3 confirms that these spherical particles, ranging in size from 2 to 5 μm, contain 90.16 % Ni. This observation leads to the conclusion that hydrogen effectively reduces nickel fluoride to elemental metallic nickel.

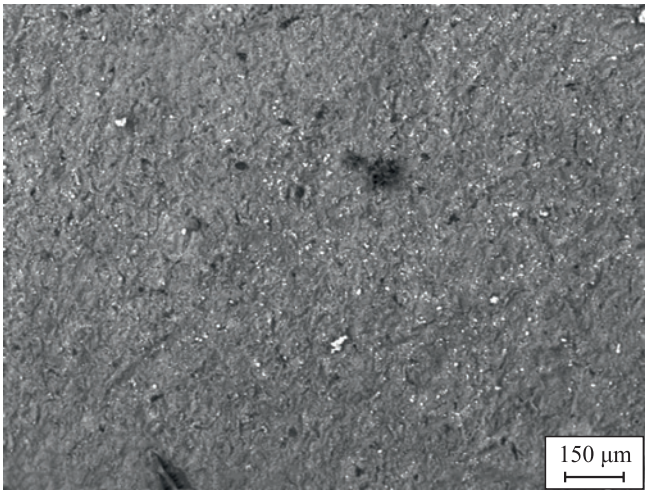

Fig. 1. Micrograph of the blade sample surface after fluorination and reduction with hydrogen

Рис. 1. Микрофотография поверхности образца лопатки после фторирования и восстановления водородом

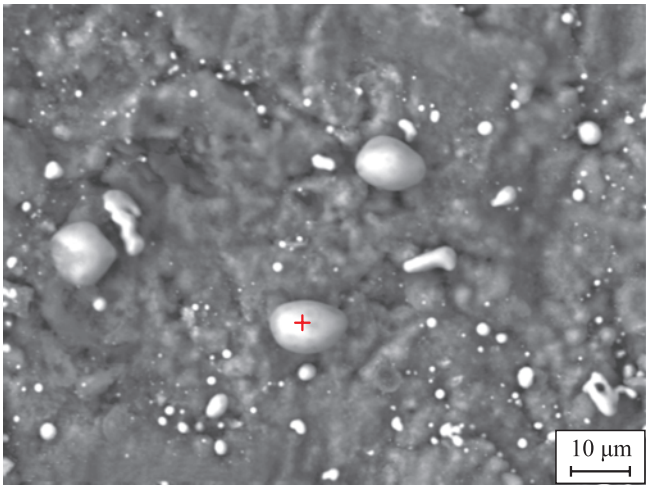

Fig. 2. Micrograph of nickel particles on the blade sample surface after fluorination and reduction with hydrogen

Рис. 2. Микрофотография частиц никеля на поверхности образца лопатки после фторирования и восстановления водородом

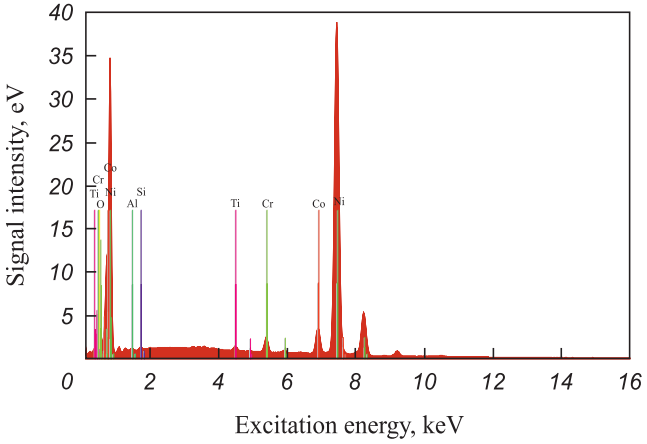

Fig. 3. Spectrum of a nickel particle on the blade sample surface after fluorination and reduction with hydrogen

Рис. 3. Спектр частицы никеля на поверхности образца лопатки после фторирования и восстановления водородом

In contrast, an experiment examining the interaction of a non-fluorinated sample with hydrogen at a temperature of 1223 K for a duration of 1 h showed different results, as depicted in Fig. 4. Unlike the previous case (Fig. 1), no nickel particles are observed on the surface of the blade. This absence of nickel reduction by hydrogen is contrary to the thermodynamic possibility of nickel oxide reduction with hydrogen. It was noted in [20] that structural and functional materials based on chromium and nickel demonstrate considerable resistance to hydrogen at both normal and elevated temperatures. The hindrance to the nickel reduction process with hydrogen seems to stem from kinetic limitations rather than thermodynamic factors. This limitation likely arises due to a dense film of aluminum, titanium, and tungsten oxides present on the sample surface. This film appears to impede

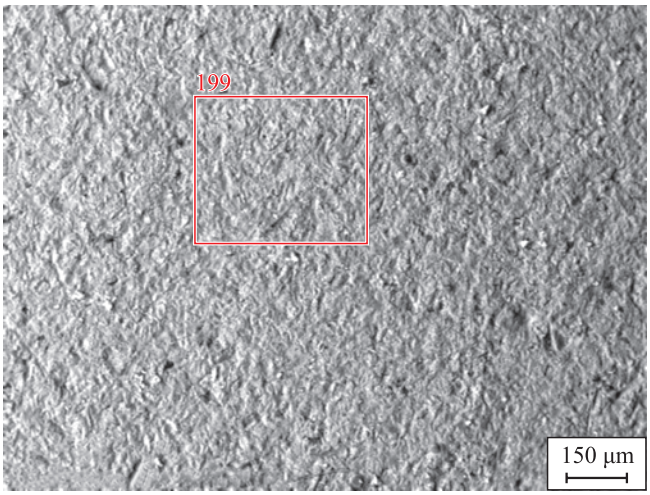

Fig. 4. Micrograph of the blade sample surface after hydrogen exposure

Рис. 4. Микрофотография поверхности образца лопатки после воздействия водорода

the process of hydrogen reduction of nickel oxide. When hydrogen fluoride interacts with the dense film comprising aluminum, titanium, and tungsten oxides, it initiates the destruction of this film. This promotes the reduction process by providing hydrogen the necessary access to the nickel oxide reaction zone.

Conclusions

A comprehensive thermodynamic analysis investigated the interaction of aluminum, titanium, nickel, and tungsten oxides with hydrogen fluoride across temperatures ranging from 273 to 1373 K. The findings revealed distinct temperature ranges for each oxide's interaction with hydrogen fluoride: aluminum oxide from 273 to 1073 K, titanium oxide from 273 to 373 K, and nickel oxide from 273 to 873 K. Notably, among the resulting fluorides, only nickel fluoride displayed reactivity with hydrogen above 673 K. Hydrogen reacts with nickel oxide over the entire temperature range, and with tungsten oxide at temperatures above 1173 K.

Further experimental observation showed that the reduction of nickel oxide occurred through fluorination followed by hydrogen reduction at 1223 K over a 1 h duration. This process resulted in the formation of 2 – 5 μm particles containing 90.16 % Ni on blade surfaces. Importantly, without fluorination, the reduction process of nickel oxide did not occur. This discrepancy was attributed to the presence of a dense film composed of aluminum, titanium, and tungsten oxides on the sample surface, impeding the hydrogen reduction of nickel oxide. Exposure to hydrogen fluoride disrupted this film by generating volatile aluminum and titanium fluorides, allowing hydrogen access to the nickel oxide reduction zone.

References / Список литературы

1. Radchenko R.V. *Hydrogen in Energy Sector*. Yekaterinburg: Izd-vo ural. un-ta; 2014:229. (In Russ.).

   Радченко Р.В. *Водород в энергетике*. Екатеринбург: Издательство Уральского университета; 2014:229.
2. Okonskii I.S., Osokin A.A., Fedyukov Yu.S. *Processes and Devices of Oxygen and Cryogenic Production*. Moscow: Mashinostroenie; 1985:256. (In Russ.).

   Оконский И.С., Осокин А.А., Федюков Ю.С. *Процессы и аппараты кислородного и криогенного производства*. Москва: Машиностроение; 1985:256.
3. Ugai Ya.A. *General and Inorganic Chemistry*. Moscow: Vyssh. shk.; 1997:527. (In Russ.).

   Угай Я.А. *Общая и неорганическая химия*. Москва: Высшая школа; 1997:527.
4. Ioffe V.B. *Basics of Hydrogen Production*. Leningrad: gos. nauchno-tekhnicheskoe izdatel'stvo neftyanoi i gorno-toplivnoi literatury; 1960:430. (In Russ.).

   Иоффе В.Б. *Основы производства водорода*. Ленинград: Государственное научно-техническое издательство нефтяной и горно-топливной литературы; 1960:430.
5. Izumi A., Ueno T., Miyazaki Y., Oizumi H., Nishiyama I. Reduction of oxide layer on various metal surfaces by atomic hydrogen treatment. *Thin Solid Films*. 2008;516(2-4):853–855. https://doi.org/10.1016/j.tsf.2007.06.097
6. Bryson J.P., Distin P.A. The recovery of nickel from laterrites by chelate formation and reduction with hydrogen. *Hydrometallurgy*. 1978;3(4):343–354. https://doi.org/10.1016/0304-386X(78)90038-5
7. Crundwell F.K., Moats M.S., Ramachandran V., Robinson T.G., Davenport W.G. Chapter 27 – Hydrogen reduction of nickel from ammoniacal sulfate solution. *Extractive Metallurgy of Nickel, Cobalt and Platinum Group Metals*. 2011:347–354. https://doi.org/10.1016/B978-0-08-096809-4.10027-9
8. Brecelj F., Mozetic M. Reduction of metal oxide thin layers by hydrogen plasma. *Vacuum*. 1990;40(1-2):177–181. https://doi.org/10.1016/0042-207X(90)90149-S
9. Guan J., Wang Y., Qin M., Yang Y., Li X., Wang A. Synthesis of transition-metal phosphides from oxidic precursors by reduction in hydrogen plasma. *Journal of Solid State Chemistry*. 2009;182(6):1550–1555. https://doi.org/10.1016/j.jssc.2009.03.026
10. Jabbour K., El Hassan N. Optimized conditions for reduction of iron (III) oxide into metallic form under hydrogen atmosphere: A thermodynamic approach. *Chemical Engineering Science*. 2022;252:117297. https://doi.org/10.1016/j.ces.2021.117297
11. Shanker Bhandari G., Dhawan N. Gaseous reduction of NMC-type cathode materials using hydrogen for metal recovery. *Process Safety and Environmental Protection*. 2023;172:523–534. https://doi.org/10.1016/j.psep.2023.02.053
12. Loginova D.I., Fomina D.D., Fedotova O.A., Poilov V.Z. Methods of cleaning the nozzle blades of a gas turbine engine from metal oxides. *Vestnik PNIPU. Khimicheskaya tekhnologiya i biotekhnologiya*. 2023;(1):19–34. (In Russ.). https://doi.org/10.15593/2224-9400/2023.1.02

   Логинова Д.И., Фомина Д.Д., Федотова О.А., Пойлов В.З. Способы очистки сопловых лопаток газотурбинного двигателя от оксидов металлов. *Вестник ПНИПУ. Хими-*

ческая технология и биотехнология. 2023;(1):19–34. https://doi.org/10.15593/2224-9400/2023.1.02

13. Fomina D.D., Poilov V.Z. Methods of cleaning the surface of blades of gas turbine engines from carbon deposits and oxidation products. In: *All-Russ. Sci. and Pract. Conf. with Int. Part. "Chemistry. Ecology. Urban Studies" April 28–29, 2022, Perm*. Perm: PNIPU; 2022:191–194.

    Fomina D.D., Poilov V.Z. Methods of cleaning the surface of the blades of gas turbine engines from carbon deposits and oxidation products. В кн.: *Всероссийская научно-практическая конференция с международным участием «Химия. Экология. Урбанистика» 28–29 апреля 2022 г., Пермь*. Пермь: Издательство «ПНИПУ»; 2022:191–194.
14. Pat. US4188237, CPC B23K 1/206. *Method for cleaning metal parts with elemental fluorine* / Jack W. Cyhasteen. 12.02.1980.
15. Pat. 4324594 US. *Method for cleaning metal parts* / Cyhasteen J.W. 13.04.1982.
16. Pat. 5071486 US. *Process for removing protective coatings and bonding layers from metal parts* / Jack W. Cyhasteen. 10.12.1991.
17. Pai Z.P., Parmon V.N., Pai V.V., Fedotenko M.A., Iakovlev I.V., Shangina A.B. *Contact solution, method and installation for cleaning the surface of metal alloys, including the surface of cracks and narrow gaps*. Patent RF no. 2419684. *Bulleten' izobretenii*. 2013;(33). (In Russ.).

    Пат. 2419684 RU. *Контактный раствор, способ и установка для очистки поверхности металлических сплавов в том числе поверхности трещин и узких зазоров* / Пай З.П., Пармон В.Н., Пай В.В., Федотенко М.А., Яковлев И.В., Шангина А.Б.; заявлено 04.06.2009; опубликовано 27.05.2011. *Бюллетень № 15*.
18. Ravdelya A.A., Ponomareva A.M. *Brief Reference Book of Physico-Chemical Quantities*. St. Petersburg: "Ivan Fedorov"; 2003:240. (In Russ.).

    Равделя А.А., Пономарева А.М. *Краткий справочник физико-химических величин*. Санкт-Петербург: «Иван Федоров»; 2003:240.
19. Myasoedov B.F. *Methods of Substances Concentration in Analytical Chemistry*. Moscow: Nauka; 1965:394. (In Russ.).

    Мясоедов Б.Ф. *Методы концентрирования веществ в аналитической химии*. Москва: Наука; 1965:394.
20. Fomina D.D., Poilov V.Z. Study of new structural and functional materials and coating resistant to hydrogen environment. *Vestnik PNIPU. Khimicheskaya tekhnologiya i biotekhnologiya*. 2022;(2):55–72. (In Russ.). https://doi.org/10.15593/2224-9400/2022.2.04

    Фомина Д.Д., Пойлов В.З. Новые конструкционные и функциональные материалы и покрытия, устойчивые к водородсодержащим средам. *Вестник ПНИПУ. Химическая технология и биотехнология*. 2022;(2):55–72. https://doi.org/10.15593/2224-9400/2022.2.04

Сведения об авторах / Information about the Authors

Дарья Дмитриевна Фомина, *ассистент кафедры «Химические технологии»,* Пермский национальный исследовательский политехнический университет
ORCID: 0009-0009-8974-2564
E-mail: Fomina97@yandex.ru

Dar'ya D. Fomina, *Assistant of the Chair of "Chemical Engineering",* Perm National Research Polytechnic University
ORCID: 0009-0009-8974-2564
E-mail: Fomina97@yandex.ru

Владимир Зотович Пойлов, *д.т.н., профессор кафедры «Химические технологии», руководитель ЦКП «Центр наукоёмких химических технологий и физико-химических исследований»,* Пермский национальный исследовательский политехнический университет
E-mail: vladimirpoilov@mail.ru

Vladimir Z. Poilov, *Dr. Sci. (Eng.), Prof. of the Chair "Chemical Engineering", Head of the Shared Collective Use Center "Center for High-tech Chemical Technologies and Physico-Chemical Research",* Perm National Research Polytechnic University
E-mail: vladimirpoilov@mail.ru

Андрей Николаевич Галлямов, *аспирант кафедры «Химические технологии»,* Пермский национальный исследовательский политехнический университет
E-mail: andrewg96@mail.ru

Andrei N. Gallyamov, *Postgraduate of the Chair "Chemical Engineering",* Perm National Research Polytechnic University
E-mail: andrewg96@mail.ru

Вклад авторов / Contribution of the Authors

Д. Д. Фомина – поиск и анализ литературных данных по методам очистки, проведение экспериментальной части фторирования, анализ данных по экспериментам, написание статьи, перевод.
В. З. Пойлов – обработка литературных данных, анализ экспериментальных данных, написание статьи.
А. Н. Галлямов – поиск и анализ литературных данных по восстановительным характеристикам водорода, проведение экспериментальной части наводораживания.

D. D. Fomina – search and analysis of literary data on purification methods, conducting the experimental part of fluoridation, analysis of experimental data, writing the text, translation.
V. Z. Poilov – processing of literary data, analysis of experimental data, writing the text.
A. N. Gallyamov – search and analysis of literary data on the reducing characteristics of hydrogen, conducting the experimental part of hydrogen-charging.

Поступила в редакцию 25.05.2023
После доработки 10.06.2023
Принята к публикации 04.09.2023

Received 25.05.2023
Revised 10.06.2023
Accepted 04.09.2023

PHYSICO-CHEMICAL BASICS OF METALLURGICAL PROCESSES / **ФИЗИКО-ХИМИЧЕСКИЕ ОСНОВЫ МЕТАЛЛУРГИЧЕСКИХ ПРОЦЕССОВ**

UDC 669.15:544.344.3:546.17:546.73
DOI 10.17073/0368-0797-2023-5-610-612

Short report
Краткое сообщение

WAGNER INTERACTION COEFFICIENT BETWEEN NITROGEN AND COBALT IN LIQUID STEEL

L. A. Bol'shov, S. K. Korneichuk, E. L. Bol'shova

Vologda State University (15 Lenina Str., Vologda 16000, Russian Federation)

korn62@mail.ru

Abstract. A simple theory of thermodynamic properties of liquid nitrogen solutions in Fe–Co alloys is proposed. This theory is completely analogous to the theory for liquid nitrogen solutions in alloys of the Fe–Cr system proposed previously by the authors in 2019. The theory is based on lattice model of the Fe–Co solutions. The model assumes FCC lattice. In the sites of this lattice are the atoms of Fe and Co. Nitrogen atoms are located in octahedral interstices. The nitrogen atom interacts only with the metal atoms located in the lattice sites neighboring to it. This interaction is pairwise. It is supposed that the liquid solutions of Fe–Co system are perfect. The initial values for the calculation are the Sieverts law constants for nitrogen solubility in liquid iron and in liquid cobalt. Result of the calculation is value of Wagner interaction coefficient in liquid iron-based alloys at 1873 K $\varepsilon_N^{Co} = 1.8$. This value is in good agreement with the experimental data obtained by Schenck, Frohberg and Graf, 1958; Maekawa and Nakagawa, 1960.

Keywords: thermodynamics, solutions, nitrogen, iron, cobalt, Wagner interaction coefficient, Langenberg interaction coefficient, Sieverts law

For citation: Bol'shov L.A., Korneichuk S.K., Bol'shova E.L. Wagner interaction coefficient between nitrogen and cobalt in liquid steel. *Izvestiya. Ferrous Metallurgy*. 2023;66(5):610–612. https://doi.org/10.17073/0368-0797-2023-5-610-612

ВАГНЕРОВСКИЙ ПАРАМЕТР ВЗАИМОДЕЙСТВИЯ АЗОТА С КОБАЛЬТОМ В ЖИДКОЙ СТАЛИ

Л. А. Большов, С. К. Корнейчук, Э. Л. Большова

Вологодский государственный университет (Россия, 160000, Вологда, ул. Ленина, 15)

korn62@mail.ru

Аннотация. Предложена простая теория термодинамических свойств жидких растворов азота в сплавах системы Fe–Co. Эта теория полностью аналогична теории для жидких растворов азота в сплавах системы Fe– Cr, предложенной авторами в 2019 г. Теория основана на решеточной модели растворов Fe–Co. Предполагается модельная решетка типа ГЦК. В узлах этой решетки располагаются атомы железа и кобальта. Атомы азота располагаются в октаэдрических междоузлиях. Атом азота взаимодействует с атомами металлов, находящимися в соседних с этим атомом узлах решетки. Это взаимодействие парное. Предполагается, что жидкие растворы системы Fe–Co являются совершенными. В качестве исходных для расчетов взяты значения констант закона Сивертса для растворимости азота в жидком железе и в жидком кобальте. Результатом расчета является значение вагнеровского параметра взаимодействия в жидких сплавах на основе железа при температуре 1873 К $\varepsilon_N^{Co} = 1{,}8$. Это хорошо согласуется с экспериментальными данными, полученными Шенк, Фроберг, Граф в 1958 г. и Маекава, Накагава в 1960 г.

Ключевые слова: термодинамика, растворы, азот, железо, кобальт, вагнеровский параметр взаимодействия, лангенберговский параметр взаимодействия, закон Сивертса

Для цитирования: Большов Л.А., Корнейчук С.К., Большова Э.Л. Вагнеровский параметр взаимодействия азота с кобальтом в жидкой стали. *Известия вузов. Черная металлургия*. 2023;66(5):610–612. https://doi.org/10.17073/0368-0797-2023-5-610-612

To predict the solubility of nitrogen in liquid steel, understanding the nitrogen solubility in liquid iron is crucial, along with at least obtaining the first order interaction coefficients between nitrogen and alloying elements. Typically, these coefficients are derived from experimental investigations of nitrogen solubility in the melts of binary metal systems like Fe – j, rwhere iron serves as the solvent and j represents the alloying element. Nevertheless, values obtained through this method often encompass experimental uncertainties, occasionally

of significant magnitude. This scenario also holds true for the interaction between nitrogen and cobalt.

Currently, cobalt finds diverse technological applications, including its use in alloying special steels known for their high-speed, magnetic, and heat-resistant properties. The significance of the Wagner interaction coefficient between nitrogen and cobalt in liquid steel lacks consensus. Hence, an intriguing avenue lies in investigating this matter from a theoretical perspective.

To delve into the thermodynamics of nitrogen solutions in the Fe – Co system's liquid alloys, we denote the concentrations of the components in molar fractions as c_{Fe}, c_{Co} and c_N. Alternatively, expressing these concentrations in mass percentages yields [% Fe], [% Co] and [% N]. Let a_N means present the thermodynamic activity of nitrogen in the solution, $\gamma_N = \frac{a_N}{c_N}$ – the rational coefficient of nitrogen activity in the solution, $f_N = \frac{a_N}{[\%\ N]}$ – the mass-percentage coefficient of nitrogen activity. The thermodynamic first order interaction coefficients between nitrogen and cobalt in liquid iron-based alloys of the Fe–Co–N systems are determined by the following formulas

$$\varepsilon_N^{Co} = \frac{\partial \ln \gamma_N}{\partial c_{Co}} \text{ при } c_{Fe} \to 1;$$

$$e_N^{Co} = \frac{\partial \lg f_N}{\partial [\%\ Co]} \text{ при } [\%\ Fe] \to 100,$$

where ε_N^{Co} is the Wagner interaction coefficient, while e_N^{Co} is the Langenberg interaction coefficient. A correlation between these parameters is presented in [1]:

$$\varepsilon_N^{Co} = 230{,}3\frac{A_{Co}}{A_{Fe}}e_N^{Co} + \frac{A_{Fe} - A_{Co}}{A_{Fe}}, \quad (1)$$

where A_{Fe} and A_{Co} are the atomic masses of the corresponding elements.

The solubility of nitrogen in liquid alloys of the Fe–Co system, expressed in mass percentage, is denoted as $[\%\ N]^*$. At a partial pressure of nitrogen in the liquid phase P_{N_2} approaching zero $P_{N_2} \to 0$, the square root law, also known as Sieverts law, applies:

$$[\%\ N]^* = K'\sqrt{\frac{P_{N_2}}{P_0}},$$

where P_0 is the standard pressure ($P_0 = 1$ atm $\approx$ ≈ 0.101 MPa); K' is the Sieverts law constant. Let $K' = K'(Fe)$ at $c_{Fe} = 1$ and $K' = K'(Co)$ at $c_{Co} = 1$.

Following the proposed simple theory regarding the thermodynamic properties of liquid nitrogen solutions in Fe–Co alloy systems, an alignment is observed with the theoretical framework governing nitrogen solutions in Fe–Cr and Ni–Cr alloy systems [2]. The abstract of this paper outlines the theoretical model. Utilizing the findings from [2], we arrive at the model presented below:

$$\varepsilon_N^{Co} = 6\left(1 - \sqrt[6]{\frac{A_{Co}K'(Co)}{A_{Fe}K'(Fe)}}\right). \quad (2)$$

At a temperature of $T = 1873$ K $K'(Fe) = 0.044$ wt. % [3] and $K'(Co) = 0.0047$ wt. % [4]. With $A_{Fe} = 55.847$ and $A_{Co} = 58.9332$. applying formula (2) yields the theoretical Wagner interaction coefficient between nitrogen and cobalt in liquid steel at $T = 1873$ K as $\varepsilon_N^{Co} = 1.8$. Subsequently, equation (1) provides the corresponding value of the Langenberg interaction coefficient $e_N^{Co} = 0.0076$.

Consideration of experimental values of the e_N^{Co} coefficient in liquid steel at $T = 1873$ K reveals various findings. In [5], nitrogen solubility in Fe–Co alloys was studied by quenching samples to a concentration of [% Co] = 24 wt. %, resulting in an estimated $e_N^{Co} = 0.0072$. Continuation of this study in [6] up to [% Co] = 100 wt. % produced an estimate for nitrogen solubility in liquid cobalt, $K'(Co) = 0.0044$ wt. %, which closely aligns with the value used in this paper, $K'(Co) = 0.0047$ wt. %.

In [7], an experimental value of $e_N^{Co} = 0.007$ was reported.

Additionally, [8] investigated the nitrogen solubility in melts of the Fe–Co system using the Sieverts method, determining an experimental estimate of the interaction coefficient at 1873 K as $e_N^{Co} = 0.011$.

Comparing these estimates of the Langenberg interaction coefficient at $T = 1873$ K: $e_N^{Co} = 0.0072$ [5] and $e_N^{Co} = 0.007$ [7] are closer to the theoretical estimate $e_N^{Co} = 0.0076$ than the experimental one $e_N^{Co} = 0.011$ [8]. Consequently, based on the theory presented in this paper, the estimates from [5] and [7] appear more plausible than the one described in [8].

Conclusions

Theoretical estimates for the thermodynamic first-order interaction coefficients between nitrogen and cobalt in liquid steel at $T = 1873$ K: $\varepsilon_N^{Co} = 1.8$; $e_N^{Co} = 0.0076$.

The experimental estimates of the Langenberg interaction coefficient $e_N^{Co} = 0.0072$ [5] and $e_N^{Co} = 0.007$ [7] appear more credible or reliable compared to the estimate $e_N^{Co} = 0.011$ [8].

References / Список литературы

1. Lupis C.H.P., Elliott J.F. The relation between interaction coefficients ε and *e*. *Transactions of the Metallurgical Society of AIME*. 1965;233(1):257–258.
2. Большов Л.А., Корнейчук С.К., Большова Э.Л. Вагнеровский параметр взаимодействия азота с хромом в жидких сплавах на основе никеля. *Известия вузов. Черная металлургия*. 2021;64(9):693–697. https://doi.org/10.17073/0368-0797-2021-9-693-697

Bol'shov L.A., Korneichuk S.K., Bol'shova E.L. Wagner interaction coefficient between nitrogen and chromium in liquid nickel-based alloys. *Izvestiya. Ferrous Metallurgy.* 2021;64(9):693–697. (In Russ.). https://doi.org/10.17073/0368-0797-2021-9-693-697

3. Turnock R.H., Pehlke R.D. The solubility of nitrogen in multicomponent liquid iron alloys. *Transactions of the Metallurgical Society of AIME*. 1966;236(11):1540–1547.
4. Blossey K.G., Pehlke R.D. Solubility of nitrogen in liquid cobalt alloys. *Transactions of the Metallurgical Society of AIME*. 1966;236(1):28–32.
5. Schenck H., Frohberg M.G., Graf H. Untersuchung über die Beeinflussung der Gleichgewichte von Stickstoff mit flüssigen Eisenlösungen durch den Zusatz weiterer Elemente (I). *Archiv für das Eisenhüttenwesen*. 1958;29(11):673–676. (In Germ.). https://doi.org/10.1002/srin.195803011
6. Schenck H., Frohberg M.G., Graf H. Untersuchung über die Beeinflussung der Gleichgewichte von Stickstoff mit flüssigen Eisenlösungen durch den Zusatz weiterer Elemente (II). *Archiv für das Eisenhüttenwesen*. 1959;30(9):533–537. (In Germ.). https://doi.org/10.1002/srin.195903074
7. Maekawa S., Nakagawa Y. The solubility of nitrogen in liquid iron alloys. II. Effect of nickel, cobalt, molybdenum, chromium and vanadium on the solubility of nitrogen in liquid iron alloys. *Tetsu-to-Hagane*. 1960;46(9):972–976. https://doi.org/10.2355/tetsutohagane1955.46.9_972
8. Pehlke R.D., Elliott J.F. Solubility of nitrogen in liquid iron alloys. I. Thermodynamics. *Transactions of the Metallurgical Society of AIME*. 1960;218(6):1088–1101.

Information about the Authors / Сведения об авторах

Leonid A. Bol'shov, *Dr. Sci. (Phys.–Math.), Prof. of the Chair of Mathematics and Informatics*, Vologda State University
E-mail: labolshov@mail.ru

Svetlana K. Korneichuk, *Cand. Sci. (Phys.–Math.), Assist. Prof. of the Chair of Physics*, Vologda State University
E-mail: korn62@mail.ru

Elina L. Bol'shova, *Assist. Prof. of the Chair of English*, Vologda State University
E-mail: labolshov@mail.ru

Леонид Абрамович Большов, *д.ф.-м.н., профессор кафедры математики и информатики*, Вологодский государственный университет
E-mail: labolshov@mail.ru

Светлана Константиновна Корнейчук, *к.ф.-м.н., доцент кафедры физики*, Вологодский государственный университет
E-mail: korn62@mail.ru

Элина Леонидовна Большова, *доцент кафедры английского языка*, Вологодский государственный университет
E-mail: labolshov@mail.ru

Contribution of the Authors / Вклад авторов

L. A. Bol'shov – formation of the article idea, writing the text.
S. K. Korneichuk – verification of the proposed method and results, formatting the paper and accompanying documents.
E. L. Bol'shova – translation of English articles, translation into English of the abstract and references.

Л. А. Большов – идея и текст статьи.
С. К. Корнейчук – анализ метода и результатов, оформление текста и документации, переписка с редакцией.
Э. Л. Большова – перевод на русский язык англоязычных статей, перевод на английский язык аннотации и библиографического списка.

Received 29.06.2023
Revised 07.07.2023
Accepted 27.08.2023

Поступила в редакцию 29.06.2023
После доработки 07.07.2023
Принята к публикации 27.08.2023

Information technologies and automatic control in ferrous metallurgy / **Информационные технологии и автоматизация в черной металлургии**

UDC 621.783.223:621.365
DOI 10.17073/0368-0797-2023-5-613-615

Short report
Краткое сообщение

On the study of pulsed metal heating

A. D. Apasova, I. A. Levitskii, K. S. Shatokhin

National University of Science and Technology "MISIS" (4 Leninskii Ave., Moscow 119049, Russian Federation)

annhope@bk.ru

Abstract. The work makes it possible to simplify development of pulsed metal heating technology. A software product was created to select the optimal values of operating parameters of pulsed heating on a mathematical model, which significantly reduces the setup time of a thermal unit using this technology. Test calculations showed adequacy of the results obtained to the operating parameters of functioning through-pass heating furnaces equipped with high-speed jet burners. The problems of controlling metal heating became particularly relevant due to the proliferation of high-performance rolling mills and increasing requirements for the quality of metal heating. In this regard, full implementation of the research program will make it possible to develop specific recommendations for increasing the productivity of heating furnaces and improving their energy efficiency.

Keywords: heating mode, automatic process control system, impulse heating, heat furnaces, mathematical model, gas burner, temperature, metal

For citation: Apasova A.D., Levitskii I.A., Shatokhin K.S. On the study of pulsed metal heating. *Izvestiya. Ferrous Metallurgy*. 2023;66(5): 613–615. https://doi.org/10.17073/0368-0797-2023-5-613-615

К исследованию импульсного нагрева металла

А. Д. Апасова, И. А. Левицкий, К. С. Шатохин

Национальный исследовательский технологический университет «МИСИС» (Россия, 119049, Москва, Ленинский пр., 4)

annhope@bk.ru

Аннотация. Результаты данной работы позволяют упростить отработку технологии импульсного нагрева металла. Создан программный продукт для подбора оптимальных значений режимных параметров импульсного нагрева на математической модели, что существенно сокращает время наладки теплового агрегата, использующего эту технологию. Тестовые расчеты показали адекватность полученных результатов режимным параметрам функционирующих проходных нагревательных печей, оснащенных скоростными струйными горелками. Проблемы управления нагревом металла стали особенно актуальны в связи с распространением высокопроизводительных прокатных станов и все более повышающимися требованиями, предъявляемыми к качеству нагрева металла. В связи с этим, полная реализация программы исследований позволит выработать конкретные рекомендации по увеличению производительности нагревательных печей и улучшению показателей их энергоэффективности.

Ключевые слова: режим нагрева, АСУ ТП, импульсный нагрев, нагревательные печи, математическая модель, газовая горелка, температура, металл

Для цитирования: Апасова А.Д., Левицкий И.А., Шатохин К.С. К исследованию импульсного нагрева металла. *Известия вузов. Черная металлургия*. 2023;66(5):613–615. https://doi.org/10.17073/0368-0797-2023-5-613-615

The pursuit of hidden reserves of energy-saving measures and their utilization represents a crucial factor in enhancing the competitiveness of products. Among finished products, rolling production ranks second in terms of energy consumption, following blast furnace ironmaking. Notably, gas and electricity constitute 95 % of the costs, with 60 % allocated to the heating of ingots for the rolling process [1].

When calculating energy costs in the technological process of metal heating, several approaches are considered:

– manufacturing furnaces with minimal heat release into the environment and the impact of these losses on the metal heating process;

– achieving optimum metal processing temperatures within a shorter duration;

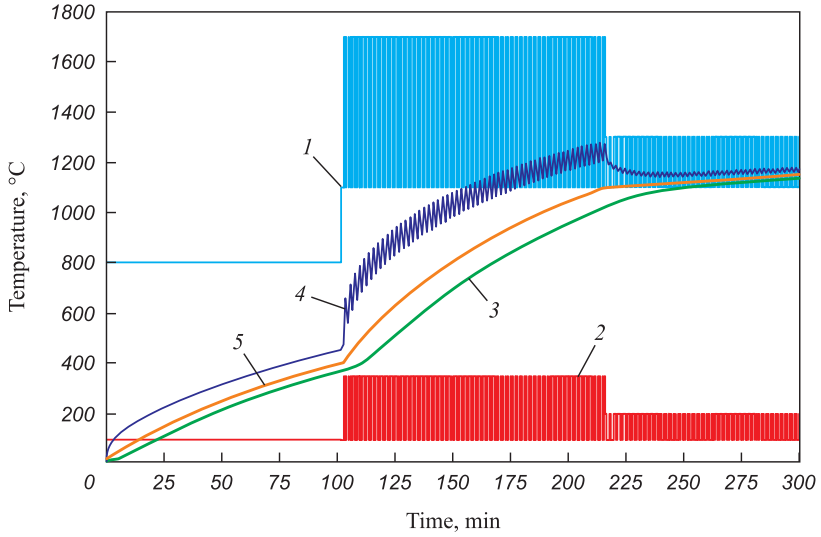

Pulse mode of metal heating:
1 – temperature of the medium, °C; *2* – heat transfer coefficient, W/(m²·K); *3* – ingot center temperature, °C;
4 – ingot surface temperature, °C; *5* – ingot average temperature, °C

Импульсный режим нагрева металла:
1 – температура среды, °C; *2* – коэффициент теплоотдачи, Вт/(м²·K); *3* – температура центра заготовки, °C;
4 – температура поверхности заготовки, °C; *5* – средняя темпертура заготовки, °C

– enhancing the automatic process control system [2 – 4].

The method employed for heating metal ingots, adhering to specified requirements, must achieve optimal temperature conditions within a brief period while exerting localized effects yet transferring adequate heat for processing ingots have a localized effect, but at the same time transfer enough heat to process ingots. Pulse modes of metal heating are considered a technology that fulfills these criteria.

High-speed jet burners operating on natural gas constitute the primary class of burner devices utilized in pulsed heating systems [5]. Pulsed heating relies on either an automatic interrupt-based positioning system or an interruption system with adjustable pulse frequency and ratio, where the "on-off" period ranges from 0.5 to 2.5 min. The convection coefficient a_{conv} can reach 300 W/(m²·K) or higher [6].

Determining the operating mode of the burners is typically achieved through experimentation during the setup of thermal generating units, a process that is time-consuming due to the high thermal inertia of furnaces. Hence, it is advisable to preliminarily determine the operating parameters of pulsed heating using a mathematical model.

A program has been developed to simulate the outcomes of the following process: an ingot in the form of a plate or cylinder, possessing a homogeneous temperature field, is placed within a through-pass heating furnace. In this setup, the zones are defined with specific temperatures and a_{conv} values corresponding to the "on" and "off" states of burners. The "on – off" modes switch once the set heating time t or the set temperature difference ΔT across the ingot's thickness is reached.

The provided figure illustrates the furnace temperature conditions and the metal heating interval, considering the following parameters:

– temperature in the methodical zone without burners: 800 °C, a_{conv}: 100 W/(m²·K);

– temperature and a_{conv} in the welding zone for the "on" and "off" modes: 1700 °C and 300 W/(m²·K), 1100 °C and 100 W/(m²·K), respectively;

– temperature and a_{conv} in the soaking zone for the "on" and "off" modes: 1300 °C and 200 W/(m²·K), 1100 °C and 100 W/(m²·K), respectively;

– burners' operation and shutdown time: 1 min.

Conclusions

The software product has been developed to optimize the operating parameters for pulsed heating of metal in through-pass heating furnaces.

Successful implementation of the research program will enable the formulation of recommendations aimed at improving furnace productivity and enhancing the energy efficiency of the ingot heating process.

References / Список литературы

1. Fastykovskii A.R. Energy saving technology for rolling varietal profiles. *Tekhnicheskie nauki – ot teorii k praktike*. 2016;11(59):52–56. (In Russ.).

Фастыковский А.Р. Энергосберегающие технологии получения сортовых прокатных профилей. *Технические науки – от теории к практике*. 2016;11(59):52–56.

2. Korobeinikov V.V., Tkachenko S.S. Energy saving heating units of new generation. *Lit'e i metallurgiya*. 2017;3(88): 34–38. (In Russ.).

   Коробейников В.В., Ткаченко С.С. Энергосберегающие нагревательные агрегаты нового поколения. *Литье и металлургия*. 2017;3(88):34–38.
3. Panferov V.I. About economic management of heating metal in industrial furnaces. *Vestnik YuUrGU. Series: Computer technologies, control, radio electronics*. 2018;18(2):71–80. (In Russ.). https://doi.org/10.14529/ctcr180207

   Панферов В.И. Об экономичном управлении нагревом металла в промышленных печах. *Вестник ЮУрГУ. Серия: Компьютерные технологии, управление, радиоэлектроника*. 2018;18(2):71–80. https://doi.org/10.14529/ctcr180207
4. Andreev S.M., Parsunkin B.N., Akhmetov T.U. Perfecting information support energy-saving modes of heating metal. *Russian Internet Journal of Industrial Engineering*. 2015;3(2):122–127. (In Russ.).

   Андреев С.М., Парсункин Б.Н., Ахметов Т.У. Совершенствование информационного обеспечения энергосберегающих режимов нагрева металла. *Машиностроение: сетевой электронный научный журнал*. 2015;3(2):122–127.
5. Boom R. Research fund for coal and steel RFCS: a European success story. *Ironamking & Steelmaking*. 2014;41(9):647–652. https://doi.org/10.1179/0301923314Z.000000000313
6. Sibikin Yu.D., Sibikin M.Yu. *Technology of Energy Saving*. Moscow: FORUM, INFRA-M; 2006:352. (In Russ.).

   Сибикин Ю.Д., Сибикин М.Ю. *Технология энергосбережения*. Москва: ФОРУМ, ИНФРА-М; 2006:352.

Information about the Authors / Сведения об авторах

Anna D. Apasova, *Postgraduate of the Chair "Energy-Efficient and Resource-Saving Industrial Technologies"*, National University of Science and Technology "MISIS"
E-mail: annhope@bk.ru

Igor' A. Levitskii, *Cand. Sci. (Eng.), Assist. Prof. of the Chair "Energy-Efficient and Resource-Saving Industrial Technologies"*, National University of Science and Technology "MISIS"
ORCID: 0000-0002-9345-3628
E-mail: lewwwis@mail.ru

Konstantin S. Shatokhin, *Cand. Sci. (Eng.), Assist. Prof. of the Chair "Energy-Efficient and Resource-Saving Industrial Technologies"*, National University of Science and Technology "MISIS"
E-mail: shatohin_ks@mail.ru

Анна Дмитриевна Апасова, *аспирант кафедры энергоэффективных и ресурсосберегающих промышленных технологий*, Национальный исследовательский технологический университет «МИСИС»
E-mail: annhope@bk.ru

Игорь Анисимович Левицкий, *к.т.н., доцент кафедры энергоэффективных и ресурсосберегающих промышленных технологий*, Национальный исследовательский технологический университет «МИСИС»
ORCID: 0000-0002-9345-3628
E-mail: lewwwis@mail.ru

Константин Станиславович Шатохин, *к.т.н., доцент кафедры энергоэффективных и ресурсосберегающих промышленных технологий*, Национальный исследовательский технологический университет «МИСИС»
E-mail: shatohin_ks@mail.ru

Contribution of the Authors / Вклад авторов

A. D. Apasova – model construction, calculations.
I. A. Levitskii – consulting on model construction.
K. S. Shatokhin – conceptualization.

А. Д. Апасова – построение модели, выполнение расчетов.
И. А. Левицкий – консультации в построении модели.
К. С. Шатохин – концепция исследования.

Received 23.06.2023
Revised 22.07.2023
Accepted 29.08.2023

Поступила в редакцию 23.06.2023
После доработки 22.07.2023
Принята к публикации 29.08.2023

On the materials of the International conference "Scientific and Practical School for Young Metallurgists" – 2023

По материалам международной конференции «Научно-практическая школа для молодых металлургов» – 2023

UDC 669.168
DOI 10.17073/0368-0797-2023-5-616-622

Original article
Оригинальная статья

Physicochemical characteristics of new complex niobium-containing alloys

O. V. Zayakin, I. N. Kel' ✉, **D. S. Renev, A. V. Sychev, L. Yu. Mikhailova, A. V. Dolmatov**

Institute of Metallurgy, Ural Branch of the Russian Academy of Sciences (101 Amundsena Str., Yekaterinburg 620016, Russian Federation)

✉ dunnington@mail.ru

Abstract. The authors studied the physicochemical characteristics of new complex alloys containing, %: 11 – 30 Nb, 23 – 28 Si, 3 – 10 Al and 3 – 4 Ti. It was shown that complex alloys have the most favorable values of density and crystallization temperatures compared to standard ferroniobium (60 wt. % Nb). Complex alloys with a low concentration of niobium have acceptable crystallization temperatures and optimal density values (5740 – 6560 kg/m^3). This allows the pieces of ferroalloy to be completely in the liquid steel when it is released into the ladle, and to be constantly in motion, which increases absorption of the leading components. When the niobium concentration increases to 30 %, phase composition of the alloy changes: a decrease in the proportion of the low-temperature FeSi phase with low density values and an increase in the proportion of the high-density ternary compound $NbFeSi_2$ with a crystallization temperature of ~1713 °C. An increase in Nb concentration from 11 to 17 % leads to a decrease in the crystallization temperature, and a further increase to 30 % Nb, on the contrary, is accompanied by an increase in the liquidus and solidus temperatures to 1700 and 1610 °C, respectively, which is consistent with liquidus line in phase diagram of the Fe–Nb system with a minimum in Nb concentration range ~18 %. The best characteristics, both from the point of view of obtaining ferroalloys and use for alloying steel, belong to an alloy containing, wt. %: 17.1 Nb, 24.6 Si, 7.6 Al and 3 Ti. This alloy is characterized by the temperature of crystallization onset (1550 °C) below the liquid steel bath temperature and belongs to the category of low-melting alloys. It has optimal density values – 6390 kg/m^3, which has a positive effect on the performance characteristics of niobium ferroalloys.

Keywords: metallurgy, niobium, silicon, physicochemical properties, crystallization temperature, density, complex ferroalloy, phase composition

Acknowledgements: The work was supported by the Russian Science Foundation, grant No. 21-19-00252, https://rscf.ru/project/21-19-00252/.

For citation: Zayakin O.V., Kel' I.N., Renev D.S., Sychev A.V., Mikhailova L.Yu., Dolmatov A.V. Physicochemical characteristics of new complex niobium-containing alloys. *Izvestiya. Ferrous Metallurgy*. 2023;66(5):616–622. https://doi.org/10.17073/0368-0797-2023-5-616-622

Физико-химические характеристики новых комплексных ниобийсодержащих сплавов

О. В. Заякин, И. Н. Кель ✉, **Д. С. Ренев, А. В. Сычев, Л. Ю. Михайлова, А. В. Долматов**

Институт металлургии Уральского отделения РАН (Россия, 620016, Екатеринбург, ул. Амундсена, 101)

✉ dunnington@mail.ru

Аннотация. В работе изучены физико-химические характеристики новых комплексных сплавов, содержащих, %: 11 – 30 Nb, 23 – 28 Si, 3 – 10 Al и 3 – 4 Ti. Показано, что комплексные сплавы с пониженной концентрацией ниобия обладают наиболее благоприятными значениями плотности и температур кристаллизации по сравнению со стандартным феррониобием, содержащим 60 % (по массе) Nb. Переход от высокопроцентного феррониобия к комплексным сплавам с пониженной концентрацией ниобия позволяет перевести сплавы из группы сверхтугоплавких в тугоплавкие, обладающие оптимальными значениями плотности (5740 – 6560 кг/м^3). Они полностью погружаются в жидкую сталь при выпуске в ковш, благодаря чему находятся в движении, не подвергаются окислению кислородом атмосферы и характеризуются более высокими и стабильными показателями степени усвоения ведущих компонентов. При увеличении концентрации ниобия до 30 % происходит изменение фазового состава сплава: снижение доли низкотемпературной фазы FeSi с низкими значениями плотности и увеличение доли высокоплотного тройного соединения $NbFeSi_2$ с температурой начала кристаллизации ~1713 °C. Увеличение концентрации ниобия с 11 до 17 % приводит

к уменьшению температуры кристаллизации, а дальнейшее повышение до 30 %, наоборот, сопровождается увеличением температур ликвидуса и солидуса до 1700 и 1610 °С соответственно. Это согласуется с линией ликвидуса на диаграмме состояния двойной системы Fe–Nb с минимумом в области концентрации ниобия ~18 %. Наилучшими характеристиками, как с точки зрения получения ферросплавов, так и применения для легирования стали, обладает сплав, содержащий, % (по массе): 17,1 Nb, 24,6 Si, 7,6 Al и 3 Ti. Данный сплав характеризуется температурой начала кристаллизации 1550 °С (ниже температуры жидкой стальной ванны) и относится к разряду легкоплавких сплавов, обладает оптимальной плотностью 6390 кг/м^3, что благоприятно отражается на служебных характеристиках ниобиевых ферросплавов.

Ключевые слова: металлургия, ниобий, кремний, физико-химические характеристики, температура кристаллизации, плотность, комплексный сплав, фазовый состав

Благодарности: Исследование выполнено за счет гранта Российского научного фонда № 21-19-00252, https://rscf.ru/project/21-19-00252/.

Для цитирования: Заякин О.В., Кель И.Н., Ренев Д.С., Сычев А.В., Михайлова Л.Ю., Долматов А.В. Физико-химические характеристики новых комплексных ниобийсодержащих сплавов. *Известия вузов. Черная металлургия*. 2023;66(5):616–622. https://doi.org/10.17073/0368-0797-2023-5-616-622

Introduction

In recent decades, there has been a significant increase in niobium consumption in Russia and globally. While previously primarily used to enhance the corrosion resistance of heat-resistant and stainless steels, niobium is now also employed to impart a strengthening effect in numerous grades of structural steel [1; 2].

Niobium, as an element, plays a crucial role in suppressing the recrystallization of austenite [3; 4]. The development of niobium carbonitrides Nb(C, N) near the grain boundaries of austenite leads to localized reduction in carbon concentration. The presence of the Nb(C, N) phase along the austenite grain boundaries serves as heterogeneous sites for initiating ferrite nucleation, thereby enhancing the metal's plastic properties. Simultaneously, dissolved niobium exists in a liquid state within the steel, resulting in a dual effect. It aids in refining grain size by impeding the growth of austenitic grains during austenitization, achieved through segregation at the grain boundary and a reduction in their energy. Consequently, this decelerates the grain-boundary transition of ferrite while promoting martensitic or bainitic transformations [4; 5]. The coexistence of both ferrite and bainite contributes to enhancements in strength, ductility, and toughness. Consequently, altering the niobium type in steel enables the modification of resulting properties.

Given the mechanism through which niobium influences steel properties, its primary application lies in structural grades of steel for various purposes such as large-diameter gas and oil pipelines, shipbuilding, transportation, etc. [4; 6 – 10].

It's important to highlight that within the global niobium consumption structure, the majority (over 88 %) is allocated for the production of high-strength low-alloy steels containing fractional percentages of niobium. The principal spectrum of niobium alloys consists primarily of various grades of ferroniobium, containing 55 – 70 wt. % Nb, manufactured through an aluminothermic process using pure niobium pentoxide or pyrochlore concentrate. Ferroalloys produced in Russian facilities typically contain, wt. %: 55 – 70 Nb; up to 6 Si; up to 8 Ti; up to 6 Al; up to 0.5 C; up to 0.3 S; up to 2 P; 1 – 8 Ta; the remaining component is Fe (State Standard GOST 16773 – 2003). The high concentration of niobium in the ferroalloy results in a higher melting point compared to the temperature of the molten metal (steel) being processed. This characteristic, in conjunction with the high density of the ferroalloy (~8500 kg/m^3), causes solid pieces of ferroniobium to settle at the bottom of the ladle, subsequently dissolving at a slower rate. Consequently, this significantly extends the steel's doping time and leads to an uneven distribution of niobium within the liquid metal volume [11].

Therefore, it is rational to explore the development of new complex niobium alloys that could offer more advantageous values for key parameters, including crystallization (melting) temperature and density [12].

The crystallization temperature (T_{cr}) plays a pivotal role in both the production technology of alloys and their operational characteristics. However, the precise definition of this term often varies among publications, leading to conflicting information. Some sources present T_{cr} as a specific value [13], while others express it as a temperature range [14]. In the case of binary and ternary compounds, T_{cr} can be derived from their phase diagrams. However, for multicomponent systems containing complex alloys, determining the crystallization temperature typically necessitates experimental investigation.

Multicomponent alloys typically exhibit a range of temperatures within which they melt. Consequently, the alloy's properties are more accurately characterized by the temperature at which crystallization initiates, known as the liquidus temperature T_l. However, discrepancies exist in publications regarding the optimal values for T_l [15 – 17]. According to the findings presented in [15], the melting temperature of ferroalloys should ideally fall within the range of 1100 – 1300 °C. Lower values might lead to oxidation of alloy components, necessitating the use of refractory materials to extend their melting duration. This paper proposes a conditional relative categorization of alloys into distinct groups based on temperature ranges: low-melting alloys ($T_l < T_{cr}$), refractory alloys ($T_{cr} < T_l < T_{st.\,bath.}$) and ultra-refractory alloys ($T_l > T_{st.\,bath.}$), where $T_{st.\,bath.}$ is the temperature of the steel bath.

Density (ρ) is an important technological property that significantly influences the degree and stability of assimilation of ferroalloy elements, the rate of their dissolution, and the uniformity of their distribution within the metal. This value is determined by the crystal structure and atomic mass of the elements comprising the alloy.

Density plays a crucial role in both the production and utilization of alloys. In ferroalloy production, it's essential that the densities of the metal and slag differ significantly. When their densities are too close, it results in increased metal losses due to inadequate separation of metal from slag. This complication significantly impacts the technology involved in ferroalloy production.

The determination of density in ferroalloys can be accomplished through both experimental methods and calculations. Rational density values for ferroalloys were established via simulation in a laboratory unit and through calculation methodologies [11]. Ferroalloys are typically categorized as heavy ($\rho > 7000$ kg/m^3), optimum ($\rho = 5000 – 7000$ kg/m^3), or light ($\rho < 5000$ kg/m^3). When introducing light ferroalloys into steel, they tend to become entrapped in slag and undergo partial oxidation. Conversely, heavy alloys settle at the bottom of ladles or melting units, slowly dissolving over time [18]. Alloys within the density range of 5000 – 7000 kg/m^3 either remain completely submerged in liquid steel or create a small open area above the surface (no more than 10 %). Such positioning allows these alloys to be in motion and avoids oxidation by atmospheric oxygen, aiding in better absorption. Typically, ferroalloys are introduced into steel in solid form during the metal's release from the furnace. The energy of the jet assists in mixing and immersing pieces of ferroalloy into the melt. Ferroalloys with optimum density are drawn into circulating bath streams, ensuring uniform distribution throughout the steel volume. This facilitates the complete and rapid dissolution of the ferroalloys.

Insufficient data regarding the properties of niobium ferroalloys are available in publications [19]. To develop rational compositions for new complex niobium-containing ferroalloys, the densities and crystallization temperatures of alloys within the Fe – Si – Al – Nb – Ti system were determined.

Materials and methods

The first stage of the experimentation involved obtaining experimental samples of complex alloys in laboratory settings using the method of melting in corundum crucibles within an argon flow, and these samples are outlined in Table 1.

Among the alloys presented in Table 1, alloy *4* was selected as the reference sample. This particular alloy, corresponding to the niobium content similar to FNb60 grade ferroniobium, was chosen due to its widespread use in modern steelmaking practices.

Table 1

Chemical composition of niobium-containing alloys, wt. %*

Таблица 1. **Химический состав ниобийсодержащих сплавов, % (по массе)***

Alloy No.	Nb	Si	Al	Ti
1	11.3	28.4	9.9	4.0
2	17.1	24.6	7.6	3.0
3	30.0	22.8	3.4	4.0
4	60.0	–	–	–

* Remainder: Fe and impurities.

To determine the crystallization temperatures, both the liquidus (T_l) and solidus (T_s) temperature curves were recorded during the cooling process of the alloys For this purpose, the samples were positioned within corundum crucibles placed in the operational zone of an electric resistance furnace. Temperature measurements were conducted using tungsten-rhenium thermocouples, specifically VR-5/20 with alundum tips, utilizing a Termodat-19M4 multimeter. During the measurements, one thermocouple's tip was placed at the center of the melt, while the other was positioned in the working space of the furnace in close proximity to the crucible containing the melt. The temperature of the melt was determined based on the readings of the first thermocouple, while the furnace temperature was determined using the second thermocouple.

The samples were heated to temperatures ranging from 50 – 100 °C above the anticipated crystallization initiation temperature. Subsequently, they were cooled at a controlled rate of 10 – 15 °C/min, and temperature plateaus were recorded on the cooling curves. The first region observed on the cooling curves corresponded to the T_l, while the second region corresponded to the T_s.

The density of solid ferroalloys was measured using the pycnometric method, which has sufficient accuracy and ease of experimentation, in accordance with State Standard GOST 22524 – 77 [20].

The chemical composition of the samples was determined using inductively coupled plasma atomic emission spectrometry. The phase composition of the samples was identified through *X*-ray phase analysis using a Shimadzu XRD 7000C diffractometer (Ural-M Center for Shared Use).

Results and discussion

The findings concerning the physicochemical characteristics of the investigated niobium-containing alloys are detailed in Table 2. It is evident that all the complex niobium alloys under study exhibit more favorable values in terms of density and crystallization temperatures

Table 2

Physicochemical characteristics of niobium-containing alloys

Таблица 2. **Физико-химические характеристики ниобийсодержащих сплавов**

Alloy No.	T_l, °C	T_s, °C	ρ, kg/m^3
1	1690	1650	5740
2	1550	1500	6390
3	1700	1610	6560
*4**	1720	–	8500

* Data from [11].

compared to high-percentage ferroniobium containing 60 % Nb.

Figs. 1 and 2 depict the relationships showcasing changes in density and crystallization temperatures of complex alloys in relation to the niobium content.

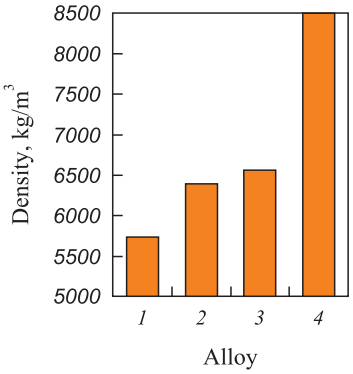

Fig. 1. Dependence of complex alloy density on niobium concentration

Рис. 1. Зависимость плотности комплексного сплава от концентрации ниобия

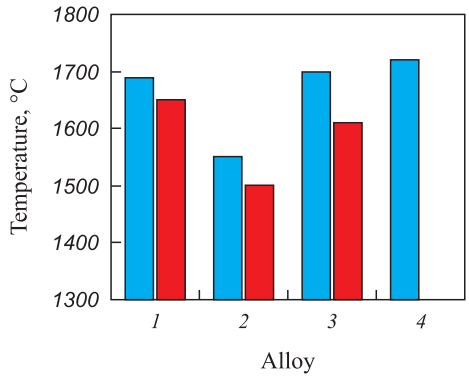

Fig. 2. Dependence of complex alloy crystallization temperatures on niobium concentration:
■ – liquidus; ■ – solidus

Рис. 2. Зависимость температур кристаллизации комплексного сплава от концентрации ниобия:
■ – ликвидус; ■ – солидус

A reduction in the niobium fraction within complex alloys from 30 to 11.3 wt. % demonstrates a positive impact on their density, notably decreasing from 6560 to 5740 kg/m^3. This is primarily attributed to niobium being the dens-

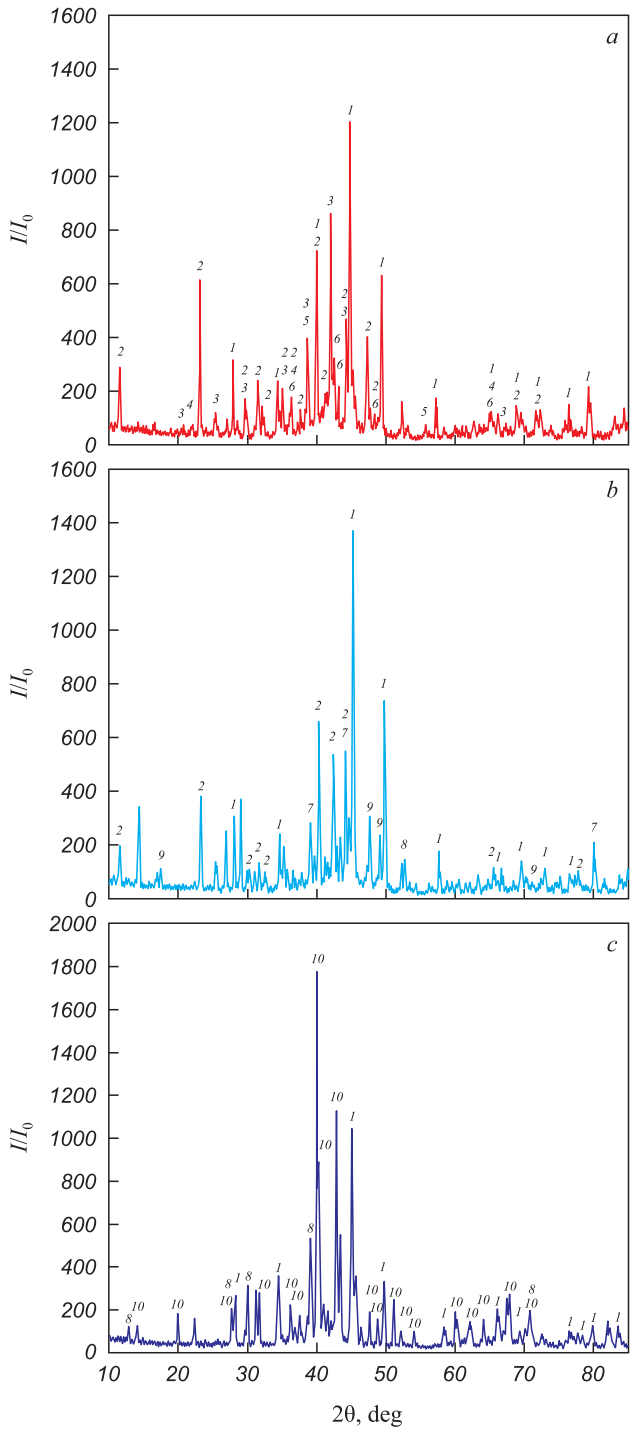

Fig. 3. XRD pattern of complex niobium-containing alloys:
a – alloy *1*; *b* – alloy *2*; *c* – alloy *3*;
1 – FeSi; *2* – $NbFeSi_2$; *3* – $Ti_{50.64}Fe_{28}Al_{41}$; *4* – α-Fe; *5* – $AlNb_7$;
6 – $Ti(Fe_{0.51}Al_{0.49})_2$; *7* – TiAl; *8* – $TiSi_2$; *9* – $FeSi_2$; *10* – $NbFeSi_{1.75}$

Рис. 3. Дифрактограммы комплексных ниобийсодержащих сплавов:
a – сплав *1*; *b* – сплав *2*; *c* – сплав *3*;
1 – FeSi; *2* – $NbFeSi_2$; *3* – $Ti_{50,64}Fe_{28}Al_{41}$; *4* – α-Fe; *5* – $AlNb_7$;
6 – $Ti(Fe_{0,51}Al_{0,49})_2$; *7* – TiAl; *8* – $TiSi_2$; *9* – $FeSi_2$; *10* – $NbFeSi_{1,75}$

est component of the alloy, with a density of 8570 kg/m^3). Additionally, alterations in the phase composition (Fig. 3) also contribute to this observed phenomenon.

In alloy *1*, a significant proportion of the FeSi phase (up to 63 %) contributes to reducing the overall density of the alloy. Conversely, in alloy *2*, the formation of a ternary compound $NbFeSi_2$ occurs, characterized by a high density of 6669 kg/m^3. Additionally, there's the presence of niobium intermetallic compound $AlNb_7$, which holds a density of 8431 kg/m^3. As the niobium concentration escalates to 30 %, there's a reduction in the fraction of the lighter FeSi phase and a subsequent increase in the fraction of the high-density ternary compound $NbFeSi_2$.

A comparable examination was conducted to investigate the impact of niobium concentration on the crystallization temperatures of complex alloys (Fig. 2).

Alloy *1* demonstrates a crystallization range spanning 1690 – 1650 °C, primarily due to the substantial presence of the FeSi phase (~60 %) with a crystallization temperature of 1550 °C. Elevating the niobium concentration from 11.3 to 17.1 % results in a decrease in the crystallization temperature, aligning with the liquidus line on the phase diagram of the Fe–Nb binary system as niobium concentration approaches ~18 % [21; 22]. A further elevation of niobium content in complex alloys to 30 % corresponds to an elevation in both the liquidus and solidus temperatures, reaching 1700 and 1610 °C, respectively. This trend mirrors the liquidus line observed in the Fe–Nb phase diagram, showing a peak at 1627 °C at ~45 % Nb. The notably high liquidus temperature values in alloy *3* are attributed to the considerable content (~53 %) of the refractory phase $NbFeSi_2$, initiating crystallization at ~1713 °C.

Overall, the findings regarding the correlation between niobium concentration and crystallization temperatures in complex alloys align qualitatively with existing data for binary alloys. Shifting from conventional high-percentage ferroniobium featuring 60 % Nb to complex alloys integrating silicon, aluminum, and reduced niobium concentrations allows the transition of alloys from super-refractory to refractory. Notably, alloy *2*, comprising 17.1 % Nb, 24.6 % Si, 7.6 % Al and 3 % Ti, represents low-melting alloys, thereby positively influencing the performance characteristics of niobium ferroalloys.

Conclusions

The research into the physicochemical properties of novel complex niobium-based alloys has revealed promising attributes. These alloys, incorporating silicon, aluminum, and reduced niobium content, exhibit notably advantageous characteristics in terms of density and crystallization temperature when compared to the standard ferroniobium alloy (60 % Nb). Among these new alloys, the one containing 17.1 % Nb, 24.6 % Si, 7.6 % Al and 3 % Ti stands out for its exceptional qualities. With a crystallization initiation temperature of 1550 °C (lower than the liquid steel bath temperature), this alloy falls into the category of low-melting alloys. It boasts an optimal density of 6390 kg/m^3, significantly enhancing its performance attributes, and making it highly recommended for steel processing in ladle applications.

References / Список литературы

1. Leont'ev L.I., Zayakin O.V., Volkov A.I. Problems of the metallurgical industry development to ensure the Russian technological sovereignty taking into account the mineral resource base state. *Vestnik RAN*. 2023;93(7):631–645. (In Russ.).
Леонтьев Л.И., Заякин О.В., Волков А.И. Проблемы развития металлургической отрасли для обеспечения технологического суверенитета России с учетом состояния минерально-сырьевой базы. *Вестник РАН*. 2023;93(7):631–645.
2. Leont'ev L.I., Zhuchkov V.I., Zayakin O.V., Sychev A.V., Mikhailova L.Yu. Potential for obtaining and applying complex niobium ferroalloys. *Izvestiya. Ferrous Metallurgy*. 2022;65(1):10–20. (In Russ.). https://doi.org/10.17073/0368-0797-2022-1-10-20
Леонтьев Л.И., Жучков В.И., Заякин О. В., Сычев А.В., Михайлова Л.Ю. Перспективы получения и применения комплексных ниобиевых ферросплавов. *Известия вузов. Черная Металлургия*. 2022;65(1):10–20. https://doi.org/10.17073/0368-0797-2022-1-10-20
3. Posti A.I. Effect of micro alloying of steel with niobium on the mechanical properties of heat-strengthened rebar. *Lit'e i metallurgiya*. 2021;(1):73–77. (In Russ.). https://doi.org/10.21122/1683-6065-2021-1-73-77
Пости А.И. Влияние микролегирования стали ниобием на механические свойства термоупрочненной арматуры. *Литье и металлургия*. 2021;(1):73–77. https://doi.org/10.21122/1683-6065-2021-1-73-77
4. Sun L.-y., Liu X., Xu X., Lei S.-w., Li H.-g., Zhai Q.-j. Review on niobium application in microalloyed steel. *Journal of Iron and Steel Research International*. 2022;29:1513–1525. https://doi.org/10.1007/s42243-022-00789-1
5. Yan P., Bhadeshia H. Austenite–ferrite transformation in enhanced niobium, low carbon steel. *Materials Science and Technology*. 2015;31(9):1066–1076. https://doi.org/10.1179/1743284714Y.0000000673
6. Nayak S.S., Misra R.D., Hartmann J.E. Microstructure and properties of low manganese and niobium containing HIC pipeline steel. *Materials Science and Engineering: A*. 2008;494(1–2):456–463. https://doi.org/10.1016/j.msea.2008.04.038
7. Akhtar M.N., Khan M., Khan S.A., etc. Determination of non-recrystallization temperature for niobium microalloyed steel. *Materials*. 2021;14(10):2639. https://doi.org/10.3390/ma14102639
8. Guo A., Misra R.D.K., Xuet J., Guo B., Jansto S.G. Ultra-high strength and low yield ratio of niobium-microalloyed 900 MPa pipeline steel with nano/ultrafine bainitic lath. *Materials Science and Engineering: A*. 2010; 527(16-17):3886–3892. https://doi.org/10.1016/j.msea.2010.02.067

9. Matrosov M.Yu., Efron L.I., Kichkina A.A., Lyasotskii I.V. A study of the microstructure of niobium-microalloyed pipe steel after different modes of controlled rolling with accelerated cooling. *Metal Science and Heat Treatment*. 2008; 50(3-4):136–141. https://doi.org/10.1007/s11041-008-9034-3

10. De Ardo A.J. Niobium in modern steels. *International Materials Reviews*. 2003;48(6):371–402. https://doi.org/10.1179/095066003225008833

11. Zhuchkov V.I., Noskov A.S., Zav'yalov A.L. *Dissolution of Ferroalloys in Liquid Metal*. Sverdlovsk: Ural Branch of the USSR Academy of Sciences; 1990:134. (In Russ.).

Жучков В.И., Носков А.С., Завьялов А.Л. *Растворение ферросплавов в жидком металле*. Свердловск: УрО АН СССР; 1990:134.

12. Zhuchkov V.I., Zayakin O.V. Development of composition and process of obtaining multicomponent ferroalloys. *Izvestiya. Ferrous Metallurgy*. 2020;63(10):791–795. (In Russ.). https://doi.org/10.17073/0368-0797-2020-10-791-795

Жучков В.И., Заякин О.В. Разработка состава и процесса получения многокомпонентных ферросплавов. *Известия вузов. Черная металлургия*. 2020;63(10):791–795. https://doi.org/10.17073/0368-0797-2020-10-791-795

13. Emlin B.I., Gasik M.I. *Handbook of Electrothermal Processes*. Moscow: Metallurgiya; 1978:288. (In Russ.).

Емлин Б.И., Гасик М.И. *Справочник по электротермическим процессам*. Москва: Металлургия; 1978:288 с.

14. Gasik L.N., Ignat'ev V.S., Gasik M.I. *Structure and Quality of Industrial Ferroalloys and Alloys*. Kiev: Tekhnika; 1975:128. (In Russ.).

Гасик Л.Н., Игнатьев В.С., Гасик М.И. *Структура и качество промышленных ферросплавов и лигатур*. Киев: Техника; 1975:128..

15. Stroganov A.I. Requirements for ferroalloys for deoxidation and alloying. In: *Transactions of Siberian Metallurgical Institute: Production of Ferroalloys*. Novokuznetsk: Izd. Kuz. PI; 1980:5–24. (In Russ.).

Строганов А.И. Требования к ферросплавам для раскисления и легирования. *Сборник Сибирского металлургического института: Производство ферросплавов*. Новокузнецк: Издательство КузПИ; 1980:5–24.

16. Ignat'ev V.S., Bespalova I.A., Tikhorevsky V.S., etc. Physical properties of alloying alloys. In: *Ferroalloy Production, ser. 5, Chermetinformatsiya. Vol. 2*. Moscow; 1973:16. (In Russ.).

Игнатьев В.С., Беспалова И.А., Тихоревский В.С. и др. Физические свойства легирующих сплавов. *Ферросплавное производство, серия 5, Черметинформация. Выпуск 2*. Москва; 1973:16.

17. Zhuchkov V.I., Vatolin N.A., Zav'yalov A.L. On melting temperatures of ferroalloys. *Metally*. 1982;(4):45–46. (In Russ.).

Жучков В.И., Ватолин Н.А., Завьялов А.Л. О температурах плавления ферросплавов. *Металлы*. 1982;(4):45–46.

18. Parimonchik I.B., Kazachkov I.P., Rezchik V.G. Modeling of ferroalloys dissolution in a steel ladle. *Metallurgiya i koksokhimiya*. 1972;(31):62–65. (In Russ.).

Паримончик И.Б., Казачков И.П., Резчик В.Г. Моделирование процесса растворения ферросплавов в сталеплавильном ковше. *Металлургия и коксохимия*. 1972;(31):62–65.

19. Petrov A.F., Kuksa O.V., Golovko L.A., Khodotova N.E. Prediction of physicochemical and thermophysical properties of standard grade ferroniobium. In: *Fundamental and Applied Problems of Ferrous Metallurgy: Coll. of Sci. Papers*. Dnipro: ICM of the National Academy of Sciences of Ukraine; 2017;31:260–265. (In Russ.).

Петров А.Ф., Кукса О.В., Головко Л.А., Ходотова Н.Е. Прогнозирование физико-химических и теплофизических свойств ферониобия стандартных марок. *Фундаментальные и прикладные проблемы черной металлургии: Сборник научных трудов*. Дніпро.: ІЧМ НАН України; 2017;31:260–65

20. Kel I.N., Zhuchkov V.I., Renev D.S., Lozovay E.Y., Galiahmetova R.I. Study of the physicochemical characteristics of complex boron-containing ferroalloys. *AIP Conference Proceedings*. 2020;2313(1):050015. https://doi.org/10.1063/5.0032689

21. Li K.W., Wang X.B., Li S.M., Wang W.X., Chen S.P., Gong D.Q., Cui J.L. Halo formation in binary Fe-Nb off-eutectic alloys. *High Temperature Materials and Processes*. 2015; 34(5):479–485. https://doi.org/10.1515/htmp-2014-0081

22. *Chemical Portal*. Available at URL: https://himikatus.ru/art/phase-diagr1/Fe-Nb.php (Accessed: 18.10.2023). (In Russ.).

Химический портал. URL: https://himikatus.ru/art/phase-diagr1/Fe-Nb.php (дата обращения: 18.10.2023).

Information about the Authors / Сведения об авторах

Oleg V. Zayakin, *Corresponding Member of RAS, Dr. Sci. (Eng.), Chief Researcher, Head of the Laboratory of Steel and Ferroalloys*, Institute of Metallurgy, Ural Branch of the Russian Academy of Sciences
ORCID: 0000-0002-9442-5928
E-mail: zferro@mail.ru

Il'ya N. Kel', *Cand. Sci. (Eng.), Senior Researcher of the Laboratory of Steel and Ferroalloys*, Institute of Metallurgy, Ural Branch of the Russian Academy of Sciences
ORCID: 0000-0001-6411-6932
E-mail: dunnington@mail.ru

Dmitrii S. Renev, *Junior Researcher of the Laboratory of Steel and Ferroalloys*, Institute of Metallurgy, Ural Branch of the Russian Academy of Sciences
ORCID: 0000-0002-4850-5273
E-mail: sense199@mail.ru

Олег Вадимович Заякин, *член-корреспондент РАН, д.т.н., главный научный сотрудник, заведующий лабораторией стали и ферросплавов*, Институт металлургии Уральского отделения РАН
ORCID: 0000-0002-9442-5928
E-mail: zferro@mail.ru

Илья Николаевич Кель, *к.т.н., старший научный сотрудник лаборатории стали и ферросплавов*, Институт металлургии Уральского отделения РАН
ORCID: 0000-0001-6411-6932
E-mail: dunnington@mail.ru

Дмитрий Сергеевич Ренев, *младший научный сотрудник лаборатории стали и ферросплавов*, Институт металлургии Уральского отделения РАН
ORCID: 0000-0002-4850-5273
E-mail: sense199@mail.ru

Aleksandr V. Sychev, *Cand. Sci. (Eng.), Senior Researcher of the Laboratory of Steel and Ferroalloys*, Institute of Metallurgy, Ural Branch of the Russian Academy of Sciences
E-mail: ntm2000@mail.ru

Lyudmila Yu. Mikhailova, *Cand. Sci. (Eng.), Senior Researcher of the Laboratory of Steel and Ferroalloys*, Institute of Metallurgy, Ural Branch of the Russian Academy of Sciences
ORCID: 0000-0002-9154-8244
E-mail: ferrostal@bk.ru

Aleksei V. Dolmatov, *Cand. Sci. (Chem.), Scientific Secretary, Senior Researcher of the Laboratory of Metallurgical Melts*, Institute of Metallurgy, Ural Branch of the Russian Academy of Sciences
ORCID: 0000-0002-6632-9533
E-mail: dolmatov.imet@gmail.com

Александр Владимирович Сычев, *к.т.н., старший научный сотрудник лаборатории стали и ферросплавов*, Институт металлургии Уральского отделения РАН
E-mail: ntm2000@mail.ru

Людмила Юрьевна Михайлова, *к.т.н., старший научный сотрудник лаборатории стали и ферросплавов*, Институт металлургии Уральского отделения РАН
ORCID: 0000-0002-9154-8244
E-mail: ferrostal@bk.ru

Алексей Владимирович Долматов, *к.х.н., ученый секретарь, старший научный сотрудник лаборатории металлургических расплавов*, Институт металлургии Уральского отделения РАН
ORCID: 0000-0002-6632-9533
E-mail: dolmatov.imet@gmail.com

Contribution of the Authors

O. V. Zayakin – development of complex ferroalloys compositions, analysis of the obtained data, writing the text.
I. N. Kel' – conducting experiments to determine the crystallization temperature of ferroalloys, writing the text.

D. S. Renev – conducting experiments to determine the density of complex ferroalloys.
A. V. Sychev – obtaining prototypes of ferroalloys, editing the text.

L. Yu. Mikhailova – analysis of phase diagrams, editing the text.

A. V. Dolmatov – obtaining prototypes of ferroalloys, visualization.

Вклад авторов

О. В. Заякин – разработка составов комплексных ферросплавов, анализ полученных данных, написание текста публикации.
И. Н. Кель – проведение экспериментов для определения температуры кристаллизации ферросплавов, написание текста публикации.
Д. С. Ренев – проведение экспериментов по определению плотности комплексных ферросплавов.
А. В. Сычев – получение опытных образцов ферросплавов, редактирование текста публикации.
Л. Ю. Михайлова – анализ дифрактограмм, редактирование текста публикации.
А. В. Долматов – получение опытных образцов ферросплавов, подготовка графического материала.

Received 10.10.2023
Revised 17.10.2023
Accepted 18.10.2023

Поступила в редакцию 10.10.2023
После доработки 17.10.2023
Принята к публикации 18.10.2023

On the materials of the International conference "Scientific and Practical School for Young Metallurgists" – 2023

По материалам международной конференции «Научно-практическая школа для молодых металлургов» – 2023

UDC 669.187.56
DOI 10.17073/0368-0797-2023-5-623-630

Original article
Оригинальная статья

Development of technology for ingots production using electroslag remelting at direct current with consumable electrode rotation

I. A. Alekseev[1], I. V. Chumanov[2], D. V. Sergeev[2]

[1] **South Ural State University** (76 Lenina Ave., Chelyabinsk 454080, Russian Federation)
[2] **Zlatoust Branch of the South Ural State University** (16 Turgeneva Str., Zlatoust, Chelyabinsk Region 456217, Russian Federation)

inbox@ivanalekseev.ru

Abstract. The paper describes the problem of increasing the productivity of electroslag remelting (ESR) furnaces. The remelting technology on direct current is proposed as the most effective method. The description of the technology touches upon positive and negative effects affecting the specific productivity of smelting, energy consumption, and quality of the obtained ingots in terms of their physical and mechanical properties and chemical purity. The authors proposed the electroslag remelting method with rotation of the consumable electrode as a new technology, and realized a brief comparison with the external magnetic field application technology. The schemes that clearly demonstrate the principle of controlling the crystallization front shape and the thermal center localization in the slag bath are considered. A stationary numerical model for the slag bath of the operating semi-industrial furnace ESR A-550 on direct current with polarity reversing ability was developed. The mathematical apparatus consisting of electrothermal, hydrodynamic and convective parts was constructed. The authors designed the mesh domain for a slag bath located between the consumable electrode and the water-cooled crystallizer with diameters of 60 and 90 mm, respectively. The height of the sub-electrode zone is 10 mm. The current limit is 800 A and the voltage is 46 V. Numerical fields of current density and temperature distribution in the slag bath volume are obtained. The range of temperature values is located in the range from 1400 to 2200 °C at the peripheral and subelectrode zones of the slag bath, respectively. The scheme of the ESR furnace modernization is given in terms of mechanical part automation and transferring to direct current.

Keywords: electroslag refining, electrothermy, consumable electrode, finite volume method, computational fluid dynamics, computer simulation, mathematical modeling, technology, rotating electrode, direct current

Acknowledgements: The work was supported by the Russian Science Foundation, grant No. 22-29-20049, https://rscf.ru/project/22-29-20049/.

For citation: Alekseev I.A., Chumanov I.V., Sergeev D.V. Development of technology for ingots production using electroslag remelting at direct current with consumable electrode rotation. *Izvestiya. Ferrous Metallurgy*. 2023;66(5):623–630.
https://doi.org/10.17073/0368-0797-2023-5-623-630

Разработка технологии получения слитков при ЭШП на постоянном токе с вращением расходуемого электрода

И. А. Алексеев[1], И. В. Чуманов[2], Д. В. Сергеев[2]

[1] **Южно-Уральский государственный университет** (Россия, 454080, Челябинск, пр. Ленина, 76)
[2] **Южно-Уральский государственный университет (национальный исследовательский университет), филиал в г. Златоуст** (Россия, 456217, Челябинская обл., Златоуст, ул. Тургенева, 16)

inbox@ivanalekseev.ru

Аннотация. В работе рассмотрен вопрос повышения производительности печей электрошлакового переплава. В качестве наиболее эффективного метода предложена технология ведения переплава на постоянном токе. Описание технологии затрагивает положительные и отрицательные эффекты, влияющие как на удельную производительность плавки, энергопотребление, так и на качество получаемых слитков в части их физико-механических свойств и химической чистоты. Способ ведения электрошлакового переплава с вращением расходуемого электрода предложен в качестве новой технологии, осуществлено краткое сравнение с используемой технологией наложения внешнего магнитного поля. Продемонстрированы схемы, которые наглядно показывают принцип управления формой

фронта кристаллизации и локализацией теплового центра шлаковой ванны. Разработана стационарная численная модель для рабочей зоны действующей полупромышленной печи ЭШП А-550 на постоянном токе со сменой полярности. Создан математический аппарат, состоящий из электротермической, гидродинамической и конвективной частей. Геометрическая расчетная область спроектирована для шлаковой ванны, расположенной между расходуемым электродом и водоохлаждаемым кристаллизатором с диаметрами 60 и 90 мм соответственно. Высота подэлектродной зоны составляет 10 мм. Предельная величина тока 800 А, напряжение 46 В. Получены числовые поля распределения плотности тока и температуры в толще шлаковой ванны. Диапазон значений температуры располагается в пределах от 1400 до 2200 °С на периферийной и подэлектродной зонах шлаковой ванны соответственно. Приведена схема модернизации печи ЭШП за счет автоматизации механической части и перевода на постоянный ток.

Ключевые слова: электрошлаковый переплав, электротермия, расходуемый электрод, метод конечных объемов, вычислительная гидродинамика, компьютерное моделирование, математическое моделирование, технология, вращающийся электрод, постоянный ток

Благодарности: Работа выполнена за счет гранта Российского научного фонда № 22-29-20049, https://rscf.ru/project/22-29-20049/.

Для цитирования: Алексеев И.А., Чуманов И.В., Сергеев Д.В. Разработка технологии получения слитков при ЭШП на постоянном токе с вращением расходуемого электрода. *Известия вузов. Черная металлургия*. 2023;66(5):623–630.
https://doi.org/10.17073/0368-0797-2023-5-623-630

Introduction

One of the promising directions for improving electroslag remelting (ESR) technology, as well as other industrial electrometallurgical processes, involves optimizing the technical and economic performance of smelting furnaces. The prevalent design of ESR equipment consists of furnaces operating on alternating current at industrial frequency [1]. In line with electrical engineering principles, direct current has an advantage over alternating current in minimizing energy losses due to the absence of inductive reactance in the main current-carrying circuit. Using this characteristic of electric current, it is rational to carry out remelting using direct current, which not only reduces energy losses, but also facilitates the arrangement of polarization in the slag bath. This directly impacts not only the localization of heat generation following the Joule–Lenz law, also known as Joule heat, but also enables electrolysis reactions [2; 3]. The inclusion of electrolysis stands as a pivotal aspect of utilizing direct current, notably employed in vacuum arc remelting (VAR) furnaces to eliminate hydrogen from the chemical composition of remelted steels and alloys. Direct current is acknowledged to have a significant adverse effect, notably evident in continuous liquid and gas environments, termed magnetic blowout [4]. In engineering, the prevalent method to counteract the negative impacts of magnetic blowout in direct current welding involves controlling the behavior of the electric arc, particularly in manual electric welding [5]. During direct current ESR, magnetic blowout distorts the crystal structure of the ingot, completely compromising its isotropic physical and mechanical properties. There exist methodologies to mitigate the influence of magnetic blowout on metal during direct current ESR, incorporating the utilization of a symmetrical current conductor to the tray and the consumable electrode. However, it remains challenging to entirely eliminate the adverse effects of magnetic blowout due to the presence of a current-conducting crystallizer, leading to magnetic blowout when employing current conductors with a pipe–spike arrangement. Consequently, ESR with direct current is exclusively performed at the maximum achievable fill factor, using reverse polarity, thereby enhancing the refining capacity of the remelting process and optimizing heat utilization, primarily emanating from the consumable electrode's end [6].

This study proposes the use of direct current in ESR technology along with a rotating consumable electrode, presenting an effective approach to enhance metal remelting. This method ensures the isotropic nature of physical and mechanical properties in resulting ingots without compromising the refining capacity inherent in ESR technology. Maintaining isotropy in physical and mechanical properties implies preserving a high-quality crystal structure characterized by a uniform orientation of dendrite axes aligned coaxially with the ingot's geometric axis, as well as achieving a higher density of crystals. The chemical properties of metal are characterized by ensuring homogeneity in the chemical composition of the base metal and addressing the presence of harmful impurities and gases. Homogeneity, in this context, refers to the uniform distribution of the base metal and particles of detrimental impurities and gases throughout the body of the crystallized ingot. This distribution occurs without permitting additional contamination during the remelting process.

The objective of this study is to acquire data of the electrothermal process occurrence within the slag bath of the A-550 ESR furnace by creating a digital twin, subsequently enabling its validation.

The research aims are as follows:

– development of a numerical model of current kinetics within the slag bath of an ESR furnace;

– acquisition of the distribution field of current density and temperature within the spatial confines of the slag bath, followed by comprehensive analysis;

– formulation of a schematic diagram designed to upgrade the A-550 ESR furnace, facilitating the implementation of a direct current-based system allowing rotation of the consumable electrode, alongside its subsequent realization.

Materials and methods

The impact of rotating the consumable electrode on the metal mirrors the effect observed when applying an external magnetic field via a coil surrounding a water-cooled crystallizer. In both scenarios, an active rotation of the slag and metal baths takes place. However, the exposure to an external magnetic field at the interface between the slag bath and the metal film, located at the consumable electrode's end, prompts the liquid slag to drag the liquid metal film due to interfacial surface tension forces [7]. In contrast, when employing the rotation of a consumable electrode, its structure captures the slag bath and transmits a co-directed rotational motion to it, gradually dissipating from the center towards the periphery [8]. The external magnetic field generated by the coil predominantly affects metal droplets at the outer edge of the consumable electrode's end, influenced by surface tension, with limited impact on the central droplets. Conversely, the rotation of the consumable electrode directly influences the entire liquid metal formed at its end until it separates into droplets due to gravitational forces.

Both methods offer means to mitigate the effects of magnetic blowout. However, utilizing the consumable electrode's rotation technology not only efficiently suppresses Ampere forces acting on the metal film and metal droplets during their transfer through the slag bath but also allows for tracking and controlling their trajectory within the slag bath and their landing on the metal bath surface. Fig. 1 presents a schematic diagram depicting the approximate trajectories of falling metal drops under two conditions: a stationary consumable electrode (or a consumable electrode rotating at an insufficient speed) and a rotating consumable electrode operating at an optimal speed.

Fig. 1 illustrates that by using the impact of the consumable electrode's rotation, it becomes feasible to efficiently mitigate the effect of magnetic blowout under any conditions while exercising control over the trajectories of falling metal drops. This control is achieved through the centrifugal force's magnitude, which is directly reliant on both the rotation speed and the diameter of the consumable electrode.

Addressing the energy efficiency concerns of a DC ESR furnace involves managing the positioning of the heat center and the associated heat release, adhering to the Joule–Lenz law. The utilization of direct current facilitates the polarization of charges within the slag bath, directly influencing the placement of the heat center. The intensity of Joule heat release correlates directly with the specific current density. Within the operational space of an ESR furnace's slag bath, the specific electrical conductivity remains relatively consistent but varies proportionally with specific temperature. As metal droplets traverse the slag bath, they encounter regions of heightened electrical conductivity, momentarily creating branches of current flow. The refinement of droplets and their increased formation represent prerequisites for elevating the specific current density within the slag bath. Fig. 2 depicts a diagram illustrating the distribution of heat within a slag bath featuring both stationary and rotating consumable electrodes.

In Fig. 2 illustrates that when employing direct polarity in direct current, the heat center within the slag bath resides at its interface with the metal bath. This displacement results in the formation of a pronounced meniscus within the resulting ingot, with its vertical extent expanding due to axial metal droplet transfer. Notably, for the sake of comparative clarity with the technology involving the rotation of the consumable electrode,

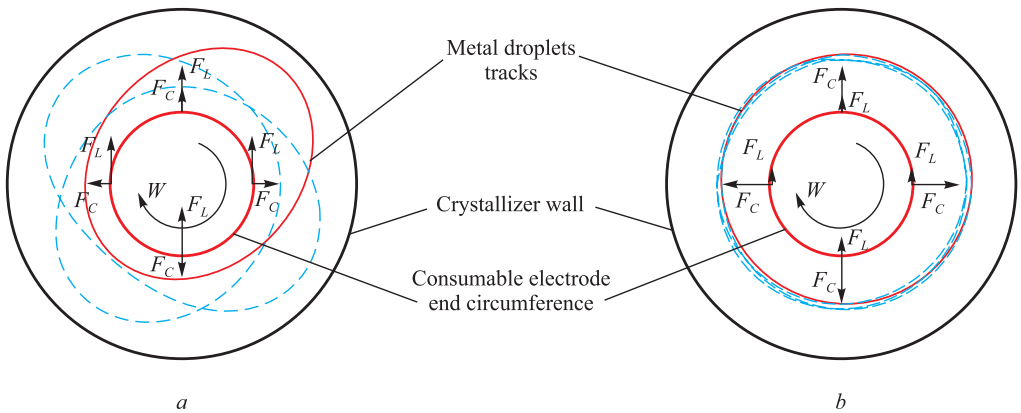

Fig. 1. Metal droplets tracks and vectors of the acting forces:
a – stationary or rotating with insufficient speed consumable electrode;
b – rotating with optimal speed consumable electrode; F_L – Lorentz force; F_C – centrifugal force

Рис. 1. Траектории падения капель металла и векторы воздействующих сил:
a – стационарный или вращающийся с недостаточной скоростью расходуемый электрод;
b – вращающийся с оптимальной скоростью расходуемый электрод; F_L – сила Лоренца; F_C – центробежная сила

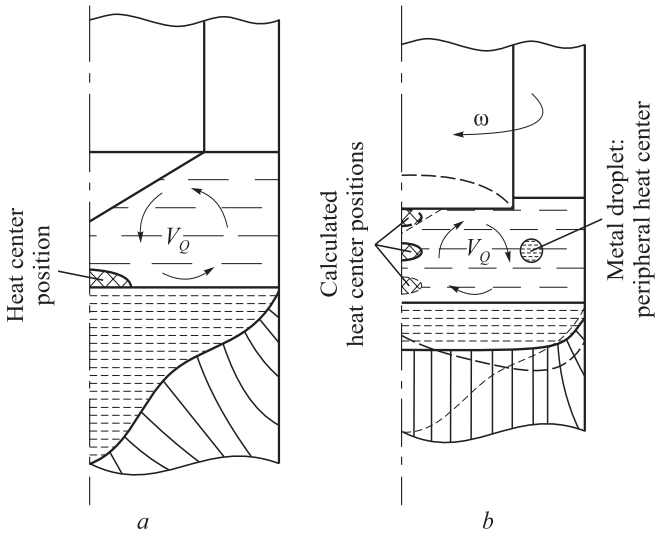

Fig. 2. Heat centers' positions and directions of the convective fluxes at stationary (*a*) and rotating (*b*) electrodes in direct current polarity: V_Q – convection in slag bath; ω – angle speed

Рис. 2. Расположение тепловых центров и направленность конвективных потоков при стационарном (*a*) и вращающемся (*b*) расходуемых электродах при прямой полярности тока: V_Q – конвекция в шлаковой ванне; ω – угловая скорость

the impact of magnetic blowout is not accounted for in this scenario. Under the rotation of the consumable electrode, active movement of the slag bath ensues, accompanied by reversed convective fluxes compared to the stationary method. The transfer of droplets shifts from the center to the periphery of the slag bath. This alteration, coupled with the revised direction of convective fluxes, modifies the shape of the crystallization front, resulting in a flatter metal bath. This alteration proves advantageous for the ingot's crystal structure. As the consumable electrode's rotation speed escalates, the intensity of droplet transfer and convective flux velocity increases. Consequently, these flows begin to wash the end of the consumable electrode upward along its axis. When combined with the direct current's polarity, this phenomenon can effectuate the displacement of the heat center along the consumable electrode's axis and within the ingot. However, surpassing critical values might lead to the formation of a concave end on the consumable electrode, diminishing droplet transfer intensity, enlarging droplet size, thereby creating an undesirable melting condition. Additionally, a peripheral meniscus in the metal bath might also form. Further insight into this issue, studied through physical simulation, is detailed in [9].

The determination of the effective current mode, coupled with the corresponding rotation mode of the consumable electrode, is achievable through the construction of a numerical model based on computational fluid dynamics principles. This approach has proven efficient in studying ESR, spanning from initial stationary problems [10; 11] to unsteady magnetohydrodynamic scenarios involving multiphase flow [12; 13]. The numerical simulation was conducted to analyze current distribution [14; 15] and the impact of external factors – such as the rotation of the consumable electrode – on melting speed [16; 17]. Additionally, electrochemical simulation concepts aimed at determining the resulting metal's chemical homogeneity were developed [18 – 20].

The task of determining the amount of Joule heat released and localizing the heat center necessitates a combined approach to solving three subproblems: electrothermal, hydrodynamic, and convective. The electrothermal problem simulates direct current kinetics, adhering to the following fundamental law of the motion:

$$\frac{\partial j}{\partial \tau} = -\nabla\varphi + \nabla(\sigma\nabla j), \qquad (1)$$

where j is the vector of specific current density, A/m^2; τ is the time step, s; ∇φ is the gradient of electrical potentials' difference, V; σ is the specific electrical conductivity of the environment, S.

The hydrodynamic problem is described by the Navier–Stokes transport equation:

$$\frac{\partial v}{\partial \tau} + \nabla v(v) = -\nabla p + \nabla(\mu\nabla v) + S_b - S_{sj}v, \qquad (2)$$

where v is the specific speed vector, m/s; p is the specific hydrostatic pressure, Pa; μ is the kinematic viscosity of the environment, Pa·s; S_b is the Archimedes buoyant force, N; S_{sj} is the origin of crystallization/melting phenomena.

The problem of convective propagation and heat distribution is addressed through the energy transport equation:

$$\frac{\partial H}{\partial \tau} + \nabla(\vec{v}H) = \nabla(\lambda\nabla t) + q_{JH} - \frac{\partial \Delta H}{\partial \tau}, \qquad (3)$$

where H is the specific enthalpy, J; λ is the specific thermal conductivity, J/kg·K; q_{JH} is the specific amount of heat released according to the Joule–Lenz law, J.

Results and discussion

Iterative calculations were carried out on a computational grid, representing a two-dimensional portrayal of a slag bath in a longitudinal section. To facilitate subsequent validation on an operational ESR furnace, the geometric dimensions corresponding to the consumable electrode and the water-cooled crystallizer were considered. The outer surface diameter of the consumable electrode is 60 mm, the internal diameter of the crystallizer is 90 mm, and the height of the subelectrode zone is set at 10 mm for enhanced result visualization. Given the relatively small length of the simulated area in comparison to the total

length of the 590 mm water-cooled crystallizer, the inclination angle of the internal surface of the crystallizer (1.2°) was disregarded. During simulation, the current regime was set at 800 A and 46 V. The electrical conductivity of the environment was fixed at 120 S.

Post the iterative calculations on the established numerical model, output data was obtained and processed visually. This processing yielded information regarding the current kinetics in the slag bath and the temperature field. Figures displaying numerical fields of direct current kinetics are presented in Fig. 3.

Observations reveal that when melting using direct current of direct polarity is executed, the highest electric current density occurs above the surface of the metal bath. This density exhibits a gradient, declining from the center to the periphery and from the metal bath surface towards the consumable electrode surface. Conversely, the reverse pattern is evident in the image depicting reverse polarity, where the highest current density is observed at the end of the consumable electrode. Since Joule heat is released in regions of highest current density, its distribution reflects the pattern of the current density distribution. The silhouette of Joule heat mirrors the current density distribution pattern, as the equation determining the amount of Joule heat yields a scalar value derived from the absolute value modulus of the current density vector. Variations exist only in the absolute values of the numerical fields.

Fig. 4 depicts the temperature distribution diagram within the space of the slag bath.

Under the application of direct polarity current, a gradual reduction in the temperature gradient is observable, extending from the center of the metal bath surface towards its periphery. This configuration highlights the hottest zone, represented as a concentrated spot at the center of the metal bath surface. The overall gradient exhibits a convex shape, tapering towards the end of the consumable electrode. However, in its vicinity, the temperature field expands somewhat, creating a distinctive hourglass shape with a lengthened lower part and a shortened upper section. A decline in temperature is evident as one approaches the periphery, particularly noticeable in the upper section of the crystallizer wall and the atmosphere – slag interface. Increased temperature at the slag-metal interface near the mold wall results from heightened current density arising due to the use of direct polarity. Upon examination of the temperature numerical field with reverse polarity current, the temperature gradient is similarly distributed from the central area towards the periphery. However, there is no evident localization of heightened current density foci akin to the direct polarity scenario. This lack of concentration could possibly stem from the smaller diameter of the consumable electrode relative to the metal bath, resulting in a reduced amount of released heat under reverse polarity. This decrease is attributed to a lesser amount of current flowing through a smaller diameter section, leading to reduced specific density. The longitudinal profile of the temperature gradient exhibits a concave shape, converging towards the surface of the metal bath but remaining nearly linear in its proximity, with a temperature drop evident towards the crystallizer wall. Here, the mold wall demonstrates higher efficiency in absorbing heat around the slag – metal interface due to the change in current direction. The vicinity surrounding the surface of the consumable electrode acts as a heightened heat source, causing relatively poorer heat removal at the atmosphere – slag interface compared to direct current polarity.

Quantitative data pertaining to current density and temperature characterizes the thermal distribution within the slag bath space, facilitating the prediction of furnace operating boundaries ranging from the complete absence of metal droplet transfer to the occurrence of jet metal transfer. Considering that the maximum temperature under direct polarity can reach 2200 °C above the metal bath's surface, it becomes imperative to employ the rotation of a consumable electrode with a 60 mm diameter,

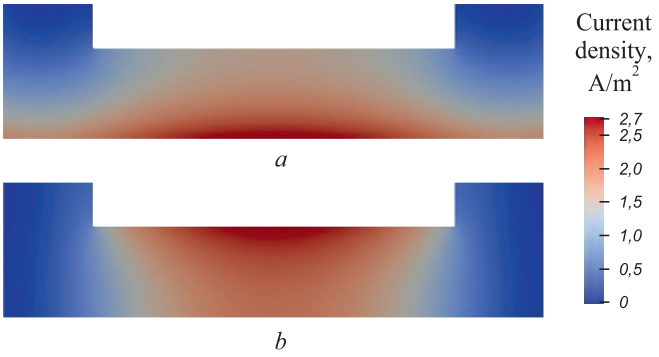

Fig. 3. Numerical fields of current density distribution in slag bath in direct (*a*) and reversed (*b*) current polarities

Рис. 3. Числовые поля распределения плотности тока в шлаковой ванне для прямой (*a*) и обратной (*b*) полярностей тока

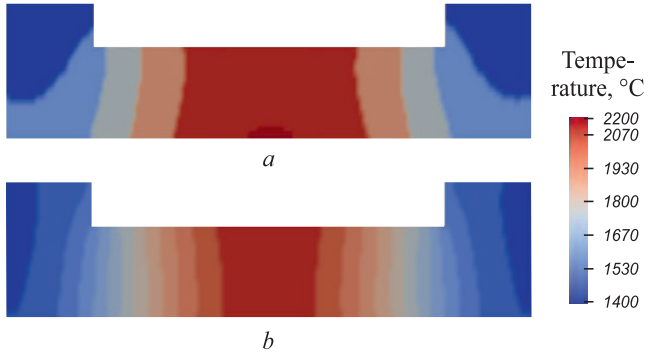

Fig. 4. Numerical fields of temperature distribution in slag bath in direct (*a*) and reversed (*b*) current polarities

Рис. 4. Числовые поля распределения температуры в шлаковой ванне для прямой (*a*) и обратной (*b*) полярностей тока

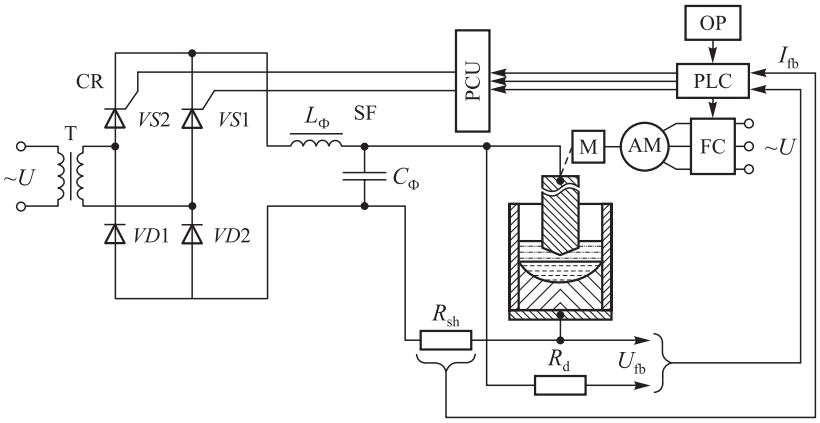

Fig. 5. Functional scheme for semi-industrial ESR furnace A-550

Рис. 5. Функциональная схема действующей полупромышленной печи ЭШП А-550

within a speed range of 80 – 120 rpm. This selection aligns with empirical results obtained from experimental melts detailed in [3]. This rotational mode, in conjunction with the designated power of the ESR furnace, necessitates conditions ensuring enhanced efficiency while maintaining the maximum achievable melting speed without transitioning to jet metal transfer.

To further advance the technology and validate the numerical model, experimental melts are essential. Throughout the project, the existing A-550 ESR furnace underwent modernization, involving the automation of mechanical and electrical components and reconfiguration to operate using direct current. Fig. 5 depicts the functional diagram of the modernized furnace.

The furnace's power supply system incorporates several key components, including a current regulator featuring a single-phase transformer (T), a controllable rectifier (CR), a phase pulse control unit (PCU), a smoothing filter (SF), a feedback loop on the current (I_{fb}), cdetected via a resistive shunt (R_{sh}), within the furnace power circuit, a control programmable logic controller (PLC), and an operator touch panel (OP). Furthermore, the automated furnace control system encompasses a slag pool voltage regulator, constructed around an electrode supply drive housing a transmission mechanism (M), an asynchronous squirrel-cage motor (AM), a transistor frequency converter (FC), a control programmable logic controller (PLC) that receives a feedback signal (U_{fb}), and an operator touch panel (OP).

Conclusions

A numerical model of an operating semi-industrial ESR furnace running on direct current of direct and reverse polarity has been developed. This model includes a computational grid, mathematical apparatus, an algorithm implemented on a computer, and a program code.

Iterative simulations were conducted, yielding results in the form of numerical fields that underwent post-processing for visualization purposes. These results clearly demonstrate the nature of the distribution of electric current and temperature in the slag bath. They do not contradict previously conducted research in this area and do not violate the laws of nature, which makes them valid for further application.

The acquired insights into temperature and current density distribution within the slag bath offer both qualitative and quantitative perspectives on the electrothermal processes occurring in this space. However, this model necessitates further development, particularly in incorporating the magnetic component of direct current, specifically the Lorentz force achieved through the rotation of the consumable electrode. Simulating this scenario, considering the magnetic aspect of the current, would require transitioning to a wave representation of electric current movement within a blend of electric and magnetic fields through their respective potentials.

The A-550 ESR furnace underwent modernization, involving the automation of its electrical and mechanical components and conversion to direct current for conducting experimental validation melts.

References / Список литературы

1. Pavlov V.A. *Special Electrometallurgy of Steels and Alloys*. Yekaterinburg: URFU; 2018:168. (In Russ.).

   Павлов В.А. *Спецэлектрометаллургия сталей и сплавов*. Екатеринбург: Издательство УрФУ; 2018:168.
2. Seliverstov D.A., Pyatygin D.A., Chumanov I.V. To the issue of economic conversion feasibility of VAR furnaces to DC ESR furnaces. *Izvestiya. Ferrous Metallurgy*. 2007;50(1): 24–26. (In Russ.).

   Селиверстов Д.А., Пятыгин Д.А., Чуманов И.В. К вопросу экономической целесообразности перевода печей ВДП в печи ЭШП на постоянном токе. *Известия вузов. Черная металлургия*. 2007;50(1):24–26.
3. Pyatygin D.A., Chumanov I.V. Influence of current type and rotation speed of consumable electrode on mechanical pro-

perties of electroslag metal. *Vestnik YuUrGU. Seriya: metallurgiya*. 2011;14(231):40–44. (In Russ.).

Пятыгин Д.А., Чуманов И.В. Влияние рода тока и скорости вращения расходуемого электрода на механические свойства электрошлакового металла. *Вестник ЮУрГУ. Серия: металлургия*. 2011;14(231):40–44.

4. Chumanov I.V., Pyatygin D.A. Influence of ponderomotive forces on the melt. In: *Computer Modeling of Physicochemical Properties of Glasses and Melts. Proceedings of IX Russ. Seminar, October 14–17, 2008, Kurgan*. Kurgan: Kurgan State University; 2008:64–65. (In Russ.).

   Чуманов И.В., Пятыгин Д.А. Влияние пондеромоторных сил на расплав. В кн.: *Компьютерное моделирование физико-химических свойств стекол и расплавов. Труды IX Российского семинара 14–17 октября 2008 г., Курган*. Курган: Издательство Курганского государственного университета; 2008:64–65.

5. Vinogradov V.S. *Equipment and Technology of Automatic and Mechanized Arc Welding*. Moscow: Academiya; 1997:319. (In Russ.).

   Виноградов В.С. *Оборудование и технология дуговой автоматической и механизированной сварки*. Москва: Издательский центр «Академия»; 1997:319.

6. Klyuev M.M., Volkov S.E. *Electroslag Remelting*. Moscow: Metallurgiya; 1984:208. (In Russ.).

   Клюев М.М., Волков С.Е. *Электрошлаковый переплав*. Москва: Металлургия; 1984:208.

7. Protokovilov I.V., Porokhon'ko V.B. Physical modeling of consumable electrode melting at ESR under external electromagnetic conditions. *Sovremennaya electrometallurgiya*. 2015;(1):8–12. (In Russ.).

   Протоковилов И.В., Порохонько В.Б. Физическое моделирование процесса плавления расходуемого электрода при ЭШП в условиях внешнего электромагнитного воздействия. *Современная электрометаллургия*. 2015;(1):8–12.

8. Chumanov I.V., Pyatygin D.A., Roschin V.E. Features of electroslag process on direct current with electrode rotation. In: *Modern Problems of Steel Electrometallurgy. Materials of XI Int. Conf., September 25–27, 2001, Chelyabinsk*. Chelyabinsk: SUSU; 2001:117–118. (In Russ.).

   Чуманов И.В., Пятыгин Д.А., Рощин В.Е. Особенности электрошлакового процесса на постоянном токе с вращением электрода. В книге: *Современные проблемы электрометаллургии стали. Материалы XI Международной конференции 25–27 сентября 2001 г., Челябинск*. Челябинск: Издательство ЮУрГУ; 2001: 117–118.

9. Sergeyev D.V. *Hollow billet production by electroslag remelting with single-electrode scheme: Cand. Tech. Sci. Diss*. Chelyabinsk; 2022:126. (In Russ.).

   Сергеев Д.В. *Технология получения полой заготовки методом электрошлакового переплава по одноэлектродной схеме: Диссертация ... кандидата технических наук*. Челябинск; 2022:126 с.

10. Dilawari A.H., Szekely J. Heat transfer and fluid flow phenomena in electroslag refining. *Metallurgical Transactions B*. 1978;9B(2):77–87. https://doi.org/10.1007/BF02822674

11. Choudhary M., Szekely J., Medovar B.I., Yemel'yanenko Yu.G. The velocity field in the molten slag region of ESR systems: a comparison of measurements in a model system with theoretical predictions. *Metallurgical Transactions B*. 1978;13B(1):35–43. https://doi.org/10.1007/BF02666953

12. Kelkar K.M., Mok J., Patankar S.V., Mitchel A. Computational modeling of electroslag remelting processes. *Journal de Physique IV*. 2004;120:421–428. https://doi.org/10.1051/jp4:2004120048

13. Kharicha A., Schutzenhofer W., Ludwig R., Tanzer R., Wu M. On the importance of electric currents flowing directly into the mould during an ESR process. *Steel Research International*. 2008;79(8):632–636. https://doi.org/10.1002/srin.200806176

14. Kharicha A., Karimi-Sibaki E., Wu M., Ludwig A. Contribution of the mold current to the ingot surface quality in the electroslag remelting process. In: *The Minerals, Metals and Materials Society. Proceedings of the 2013 Int. Symp. on Liquid Metal Processing & Casting, September, 2013 TMS*; 2013:95–99. https://doi.org/10.1002/9781118830857.ch13

15. Kharicha A., Wu M., Ludwig A., Karimi-Sebaki E. Simulation of the electric signal during the formation and departure of droplets in the electroslag remelting process. *Metallurgical and Materials Transactions B*. 2016;47(2):1427–1434. https://doi.org/10.1007/s11663-015-0550-4

16. Wang F., Wang Q., Lou Y., Chen R., Song Z., Li B. Investigation of heat transfer and magnetohydrodynamic flow in electroslag remelting furnace using vibrating electrode. *JOM*. 2015;68(1):410–420. https://doi.org/10.1007/s11837-015-1684-1

17. Wang Q., Gosselin L., Li B. Effect of rotating electrode of magnetohydrodynamic flow and heat transfer in electroslag remelting process. *ISIJ International*. 2014;54(12):2821–2830. https://doi.org/10.2355/isijinternational.54.2821

18. Karimi-Sibaki E., Kharicha A., Wu M. Toward modeling electrochemical reactions during electroslag remelting (ESR) process. *Steel Research International*. 2017;88(5):1700011. https://doi.org/10.1002/srin.201700011

19. Karimi-Sibaki E., Kharicha A., Wu M., Ludwig A., Bohacek J. A numerical investigation on the electrochemical behavior of CaO and Al_2O_3 in the ESR slags. *Metallurgical and Materials Transactions B*. 2020;51:871–879. https://doi.org/10.1007/s11663-020-01795-y

20. Wang Q., Li G., He Z., Li B. A three-phase comprehensive mathematical model of desulfurization in electroslag remelting process. *Applied Thermal Engineering*. 2017;114:874–886. https://doi.org/10.1016/j.applthermaleng.2016.12.035

Information about the Authors

Ivan A. Alekseev, *Postgraduate of the Chair "Pyrometallurgical and Foundry Technologies"*, South Ural State University
E-mail: inbox@ivanalekseev.ru

Il'ya V. Chumanov, *Dr. Sci. (Eng.), Prof., Head of the Chair "Technique and Technology of Materials Production"*, Zlatoust Branch of the South Ural State University
E-mail: chumanoviv@susu.ru

Dmitrii V. Sergeev, *Cand. Sci. (Eng.), Engineer of the Chair "Technique and Technology of Materials Production"*, Zlatoust Branch of the South Ural State University
E-mail: sergeevdv@susu.ru

Сведения об авторах

Иван Андреевич Алексеев, *аспирант кафедры «Пирометаллургические и литейные технологии»*, Южно-Уральский государственный университет
E-mail: inbox@ivanalekseev.ru

Илья Валерьевич Чуманов, *д.т.н., профессор, заведующий кафедрой «Техника и технологии производства материалов»*, Южно-Уральский государственный университет (национальный исследовательский университет), филиал в г. Златоуст
E-mail: chumanoviv@susu.ru

Дмитрий Владимирович Сергеев, *к.т.н., инженер кафедры «Техника и технологии производства материалов»*, Южно-Уральский государственный университет (национальный исследовательский университет), филиал в г. Златоуст
E-mail: sergeevdv@susu.ru

Contribution of the Authors

I. A. Alekseev – mathematical and computer modeling, development of melting mode, development of furnace automation electric scheme, preparation of the manuscript.
I. V. Chumanov – setting goals and objectives, scientific and methodological guidance.
D. V. Sergeev – organization and implementation of ESR furnace modernization.

Вклад авторов

И. А. Алексеев – математическое и компьютерное моделирование, разработка режима плавки, разработка электрической схемы автоматизации печи, подготовка рукописи.
И. В. Чуманов – постановка целей и задач работы, научно-методическое руководство.
Д. В. Сергеев – организация и осуществление работ по модернизации печи ЭШП.

Received 01.09.2023
Revised 30.09.2023
Accepted 09.10.2023

Поступила в редакцию 01.09.2023
После доработки 30.09.2023
Принята к публикации 09.10.2023

Наукометрические показатели журнала

В 2017 году международная база данных Scopus возобновила индексирование журнала «Известия ВУЗов. Черная металлургия». На инфографике отражены текущие показатели.

Данные предоставлены сайтами https://www.scopus.com, https://www.scimagojr.com и https://www.scival.com

Над номером работали:

Л.И. Леонтьев, *главный редактор*

Е.В. Протопопов, *заместитель главного редактора*

Е.А. Ивани, *заместитель главного редактора*

Л.П. Бащенко, *заместитель ответственного секретаря*

Е.Ю. Потапова, *заместитель главного редактора по развитию*

О.А. Долицкая, *научный редактор*

Е.М. Запольская, *ведущий редактор*

А.О. Гашникова, *ведущий редактор*

В.В. Расенець, *верстка, иллюстрации*

Г.Ю. Острогорская, *менеджер по работе с клиентами*

Подписано в печать 25.10.2023. Формат 60×90 $^{1}/_{8}$. Бум. офсетная № 1.
Печать цифровая. Усл. печ. л. 15,25. Заказ 18446. Цена свободная.

Отпечатано в типографии Издательского Дома МИСИС.
119049, Москва, Ленинский пр-кт, д. 4, стр. 1.
Тел./факс: (499) 236-76-17

Зарегистрирован Федеральной службой по надзору в сфере связи, информационных технологий и массовых коммуникаций. Свидетельство о регистрации ПИ № ФС77-35456.

Подписной индекс 70383.